Effect of iron endpoint during Peirce-Smith converting on matte mineralogy and downstream processing of base and platinum-group metals

by

Elton Llyle Thyse

Dissertation presented for the Degree

of

DOCTOR OF PHILOSOPHY
EXTRACTIVE METALLURGICAL ENGINEERING

in the Faculty of Engineering
at Stellenbosch University

Supervisor
Prof. G. Akdogan

December 2014

DECLARATION

By submitting this dissertation electronically, I declare that the entirety of the work contained therein is my own, original work, that I am the sole author thereof (save to the extent explicitly otherwise stated), that reproduction and publication thereof by Stellenbosch University will not infringe any third party rights and that I have not previously in its entirety or in part submitted it for obtaining any qualification.

Date: ……..

ABSTRACT

The process route for the production of base and platinum-group metals from natural sulfide ores commonly requires the conversion of high-iron furnace matte into an iron-lean converter matte. This is followed by pre-treatment through cooling of the iron-lean molten matte, physical processing of the solidified matte and hydrometallurgical metal extraction. Lonmin is the third largest producer of platinum-group metals in the world and utilizes Peirce-Smith converters for blowing high-iron furnace matte with air to a final iron concentration or endpoint. The molten matte is water granulated and solidification occurs via fast-cooling. The solidified matte is ground in a closed circuit ball mill with hydrocyclone classification and subjected to first stage atmospheric leaching. The specification of an ideal or desirable converter iron endpoint requires careful consideration. Most importantly, it must ensure the crystallization of converter matte with mineralogical qualities that are within the setpoints of the downstream unit processes and techniques. An additional consideration is for the final blown converter matte to achieve an optimum bulk concentration of the base metals Ni and Cu and platinum-group metals Pt, Pd, Rh, Ru and Ir.

Mattes characteristic of variable iron endpoints were regularly produced at the Lonmin converter plant section. Uncertainty by plant metallurgists in knowing the desirable iron endpoint, particularly within the context of the Lonmin base metal refinery, and poor control has had detrimental effects on the mineralogical quality of the final matte and hence on the processing characteristics of the solidified matte particles downstream. A desirable iron endpoint required investigation, selection and implementation at Lonmin. The primary focus of this study was therefore to quantify the effect of a specific iron endpoint on the mineralogy and mineral chemistry of solidified converter matte. A fundamental examination of the solidification process upon cooling was regarded as critical to an in-depth understanding of the attained mineralogy and mineral chemistry as a function of a specific iron endpoint. It became equally important to quantify the effect of the

resultant mineralogy, and hence iron endpoint, on the physical property of mineral structures in relation to downstream grinding, liberation and leaching characteristics.

Despite considerable industry context, limited in-depth and coherent studies on the effect of a specific iron endpoint on fast-cooled converter matte systems were found in both industrial and scholarly literature. Previous findings in literature offered a limited quantitative understanding of the effect on mineralogy and mineral chemistry. Phase and cooling equilibria of multi-component, iron endpoint specific Ni-Cu-S matte systems were also not fully available. These would have been particularly useful in understanding the complexities of converter matte solidification as a function of iron endpoint. Physical property knowledge of converter matte mineral structures was hardly available and even less so in relation to grinding, liberation and leaching processes. A comprehensive investigation was therefore required to address these extensive knowledge gaps with respect to fast-cooled converter matte systems in an industrial framework.

Three Peirce-Smith converter production samples, representative of the extent in variability of iron endpoints attained at the converter plant, were used in a systematic investigation coupled to a novel combination of modern analytical techniques, computational thermochemistry and metallurgical testwork. The modern analytical techniques included the application of high resolution transmission electron microscopy and focused ion beam scanning electron microscopy tomography. Computational thermochemistry was applied through the use of MTDATA phase diagram software. Metallurgical testwork involved laboratory batch grinding at various specific energies. Closely associated leach experiments were also considered relevant to this wide-ranging investigation.

The Peirce-Smith converter samples investigated were indicative of mattes that attained specific endpoints of 5.17%, 0.99% and 0.15 weight% Fe. The highest combined bulk concentration of the important base and platinum-group metals was achieved in the matte which attained a specific iron endpoint of 0.99%. The mineralogy of all three converter mattes was dominated by nickel sulfide mineral structures matched to the natural mineral of heazlewoodite. Mineral structures of

copper sulfide, NiCu-alloy, spinel and OsRu-alloy were also constituents of the different converter mattes. The attainment of a specific iron endpoint was found to result in measurable mineralogical differences with respect to relative mineral abundances, external morphological characteristics and mineral chemistry. The mineralogical differences were particularly distinct between mineral structures of the high (5.17%) and low (0.99% and 0.15%) iron mattes. Subtle mineralogical differences were evident between mineral structures of the low iron mattes.

The 0.99% Fe matte was characteristic of a significantly higher NiCu-alloy relative abundance, compared to the 5.17% Fe matte. The NiCu-alloy structures were found to act as the primary collectors of the economically significant platinum-group metals. Mineralogical observations were used to develop an understanding of the underlying mineralization mechanism of NiCu-alloy structures. High-fidelity color and grayscale 3D reconstructions were produced of the resultant mineralized structures. It was shown theoretically that variations in iron endpoint specific starting compositions of oxygen-free liquid matte systems alter the solidification pathway towards the eutectic. Moreover, a quantitative understanding of liquid phase solidification of the high and low iron matte systems, including oxygen, was developed to within ±2.5 ^{o}C. Most of the specific energy available for grinding was expended breaking the nickel sulfide matrix, particularly of the high iron matte. The breakage rates of copper sulfide mineral structures in the 5.17% Fe matte were calculated to be higher than in the 0.15% Fe matte at 25kWh/t specific energy. The degree of copper sulfide liberation was shown to be higher for the 5.17% Fe matte than for the 0.15% Fe matte at the same specific energy of grinding. A higher degree of Ni extraction and Cu cementation could be achieved when leaching low iron matte particles. The production of converter matte attaining a specific iron endpoint of 0.99% was found to be the most suitable with respect to endpoint selection criteria. A practical iron endpoint range of 1.6% to 1.0% was recommended for the production of converter matte with a resultant mineralogical quality within the constraints of the Lonmin base metal refinery.

This study offers an integrated understanding of base and platinum-group metals production as a function of a desirable iron endpoint at Lonmin. This was not previously available in metal production literature. New technology for the monitoring and consistent control of such a practical iron endpoint range can subsequently be implemented.

OPSOMMING

Die prosesroete vir die produksie van onedel en platinumgroepmetale uit natuurlike swawelertse vereis gewoonlik die omsetting van ’n ysterryke hoogoondmat in ’n ysterarm omsettermat. Hierna volg voorbehandeling deur die afkoeling van die ysterarm gesmelte mat, fisiese verwerking van die soliede mat, en hidrometallurgiese metaalekstraksie. Lonmin is die derde grootste produsent van platinumgroepmetale ter wêreld en gebruik Peirce-Smith-omsetters om ysterryke hoogoondmat met lug te blaas totdat dit ’n finale ysterkonsentrasie- of ystereindpunt bereik. Die gesmelte mat word met water granuleer, en solidifikasie vind deur middel van snelafkoeling plaas. Die soliede mat word in ’n geslotekring-balmeul met hidrosikloonklassifikasie gemaal en aan eerstestadium- atmosferiese loging onderwerp. Die spesifikasie van ’n ideale of gewenste ystereindpunt verg deeglike oorweging. Bowenal moet dit verseker dat die omsettermat kristalliseer met mineralogiese eienskappe wat binne die setpunte van die eenheidsprosesse en -tegnieke verder af in die prosesstroom val. ’n Bykomende oorweging is dat die uiteindelike geblaasde omsettermat ’n optimale massakonsentrasie van die onedel metale Ni en Cu en die platinumgroepmetale Pt, Pd, Rh, Ru en Ir moet bevat.

Matte met die kenmerke van wisselende ystereindpunte is gereeld by die Lonmin-omsetteraanleg geproduseer. Die onsekerheid van metallurge by die aanleg oor die gewenste ystereindpunt – veral binne die konteks van die Lonmin-raffinadery vir onedel metale – sowel as swak beheer het ’n nadelige uitwerking gehad op die mineralogiese gehalte van die uiteindelike mat, en dus ook op die verwerkingskenmerke van die soliede matdeeltjies verder af in die prosesstroom. Die bepaling van die gewenste ystereindpunt het sorgvuldige ondersoek, seleksie en toepassing deur Lonmin vereis. Hierdie studie is dus hoofsaaklik uitgevoer om die uitwerking van ’n spesifieke ystereindpunt op die mineralogie en minerale chemie van soliede omsettermat te kwantifiseer. ’n Grondliggende ondersoek na die solidifikasieproses by afkoeling is as noodsaaklik beskou vir ’n diepgaande begrip van die verworwe mineralogie en minerale chemie as ’n funksie van ’n spesifieke

ystereindpunt. Mettertyd het dit egter ewe belangrik geword om die uitwerking van die gevolglike mineralogie, en dus die ystereindpunt, op die fisiese eienskappe van minerale strukture met betrekking tot maling-, vrystellings- en loogprosesse verder af in die prosesstroom te kwantifiseer.

Ondanks heelwat bedryfskonteks, het nóg bedryfs- nóg vakkundige literatuur veel diepte- en samehangende studies oor die uitwerking van ’n spesifieke ystereindpunt op snelafgekoelde omsettermatstelsels opgelewer. Vorige bevindinge in die literatuur het boonop ’n beperkte kwantitatiewe begrip van die uitwerking op mineralogie en minerale chemie getoon. Die fase- en afkoelingsekwilibriums van ystereindpuntspesifieke Ni-Cu-S-matstelsels met veelvuldige komponente was ook nie ten volle beskikbaar nie. Dít sou veral goed te pas gekom het om die kompleksiteite van omsettermatsolidifikasie as ’n funksie van ystereindpunt te verstaan. Kennis van die fisiese eienskappe van die minerale strukture van omsettermat was kwalik beskikbaar, terwyl selfs minder inligting oor maling-, vrystellings- en loogprosesse opgespoor kon word. Daarom was ’n omvattende ondersoek nodig om hierdie beduidende kennisleemtes met betrekking tot snelafgekoelde omsettermatstelsels in ’n nywerheidsraamwerk aan te vul.

Drie Peirce-Smith-omsetterproduksiemonsters wat die wisselende bestek van ystereindpunte by die omsetteraanleg verteenwoordig, is in ’n stelselmatige ondersoek gebruik, tesame met ’n vernuwende kombinasie van moderne ontledingstegnieke, gerekenariseerde termochemiese bewerkings en metallurgiese toetswerk. Die moderne ontledingstegnieke sluit onder andere in hoëresolusie-transmissie-elektronmikroskopie (HRTEM) en gefokusdeioonstraalskandering-elektron-mikroskopie (FIB SEM) tomografie. Die gerekenariseerde termochemiese bewerkings is met behulp van MTDATA-fasediagramsagteware uitgevoer. Metallurgiese toetswerk het die maling van laboratoriumlotte teen verskillende spesifieke energieë behels. Nou verwante loogproefnemings is ook as relevant vir hierdie omvattende studie beskou.

Die bestudeerde Peirce-Smith-omsettermonsters het op matte met spesifieke eindpunte van 5.17%, 0.99% en 0.15 gewig% Fe gedui. Die hoogste gekombineerde massakonsentrasie van die belangrike onedel en platinumgroepmetale is in die mat

met ’n spesifieke ystereindpunt van 0.99% gevind. Die mineralogie van ál drie omsettermatte is oorheers deur die minerale strukture van nikkelsulfied, wat met die natuurlike mineraal heazlewoodiet ooreenstem. Die verskillende omsettermatte het ook die minerale strukture van kopersulfied, NiCu-allooi, spinel en OsRu-allooi bevat. Daar is bevind dat die verkryging van ’n spesifieke ystereindpunt tot meetbare mineralogiese verskille in die relatiewe volopheid van minerale, die eksterne morfologiese kenmerke sowel as minerale chemie lei. Die mineralogiese verskille was veral duidelik te sien tussen die minerale strukture van die ysterryke (5.17% Fe) en ysterarm (0.99% en 0.15% Fe) matte. Fyn mineralogiese verskille is ook tussen die minerale strukture van die ysterarm matte bespeur.

Die 0.99% Fe-mat het tipies beduidend meer NiCu-allooi as die 5.17% Fe-mat bevat. Die NiCu-allooistrukture tree oënskynlik op as die hoofversamelaars van die ekonomies belangrike platinumgroepmetale. Mineralogiese waarnemings is gebruik om ’n begrip te ontwikkel van die onderliggende mineralisasiemeganisme van NiCu-allooistrukture. Die gevolglike gemineraliseerde strukture is met behulp van driedimensionele rekonstruksies met hoë kleurgetrouheid sowel as in grysskaal voorgestel. Daar is teoreties aangetoon dat variasies in ystereindpuntspesifieke beginsamestellings van suurstofvrye vloeibare matstelsels die solidifikasieroete na die eutetikum wysig. Daarbenewens is die vloeifasesolidifikasie van die ysterryke en ysterarm matstelsels, wat suurstof insluit, op sowat ±2.5 ^{o}C gekwantifiseer. Die meeste van die spesifieke energie wat vir maling beskikbaar was, is gebruik om die nikkelsulfiedmatriks te breek, veral vir die ysterryke mat. Berekeninge toon dat die breektempo’s van die minerale strukture van kopersulfied by die 5.17% Fe-mat hoër was as by die 0.15% Fe-mat teen ’n spesifieke energie van 25 kWh/t. Die mate van kopersulfiedvrystelling was hoër by die 5.17% Fe-mat as by die 0.15% Fe-mat by dieselfde spesifieke energie vir maling. ’n Hoër mate van Ni-ekstraksie en Cu-sementasie is verkry toe ysterarm matdeeltjies geloog is. Wat eindpuntseleksiemaatstawwe betref, is die produksie van ’n omsettermat met ’n spesifieke ystereindpunt van 0,99% as die mees geskikte aangewys. ’n Praktiese ystereindpuntbestek van 1.6% tot 1.0% word aanbeveel vir die produksie van ’n omsettermat met ’n gevolglike mineralogiese gehalte wat binne die perke van die Lonmin-raffinadery vir onedel metale val.

Hierdie studie bied ’n geïntegreerde begrip van die produksie van onedel en platinumgroepmetale as ’n funksie van ’n gewenste ystereindpunt by Lonmin. Hierdie inligting was nie voorheen in literatuur oor metaalproduksie beskikbaar nie. Nuwe tegnologie vir die monitering en konsekwente beheer van so ’n praktiese ystereindpuntbestek kan dus op grond hiervan in werking gestel word.

DEDICATION

This dissertation is dedicated to the loving memory of my late mother, Augusta Petronella Thyse, a strong yet tender soul. Words can never express the amount of inspiration your passing brought.

ACKNOWLEDGEMENTS

The following people fulfilled an important role during the course of this study and deserve just acknowledgement:

i. My supervisor, Prof Guven Akdogan, for his admirable technical and scholarly guidance. It was his understanding of material science that resulted in some aspects being integrated with the classical metallurgical approach. I would also like to thank him for his professional mentorship and friendship.

ii. Prof Jan Neethling, Dr Jaco Oliver, William Goosen and Jacques O'Connell from the HRTEM Centre, Nelson Mandela Metropolitan University, for technical assistance during the usage of world class, high resolution electron microscopy facilities and prolific collaborations on the mineralogical studies.

iii. Dr Frik Koch, from the Physics Department, University of the Western Cape, for technical assistance with the HRSTEM analysis.

iv. Prof Pekka Taskinen, from the Metallurgical Thermodynamics and Modeling Group, Aalto University in Finland, for prolific collaborations on the solidification thermochemistry of matte systems. I would also like to thank him for hosting me during a technical visit to Aalto University in March 2011.

v. Archie Corfield, from the Mineralogy Division, Mintek, for technical assistance during electron probe microanalysis.

vi. Prof Fanus Viljoen, from the Department of Geology, University of Johannesburg, for technical assistance and collaborations on MLA based characterization and liberation studies.

vii. Dr Johnny Kalala and Abel Mokwena, previously from the Comminution Division, Mintek, for technical assistance during laboratory grinding tests.

viii. Prof Aubrey Mainza, from the Centre for Minerals Research, University of Cape Town, for collaborations on applying the perfectly mixing ball mill model to assess the breakage rates of particles and minerals.

ix. Western Platinum Ltd. (Lonmin Plc.) for financial support.

x. The technical and administrative personnel, from the Process Engineering Department, Stellenbosch University.

xi. Finally, I thank my God, immediate family and loved one.

LIST OF PUBLICATIONS AND PRESENTATIONS

The publications resulting from this study are listed below:

i. Thyse, E.L., Akdogan, G., Eksteen, J.J., 2011. The effect of changes in iron endpoint during Peirce-Smith converting on PGE-containing nickel converter matte mineralization. Minerals Engineering, Special Issue: Processing of Nickel Ores and Concentrates, Volume 24, Issue 7, pp. 688 – 697.

ii. Thyse, E.L., Akdogan, G., Olivier, E.J., Neethling, J.H., Taskinen, P., and Eksteen, J.J., 2011. Partitioning of PGEs in nickel converter matte phases: Direct observations by electron microscopy and electron probe microanalysis. Minerals Engineering, Special Issue, Process Mineralogy, Volume 24, Issue 12, pp. 1288 – 1298.

iii. Thyse, E.L., Akdogan, G., Taskinen, P., and Eksteen, J.J., 2011. The distribution of metallic elements in granulated nickel converter matte phases. Proceedings, Southern African Pyrometallurgy 2011, Edited by R.T Jones and P. den Hoed, Southern African Institute of Mining and Metallurgy, pp. 173 – 184.

iv. Thyse, E.L., Akdogan, G., Olivier, E.J., Neethling, J.H., Goosen. W.E., and Eksteen, J.J., 2011. The effect of granulated nickel converter matte mineralogy on phase-specific hardness and associated breakage characteristics. Proceedings, 10th International Congress for Applied Mineralogy, pp.673 – 681.

v. Thyse, E.L., Akdogan, G., Olivier, E.J., O'Connell, J.H., Neethling, J.H., Taskinen, P., and Eksteen J.J., 2013. 3D insights into nickel converter matte phases: Direct observations via TEM and FIB SEM tomography. Minerals Engineering, Special Issue, Process Mineralogy, Volume 52, pp. 2 – 7.

vi. Thyse, E.L., Akdogan, G., Taskinen, P., Viljoen, K.S. and Eksteen, J.J., 2013. Towards understanding nickel converter matte solidification. Minerals Engineering, Special Issue, Processing of Nickel Ores and Concentrates, Volume 54, pp. 39 – 51.

The following conference presentations were made:

i. Thyse, E.L., Akdogan, G., Eksteen, J.J., 2010. The effect of changes in iron endpoint during Peirce-Smith converting on PGE-containing nickel converter matte. Presented at Nickel Processing 10, 18-19 June, Falmouth, United Kingdom.

ii. Thyse, E.L., Akdogan, G., Olivier, E.J., Neethling, J.H., Taskinen, P., and Eksteen, J.J., 2010. Partitioning of PGEs in nickel converter matte phases: Direct observations by electron microscopy and electron probe microanalysis. Presented at Process Mineralogy 10, 10-12 November, Cape Town, South Africa.

iii. Thyse, E.L., Akdogan, G., Taskinen, P., and Eksteen, J.J., 2011. The distribution of metallic elements in granulated nickel converter matte phases. Presented at the Southern African Pyrometallurgical 2011 International Conference, 6-9 March, Johannesburg, South Africa.

iv. Thyse, E.L., Akdogan, G., Olivier, E.J., Neethling, J.H., Goosen. W.E., and Eksteen, J.J., 2011. The effect of granulated nickel converter matte mineralogy on phase-specific hardness and associated breakage characteristics. Presented at the International Congress of Applied Mineralogy 10, 01-05 August, Trondheim, Norway.

v. Thyse, E.L., Akdogan, G., Olivier, E.J., O'Connell, J.H., Neethling, J.H., Goosen, W.E., 2012. The characterisation of matte mineralogy and downstream processing properties. Presented at the Microscopic Society of South Africa Annual Conference, 5-7 November, Cape Town, South Africa.

vi. Thyse, E.L., Akdogan, G., Olivier, E.J., O'Connell, J.H., Neethling, J.H., Taskinen, P., and Eksteen J.J., 2012. 3D analysis of solidified nickel

converter matte phases: Direct observations via TEM and FIB SEM tomography. Presented at Process Mineralogy 12, 7-9 November, Cape Town, South Africa.

vii. Thyse, E.L., Akdogan, G., Taskinen, P., Viljoen, K.S. and Eksteen, J.J., 2012. Towards understanding nickel converter matte solidification. Presented at Nickel Processing 12, 14-15 November, Cape Town, South Africa.

TABLE OF CONTENTS

LIST OF TABLES

LIST OF FIGURES

LIST OF EQUATIONS

LIST OF ABBREVIATIONS

3D	Three dimensional
Atm	Atmosphere
Awr	Awaruite
BMR	Base metal refinery
BSE	Backscattered electron
Cc	Chalcocite
CCD	Charge-coupled device
CSTR	Continuously stirred tank reactor
DON	Direct Outokumpu nickel
EDX	Energy dispersive X-ray spectrometry
EELS	Electron energy loss spectroscopy
Fcc	Face-centred cubic
FEG MLA	Field-emission gun mineral liberation analyzer
FEG SEM	Field-emission gun scanning electron microscope
FIB SEM	Focused ion beam scanning electron microscopy
GXMAP	Grain X-ray mapping
HRSTEM	High-resolution scanning transmission electron microscope
HRTEM	High-resolution transmission electron microscopy
Hw	Heazlewoodite
ICP-OES	Inductively coupled plasma optical emission spectrometry
LPG	Liquefied petroleum gas
Mgn	Magnetite

MLA	Mineral liberation analyzer
MTDATA	Metallurgical and thermochemical databank
NMMU	Nelson Mandela Metropolitan University
NPL	National Physical Laboratory
PGM	Platinum-group metal
PIXE	Particle induced X-ray emission
PMR	Precious metal refinery
Pn	Pentlandite
QEM*SEM	Quantitative evaluation of minerals by scanning electron microscopy
QXRD	Quantitative X-ray diffraction
RBMR	Rustenburg base metal refinery
SEM	Scanning electron microscopy
SOI	Site of interest
Sp	Spinel
STEM	Scanning transmission electron microscopy
TEM	Transmission electron microscopy
Tvr	Trevorite
WDS	Wavelength dispersive spectrometry
Wt	Weight
XBSE	Extended backscattered electron
XMOD	X-ray modal abundance
XRD	X-ray diffraction

Chapter 1
INTRODUCTION

1.1. Project Relevance

The pyrometallurgical smelting of sulfide concentrates in coordination with hydrometallurgical extraction and refining is integral to global base and platinum-group metal (PGM) production. The process routes are often customized with respect to primary sulfide source variability, unit process interconnection and the specification of saleable end and by-products. Although considerable primary sources of nickel sulfide are located within the Canadian Sudbury, Russian Norilsk and Kola-Pechanga regions (Warner et al., 2007), the most significant primary source of PGM sulfide are within the Bushveld Complex of South Africa (Nell, 2004). Nickel, copper and cobalt would typically be extracted as base metal by-products of PGM smelting and refining (Jones, 2004) by several integrated mine-to-PGM producers, located within the Bushveld Complex, including Lonmin Platinum (hereafter referred to as Lonmin).

Sulfide smelting, as practiced at Lonmin, consists of primary furnaces; producing and separating metal-rich sulfide matte from silicate-iron rich slag (Jones, 2005). Peirce-Smith converters are operated to blow the furnace matte with air during several stages of converting. The iron concentration of the matte is blown to an endpoint so as to produce an iron-lean matte further enriched in nickel, copper, cobalt and PGMs. An initial consideration during the final stages of converting is optimizing the composition of the matte with respect to a relatively low iron endpoint. The critical endpoint consideration would be downstream unit process constrains, as the capacity and technology of base metal refineries, in particular, are developed within a small iron setpoint range. Variable iron endpoints were often achieved at the Lonmin converter plant (Warner et al., 2007; Schouwstra, 2008; Eksteen, et al., 2011), which is indicative of a limited understanding of its effect on the matte mineralogy. Monitoring of the Peirce-Smith converter iron endpoint at Lonmin was based on visual operator experience and prone to poor control due to false and variable endpoint detection (Eksteen et al., 2011).

The cooling of molten converter matte is a critical pre-treatment step intended to produce solidified matte as an intermediate product for base metal extraction and PGM refining. Molten matte from Peirce-Smith converters is water granulated and solidification of matte occurs through a fast-cooling process. A coordinated process step involves grinding the solidified matte in a closed circuit ball mill with hydrocyclone classification to produce sufficient fine product to assist matte dissolution in a base metal refinery (BMR). First stage atmospheric and 2nd stage pressure leaching is utilized to produce nickel sulfate crystals, copper cathode and a PGM concentrate at the BMR (Steenekamp and Dunn, 1999). An efficient BMR would be able to extract the base metals over nominal instance coupled to producing a high grade PGM concentrate and thereby improve the quantities of PGMs available in the extraction and refining circuits (Eksteen et al., 2011). The PGM concentrate from the BMR is treated at the precious metal refinery (PMR).

1.2. Project Statement

There is, at present, an increasing worldwide commitment towards lean, integrated and efficient metal production processes. Lonmin also considered improving smelter and extraction unit process integration and efficiency by selecting an ideal or desirable iron endpoint. However, an ideal iron endpoint had to be investigated considering that the effect of iron endpoint on matte mineralogy was poorly understood and therefore quantified. The selection of an ideal iron endpoint must ensure the solidification of matte with consistent physical and chemical properties that remains within the setpoints of downstream processes. There is also little in-depth knowledge available concerning the effect of the mineralogical quality on the downstream processes such as grinding and leaching. Lonmin therefore, initiated the current study to understand the effect of variable iron endpoint on matte mineralogy and on the downstream processing of base metals and PGMs. It was envisaged by Lonmin that new findings from this study could be used in converter flame optical spectrometry to control the iron endpoint, as described by Bezuidenhout et al., (2010), and also to delineate the wide-ranging effect and selection of an ideal iron endpoint.

1.3. Aims of this Study

The primary aim of this study was to systematically investigate and develop a quantitative basis for understanding the effect of Peirce-Smith converter iron endpoint on matte mineralogy. Comparative investigations were conducted based on variable iron endpoints which are specific to the bulk composition of solidified mattes. It was critical to unlock a relation between iron endpoint, the formation of fast-cooled microstructures and the resultant mineralogy.

The secondary aim of this study was to methodically investigate and understand the effect of the mineralogy on downstream processing, which would be a prerequisite in selecting an ideal iron endpoint and thereby improving the smelter and extraction unit process interconnection and efficiency.

1.4. Objectives of this Study

The primary objectives of this study were as follows:

i. To investigate the chemistry, physical characteristics and mineralogy of the granulated nickel-PGM matte as a function of iron endpoint from actual Peirce-Smith converter production samples through a combination of analytical techniques including X-ray diffraction (XRD) and electron microscopy;

ii. To investigate the mineral chemistry, in particular the partitioning trends, of base metals and PGMs into mineral structures as a function of iron endpoint *via* electron probe microanalysis together with high resolution electron microscopy. This includes establishing mineralization behavior and microstructure formation using advanced analytical techniques such as focused ion beam scanning electron microscopy (FIB SEM) tomography;

iii. To develop a fundamental understanding of the critical matte solidification process through the application of computational thermochemistry, with reference to equilibrium systems of variable iron endpoint compositions; and

iv. To investigate the micro-hardness and breakage characteristics of individual mineral structures towards establishing an empirical dependence with underlying

mineralogy related to iron endpoint. Such dependence would be the basis for further investigations in relation to downstream processing. Therefore, related secondary objectives were:

a. To investigate the grinding characteristics of matte particles through laboratory batch grinding testwork;

b. To determine the liberation characteristics of mineral structures of interest through the use of a mineral liberation analyzer (MLA);

c. To relate the grinding and liberation characteristics conceptually to the first stage leach in an integrated downstream processing context as a distinguishing effect of the Peirce-Smith converter iron endpoint.

1.5. Significance of this Study

This study has made the following industrial and scholarly contributions:

i. The effect of variable iron endpoints on matte mineralogy has been systematically and fully quantified and by this means provides plant metallurgists with an improved understanding of the basic mineralogy and mineral chemistry of the resultant mineral structures. This could be useful for the automated monitoring and control of a desired iron endpoint for producing an intermediate matte product with a consistent metallurgical quality within the setpoints of the Lonmin BMR;

ii. The study has provided a fundamental thermochemical basis for understanding the solidification of matte to advance knowledge of the relevant phase equilibria, which is not fully available in literature despite its industrial importance. This knowledge is important in considering theoretical matte solidification paths in relation to the mineralogy and chemistry as a function of actual iron endpoint. The theoretical knowledge acquired may also be useful to scholars in the field of sulfide equilibria.

iii. The formation mechanism and subsequent mineralization of alloy mineral structures are regarded as complex. Findings from this study can be used to obtain

an improved understanding of alloy microstructure formation and the PGM collection process, which could potentially be used to influence mineralization during the fast-cooling process. The knowledge gained may also be applicable in part to the slow-cooling, matte-based PGM collection process;

iv. The three dimensional (3D) visualization and analysis of fine-scale converter matte microstructures was completed successfully as a first study in this field and is regarded as an innovative contribution towards illustrating microstructure morphology, as a function of iron endpoint. The study of 3D pyrometallurgical microstructures is in its infancy and has yet to be considered for producing specific information with respect to downstream metallurgy.

v. There is limited microstructure-specific physical property data available in literature, particularly for converter matte as a function of iron endpoint. This study provides quantitative and qualitative physical property data for micro-hardness and breakage, respectively, of individual microstructures. In addition, physical property data and the associated mineralogy are used to develop a unique insight into matte grinding.

vi. The systematic effect of the underlying mineralogy (from pyrometallurgical origin) on downstream processing was not considered previously in the metal production literature at large. This dissertation suggests an integrated approach for the production of nickel, copper and PGMs as a function of an ideal iron endpoint, which is based on understanding the multi-physics of coupled process steps.

1.6. Scope and Delimitations

This study provided multi-faceted scope for both industrial and scholarly research in pyrometallurgy, mineralogy, comminution, liberation and hydrometallurgy coupled to iron endpoint selection, as illustrated in Figure 1.1. The starting point for the study was the variable iron endpoints achieved during the Peirce-Smith converting process, and based on actual operating data from Lonmin. The investigation of factors other than variable iron endpoints were not considered in this study. The focus at first was on quantifying the mineralogy of converter matte mineral structures and the concurrent investigation into the

fast-cooling process. This was done to provide plant metallurgist with essential data for understanding the effect of iron endpoint on matte mineralogy. Extensive emphasis was placed on the use of modern analytical and computational techniques to resolve fine microstructure detail and complex process intricacies. Characteristics of matte grinding and liberation were subsequently investigated as function of underlying mineralogy, as well as published experimental leaching data closely associated with this study.

The sulfides investigated in the study are industrial matte composed of synthetic mineral structures. However, natural mineral names were used throughout this dissertation to recognize the synthetic equivalents. It should be noted that the concentration and deportment of impurities such as arsenic, tellurium, selenium and antimony were beyond the scope of the current study. Furthermore, the investigation of the associated converter slag phase was deemed less significant with respect to the priorities of the sponsoring company.

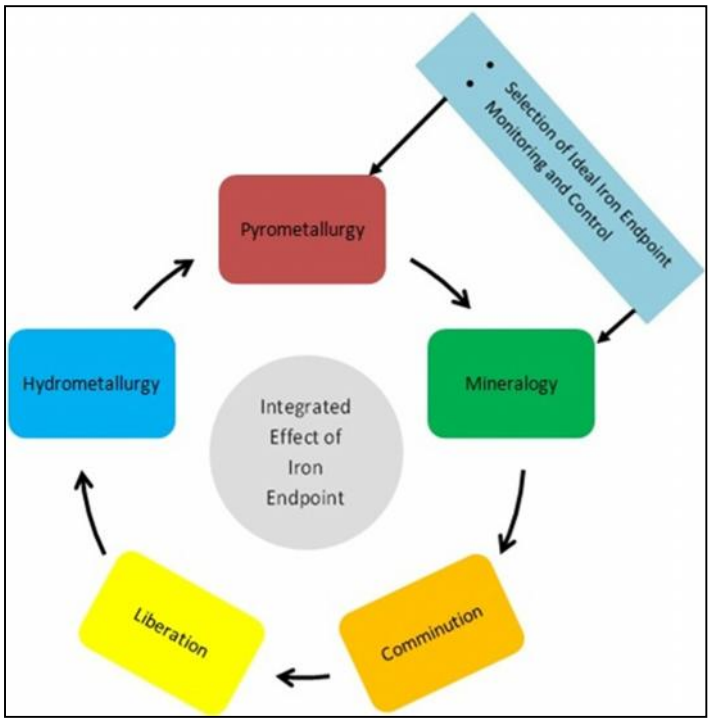

Figure 1.1: Illustration of the multi-faceted scope of research in this study involving pyrometallurgy, mineralogy, comminution, liberation and hydrometallurgy with importance to iron endpoint selection.

1.7. Layout of this Dissertation

This dissertation is divided into eight chapters. The project relevance, project statement, study aims, objectives and significant contributions are presented in Chapter 1. Chapter 2 provides a literature review on the relevant metal production process and techniques, the Lonmin operational infrastructure, sulfide mineralogy and phase equilibria, and relevant findings in the fields of comminution, liberation and hydrometallurgy. The next chapter, Chapter 3, describes the sampling, analytical and computational techniques that were used.

The remainder of the chapters is presented along the major themes of mineralogy, mineral chemistry, solidification analysis and downstream processing characteristics. These major themes are presented in several investigative study chapters, each having its own introduction, results and discussion followed by key findings. Chapters 4 and 5 express the mineralogy and mineral chemistry investigations ordered along iron endpoint comparisons, integrated with illustration and understanding of fine microstructure detail. Chapter 6 develops a unified and fundamental understanding of the matte solidification process, while Chapter 7 focus on the effect of the mineralogy on physical property, grinding and liberation characteristics with relevance to leaching. Conclusions and recommendations are provided in Chapter 8. Detailed results from key analyses and computations are provided in the Appendices, including an atlas of mineral structures, movies of 3D mineral structures, metallurgical and thermochemical databank (MTDATA) phase mass and compositional analyses and batch grinding size data as function of iron endpoint.

Chapter 2
LITERATURE REVIEW

2.1. The Relevance of Metals

The discovery of metals, and their initial rudimentary production from ores, has played an important role in the advancement of civilization. Copper was reportedly discovered in 4200 BC (Cramb, 2012) and used regularly soon after this. According to Jones (2005), platinum was arguably in usage much earlier in Egypt, although its discovery is officially recognized to have occurred in 1751. Relevant metal discoveries in the 18th century include that of nickel and cobalt while iridium, rhodium, palladium and ruthenium were discovered in the 19th century (Cramb, 2012).

These metals have always been viewed as resourceful and were essential to the structure of materials for several industries. At present, the metals are progressively applied in advance technologies and have become of particular economic and strategic value to primary producers and their host countries. Crundwell et al., (2011) draws attention to the current industrial applications of nickel, cobalt and PGMs and, in addition accounts for their inclusive primary production. Table 2.1 reports the respective metal production tonnes and associated values in 2009. It is evident from Table 2.1 that the PGMs have a considerable higher value per unit ton than cobalt and nickel. The consumption of these metals will continue and is expected to increase alongside developments in new applications.

Table 2.1: Nickel, cobalt and PGM production data and their associated values in 2009 (modified after Crundwell et al., 2011).

Metal	Tonnes	Value (million US$)
Nickel	1 500 000	30 000
Cobalt	60 000	3 000
PGMs	450	15 000
Total	**1 560 450**	**48 000**

2.2. Primary Sources, Occurrences and Mining Regions

Natural sulfide ores are known to be the primary source of base metals and PGMs, as well as several metals of industrial value. The sulfide minerals are regarded as the most valuable group of ore minerals (Vaughan, 2005). The most important nickel-copper sulfide ore is located within the Canadian Sudbury region (Warner et al., 2007), which produces more than 66% of the nickel used globally. A large number of mines are sited within the Sudbury basin, including the first integrated nickel mining, concentrating, smelting and refining complex. Further significant nickel-copper sulfide ores are located within the Russian Noril'sk-Talnakh and Pechenga regions and the Jinchuan and Kambalda districts in China and Australia, respectively. South Africa, in 2006, contributed 2.9% towards the global mine production output, which made it the tenth leading nickel producer at the time (Andrews, 2008). According to Riekkola-Vanhanen (1999), nickel is significantly mined in twenty-one countries and produced in twenty-three countries.

The major PGM-rich sulfide ores are located in South Africa within the Bushveld Complex, Zimbabwe within the Great Dyke and the Stillwater and Lac des Iles Complexes in the USA and Canada, respectively (Jones, 2004). Minor PGM-rich sulfide ores are also located within Finland and the Duluth Complex in the USA. Many of the nickel-copper sulfide dominant regions also produce PGMs as by-products. Figure 2.1 illustrates the worldwide occurrence of the major and minor nickel-copper dominant and PGM-rich sulfide ores.

The Bushveld Complex holds most of the known platinum resources in the world and is the leading supplier of PGMs (Nell, 2004). The British Geological Survey (2009), estimated that the Bushveld Complex comprises an aerial coverage of 66 000km^2 and a thickness of 9km. Furthermore, the Complex can be divided into Western, Eastern and Northern Limbs. The important Merensky Reef and UG2 chromitite mining horizons occur within the Critical Zone of the Complex and can be found in the Western and Eastern Limbs. The mining horizons are chiefly processed for PGM content, which is present among base metal sulfides (Jones, 2004). Moreover, the UG2 chromitite mining horizon is set apart from the Merensky Reef by a lower base metal sulfide and considerably higher chromite content. The Platreef is a third mining horizon with a lower PGM content and present only in the Northern Limb (British Geological Survey, 2009).

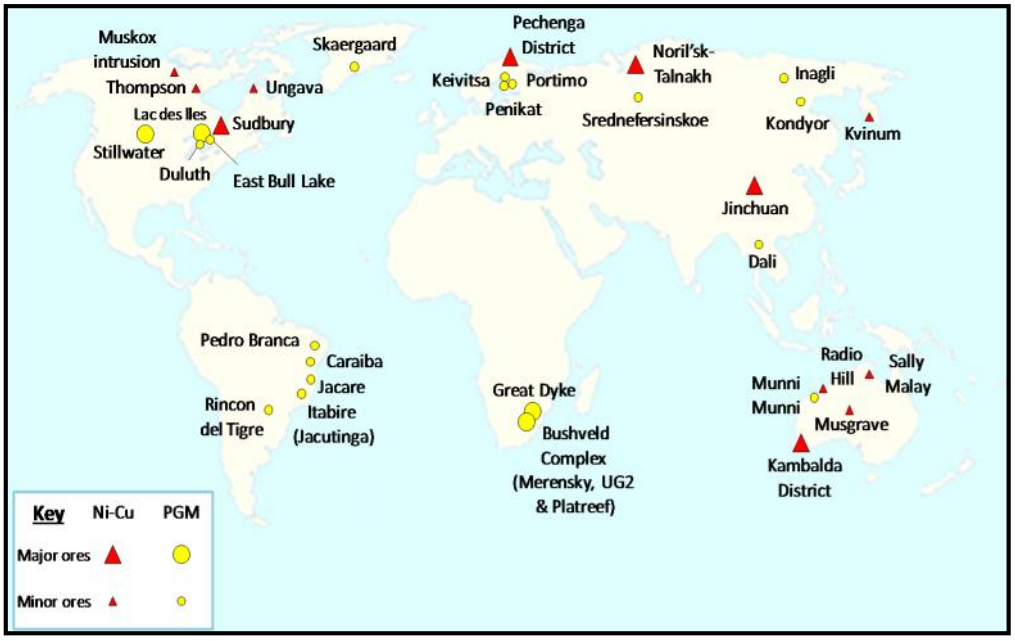

Figure 2.1: The worldwide occurrence of nickel-copper dominant and PGM-rich sulfide ores (redrawn after the British Geological Survey, 2009).

Mining of the PGM-rich sulfide horizons within the Bushveld Complex started in around 1926, and selected history and pivotal operational developments are provided by several authors (Jones, 2005; Andrews, 2008; Eksteen, et al., 2011). PGM production within the Bushveld Complex at present is dominated by the integrated mine-to-metal companies of Anglo Platinum, Impala Platinum, Lonmin and Northam Platinum. Anglo Platinum generally aims to produce the PGMs referred to as 4E (Pt, Pd, Rh and Au). Impala Platinum and Lonmin, on the other hand, target the production of the PGMs referred to as 5E (Pt, Pd, Rh, Ru and Ir) plus Au. Osmium, notably, is not included in the production targets for any of the producers while base metals such as nickel, copper and cobalt are produced as by-products. Lonmin is currently the third leading producer of PGMs in the world and comprises the subsidiary companies of Western Platinum Limited, Eastern Platinum Limited and Karee Mine (Eksteen, et al., 2011). Figure 2.2 illustrates the location of PGM mines and holding companies within the Bushveld Complex.

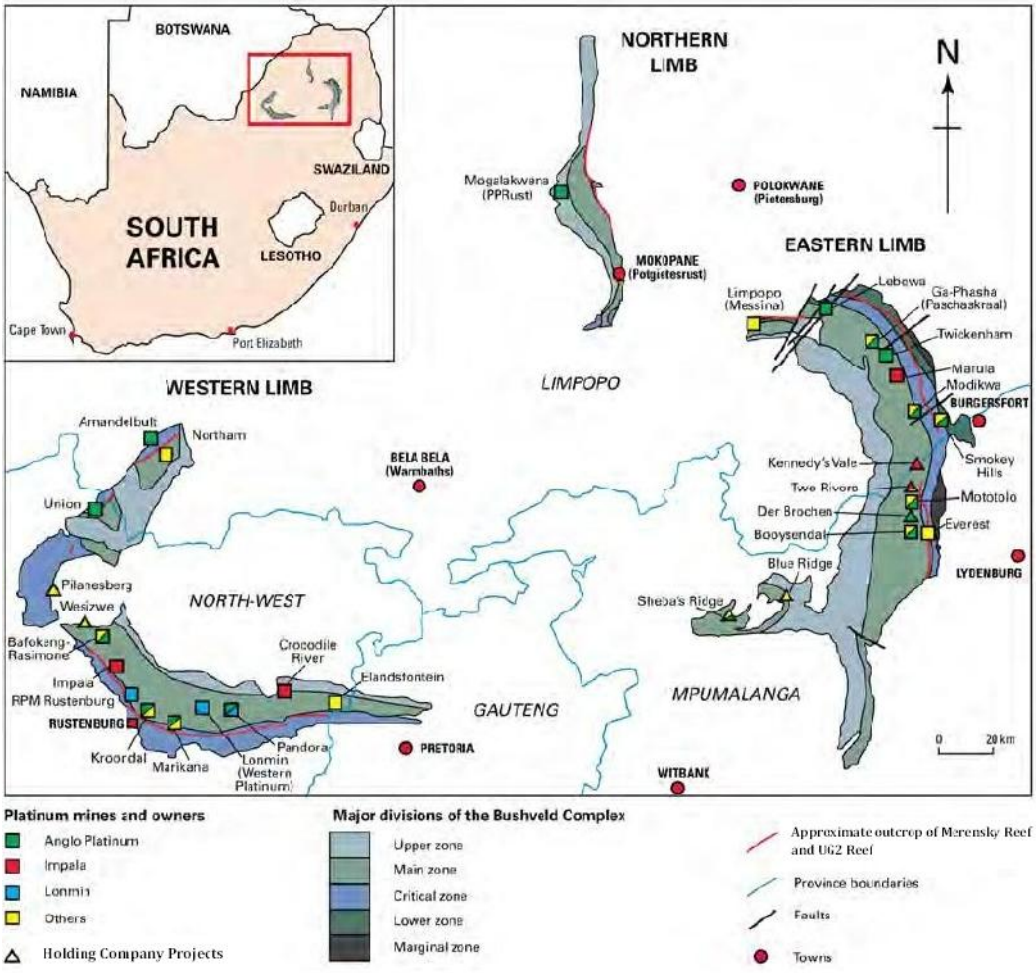

Figure 2.2: The location of PGM mines and holding companies within the Bushveld Complex (modified after the British Geological Survey, 2009).

2.3. Metal Production Processes and Techniques

The mineralogical and chemical variability of sulfide ores commonly warrants different approaches to metal production processes, in order to fully exploit the mine-to-metal value of this ore (Warner et al., 2007; Jones, 2005). It is also typical for non-ferrous processes to be influenced by the constituent ferrous metal and ligand content of sulfide ores, in particular iron and sulfur, respectively. The various techniques of metal production are designed to systematically upgrade the valuable components of mined ores. The following sub-sections present an overview of the pivotal metal production processes and the techniques relevant to nickel and PGM production.

2.3.1. Physical Processes

Physical processes include the unit operations of comminution and sizing, in which mined sulfide ore is reduced in particle size, thereby liberating the target minerals from the gangue matrix. The techniques of crushing, grinding and classification are generally employed in combination with gravity beneficiation to produce a valuable mineral concentrate. These techniques are knowledge areas in its own and grinding, in particular will be elaborated upon in sub-section 2.6.1. The mineral concentrate is beneficiated further by the technique of froth flotation. This technique requires adding chemical reagents to a gravity concentrated pulp with the intended purpose of rendering the target mineral surfaces hydrophobic and the gangue mineral surfaces hydrophilic. Rising air bubbles generated in flotation cells deliver the target minerals to the surface of the pulp and establish a concentrated froth. The gangue minerals remain in the pulp, while the concentrated froth is regularly skimmed off. The principles of froth flotation have been studied by several authors (Rogers, 1962; Herrera-Urbina et al., 1990; Wills and Napier-Munn, 2006).

It was found that differences in physical processing practices, in conjunction with sulfide ore variability, inevitably results in a wide range of nickel-copper dominant and PGM-rich concentrate compositions (Warner et al., 2007). The focus of physical processing practices at Lonmin is to operate small-to medium-size concentrator plants required to produce PGM-rich concentrates using low mass pulls (Eksteen, et al., 2011). Table 2.2 reports the bulk composition of a typical Merensky Reef and UG2 chromitite concentrate blend at Lonmin.

Table 2.2: Bulk composition of a typical Merensky Reef and UG2 chromitite concentrate blend (modified after Eksteen, et al., 2011).

Constituent	**Ni**	**Cu**	**Co**	**PGM (g/t)**	**Fe_{Total} (as FeO)**	**S**	**SiO_2**	**MgO**	**Al_2O_3**	**CaO**	**Cr_2O_3**
Mass %	2.8	1.6	0.1	260	20	5.3	40.4	17.7	4.0	3.0	2.3

2.3.2. Pyrometallurgical Processes

Extractive metallurgy developed at an early stage into an important branch of the applied sciences (Cramb, 2012). The current extractive metallurgy of mineral concentrates of sulfide

origin seems to be dominated by the unit process of pyrometallurgy, in arrangement with hydrometallurgical extraction and refining (Aspola et al., 2012). Pyrometallurgical processing, in particular, tends to be intricate and is used to describe the high temperature techniques in metal production processes (Hayes, 2003). Depending on its relevance, the techniques of roasting, smelting and converting can be considered as central to non-ferrous pyrometallurgical process routes (Mäkinen and Taskinen, 2006). Roasting is a solid state pyrometallurgical technique which involves the oxidative heating of sulfide minerals (Hayes, 2003).

Primary smelting is aimed at the melting of the solid mineral concentrate, followed by separation of the valuable sulfide and non-valuable gangue silicate phases (Liddell et al., 1986). In effect, melting down the solid mineral concentrate results in the formation of a sulfide-dominant liquid matte and a silicate-iron-dominant slag phase with bulk density ranges of 4.8 – 5.3g/cm^3 and 2.7 – 3.3g/cm^3, respectively (Jones, 2005). This difference in bulk density allows for a separation between the denser matte and the lighter silicate-iron-dominant slag. Converting is a liquid state pyrometallurgical technique required to affect certain chemical changes to a desired level in primary smelting matte. In particular, it is required to remove iron, sulfur and other deleterious elements in order to provide nickel-copper-PGM mattes of suitable mineralogical quality for subsequent pre-treatment and physical processing prior to hydrometallurgical extraction processes. These aspects of converting are of interest to this study and will be examined in detail in sub-section 2.4.2.

Various technologies can, at present, be used in the application of pyrometallurgical techniques. It is appropriate to consider the circumstances and key achievements in their development, leading to modern non-ferrous pyrometallurgical practices. Most of the early technologies were rudimentary, whereas high shipping costs to distant locations provided the impetus to perform extractive metallurgical processing within mine sites (Fraser, 1952). The same author reported, for example, that roasting of sulfide ore was performed on open heaps. Blast furnaces were then used to smelt the roasted product to a primary matte, followed by the removal of iron and sulfur by Bessemerizing (Fraser, 1952). Southwick (2008) provided an interesting historic overview of Bessemerizing leading to the installation of the first Peirce-Smith converting technology at a smelter facility in Utah, USA circa 1910.

The description that follows is based on this historic overview. In 1856, Henry Bessemer, working in the steel industry, invented the original air blown converter. It was described as a pear-shaped vessel including tuyeres along the bottom for the inlet of air. The top had a cone-shaped mouth for the multipurpose of feeding, emitting gas and the pouring of product contents. Figure 2.3 provides a historic depiction of the original converter invented by Henry Bessemer. The tyueres required for the distribution of air from the bottom is not visible in Figure 2.3.

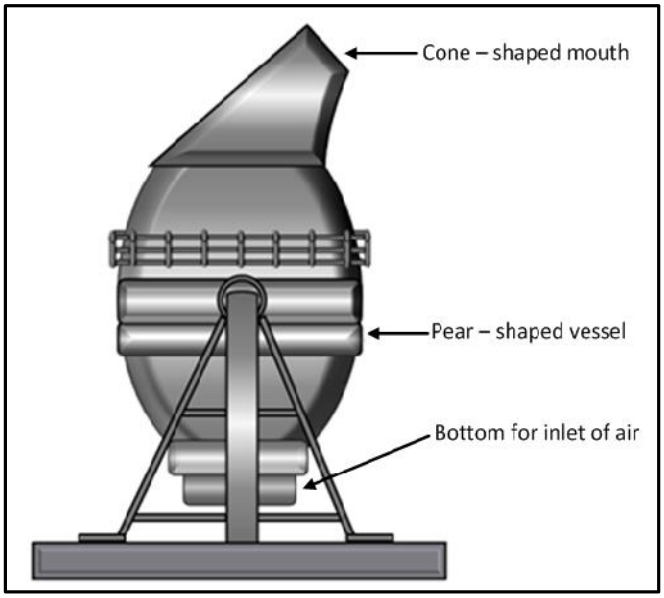

Figure 2.3: The original air blown converter, invented in 1856 by Henry Bessemer (redrawn after Southwick, 2008).

The subsequent invention of pneumatic copper converter technology was based on the original ideas of Henry Bessemer. Particular studies by William Peirce and E.A. Cappelen Smith were aimed at improving the design and refractory lining of operating copper converters. Side-and end elevations including the cross-sectional view of an initial Peirce-Smith converter design is illustrated in Figure 2.4.

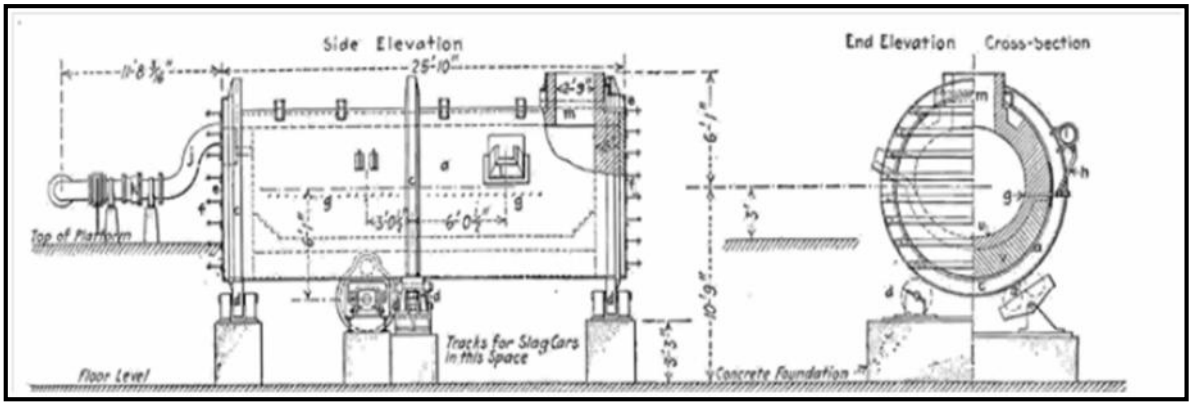

Figure 2.4: Technical drawing of an initial Peirce-Smith converter design showing the side-and end elevation as well as cross-sectional view (from Southwick, 2008).

Their contribution towards a chemical-efficient converting technology, which is performed in what is aptly known as Peirce-Smith converters, is widely recognized within the pyrometallurgical fraternity (Southwick, 2008).

Blast furnaces coupled to Great-Falls-type converters were operated around the 1930s in Rustenburg, South Africa (Nell, 2004) to process the concentrates from the then recently discovered Merensky Reef. These were replaced in the 1960s by rectangular six-electrode electric furnaces and Peirce-Smith converters. Flash smelting technology was initially developed during the 1940s by the Finnish company Outokumpu to treat copper concentrates with improved energy and environmental efficiencies (George et al., 1999). Flash smelting furnaces were coupled to Peirce-Smith converters during the late 1950s at the smelting facility in Harjavalta, Finland for the treatment of nickel concentrates (Mäkinen and Taskinen, 2006). Inco flash smelting technology was subsequently developed to smelt concentrates in an Inco oxygen flash furnace as an alternative to the conventional Outokumpu flash furnace. Similar developments on energy efficient bath smelting technological developments include that of Noranda, Mitsubishi and ISASMELT™ (George et al., 1999). Furthermore, continuous smelting technology without subsequent converting was also investigated by several companies, including Mitsubishi and Outokumpu. The investigations by Outokumpu, for example, led to the development of their direct-oxygen-to-final-matte or direct Outokumpu nickel (DON) technology, with which an iron-lean matte can be produced within a single flash smelting furnace (Riekkola-Vanhanen, 1999).

Global survey studies describing modern nonferrous pyrometallurgical practices were completed by several authors (Jones, 2004; Jones, 2005; Warner et al., 2007). Electric furnace and conventional flash smelting technologies are mostly applied to the processing of nickel concentrates and their recycled smelting product (Warner et al., 2007). Electric furnaces, in particular, are coupled to Peirce-Smith converters at primary nickel producers such as Xstrata Nickel in Sudbury, Canada and Norilsk Nickel in Norilsk, Russia. Electric furnace smelting technologies are applied, however, exclusively to the processing of PGM-rich concentrates (Jones, 2004). The electric furnaces are either coupled to Peirce-Smith, Ausmelt or top-blown rotary converters at the respective primary PGM producers. Lonmin, for example, employs Peirce-Smith converters while Anglo Platinum prefers the usage of continuous Ausmelt converters (Jones, 2005). It can be concluded that a similar range of interconnected technologies are applied to modern pyrometallurgical process routes treating nickel and PGM-rich concentrates. The respective pyrometallurgical routes also serve the common purpose of processing high-iron furnace matte into an iron-lean converter matte.

2.3.3. Intermediate Matte Pre-treatment and Processes

The product of converting requires pre-treatment in combination with physical processes to yield it amenable to hydrometallurgical extraction (Jones, 2005; Warner et al., 2007; Crundwell et al., 2011). The final molten matte from the various converter technologies is justly diverse and more so with respect to imposed iron and sulfur levels. A large proportion of the final matte from operating sulfide smelting facilities is first subjected to cooling, an important liquid phase pre-treatment step for the attainment of matte solidification. The solidified matte is considered as an intermediate pyrometallurgical product and the starting point for the coordinated application of typical batch grinding, followed by classification techniques. The resulting matte at some operations may also be beneficiated by selective physical separation techniques. Major PGM producers, such as Anglo Platinum and Lonmin, apply vastly different matte pre-treatment and physical processing practices. The molten matte at Anglo Platinum is subjected to slow cooling, followed by grinding, classification and magnetic separation. In contrast, the molten matte at Lonmin is granulated, ground and classified prior to hydrometallurgical processing. The liquid phase pre-treatment step is

generally arranged within the smelter facilities, while the subsequent physical processing occurs close to or within the hydrometallurgical facilities. The intermediate matte pre-treatment and process steps at Lonmin are central to this study.

2.3.4. Hydrometallurgical Extraction Processes

The field of hydrometallurgy is relatively new, in contrast to pyrometallurgy (Habashi, 2005). Hydrometallurgy provides for the aqueous extraction of metals from their concentrates (Habashi, 1999). The techniques of leaching, purification and precipitation can generally be considered as the major process steps. Leaching is the initial process step, aimed at solubilizing the target metals through the use of suitable chemical agents. The dissolved metals are then separated from the pregnant solution by a precipitation technique. A purification technique may be applied to the pregnant solution at first in order to affect extraction efficiencies. The process chemistry during leaching tends to be unique to the decomposition of the minerals being treated, rendering application of the technique variable and hugely selective (Peters, 1976).

Saleable base and platinum-group metals are usually customized end products, although their hydrometallurgical extraction may commence from a diverse converter matte. The extraction of base metals from converter matte is usually accomplished in a base metal refinery, using process technology purposely designed to operate efficiently within impurity setpoints. Rustenburg Base Metal Refineries (RBMR), for example, was established as early as 1953 in Rustenburg, South Africa for the exclusive extraction of base metals from converter matte (Hofirek and Kerfoot, 1992; Hofirek and Nofal, 1995). Anglo Platinum treats only the base metal containing, non-magnetic fraction at the RBMR (Jacobs, 2006). In comparison, Lonmin treats all its prepared converter matte at its base metal refinery in Marikana, South Africa (Jones, 2005). The chief objective of the Lonmin base metal refinery is to extract the base metals as early as possible, in order to produce a PGM concentrate for further processing (Eksteen et al, 2011). The base metal refinery operation and improvements at Lonmin are described fully by Steenekamp and Dunn (1999). The first stage atmospheric leach of the base metal refinery is, to some extent, relevant to this study and is therefore discussed in appropriate detail in sub-section 2.6.2.

2.3.5. Refining Processes

Refinement of the PGM concentrate is aimed at producing separate platinum-group metals as final products. The refining techniques are applied within a precious metal refinery typically secluded from the base metal refinery (Riekkola-Vanhanen, 1999). The PGM-containing, magnetic converter matte concentrates from Anglo Platinum operations are dispatched to a precious metal refinery (Jacobs, 2006). Similarly, the PGM concentrate from Lonmin operations are refined at its precious metal refinery in Brakpan, South Africa (Eksteen et al., 2011). Figure 2.5 presents a flow diagram common to PGM and base metal production from sulfide ores within the Bushveld Complex of South Africa. The construction of the flow diagram is based on information in the preceding sub-sections and particularly illustrative of the interconnectivity of the metal production processes and techniques.

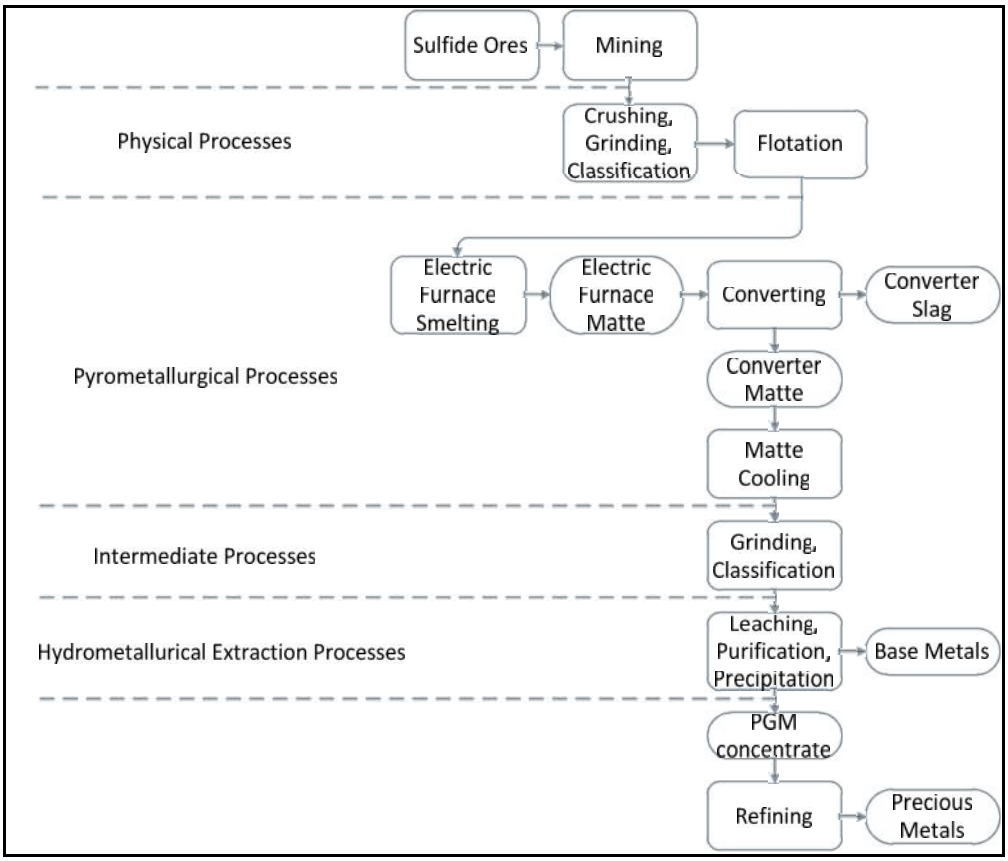

Figure 2.5: A flow diagram common to PGM and base metal production from sulfide ores within the Bushveld Complex of South Africa.

In conclusion, this section has provided the background to the next, in which the intermediate matte pre-treatment and process steps will be fundamentally described and

analyzed.

2.4. The Lonmin Smelter Facility

The following description is mainly based on information provided by Eksteen et al., (2011) and Jones (2005). The Western Platinum Smelter can, at present, be regarded as a modern pyrometallurgical facility, despite coming into production in around 1971 (Eksteen et al., 2011). A block diagram illustrating the relevant smelter technologies and process flows within the smelter facility is shown in Figure 2.6. The sub-sections that follow describe the components of the block diagram relevant to this study in more detail.

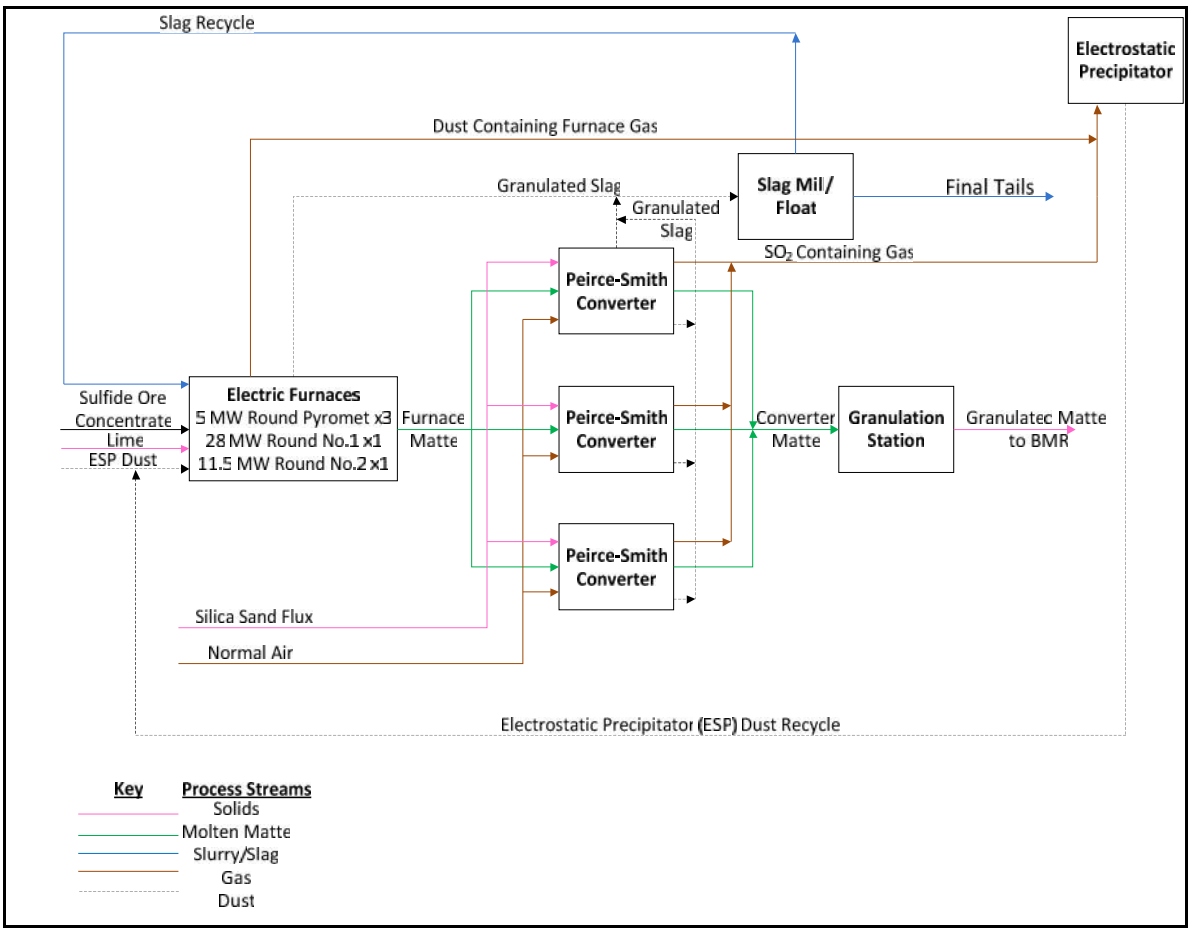

Figure 2.6: A block diagram illustrating the technology and process flows within the Western Platinum Smelter Facility (modified after Eksteen et al., 2011).

2.4.1. The Smelting Plant

The illustration of the smelting plant in Figure 2.6 is somewhat simplified and includes five electric furnaces being fed by several solid streams, including sulfide ore concentrate, and

lime for purpose of fluxing. In actual fact, Merensky Reef and UG2 chromitite concentrates are smelted using dissimilar electric furnaces and the separate matte produced is combined at the converters (Jones, 2005). A baseline matte fall of 15% is regarded as essential to affect PGM collection mechanisms by furnace matte (Andrews, 2008). The furnace and converter slag is jointly granulated, after which entrained matte is recovered by milling and flotation practices, and then recycled to the smelting plant. The furnace and converter off-gas is allowed to flow to an electrostatic precipitator for cleaning. Table 2.3 reports the bulk composition of combined furnace matte prior to converting. The enrichment in PGM concentration after smelting is considerable when compared to the grade following physical processes, as indicated previously in Table 2.2.

Table 2.3: Bulk composition of combined furnace matte at the Western Platinum smelting plant (modified after Jones, 2005).

Constituent	**Ni**	**Cu**	**Fe**	**Co**	**Cr**	**S**	**PGM (g/t)**
Mass %	17.0	9.8	36.0	0.5	0.3	28.0	1750

2.4.2. The Converter Plant

The illustration of the converter plant in Figure 2.6 includes three Peirce-Smith converters that can be regarded as similar (Eksteen et al., 2011). Their key operating details are considered in Table 2.4.

Table 2.4: Key operating details of a Peirce-Smith unit at the converter plant (from Eksteen et al., 2011).

Diameter of Converter (m)	Length of Converter (m)	Number of Tuyeres	Diameter of Tuyeres (mm)	Number of Blowers	Average Blowing Rate (Nm^3/h)
3.0	4.6	16	50	3	13 000

The respective molten furnace matte is transferred *via* ladles and crane for charging into batch mode Peirce-Smith converters (Jones, 2005). Figure 2.7(a) shows an actual operating unit at the converter plant. Air is supplied from blowers and injected *via* tuyeres into the molten matte for the specific purpose of oxidizing the iron and sulfur within to iron oxide

and sulfur dioxide, respectively. The converter tuyere and bustle pipe assembly is shown in Figure 2.7(b). Silica sand is added as flux to promote a fayalitic slag forming process by reaction with iron oxide. A brief account of the converting process chemistry is provided in the next sub-section.

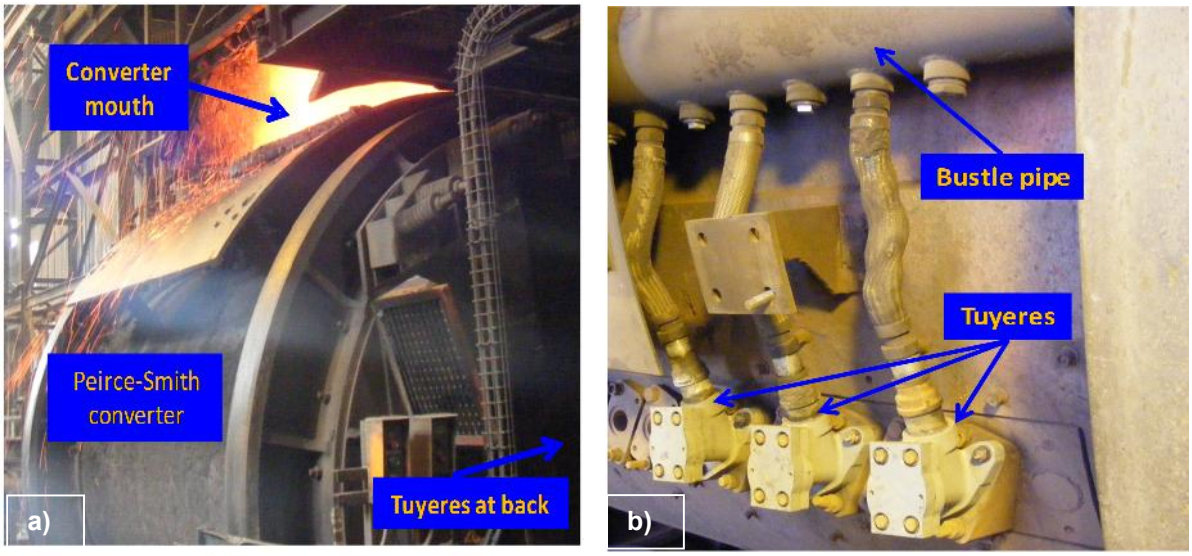

Figure 2.7: Photographs showing (a) an actual operating Peirce-Smith converter unit and (b) tuyere and bustle pipe assembly at the converter plant (photographs courtesy of Lonmin).

2.4.2.1. Converting Process Chemistry

The converting process chemistry of nickel-dominant mattes is fundamentally known. Kyllo and Richards (1991) provided a basic equilibrium understanding of the mass and heat balances of iron and sulfur during the various matte blows. A subsequent study by Kyllo et al., (1992) indicated that most of the oxygen injected in the initial matte blow reacts with the available iron in the molten matte, leading to a considerable rise in bath temperature. The coupled iron oxidation and slag formation reaction is represented by Reaction 2.1 (Crundwell et al., 2011):

$$2Fe\,(l) + O_2\,(g) + SiO_2\,(s) \rightarrow Fe_2SiO_4\,(l) \qquad [2.1]$$

At the Western Platinum converter plant, bath temperatures are measured with a pyrometer and maintained under 1270 ^{o}C (Eksteen et al., 2011). Sulfur will increasingly react with oxygen as the iron in the matte is removed. The sulfur oxidation reaction is given by Reaction 2.2:

$$S\,(l) + O_2\,(g) \rightarrow SO_2\,(g) \qquad [2.2]$$

Converting includes several more blows during which iron is steadily removed from the matte with resultant changes in bulk matte composition. Moreover, the slag produced would be tapped intermittently, after which fresh charge is added, permitting the accumulation of converted matte (Jones, 2005). Most of the PGMs and even copper may be too noble to be oxidized during converting, and their enrichment follows progressively within the matte. Osmium and ruthenium tetroxides may be produced under oxidizing conditions and would be lost to the gas phase (Eksteen et al., 2011). Tshilombo and Pistorius (2006) demonstrated that measured oxygen activities can be used to indicate the extent of iron removal in converting reactions. It is therefore possible to relate the partial pressure of oxygen to matte iron levels (Sridhar et al., 1997). The chemistry of converting has also been successfully studied by Selivanov et al., (2009). The rate and quality of injected oxygen are regarded as the foremost converting reaction parameters (Kyllo et al., 1992).

Converted matte is accumulated to a predetermined batch before a finishing blow is applied to end the converting reactions at a desired iron level in step with downstream base metal refinery limitations. The controlled final blowing of matte is key to achieving the desired iron endpoint. An additional intention would be to optimize the valuable base metal and PGM enrichment within the bulk matte. The converted matte is usually tapped after the attainment of iron endpoint. The finished matte at the Western Platinum converter plant may have a bulk composition (excluding PGMs) as indicated in Table 2.5.

Table 2.5: Bulk composition of converted matte at the Western Platinum converter plant (from Eksteen et al., 2011).

Constituent	Ni	Cu	S	Fe	Co
Mass %	48.0	29.0	21.0	1.0	0.35

2.4.2.2. Iron Endpoint

The iron endpoint achieved for the particular finished matte composition in Table 2.5 is reported as 1.0%. It is interesting to note, in Table 2.6, the dissimilarities in reported iron endpoints for major PGM producers (including Lonmin).

Table 2.6: Comparison in iron endpoints for major PGM producers (modified after Warner et al., 2007).

PGM Producer	Lonmin (Marikana, SA)	Anglo (Waterval, SA)	Northam (Northam, SA)	Zimplats (Selous, Zimbabwe)	Stillwater Mining Complex (Montana, USA)
Iron Endpoint (mass % Fe)	1.4	3.0	1.0	0.6	2.0

The iron endpoints above range from 0.6% to 3.0% and are a manifestation of the individual operating variability and downstream process requirements of the respective producers. Within PGM producers, however, ambiguity in the ideal iron endpoint composition and inconsistent control thereof can have considerable effect on the mineralogical quality of the matte produced. It follows that the effect of the iron endpoint on the matte mineralogy, is poorly understood and therefore quantified by plant metallurgist. Iron endpoint monitoring at the Western Platinum converter plant is based on the consideration of flame color and historically concluded by an experienced operator (Eksteen et al., 2011). It was not clear from literature by which method the rest of the PGM producers, listed in Table 2.6, monitor and control the iron endpoint.

2.4.3. Matte Granulation

The converter plant typically produces between 40 and 60 tons of final molten matte per day, which is tapped into ladles. The granulation station would receive the tapped ladles by overhead crane. The description of the matte granulation system that follows is based on actual observations within the Lonmin Smelter Facility. A hydraulic tilter is used for pouring the molten matte within the ladles into a granulation launder. A jet of water located below the granulation launder is used to shear quench the molten matte. Relatively fine matte granules or particles are formed upon contact with the water, which next collects in a settling matte pond and is reclaimed by grab cranes. Figure 2.8 is illustrative of the matte granulation system in use at the Lonmin Smelter Facility.

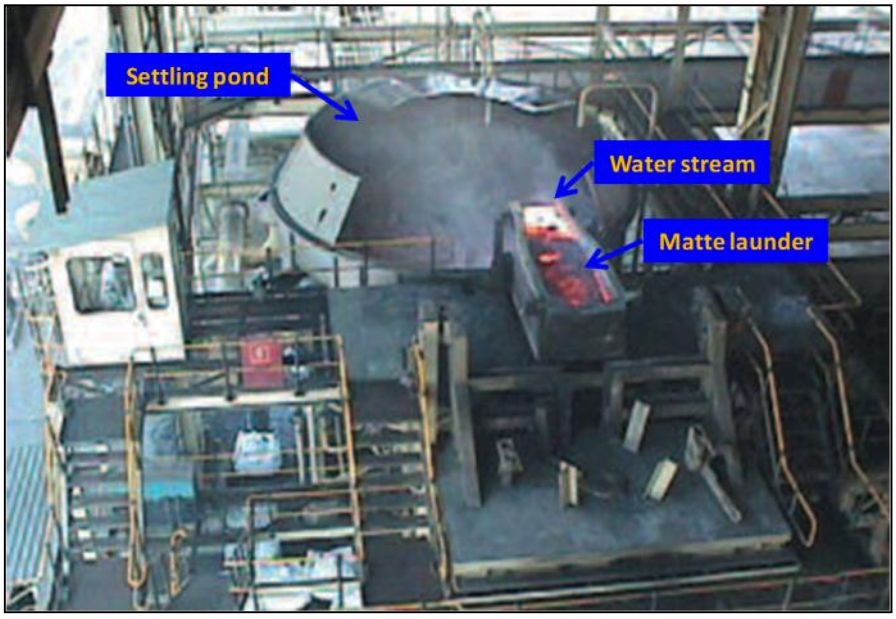

Figure 2.8: Photograph illustrative of the matte granulation system in use at the Lonmin Smelter Facility (photograph courtesy of Bateman, 2013).

The granulated matte particles are conveyed to the BMR for initial batch grinding and hydrocyclone classification prior to first stage atmospheric leaching (Bircumshaw, 2008). According to Jones (2005), the final molten matte at Lonmin Platinum used to be slow cooled. This practice, in combination with undesired iron endpoint compositions, resulted in the formation of some deleterious spinel phases. These characteristically remain unresponsive during leaching, and in turn, contaminate the resultant PGM concentrate (Jones, 2005). Granulation, on the other hand, is considered, within context as a fast-cooling and possible quenching treatment intended to suitably affect the chemical and physical transformation of molten to solidified matte (Norval, 2005). The technical aspects of granulation within the South African metallurgical industry have been discussed in certain publications (Norval, 2005; Norval and Oberholster, 2011). Although matte granulation, instead of slow cooling, is now successfully practiced within the Lonmin Platinum Smelter Facility, it is important to link the practice to a desired iron endpoint composition.

2.5. Sulfide Mineralogy and Phase Equilibria

The focus of the literature review now shifts to critically establishing the theoretical basis for understanding matte pre-treatment with respect to the underlying sulfide mineral systems. The scientific literature on natural and synthetic sulfide mineralogy and their phase

equilibria is substantial and indicative of a methodically studied knowledge area (Vaughan, 2005). Fundamental studies of sulfide microstructures stimulated the parallel development of microanalytical techniques for their characterization (Vaughan and Craig, 1978). According to Djurle (1958), for example, copper sulfide structures were readily identified at the time using the emergent technique of powder X-ray diffraction. The crystallography of nickel sulfide structures were also successfully confirmed using the same technique applied to their synthetic powders (Fleet, 1972; 1977). Numerous experimental studies and laboratory investigations, coupled to advancement in analytical techniques, allowed for the systematic determination and diagrammatical representation of sulfide phase equilibria (Firdu and Taskinen, 2010). The coverage below, describes the basics of sulfide mineral structures, followed by an examination of relevant natural and synthetic sulfide phase relations. The mineralogy and phase relations of analogous converter matte mineral structures (of pyrometallurgical origin) are of particular importance to this study, and discussed in the end.

2.5.1. The Basics of Sulfide Mineral Structures

Most mineral structures of sulfide origin have fundamentally been identified and categorized depending on relevant criteria. Table 2.7 is indicative, for instance, of the categorization of sulfide minerals (relevant to this study) into major groups based on common structural features.

Pyrrhotite and chalcopyrite were found to have derivative structures based on ordered modifications to their original parent structures. Sulfide mineral structures may also exhibit polymorphism at certain inversion points. Williams (1960) reported that natural awaruite minerals were analyzed during the late 1940s and confirmed its composition as a predominantly nickel and iron alloy. Awaruite was also observed to co-exist alongside heazlewoodite and pentlandite within the same samples. The chemical formula of ideal awaruite is generally accepted as Ni_3Fe. The crystal structure has been described by Rubin (1991) as face-centred cubic (fcc), in which nickel and iron atoms are respectively located at the centre and corners along the faces of unit cells.

Table 2.7: Categorization of relevant sulfide minerals into major structural groups (modified after Vaughan, 2005).

Sulfide Structural Group	Mineral Structure	Mineral Name	Chemical Formula
Metal Excess Group	Nickel Sulfide Structure	Heazlewoodite	Ni_3S_2
		Millerite	NiS
	Chalcocite Structure	Chalcocite	Cu_2S
		Djurleite	$Cu_{1.96}S$
	Digenite Structure	Digenite	Cu_9S_5
	Pentlandite Structure	Pentlandite	$(Ni,Fe)_9S_8$
Layer Sulfides Group	Covellite Structure	Covellite	CuS
Nickel Arsenide Group	Ordered Omission Derivatives	Pyrrhotite	$Fe_{1-x}S$ (several varieties)
Disulfide Group	Pyrite Structure	Pyrite	Fe_2S
Sphalerite Group	Ordered Substitution Derivative	Chalcopyrite	$CuFeS_2$

The chemistry of sulfide minerals is essentially understood despite their compositional variations, non-stoichiometry and tendency to form solid-solutions (Vaughan, 2005; Firdu and Taskinen, 2010). Non-stoichiometry of sulfide minerals can generally be ascribed to metal atomic vacancies within their unit cell arrangements. Moreover, non-stoichiometry would influence the microscopic to macroscopic properties of the constituent sulfide minerals. Sulfide minerals are mostly considered to form covalent or metallic bonds (Firdu and Taskinen, 2010). Chemical bonding in sulfide minerals remains a complex subject matter despite progress in the present understanding thereof (Vaughan, 2005).

The micro-to macroscopic properties of most natural sulfide minerals have been determined (Vaughan and Craig, 1978; Vaughan, 2005). The following findings are based on the important sulfide mineral review completed by Vaughan and Craig (1978). Physical properties such as luster, streak, specific gravity and hardness are regarded as basic to an understanding of mineralogy and can strongly be associated with the composition of the sulfide minerals. The property of hardness is commonly defined as resistance to plastic

deformation and incorporates several mechanical strength quantities. Various measurement techniques and scales for hardness and micro-hardness were developed. The conventional Mohs-scale provides a relative measure of macro-hardness while indentation techniques allow for the quantitative determination of micro-hardness. However, there is limited physical data describing microscopic properties of converter matte mineral structures available in the open literature.

2.5.2. Sulfide Phase Equilibria

Understanding sulfide phase equilibria is important to a number of researchers, including those in the fields of geology, experimental petrology, mineralogy, metallurgy and materials. Natural and synthetic mineral systems tend to be described by their equilibrium sub-systems with respect to composition, pressure or activity measures as a function of temperature (Vaughan and Craig, 1978). The fundamental sulfide binary, ternary and higher order systems relevant to this study will now be described.

2.5.2.1. The Ni-S Binary System

The mineral phases that exist between 200 ^{o}C and 1030 ^{o}C within the Ni-S binary system include, in order of increasing thermal stability: polydymite (Ni_3S_4), millerite (NiS), heazlewoodite (Ni_3S_2), godlevskite (Ni_7S_6) and vaesite (NiS_2). Seminal experimental investigations were conducted by Kullerud and Yund (1962), Fleet (1972) and Arnold and Malik (1975). According to Kullerud and Yund (1962), hexagonal Ni_3S_2 inverts at 556 ^{o}C to a higher temperature polymorph, α-Ni_3S_2, with a tetragonal structure. The thermal stability of the polymorph also extends to 806 ^{o}C. Fleet (1971) pointed out that Ni_7S_6 is stable between 400 ^{o}C and 573 ^{o}C and can also exist as a polymorph, α-Ni_7S_6, below 400 ^{o}C. The latter phases can also be characterized by solid solution formations within a limited compositional range. Arnold and Malik (1975) found the thermal stability of NiS_2 at 1022 ^{o}C higher than initially reported. The experimental phase diagram for the Ni-S binary system in the concentration range of 18-56 weight (wt)% S as a function of the temperature range 200-1100 ^{o}C, is shown in Figure 2.9. The underlying thermodynamic measures of the Ni-S binary system were also investigated by several authors, including Nagamori and Ingraham (1970) and Sharma and Chang (1980b).

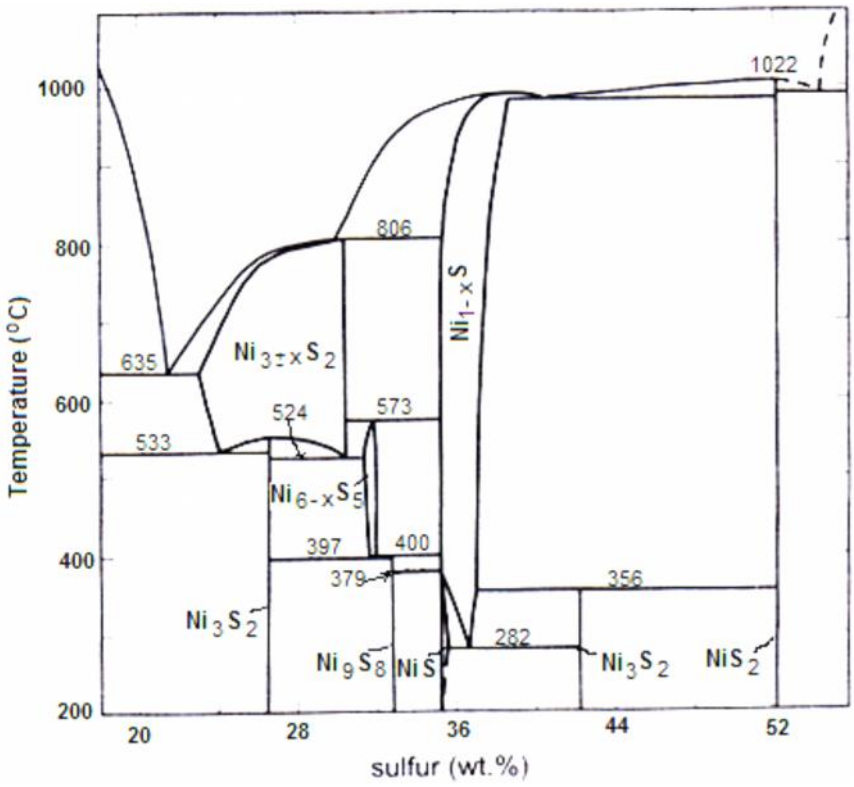

Figure 2.9: Experimental phase diagram for the Ni-S binary system showing the thermal stability fields of the various nickel sulfide mineral phases (from Firdu and Taskinen, 2010 and references therein).

2.5.2.2. The Cu-S Binary System

The Cu-S binary system is more complex than the Ni-S binary system and has been described and modified in numerous publications. Chalcocite (Cu_2S) and covellite (CuS) phases were already investigated by the early 1940s. A phase with approximate formula $Cu_{1.96}S$ was successfully synthesized in the laboratory by Djurle (1958). Roseboom (1966) subsequently studied the natural equivalent and aptly termed it djurleite. Monoclinic chalcocite was found to invert at 103 °C to a hexagonal polymorph that, in turn, inverts to cubic form at 435 °C. Moreover, digenite was found to exist at low temperatures within compositional range $Cu_{1.77}S$ to $Cu_{1.84}S$. Morimoto and Koto (1970) indicated that natural assemblages of digenite incorporated iron into their structures, and are therefore best studied in the Cu-Fe-S ternary system. Potter (1977) employed electrochemical techniques to study low stability phase relations within the Cu-S system. Low stability relations between chalcocite and djurleite were found to be characteristic of intergrowth patterns (Evans, 1981). Posfai and Buseck (1994) used high-resolution transmission electron microscopy (HRTEM) to

investigate the intergrowth on nanoscale between chalcocite and djurleite. Figure 2.10 illustrates a region of the experimental phase diagram for the Cu-S binary system. Various thermochemical aspects of the Cu-S binary system were also covered by Sharma and Chang (1980a) and Chakrabarti and Laughlin (1983).

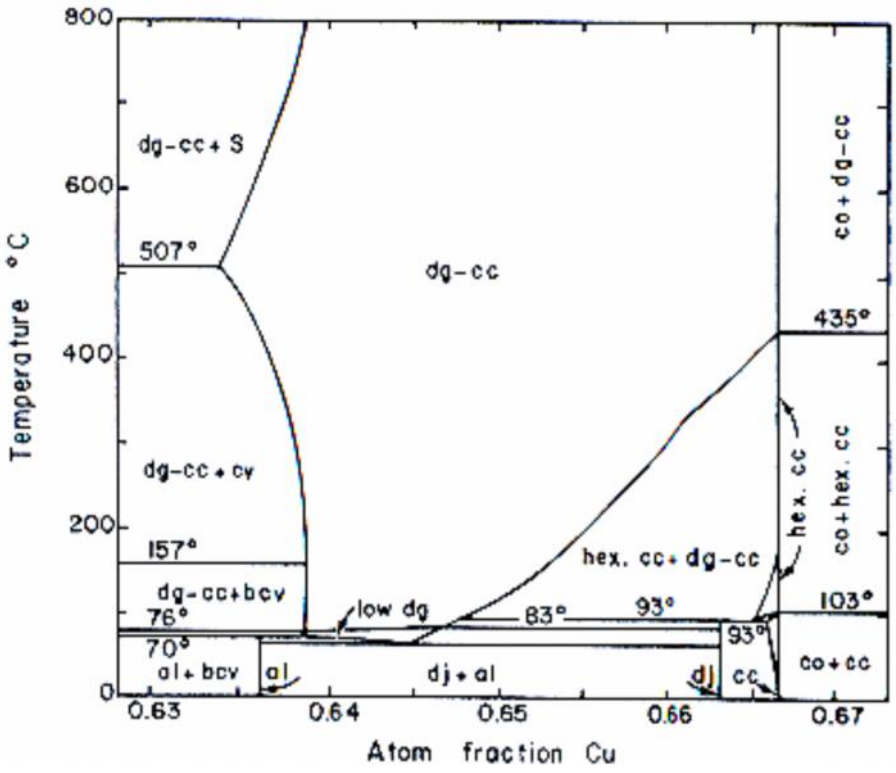

Figure 2.10: Experimental phase diagram for the Cu-S binary region indicating the thermal stability fields of the various copper sulfide mineral phases. The following abbreviations are applicable: al-anilite, bcv-blue-remaining covellite, cc-chalcocite, cv-covellite, co-copper, dg-digenite and dj-djurleite. (from Firdu and Taskinen, 2010 and references therein).

2.5.2.3. The Fe-S Binary System

Mineral phases of possible relevance to this study, due to low final matte iron concentration, include pyrite (FeS_2) and pyrrhotite ($Fe_{1-x}S$). Stable pyrite-to-pyrrhotite phase relations were investigated by Kullerud and Yoder (1959). Pyrite was reportedly stable to 742 ^oC and may also be present as the low temperature polymorph marcasite. Hexagonal pyrrhotite, on the other hand, is stable to 1192 ^oC and incorporates solid solution formation. Thermochemical studies of the Fe-S binary system were also undertaken (Toulmin and Barton, 1964; Waldner and Pelton, 2005).

2.5.2.4. Ternary Systems

Phase relations in the Ni-Fe-S ternary system are dominated by the existence of an extensive ternary phase that transforms upon cooling to pentlandite (Hawley et al., 1943). Kullerud (1963) reported the thermal stability of synthetic pentlandite from 610 ^{o}C. Clark and Kullerud (1963) found the ternary (solid solution) phase, $(Ni,Fe)_{1-x}S$, and liquid sulfur both present above approximately 729 ^{o}C. Pyrite and pentlandite co-exist at low temperatures in the pentlandite portion of the system (Shewman, 1966; Craig, 1973). Thermochemical measurements of sulfur were also conducted for Ni-Fe-S matte systems at 1250 ^{o}C (Byerley and Takebe, 1972).

Phase relations in the Cu-Fe-S ternary system were initially investigated by Merwin and Lombard (1937). Bornite (Cu_5FeS_4), chalcopyrite ($CuFeS_2$) and pyrrhotite ($Fe_{1-x}S$) were reported to exist as solid solutions from 700 ^{o}C to 200 ^{o}C (Yund and Kullerud, 1966). An isothermal section of the Cu-Fe-S system at 600 ^{o}C was constructed by Cabri (1973). A phase diagram was provided for the CuFe-S join between 400 ^{o}C and 700 ^{o}C (Barton, 1973), while Sugaki et al., (1975) constructed isothermal sections at 300 ^{o}C and 350 ^{o}C. Moh and Kullerud (1963) experimentally studied the Ni-Cu-S ternary system at low thermal stabilities.

2.5.2.5. Quaternary and Higher Order Systems

Most of the information that follows is based on a relatively recent review of the Ni-Cu-Fe-S quaternary system by Raghavan (2004). Quaternary phase relations in the Ni-Cu-Fe-S system were established by 1965, but were based on extrapolation of the Ni-Fe-S, Cu-Fe-S and Ni-Cu-S ternary systems. Semi-quantitative diagrams of the system were produced at 400 ^{o}C, 850 ^{o}C and 1000 ^{o}C. Quaternary sulfide liquid and $Fe_{1-x}S$-Ni_{1-x} monosulfide solid solution were found to exist in the system at 1000 ^{o}C. The liquidus surface of the system was not well defined and experimental studies were conducted to improve the construction thereof (Sineva et al., 2009; Starykh et al., 2009).

Experimentalist in the field of petrology studied the Ni-Cu-Fe-S quaternary system within the composition region of magmatic sulfide melt crystallization processes. Co-existing monosulfide solid solution $[(Fe,Ni)_{1-x}S]$ and sulfide melt quaternary phase relations were explored in the system at 50% and 52.5% atomic S, 800 ^{o}C to 1050 ^{o}C and low pressure (Fleet and Pan, 1994). The thermal stability of intermediate solid solution $[(Cu,Fe)S_{1-x}]$ was

reported as 900 ^{0}C and extended to 950 ^{o}C. A ternary solid solution with composition (Fe,Cu, Ni)S was also found to be present at 850 ^{o}C and subsequent lower temperatures. Mungall (2007) developed empirical parameterization for understanding base metal and sulfur partitioning between sulfide melt and monosulfide solid solution in the Ni-Cu-Fe-S-O system.

The influence of the metal/sulfur atomic ratio on base metal and PGM partitioning into monosulfide solid solution and sulfide melt were quantified for the Ni-Cu-Fe-S-PGM system (Ballhaus et al., 2001). The partition coefficient for nickel was found to be significantly influenced by the metal/sulfur atomic ratio and temperature. In contrast, the metal/sulfur atomic ratio had little influence on the partition behavior of PGMs. The individual partitioning behavior of PGMs during fractional crystallization sequences of magmatic sulfide melts was investigated by several authors (Fleet and Stone, 1990; Andrews and Brenan, 2002; Holwell and McDonald, 2010).

2.5.3. Converter Matte Mineralogy and Equilibria

The mineralogy of slow cooled, water quenched and rapidly air cooled matte samples was investigated separately during commissioning of a flash smelting furnace at the Kalgoorlie Nickel Smelter in Western Australia (Page, 1982). The following findings are based on the mineralogical investigations. The individual matte samples retained a particular high final iron content ranging from 22.1% to 32.5% Fe. The major phase structures present were identified as pentlandite, heazlewoodite and awaruite. Less abundant phase structures included that of bornite, chromite, magnetite and fayalite. The slow cooled matte was found to contain less heazlewoodite, but more rounded awaruite phase structures than the water quenched sample. The subordinate presence of heazlewoodite in the slow cooled matte could be correlated to the lower concentration of nickel within its bulk composition. The slow cooled and quenched matte was both characteristic of skeletally arranged awaruite structures. Awaruite phase structures within the quenched matte were analyzed by XRD and found to have an fcc crystal structure. This finding is in agreement with the description provided in sub-section 2.5.1. The microtexture of the slow cooled sample was also observed to be coarser compared to the rapidly air cooled and quenched samples. Matte chemistry was concluded as being influential with respect to exsolution of phase structures

and their constituents. It was proposed that the phase structures crystallized under non-equilibrium operating conditions.

There has been considerable experimental effort to understand the effect of variable converter matte starting compositions on the slow cooled Ni-Cu-S system within the context of the Anglo Platinum process route (Viljoen, 2001). These experimental investigations were limited to a temperature interval (100 ^{o}C) and range (700 ^{o}C to 1200 ^{o}C). A notable finding was the difference in the solidification path of liquid matte as a function of variable starting iron concentration and temperature. This finding supports the baseline or starting point selected for this new study as described in Chapter 1 (section 1.6). The Anglo Platinum industrial converter matte slow-cooling process was also extensively investigated from both a mineralogical and resource management perspective (Schouwstra, 2000; 2003). The mineralogical investigation led to a practical understanding of crystallization processes within a slow-cooled ingot. A formation mechanism of PGM-containing alloy phase structures was also suggested, with a particular emphasis on platinum and palladium exsolution. The resource management perspective allowed for the optimisation of key downstream process steps with respect to resultant mineralogy. There has been limited effort to understand the fuller effect of variable starting compositions on fast-cooled, multi-component and Ni-PGM valuable matte systems, more so from a Lonmin process perspective. This was evident from insufficient coherent data available in the open and relevant industrial literature.

Electron microscopy has progressively become indispendable as an analytical tool within the fields of petrology, mineralogy (Zussman, 1987; Ferrow, 1994) and, by extension, metallurgy and materials. The application of mineralogical analytical techniques to specific investigations of pyrometallurgical products is regarded as useful for the monitoring and control of process conditions (Hagni et al., 1987; Andrews, 2007; 2008; Andrews and den Hoed, 2011). Govender (2006) applied a variety of analytical techniques, including particle induced X-ray emission (PIXE), to determine the trace element concentration of converter matte. Schouwstra (2008) also investigated converter matte from different PGM producers (including Lonmin) using various analytical techniques to identify a possible (forensic) mineralogical signature. The investigation revealed that mattes from all producers

predominantly consist of nickel and copper sulfide phase structures. Copper-iron sulfide phase structures may be present, provided the bulk matte iron concentration is sufficient. The Lonmin matte achieved an iron concentration (or iron endpoint) of 0.5%. Additional Lonmin matte characteristics include having a bulk density of 6.3g/cm^3 and displaying the highest alloy content of the local PGM producers. Spinel phase structures showed the highest nickel content within the Lonmin matte.

Although this section has so far focused on experimental studies and laboratory investigations, the availability of critically evaluated thermodynamic data underpinning metallurgical equilibria has increased considerably (Dinsdale, 1984). It is possible at present to calculate phase and chemical equilibria for complex and industrially relevant metallurgical systems with the aid of advanced computational software.

2.6. The Lonmin Base Metal Refinery

Matte grinding and aspects of the first stage atmospheric leach will now be discussed within the settings of the Lonmin BMR. A pictorial flow diagram illustrating the relevant batch grinding operation and unit leach process within the BMR is shown in Figure 2.11.

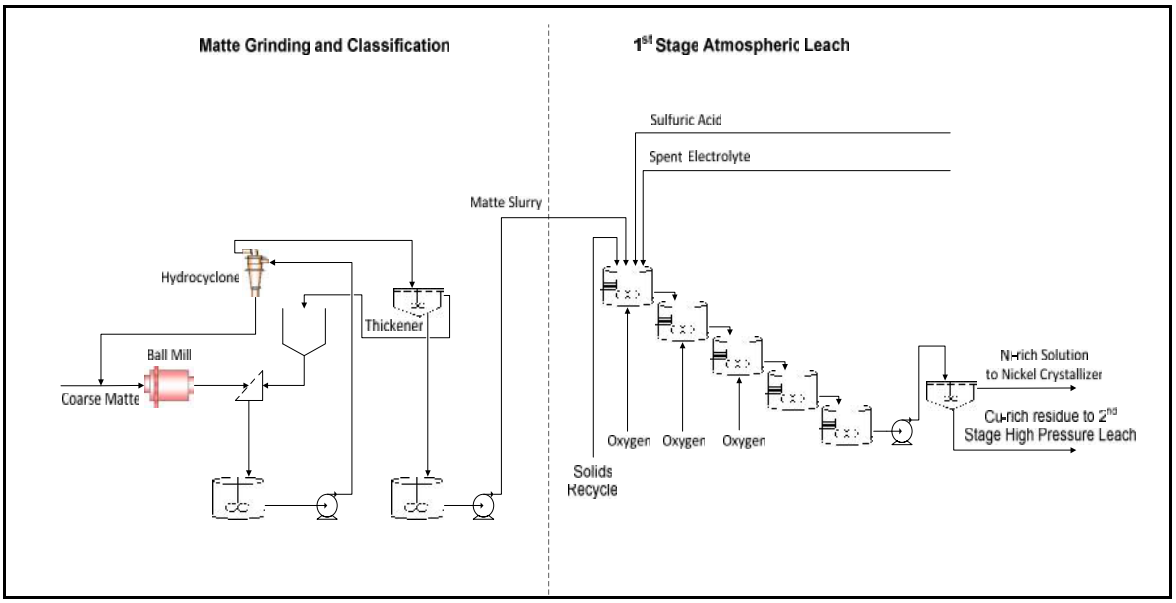

Figure 2.11: A pictorial flow diagram illustrating the grinding batch operation and leaching unit process within the BMR (modified after Bircumshaw, 2008).

2.6.1. Matte Grinding and Liberation

The matte grinding section includes a ball mill in closed configuration with a hydrocyclone, followed by thickening of the matte slurry. A required product size of 90% by weight passing 100µm is generally regarded as effective to liberate sufficient mineral surface area for exposure to the leaching step (Bircumshaw, 2008). Key ball mill variables were found to be of ambiguous importance to the industrial operation. The grinding of converter matte is not covered in any significant detail in the literature.

Grinding, within a wider metal production context, is regarded as the oldest mineral processing technique (Lynch and Rowland, 2005). It therefore has an extensive knowledge base. The early grinding laws were focused on understanding the relation between applied energy and degree of size reduction. A third law was developed following considerable laboratory investigations into grinding by Bond (1952). The correctness of the law was confirmed in a later publication, as there were queries regarding the pseudo-scientific nature of the observed size distribution patterns (Bond, 1960). The third law presented a work index equation, which has remained of practical importance. Overall, the grinding laws are considered useful, although in many cases they are not entirely applicable to industrial processes (Napier-Munn et al., 2005). Size reduction in grinding processes was found to occur due to impact, abrasion and chipping actions (Crabtree et al., 1964).

Grinding models incorporating energy-size reduction law variations and certain machine aspects were developed over time and became of practical value to industry practitioners (Napier-Munn et al., 2005). The population balance and perfect mixing ball mill models are examples of black box type models in common usage. The population balance model solves the mass balance for individual size fractions as a function of breakage and mixing events. The perfect mixing ball mill model is regarded as a special treatment of the population balance model with particular assumptions concerning mixing and residence time. These models are readily accessible through programmes such as JKSimMet, MODSIM and HSC.

The grindability of a material is considered as inherent resistance to breakage and can be determined through several industry standard laboratory tests (Napier-Munn et al., 2005). The Bond, batch grinding and single particle breakage tests are widely used within the metal production industry. The aim of Bond tests, for example, is to determine the work index

value as a numerical indication of the grindability. Batch grinding tests are based on the useful assumption that grinding can be examined and solved as a first-order rate equation within the context of a size-mass balance model (Reid, 1965; Austin, 1971; Austin et al., 1984). It has been shown that a specific rate of breakage and matrix set breakage distribution function can be defined to demonstrate the kinetics of the grinding process as a function of grinding time. It was noted from several plots in literature that the specific rates of breakage become lower within decreasing size classes (Austin et al., 1984; Yan and Eaton, 1994; Austin et al., 2007). Single particle breakage tests, in contrast, are conducted to determine impact breakage characteristics independently from a grinding device (Napier-Munn et al., 2005). The same author also indicated that aspects of material properties, particularly on the atomic- and micro-scale, are not readily integrated into an understanding of grinding.

The concept of mineral liberation can intuitively be associated with breakage events during grinding. King (1994a) defined liberation as the disordered breakage of particles to sizes within the constituent mineral grain scale. The same author considered the measurement and description of liberation spectra as an intricate geometrical challenge. Several models of liberation were developed largely based on the supposition of non-preferential breakage (Gay, 1999; King, 1994b; Gay, 2004a; 2004b). Stereological correction was considered essential to convert areal to volumetric liberation measurements (Leigh et al., 1996; Spencer and Sutherland, 2000; Wiegel, 2010). Liberation distributions for most ore types can be reliably measured at present using automated electron beam based systems, such as quantitative evaluation of minerals by scanning electron microscopy (QEM*SEM) and MLA (Sutherland and Gottlieb, 1991; Gottlieb et al., 2000; Gu, 2003).

2.6.2. Matte Leaching

The atmospheric leaching of matte slurry occurs at temperatures between 85 ^{o}C and 95 ^{o}C and commences within the first of five continuously stirred tank reactors (CSTRs), cascading in series (Bircumshaw, 2008), as previously shown, in Figure 2.11. Sulfuric acid, spent electrolyte and recycled solids are also supplied to the first CSTR. The supply of oxygen is limited to the first three CSTRs, while the last two would provide residence time for further leaching reactions. The aim of the first stage leach is to solubilize the nickel from matte

while precipitating copper in the recycled spent solution (Bircumshaw, 2008). Matte containing iron outside the BMR setpoint range would influence the selectivity of such a leaching step, and thereby, create instability within the leach circuit. The leaching kinetics of Lonmin converter matte, characteristic of variable iron endpoint compositions, was experimentally investigated in a related study, at atmospheric conditions (van Schalkwyk et al., 2011; 2013). It would therefore, also be essential, to link efficient and stable leach circuits to a desired iron endpoint composition.

2.7. Conclusion

This Literature Review Chapter comprises six sections. Sections 2.1 and 2.2 established the importance of metals, primary sources, worldwide occurrences and mining regions. It is evident from section 2.1 that global demand for the relevant base and platinum-group metals will continue. Lonmin has been recognized in section 2.2 as the third largest mine-to-PGM producer in the world and also serves as the operational setting for this dissertation study.

Section 2.3 is divided into several sub-sections, each of which has described coupled metal production processes relating complex techniques intended to systematically upgrade the valuable metal concentration. Iron and sulfur were identified in sub-section 2.3.2 as being particularly influential during the converting process. Literature from global survey studies indicated that Peirce-Smith converters are still in common usage for specifically reducing iron to an acceptable concentration in relation to downstream processing setpoints.

The converter plant is covered in sub-section 2.4.2 and provides background to the important theory of converter process chemistry in understanding the attainment of iron endpoint composition. The starting point for this dissertation study is the variable iron endpoints achieved at the end of the final matte blow. Different iron endpoints for Lonmin mattes were, for example, reported in sub-sections 2.4.2.1, 2.4.2.2 and 2.5.3 and are mainly due to uncertainty in a desired iron endpoint coupled to inconsistent operator control. The uncertainty though, can be related to an insufficient understanding of the effect of iron endpoint on the matte mineralogy by plant metallurgists. The formation of mineral structures during the granulation or fast-cooling pre-treatment process of final matte is

expected to be influenced by the variable iron concentration. This is evident from the converter matte mineralogical findings in sub-section 2.5.3.

Sub-sections 2.5.1 and 2.5.2 were included to demonstrate the depth and progression of theoretical findings during empirical studies of relevant synthetic and natural sulfide minerals, including their underlying phase relations and microscopic properties. A similar level in understanding the mineralogy and phase equilibria of fast-cooled industrial converter matte microstructures is not available in literature, despite its economic significance. The findings based on the experimental and laboratory studies of the slow-cooled Ni-Cu-S system were of limited application to the fast-cooling of converter matte. The grinding and first stage atmospheric leaching of converter matte were discussed in relevant detail in section 2.6. There appeared to be a limited understanding of converter matte grinding with respect to variable iron endpoints, in addition to the unknown effect on microstructure liberation and leaching.

This research was therefore required to systematically investigate a functional dependence between variable iron endpoints and matte mineralogy. It was further required to investigate the effect of the resultant mineralogy on matte grinding and liberation behavior with relevance to the first stage leach step. The findings of the current study can provide the basis for selecting a desired iron endpoint in step with downstream processing requirements and setpoints. This could lead to the implementation of new technology to accurately monitor and control the selected iron endpoint at the converter plant. A systematic laboratory study, coupled to modern analytical and computational techniques, became essential to unlock the wide-ranging effect of the iron endpoint. The sampling, analytical and computational techniques used during the various investigations, are described in the next chapter.

Chapter 3
SAMPLING, ANALYTICAL AND COMPUTATIONAL TECHNIQUES

3.1. Introduction

A description of the sampling techniques, chemical and density analysis required to investigate the bulk characteristics of different Peirce-Smith converter mattes are provided at first. This is followed by a description of the systematic mineralogical analysis essential to mineral microstructure investigations. The application of computational thermochemistry, laboratory batch grinding testwork and liberation analysis is sequentially described in the end.

3.2. Converter Plant and Research Laboratory Sampling

Ten primary converter matte samples, each having a mass between seven and eight kilograms, were representatively sampled following granulation by means of the automated sampling system at the Western Platinum Smelter. The samples were obtained from different converter batches produced during February and March of 2009. These samples were initially distinguished by the production date, blow numbers and preliminary bulk chemistry obtained from the in-house laboratory at Lonmin. The primary matte samples are indicative of variable final stage converting practice and also reflect dissimilar final iron endpoint compositions. Focus was placed on three primary production samples, representing the range in ambiguous iron endpoints, as described in Chapter 2 (sub-section 2.4.2.2). The three production samples were indicative of blow numbers 171, 202 and 216. A multi-step mass reduction procedure was subsequently followed in the research laboratory to generate representative samples (Petersen et al., 2004; Pitard, 2005) for the purpose of analyses and computations. The sampling techniques of riffle and rotary splitting were applied during the mass reduction procedure. The sampling tree illustrative of this multi-step mass reduction procedure is presented in Figure 3.1. The production sample for blow 171 is also visualized in Figure 3.1.

3.3. Bulk Chemical Analysis

The bulk chemical analyses of the final samples with respect to selective iron endpoints were determined at the Analytical Services Division of Mintek in Johannesburg, South Africa. The base metal, PGM, sulfur and oxygen concentrations were determined using the techniques as described on the next page.

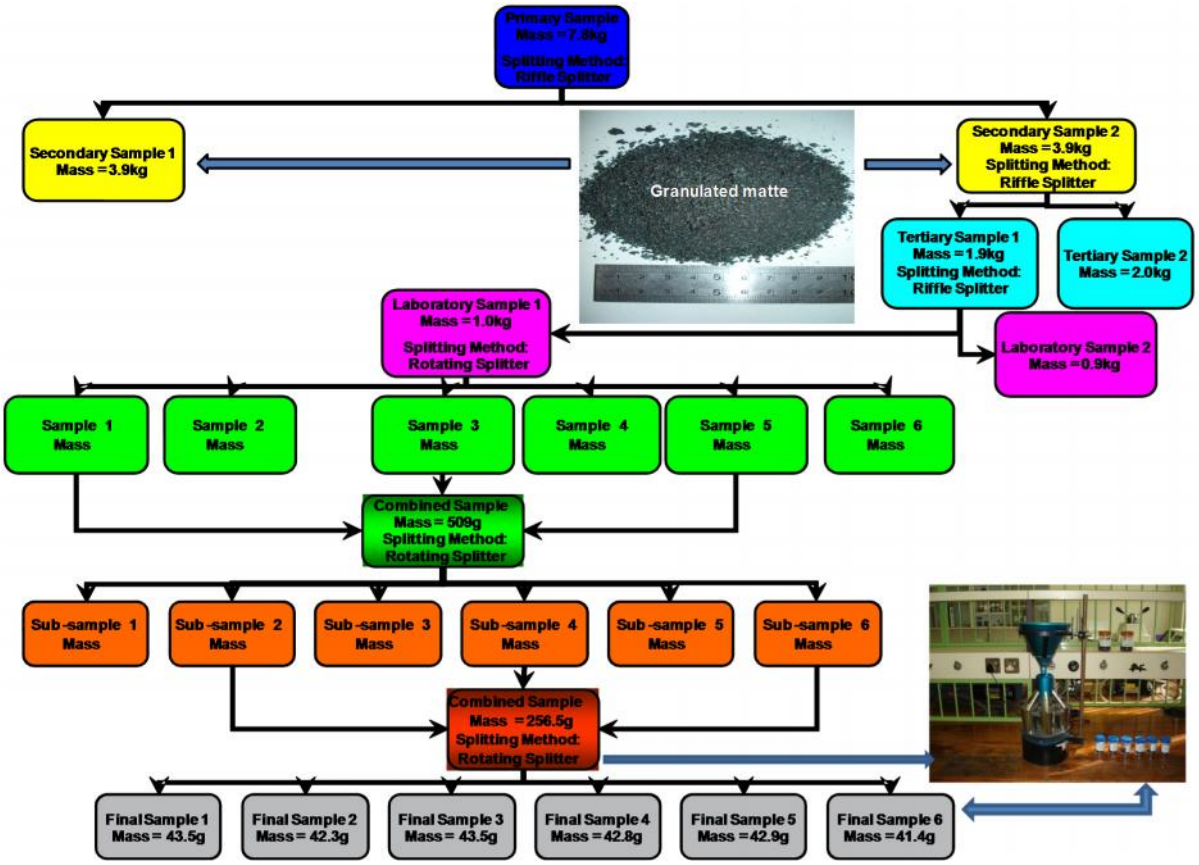

Figure 3.1: The sampling tree illustrative of the multi-step mass reduction procedure used to generate representative samples for analyses and computations.

3.3.1. Determination of Base Metals

The Ni, Cu, Fe and Co concentrations were simultaneously determined by inductively coupled plasma optical emission spectrometry (ICP-OES). A 1g mass of sample, pulverized to 90% passing 20µm, was fused with sodium peroxide at liquefied petroleum gas (LPG) flame temperature to form a basic oxide. The fused mass was leached in water and then acidified. The resulting solution was analysed on a Varian Vista Pro ICP-OES instrument with a charge-

couple device (CCD) detector. The determination limit was specified as 0.05wt%. Following an acid digestion technique, the Pb concentration was determined separately. The determination limit was reported as between 0.1 and 500ppm. A referral to the technique, as ICP1, can be found in the schedule of services of the Analytical Services Division at Mintek.

3.3.2. Determination of PGMs

The Pt, Pd, Rh, Ru and Ir concentrations were determined by Fire Assay with an ICP finish. A 10g mass of sample, pulverized to 90% passing 75µm, was accurately weighed on an analytical balance. The sample was homogenized with NiS flux and placed within a fusion furnace at 1150 ^{o}C for nearly 50 minutes. The conditions within the fusion furnace reduced NiS into metallic Ni that formed a complex with PGMs.

The Ni button was crushed to fragments on a hydraulic press. The fragments were placed within a 600ml beaker with suitable chemical reagents, including hydrochloric acid. The dissolution of the PGMs was performed in a steam bath located in a fume cupboard for almost 16 hours. The solution was subsequently filtered using a 0.45 micron Dura pore membrane filter. The PGM-containing residue was then dissolved through acid by gradual heating on a hot plate.

This solution was added to a flask containing the required volumetric ratio of acid and internal standard and assayed on the Varian Vista Pro ICP-OES. The determination limit was reported as 0.1ppm. A referral to the technique, as FA4, can be found in the schedule of services of the Analytical Services Division at Mintek.

3.3.3. Determination of Sulfur and Oxygen

The S concentration was determined with a LECO CS200 Analyzer using a combustion method. A 1g mass of sample was analyzed and the determination limit specified as 0.01ppm. The O concentration was determined with an Eltra ON900 Analyzer and the determination limit reported as 20ppm.

3.4. Bulk Density Analysis

The bulk density was determined using a Micromeritics 4300 Pycnometer at the Analytical Services Division of Mintek. A weighted portion of a 100g sample was placed into a 10ml sample cup. The volume of the cup was accurately known. The cup was placed into the instrument and high-purity helium gas was pumped into the remaining space in the cup to a specific pressure. This included any space above the sample and between sample particles. The instrument measured how much helium gas was used to fill the spaces, and from this, the volume occupied by the sample was calculated. The bulk density was calculated from the known sample mass and calculated sample volume. The results were reported in g/cc.

3.5. Mineralogical Characterization

The application of a combination of standard mineralogical and specialist analytical techniques was necessary to systematically unlock the characteristics of granulated nickel converter matte as a function of iron endpoint. The X-ray and electron beam based techniques relevant to the mineralogical characterization are described in the following sub-sections.

3.5.1. Powder X-ray Diffraction

Powder X-ray diffraction was utilized as a standard technique for phase or mineral identification (de Villiers and Verryn, 2007). Analytical samples were micronized using a McCrone micronising mill to a particle size smaller than 10μm. The milled samples were mounted in specific holders and analyzed using a Siemens D500 diffractometer. A step size and counting time of 0.02° 2θ and three seconds per step, respectively, were applied across a range of 5 to 80° 2θ. The technique uses the net intensity of the main peaks of the phases and identification is based on matching the crystal structure of crystalline phases to an extensive structural database. Quantitative X-ray diffraction (QXRD) was employed for quantitative analysis within 1σ associated error. Quantitative results were obtained by using TOPAS software which employs Rietveld refinement (Rietveld, 1969) using a fundamental parameters approach. The instrument is located at the Mineralogical Division of Mintek.

3.5.2. Scanning Electron Microscopy

Scanning electron microscopy (SEM) was employed as a routine technique for compositional and morphological analysis of mineral structures (Lloyd, 1987). High quality sample preparation is essential to accuracy of analyses and was therefore performed with due consideration. Analytical samples were embedded in 30mm diameter resin blocks, ground and polished to obtain smooth matte particle sections. The sample preparation method applied and equipment used is reported in Appendix A (Table A.1). Sample preparation was completed by coating the polished matte particle sections with carbon to avoid charge accumulation during electron beam analysis. Several 30mm diameter resin blocks prepared for SEM analysis are shown in Figure 3.2.

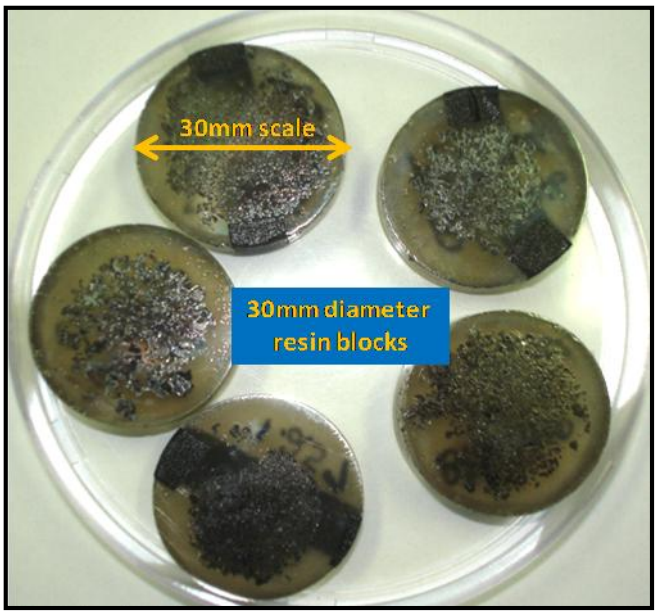

Figure 3.2: Photograph of several 30mm diameter resin blocks prepared for scanning electron microscopy analysis.

A Philips XL30 SEM integrated with an EDAX DX4 energy dispersive X-ray spectrometry (EDX) system with detectors for secondary electrons, backscattered electrons, X-rays, cathodoluminescence and electron beam induced current was made available for analysis. The instrument was operated at 20kV accelerating potential with 2000 peak counts per second for 100 live seconds, which resulted in 200,000 total counts per analysis. Additionally, a high resolution JEOL JSM-7001F field-emission scanning electron microscope (FEG SEM) equipped with a number of detectors was utilized. An accelerating voltage of

15kV and probe current of 90µA proved optimal for analysis of the respective mineral structures. The instruments were operated at the High Resolution Transmission Electron Microscopy (HRTEM) Centre at the Nelson Mandela Metropolitan University (NMMU) in Port Elizabeth, South Africa.

3.5.3. Transmission Electron Microscopy

Transmission electron microscopy (TEM) was applied as a specialist technique to examine the compositional and morphological detail of mineral structures at higher resolution and magnification (Lorimer, 1987; Grobéty, 2005). The preparation of high quality conventional TEM samples is an expert task, as it requires samples to be reduced to electron-transparent thinness. Matte particles were agglomerated and glued onto a thin glass slide using a Gatan G2 resin. Following curing of the resin, the exposed side of the particle agglomeration was mechanically ground and polished to a 1µm diamond finish. A 3mm copper TEM grid with a centralised opening was glued onto the flat and polished surface using Gatan G2 resin. After curing, the glass side of the agglomeration was mechanically ground to an approximate overall thickness of 40µm and polished to a 1µm surface finish. Small pieces of the sample overhanging the TEM grid were nipped of using a scalpel when the sample was sufficiently thin to do so. The final step entailed ion-milling of the sample with a Gatan PIPS II system using an Argon ion beam at 5kV. An electron-transparent matte sample prepared for this study is shown in Figure 3.3. The reader is also referred to Sridhara Rao, et al., (2010) for more information on TEM sample preparation techniques.

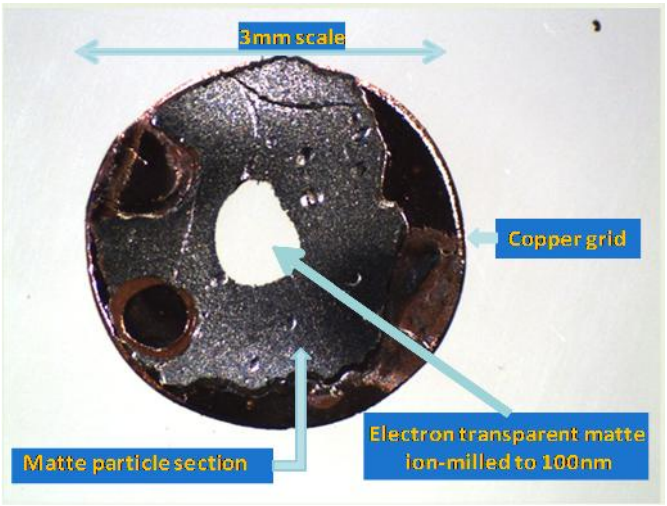

Figure 3.3: Photograph of a specially prepared electron-transparent matte sample used for transmission electron microscopy analysis.

In addition, TEM sample preparation of a site of interest (SOI) on a matte particle section was completed by using an FEI HELIOS Nanolab 650 focused ion beam scanning electron microscope (FIB SEM). The microscope is fitted with a Tomahawk Ga ion beam column for milling, a carbon precursor gas injection system for deposition of carbon and an Omniprobe autoprobe 200 for manipulation of TEM lamella. The TEM analysis was specifically required to provide compositional and morphological analysis along a planar section. For the preparation of the TEM lamella, a SOI on the sample was selected in backscattered electron (BSE) imaging mode. Figure 3.4a illustrates the proposed FIB section along the selected SOI.

After identification of the SOI, a protective layer of carbon was deposited over the area of interest before the commencement of 30kV ion beam milling of trenches on either side of the SOI. This was done to expose and prepare a 5 X 10 X 2µm lamella for removal (see micrograph in Figure 3.4b) from the SOI and attachment onto a copper finger on a special TEM grid. The removal of the lamella is achieved by attaching the Omniprobe needle to the lamella using C deposition. After the lamella is attached to the needle, it is cut free using the ion beam and moved to a prepared position on the copper finger for attachment. After careful manipulation, the lamella is placed into slight contact with the copper finger and fixed into place by deposition of C. The lamella was then progressively thinned using the ion beam from both sides to a final thickness of approximately 30nm, as confirmed by edge on SEM imaging. Final polishing of the lamella was done using 2kV and 500V ion beam energy to ensure removal of amorphous material from the surface of the lamella.

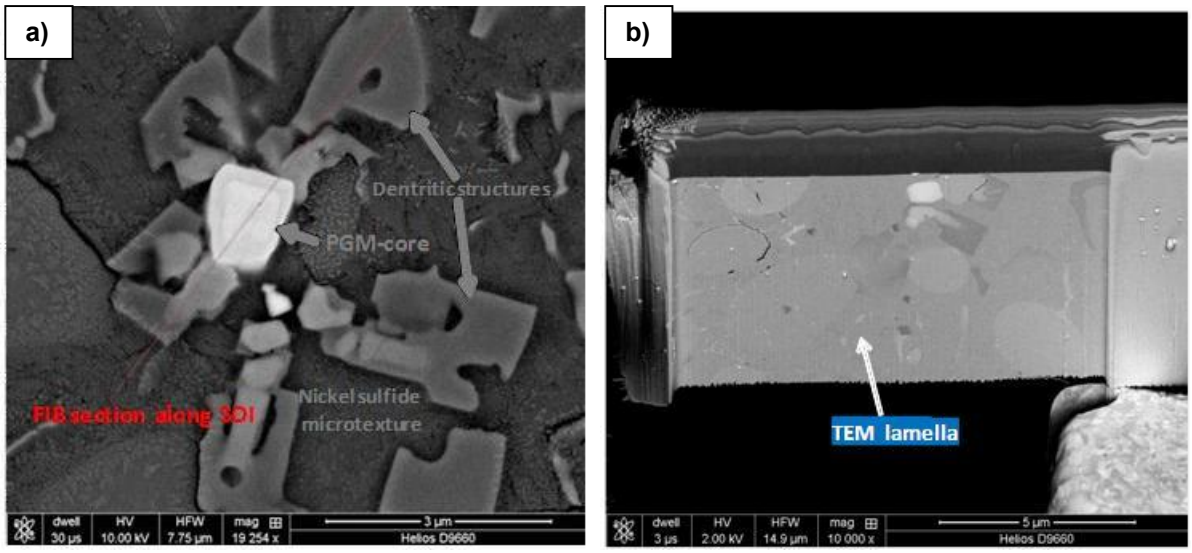

Figure 3.4: Backscattered electron-induced micrographs showing (a) the proposed FIB section along the selected site of interest (SOI) at 3µm size scale and (b) the manipulation of TEM lamella at 5µm size scale.

The analyses of the conventional TEM samples were performed using a Philips CM20 TEM instrument operating at 200kV, with a point-to-point resolution of 0.27nm interfaced with an EDAX DX4 energy dispersive X-ray spectrometer system. The analysis of the TEM lamella was exclusively performed with a 200kV JEOL JEM-2100 LaB_6 TEM equipped with an Oxford Instruments XMax 80 SDD EDS detector. Both TEM and scanning TEM (STEM) modes were used along with selected EDX. The instruments were operated at the HRTEM Centre at NMMU. A Tecnai F20 TEM operating at 200kV acceleration voltage was used in high resolution scanning transmission electron microscope (HRSTEM) mode for dark field analysis of conventional TEM samples. This instrument was used at the Physics Department at the University of the Western Cape in Bellville, South Africa.

3.5.4. Electron Probe Microanalysis

Electron probe microanalyses were conducted to determine the composition of mineral structures at lower detection limits (Castaing, 1960). Analytical samples were prepared using a similar method to that described in Appendix A. Figure 3.5 is illustrative of a smaller region on a 30mm diameter resin block showing embedded and inscribed matte particle sections selected for electron probe microanalysis. Black marker lines served during the analyses as indicators to inscribed matte particle sections.

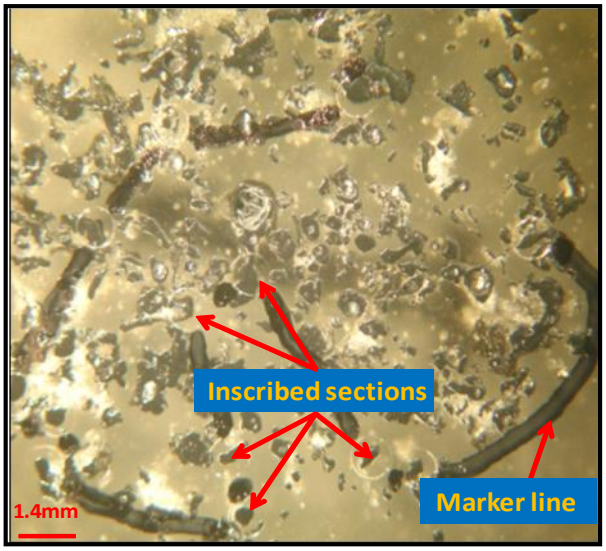

Figure 3.5: Photograph of a smaller region on a 30mm resin block showing embedded and inscribed matte particle sections selected for electron probe microanalysis.

A Cameca SX50 microprobe equipped with four wavelength dispersive spectrometers (WDS) and EDX was used at the Mineralogy Division of Mintek. The system was calibrated with reference standards of pure Fe, Co, Ni, Cu, Pb, Pd, Pt, Rh, Ru, Ir and Os and a pyrrhotite (FeS) reference was used for S. The analysis was performed exclusively on WDS and conducted in a semi-sequential manner on three of the spectrometers that were suitably equipped to detect the element suite of interest. An accelerating voltage of 30kV was used with a beam cup current of 30nA. A counting time of 20s on peak and 10s on each of two background positions was employed. The following lines were measured: Ka: S, Fe, Co, Ni, Cu; La: Ru, Rh, Pd, Ir, Pt, Pb; Ma: Os. Matrix correction was based on the ZAF procedure (Philibert and Tixier, 1968) in the SAMX Analysis software (http://www.samx.com). Detection limits are as follows in parts per million: S (300), Fe (200), Co (200), Ni (700), Cu (700), Pb (1200), Pd (600), Pt (800), Rh (700), Ru (700), Ir (800) and Os (800). The analytical precision was limited by the 2µm electron beam diameter and the heterogeneity of the mineral structures.

3.5.5. FIB SEM Tomography

The specialist technique of FIB SEM tomography was deemed suitable to acquire 3D projections of mineral structures with subsequent reconstruction for 3D visualization and analysis (Uchic et al., 2006; Ritter and Midgley, 2010). A tomography reconstruction of several serially sectioned slices obtained from a SOI in an analytical sample was completed

using the slice and view facility of the FEI HELIOS Nanolab 650 FIB SEM. After selection of an appropriate region, trenches were milled around a rectangular volume in the sample. The rectangular volume was then sequentially sliced by the ion beam and the exposed cross-sectional surface imaged in BSE mode using the electron column. Each section or slice was 20nm apart and resulted in 246 images or slices. The resolution of each slice was related to the features within and finer than the slice thickness. The overall resolution of the tomography reconstruction was a function of their combination.

After acquisition of the images, a normalization routine was used in the processing program ImageJ to remove any background contrast gradients on individual images and also to normalize contrast limits between images. Noise reduction was then completed on the images. The image stack was then imported into the software package Amira, aligned and cropped. Following this, a slight smoothing of the image stack was done. Segmentation and 3D volume representation of the stack was then completed using contrast thresholding. Figures 3.6a and b show the reconstructed rectangular volume and a single sectioned slice in BSE mode at 17.5µm x 8µm size scale, respectively. The instrument was operated at the HRTEM Centre at NMMU.

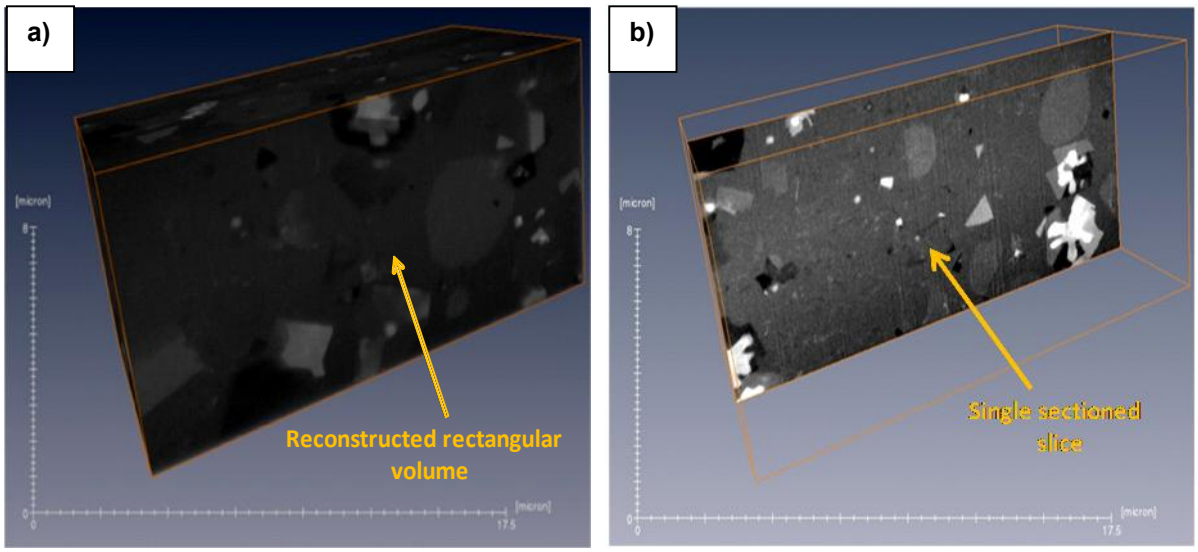

Figure 3.6: Backscattered electron-induced micrographs showing (a) the reconstructed rectangular volume and (b) a single sectioned slice at 17.5µm x 8µm size scales, respectively.

3.5.6. Automated Mineralogical Analysis

Automated analysis (Sutherland and Gottlieb, 1991; Gu, 2003) was applied as a complementary (and challenging) technique to acquire modal abundances, size distributions and morphological detail of fine-scale converter matte mineral structures on a statistically valid scale. The technique and corresponding sample preparation method were found to be sensitive to wide particle size distributions. It was therefore required to screen out and use only particles less than 2mm within the analytical samples. Three representative aliquots of 3g respectively were split out per analytical sample. Graphite was mixed into each aliquot and jointly embedded in 30mm diameter resin blocks, ground, polished and coated. Graphite was added as a spacer to separate the particle boundaries within each aliquot. An FEI 600F field-emission mineral liberation analyzer (FEG MLA), integrated with two liquid-nitrogen-free Bruker Xflash silicon drift detectors, was made available at the Geology Department at the University of Johannesburg.

A mineral standard file specific to converter matte microstructures had to be compiled for the classification of raw data files, as an FEG MLA instrument is not programmed with an extended list of natural mineral information. Backscattered electron image analyses in combination with X-ray spectra allowed for the identification of the constituent converter matte microstructures. The mineralogical knowledge acquired from the preceding analyses became particularly useful during the inspection of matte microstructures and in the ultimate construction of the mineral standard file. The instrument made use of the X-ray modal abundance (XMOD) analytical routine, set at 8x8 pixel line spacing, intended for the collection of X-ray spectra in a stepwise pattern. The raw data files were processed offline using the MLA ParticleX programme, including their classification with respect to the mineral standard file. Mineral modal abundance was calculated with respect to the X-ray point count area% of the matte microstructures identified within 1 469 452 particles or analyzed points. The grain X-ray mapping (GXMAP) analytical routine, set between grey levels of 20 and 225, was used to segment BSE images into particles and grains, as well as for stepwise X-ray analysis. The raw data files were processed offline, using in order, the MLA ParticleX (including mineral standard file classification), MLA Image Tool, MineralDataBaseMaker and Dataview programmes. The MLA Image Tool programme

allowed for the mapping of grains, while the Dataview programme version 3.1.1.280 permitted the reporting of grain size distribution data. The data is based on equivalent circle diameter estimation of grain area.

3.5.7. Nano-Indentation Testing, Breakage and Atomic Force Microscopy

Nano-indentation testing was specifically used to measure the indentation hardness of mineral structures (Oliver and Pharr, 1992). Representative analytical samples were mounted in resin, ground and polished. Load *versus* penetration-depth was tested in a 15 × 15 grid of 225 indentations (for each prepared sample) using a CSM Nano-Indentation Tester, operated at a specified load range of 0.1–500mN, load resolution of 0.04µN, maximum depth of 200µm and a depth resolution of 0.04nm. A Berkovich indenter tip with a three-sided pyramidal geometry was driven into the surfaces of mineral structures and the applied load and depth were measured dynamically during a loading–unloading rate of 6mN/min. As a general rule of thumb, the penetration-depth measurements were assumed to be below 10% of the unknown thickness of the mineral structures. The resulting indentation load and penetration-depth data, in combination with established force-displacement models, were then used to calculate indentation hardness values for the respective mineral structures.

Using additional CSM Instruments software, 3D hardness mapping could be correlated to the residual hardness impressions and collected indentation test data. The indentation system also had the ability to test the breakage characteristics of the respective mineral structures by applying a preset load of 450mN at a loading–unloading rate of 1000mN/min. Three dimensional (3D) topographical micrographs obtained from atomic force microscopy were also produced as an aid in analyzing the resultant breakage characteristics in relation to single hardness impressions. The instruments were used at the HRTEM Centre at NMMU.

3.6. Computational Thermochemistry

Computational thermochemistry was applied to develop an understanding of liquid matte solidification upon cooling, with reference to equilibrium systems. Predictive equilibrium calculations specific to iron endpoint correlated multi-component systems were initiated for the study of equilibrium cooling processes. The main assumption underpinning the

predictive calculations was that phase and chemical equilibria can be reliably calculated from critically assessed structural and thermodynamic data using MTDATA phase diagram software version 5.02 from the National Physical Laboratory, UK (NPL) (Davies et al., 2002). The thermodynamic data used in the calculations was extracted from the extensive and critically assessed Mtox database version 7, which has been validated in a number of industrial and phase diagram case studies dealing with sulfide smelting (Gisby et al., 2002, 2007; Taskinen et al., 2005). The sulfide phases have been modelled in the database as non-ideal solutions and further details are provided in Table 3.1.

Table 3.1 Details of all phases included in the analysis following the principal calculations (from Barry et al., 1992; Barry et al., 1993).

Phase	**Solution Model**	**Constituent Configuration**
Liquid	Associated	e.g. Cu, Cu_2O, Cu_2S, FeO, $FeO_{1.5}$ and $FeSiO_3$
Digenite	Sublattice	$(Co_{½},Cu,Fe_{½},Ni_{½},Va)_2(Cu,Va)_1(S)_1$
Ni_3S_2	Sublattice	$(Co,Cu,Fe,Ni,Va)_2(S,Va)_2$
Pyrite	Sublattice	$(Co,Cu,Fe,Ni)_1(S)_2$
Pyrrhotite	Sublattice	$(Co,Cu,Fe,Ni,Va)_1(S)_1$
FCC_A1	Sublattice	$(Co,Cu,Fe,Ni,S)_1(Va)_1$
Spinel	Sublattice	$(Co^{2+},Cu^{2+},Cu^{+},Fe^{2+},Fe^{3+},Ni^{2+})_1$ $(Co^{3+},Co^{2+},Cu^{2+},Fe^{2+},Fe^{3+},Ni^{2+},Va)_2(Fe^{2+},Va)_2(O^{2-})_4$
Halite	Sublattice	$(Co^{2+},Cu^{2+},Fe^{2+},Fe^{3+},Ni^{2+},Ni^{3+},Va)_1(O^{2-})_1$
Pentlandite	Sublattice	$(Co,Cu,Fe,Ni)_9(S)_8$
Heazlewoodite	Sublattice	$(Co,Ni)_3(S)_2$
Chalcopyrite	Substitutional	$Cu_{1/6}Fe_{1/3}S_{1/2}$ and $Cu_{1/2}Fe_{1/9}S_{7/18}$
Beta-chalcocite	Stoichiometric	Cu_2S
Ni_7S_6	Stoichiometric	Ni_7S_6

* Va: Vacancy.

The following principal calculations were performed during the systematic determination of equilibrium cooling characteristics for different matte systems. Liquidus equilibria were calculated for the Ni-Cu-S system in the context of variable iron endpoint concentrations. The Ni and Cu corners were treated as mixtures of chemical elements and composite purposely with iron concentrations of 5%, 1% and 0.1% for the respective systems. The list of active elements in the calculations was therefore Ni, Cu, S and Fe. All percentages used in pseudo-ternary constitution were in weight% unless specifically otherwise acknowledged. The upper and lower temperature limits were set to 1423 K (1150 ^{o}C) and 923 K (650 ^{o}C) within the pseudo-ternary systems. The set temperatures were stepped using 50 K intervals. The calculations were carried out at 1 atm pressure (101.325kPa).

Further conditions and elements were set in the constitution of comparable systems. Liquidus and primary phase equilibria were subsequently calculated for Ni-Cu-S systems, including iron and cobalt concentrations. The list of active elements in the calculations was Ni, Cu, S, Fe and Co. The Cu, S and Ni corners were composite with 5%Fe1%Co, 1%Fe0.5%Co and 0.2%Fe0.3%Co for the respective systems. The end composition of the Cu and S corners were selected at 70% mixtures of constituent chemical elements. The upper, step and lower temperature limits were set to 1673 K (1400 ^{o}C), 25 K and 773 K (500 ^{o}C), respectively. Corresponding true (normalized) liquid matte starting compositions (including set iron, cobalt and oxygen concentrations) were subsequently specified and their assays were calculated as a function of liquidus equilibria. The list of active elements in the calculations was Ni, Cu, S, Fe, Co and O. Similarly, the upper and lower temperature limits for the calculations were set to 1123 K (850 ^{o}C) and 873 K (600 ^{o}C). The set temperatures were stepped using 25 K intervals. The liquid matte starting compositions and calculated assays were superimposed on relevant Ni-Cu-S_FeCo pseudo-ternary systems.

Multiphase cooling equilibria were calculated (supported by the Mtox database) for the matte system Ni-Cu-S–Fe–Co–O (also the list of active elements in the calculations) in the context of corresponding true liquid matte starting compositions. The database contains assessed thermodynamic descriptions for the base matte system and thus allowed construction of a selection of equilibrium features with associated compositional analysis. Upper, step and lower temperature limits were respectively set to 1773 K (1500 ^{o}C), 2.5 K

and 473 K (200 °C) for these computations. The MTDATA phase diagram software and Mtox database within the Metallurgical Thermodynamics and Modelling Research Group at Aalto University in Helsinki, Finland was made available for this study.

3.7. Laboratory Batch Grinding

Laboratory batch grinding tests were conducted to investigate the grinding characteristics of converter matte particles in relation to the mineralogical findings. Each representative feed or test sample had a mass of approximately 1.9kg. The scope of the laboratory batch grinding testwork is outlined in Figure 3.7.

Figure 3.7: Outline showing the scope of the laboratory batch grinding testwork involving converter matte particles.

The feed samples were weighed prior to the determination of particle size distribution using a $\sqrt{2}$-series of sieves from 6.70mm to 53µm. More specifically, wet sieving was performed at 53µm after which the +53µm samples were dried. The particle size distribution of the

+53µm samples were determined from 6.70mm to 53µm. The -53µm samples were filtered, dried and weighed. The size fractions were subsequently recombined for the commencement of wet grinding at 50% solid matte particle content. The tests were performed in a steel-lined batch mill with dimensions of 265mm x 305mm, seasoned steel ball charge of about 35% mill volume and a maximum ball size of 30mm. A load cell and tachometer were used to monitor mechanical torque and mill speed. The sensor outputs were interfaced to a computer to permit real-time estimation of net energy consumption. The mill was operated at 75% of the critical speed and 5kWh/t specific input energy. The product was filtered and dried. The particle size distribution was determined following grinding at the specific energy input. Once product size analysis was completed, the fractions were re-combined for wet grinding at 15kWh/t specific energy input. This step was repeated once more to accomplish wet grinding at 25kWh/t specific energy input. The batch grinding tests were conducted at the Comminution Division of Mintek.

The perfect mixing ball mill model was subsequently used to assess the breakage rates of matte particles and minerals. The model assumes that the mill contents are perfectly mixed. The mass balance expression used in the perfect mixing ball mill model is shown in equation 3.1.

$$f_i - p_i + \sum_{j=1}^{i-1} \left(a_{ij} r_j s_j\right) - r_i s_i = 0$$

Equation 3.1: The size-mass balanced equation describing the perfect mixing ball mill model (from Napier-Munn et al., 2005).

where f_i and p_i is the mass flow rate of the feed and product content with respect to size fraction *i*. The mass fraction arriving in the size fraction *i*, from breakage of a larger size fraction *j*, can be represented by the appearance function (a_{ij}). The mill size fraction of interest (s_i) can be linked to the respective product rate as shown in equation 3.2.

$$s_i = \frac{p_i}{d_i}$$

Equation 3.2: Showing the relation between size fraction and product rate for the perfect mixing ball mill model (from Napier-Munn et al., 2005).

where d_i is the discharge rate with respect to the size fraction of interest. If equation 3.2 is substituted into equation 3.1, then equation 3.3 is formed.

$$f_i - p_i + \sum_{j=1}^{i-1}\left(a_{ij} r_j \frac{p_j}{d_j}\right) - r_i \frac{p_i}{d_i} = 0$$

Equation 3.3: The modified size-mass balanced equation for the perfect mixing ball mill model (from Napier-Munn et al., 2005).

If the mill feed and product rates are known, then the breakage rate (r_i) can be calculated provided that a reasonable breakage distribution function is used. The breakage distribution function for fine particle breakage by Eksi et al., (2011) was used to solve the perfect mixing ball mill model mass balance.

3.8. Liberation Analysis

Liberation analyses were performed to investigate the liberation characteristics of mineral structures of interest. Three representative analytical samples were obtained from the respective ground products after each specific energy grind. Each sample was split into three aliquots of approximate equal amounts. The aliquots were prepared using the same method as that described in sub-section 3.5.6. The FEI 600F FEG MLA was, also previously mentioned, used for the liberation analysis. The more advanced XBSE (Extended Backscattered Electron) analytical routine was used for the liberation measurements. The raw data files were first processed online using the MLA ParticleX programme. The mineral standard file classification was done offline as well as the creation of a mineral density and chemistry database using the MineralDataBaseMaker. The Dataview programme was used to generate size distribution data and the final quantitative (2D) liberation output.

3.9. Conclusion

Granulated Ni-PGM converter matte is a complex intermediate pyrometallurgical product. Their investigation as a function of iron endpoint had required the selection and application of modern analytical and computational techniques, as well as testwork. The sampling techniques of riffle and rotating splitting were used to reduce actual industrial production samples to representative analytical samples. Chemical analyses were used to determine the bulk composition of three iron endpoint mattes. Powder X-ray diffraction, scanning

electron microscopy and electron probe microanalysis were considered as automatic selection for the investigation of mineral microstructures as a function of iron endpoint. Transmission electron microscopy and focused ion beam scanning electron microscopy are highly specialized techniques (particularly in the field of material science) and were used to provide microstructure detail at a higher magnification and resolution. High quality and often challenging sample preparation was regarded as essential to the successful application of the various analytical techniques. The automated analysis using an FEG MLA was equally challenging and used to provide mineralogical information over a statistically valid range.

Computational thermochemistry, through the use of MTDATA phase diagram software, was applied to analyze the solidification of iron endpoint related matte systems upon cooling. Micro-hardness and breakage characteristics of mineral structures were simultaneously investigated using specialized indentation techniques. Laboratory batch grinding test were conducted and the perfect mixing ball mill model was used to calculate the breakage rates of matte particles and minerals. The liberation of mineral microstructures, produced during the grinding tests, was investigated for each specific energy grind. Published experimental converter matte leaching data will also be drawn upon, to emphasize the integrated effect of iron endpoint and also for a well-rounded approach. The next chapter, is the first of four investigative study chapters, and presents the effect of the converter iron endpoint on matte mineralogy.

Chapter 4
EFFECT OF IRON ENDPOINT ON MATTE MINERALOGY

4.1. Introduction

According to Chapter 2, variable iron endpoints were often achieved by the converter plant at the Western Platinum Smelter Facility. This was primarily due to the uncertainty in a desired iron endpoint and related to a poor understanding and quantification of the effect on matte mineralogy by plant metallurgists. The aim of this chapter is to systematically investigate and quantify the chemical, physical and mineralogical characteristics of bulk granulated Ni-PGM matte as a function of the variable iron endpoints attained during the final Peirce-Smith converting stage.

4.2. Results and Discussion

The results of the chemical analysis of the bulk matte are reported at first, as it reveals, more importantly, the specific iron endpoint achieved during converting. This is followed by the density and mineralogical investigation and quantification arranged with respect to iron endpoint comparison. This includes the examination and illustration of mineral composition and morphology.

4.2.1. Bulk Matte Chemistry

The bulk matte chemical analysis, as described in Chapter 3 (section 3.3), provides the finished matte composition achieved during the final converting stage. Table 4.1 reports the final composition of three different mattes, sampled after granulation at the Western Platinum Smelter Facility. The different mattes can be considered as representing the typical range in Peirce-Smith converter operating variability.

The standard deviation of the analyses performed in duplicate is reported within parenthesis in Table 4.1. The enrichment in base metals (Ni, Cu and Co) and PGMs is evident in Table 4.1, when compared to the grades following physical and primary smelting processes, as indicated previously in Chapter 2 (Tables 2.2 and 2.3, respectively). The extent of iron removal in converting is particularly apparent when comparing the concentration in

Table 4.1 to that previously in Table 2.3. The specific iron endpoints attained for the finished matte compositions in Table 4.1 are notably variable and reported as 5.17, 0.99 and 0.15wt% Fe (hereafter referred to, for example, as iron endpoint 5.17% or 5.17% Fe). Variable iron endpoints were also previously reported for Lonmin matte in Chapter 2 (sub-sections 2.4.2.1, 2.4.2.2 and 2.5.3). The increase in Ni, Cu and PGM concentration, indicated in Table 4.1, corresponds with a lowering in the iron endpoint and the trend is in good agreement to that expected. In contrast, the Co, Pb and O concentrations decrease with a corresponding increase in iron removal. In practice, the oxygen concentration in converter matte is generally not measured (Warner et al., 2007).

Table 4.1: The final composition of three different Peirce-Smith converter mattes sampled following granulation and acquired through bulk chemical analysis.

Element	Matte 1 (wt%)	Matte 2 (wt%)	Matte 3 (wt%)
Ni	43.80 *(0.07)	47.90	49.50
Cu	25.00 *(0.07)	29.50	29.50
Fe	5.17 *(0.01)	0.99	0.15
Co	0.72 *(0)	0.38	0.36
Pb	559ppm *(3.54)	551ppm	541ppm
S	23.69 *(0.52)	18.78	19.15
O	1.62 *(0.06)	1.49 *(0.01)	1.24 *(0.10)
Ru	675ppm	986ppm	843ppm
Rh	381ppm	574ppm	487ppm
Pd	1160ppm	1780ppm	1500ppm
Ir	224ppm	296ppm	235ppm
Pt	2530ppm	4000ppm	3360ppm

* Standard deviations in parenthesis.

It is important at first to optimize the concentration of the valuable base metals and PGMs within the matte in relation to the attainment of a low iron endpoint. Table 4.2, which is

inferred from Table 4.1, reports the summation of base metals and PGMs, including useful element ratios as a function of the iron endpoint attained.

Table 4.2: The summation of base metal and PGM concentrations, including useful element ratios as a function of the iron endpoint attained.

Iron Endpoint (% Fe)	SUM NiCuCo (%)	SUM 5PGMs (ppm)	Ni:S	Cu:S	(NiCuCo):S
5.17	69.52	4970	1.85	1.06	2.93
0.99	77.78	7636	2.55	1.57	4.14
0.15	79.36	6425	2.58	1.54	4.14

The five PGMs (expressed in Chapter 2, section 2.2) important to Lonmin showed the highest concentration for the matte, with an iron endpoint of 0.99%. The base metals Ni, Cu and Co are produced as by-products and showed the highest combined concentration for the 0.15% Fe matte. Based on the metal values per unit ton reported in Chapter 2 (Table 2.1, section 2.1), the combined metal concentrations for the 0.99% Fe matte appears to be the most valuable. It is interesting to note, from Table 2.1, that Co would obtain a higher value per unit ton than Ni and Cu; however, its concentration tends to decrease as a function of iron removal.

4.2.2. Bulk Matte Density

Table 4.3 reports the bulk density analysis, described in Chapter 3 (section 3.4), in relation to the specific iron endpoint achieved.

Table 4.3: The bulk density analysis of iron endpoint specific converter mattes based on actual production samples from Lonmin.

Iron Endpoint (% Fe)	Density (g/cc)
5.17	5.64 *(0.01)
0.99	5.93
0.15	6.07

* Standard deviations in parenthesis.

The bulk density, in Table 4.3, shows an increase with the corresponding lowering in the iron endpoint. Schouwstra (2008) reported a bulk density of 6.3 g/cc for Lonmin matte with an iron endpoint of 0.5%. According to Vaughan and Craig (1978), density can be regarded as a function of mineral structure, abundance and composition.

4.2.3. Mineral Structure Identification and Abundance

Figure 4.1 presents diffractograms with respect to variable iron mattes, in a comparative off-set collection of single-phase X-ray powder diffraction patterns, as peak positions at 2θ and X-ray counts (intensity). The standard application of powder X-ray diffraction analysis is described in Chapter 3 (sub-section 3.5.1).

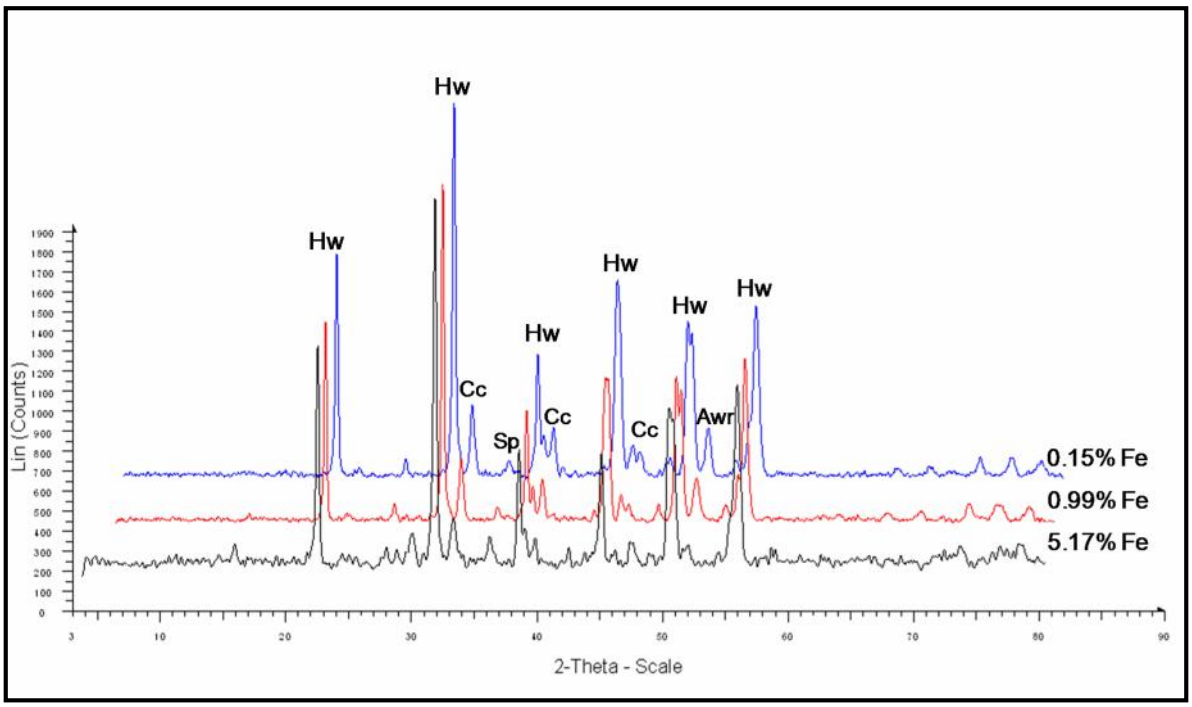

Figure 4.1: Diffractograms acquired from powder X-ray diffraction analysis with respect to 5.17%, 0.99% and 0.15% Fe mattes.

All three matte samples analyzed display similar diffraction patterns. The characteristic peaks, in relative order of intensity, could be matched with crystal structures similar to that for heazlewoodite (Hw), chalcocite (Cc), awaruite (Awr) and spinel (Sp) natural minerals or phases. The annotations in Figure 4.1 indicate the more significant peak positions of the minerals, also with respect to iron endpoint. The characteristic awaruite peak for 5.17% Fe displays a notably lower intensity than the comparative peaks for 0.99% and 0.15% Fe.

Heazlewoodite and chalcocite natural minerals can be categorized as members of the metal excess sulfide structural group (Vaughan, 2005).

The QXRD results, obtained using TOPAS software, are presented in Table 4.4. This table compares 5.17%, 0.99% and 0.15% Fe mattes with respect to the natural mineral, ideal chemical formula and relative abundance (wt%), with the associated error on the 1σ standard deviation level.

Table 4.4: Quantitative X-ray diffraction results, including relative abundances in wt%, with the associated 1σ error for iron endpoints (a) 5.17% (b) 0.99%, and (c) 0.15%.

Topas		**(a) 5.17% Fe**		**(b) 0.99% Fe**		**(c) 0.15% Fe**	
Mineral	Ideal Formula	Abundance (wt%)	Error (1σ)	Abundance (wt%)	Error (1σ)	Abundance (wt%)	Error (1σ)
Hw	Ni_3S_2	77.89	0.50	62.92	0.42	63.67	0.75
Cc	Cu_2S	12.04	0.42	18.56	0.33	17.86	0.38
Pn	$(Fe,Ni)_9S_8$	6.97	0.15	*N.D.	*N.D.	*N.D.	*N.D.
Mgn	Fe_3O_4	2.30	0.24	*N.D.	*N.D.	*N.D.	*N.D.
Awr	Ni_3Fe	0.80	0.23	16.43	0.36	14.23	0.40
Tvr	$NiFe_2O_4$	*N.D.	*N.D.	2.08	0.27	4.22	0.63

* N.D.: Not Detected.

Table 4.4 reports the quantified results, for 5.17% Fe, in order of decreasing relative abundance with heazlewoodite (Ni_3S_2) at 77.89wt.%, forming the dominant (>50%) mineral. The best fit for the copper sulfide indicates this to be chalcocite (Cu_2S) Q, a tetragonal form of chalcocite (space group P3212), forming a minor (5–15%) mineral with a relative abundance of 12.04wt%. If a high iron concentration was present in the analytical sample, a minor iron-nickel sulfide mineral corresponding to pentlandite $(Fe,Ni)_9S_8$ was present, with a relative abundance of 6.97wt%. Pentlandite (Pn) can also be considered as a member of the metal excess sulfide structural group (Vaughan, 2005). Accessory (<5%) minerals include spinel and base metal alloy reported as magnetite (Fe_3O_4) and awaruite (Ni_3Fe), with relative abundances of 2.30% and 0.80wt%, respectively. The sulfide minerals constitute 96.90% of

the minerals present within the 5.17% Fe matte. In comparison, sulfide minerals constitute 81.48% and 81.53% of the minerals present within the respective 0.99% and 0.15% Fe matte.

Moreover, the following differences are noted between the high (5.17%) and the lower (0.99% and 0.15%) iron mattes relating to the relative mineral abundances in Table 4.4:

i. Iron endpoint 5.17% is characterized by significantly higher heazlewoodite (Hw) relative abundance in contrast to iron endpoints 0.99% and 0.15%;

ii. Iron endpoints 0.99% and 0.15% are characterized by higher chalcocite (Cc) relative abundance in comparison to iron endpoint 5.17%;

iii. The mineral pentlandite (Pn) is only present in the high iron endpoint;

iv. Magnetite (Mgn) is present in the high iron endpoint, in contrast to the presence of trevorite (Tvr) in the lower iron endpoints; and

v. The lower iron endpoints are characterized by significantly higher awaruite (Awr) relative abundance in contrast to the high iron endpoint.

4.2.4. Descriptive Mineralogy

It became important to correlate the bulk matte chemistry, density, mineral identification and relative abundance with microstructure compositional and morphological investigations, and thereby produce a richer composite understanding of the converter matte mineralogy as a function of iron endpoint. The following sub-sections include the results and discussion of nickel and copper sulfide, base metal alloy, osmium and spinel mineral structures.

4.2.4.1. Nickel and Copper Sulfide

Results

Scanning electron microscopy EDX based analysis (described in Chapter 3, sub-section 3.5.2) at various points on 5.17% Fe matte particle sections confirms the presence of nickel sulfide minerals containing 51.7–62.3% Ni, 24.2–26.2% S, 5.8–16.3% Cu, 4.5–7.3% Fe, 1.1–1.5% Co, and copper sulfide minerals containing 53.9–73.4% Cu, 19.8–22.8% S, 2.5–17.5% Ni, 4.4–5.8% Fe, 0–0.6% Co. X-ray microanalysis at different points on 0.99% Fe matte particle

sections indicates a nickel sulfide mineral containing 64.7% Ni, 24.1% S, 7.5% Cu, 1.2% Fe, 0.9% Co, and a copper sulfide mineral containing 60.8% Cu, 20.9% S, 16.2% Ni, 1.4% Fe and 0.6% Co. Different points analyzed on 0.15% Fe matte particle sections indicates a nickel sulfide mineral containing 69.3% Ni, 25.8% S, 4.9% Cu, and a copper sulfide mineral containing 74.6% Cu, 20.1% S and 3.2% Ni.

Figure 4.2 allows for a comparative mineralogical examination of the dominant nickel sulfide, major copper sulfide and, to some extent, the minor base metal alloy minerals for 5.17%, 0.99% and 0.15% Fe mattes.

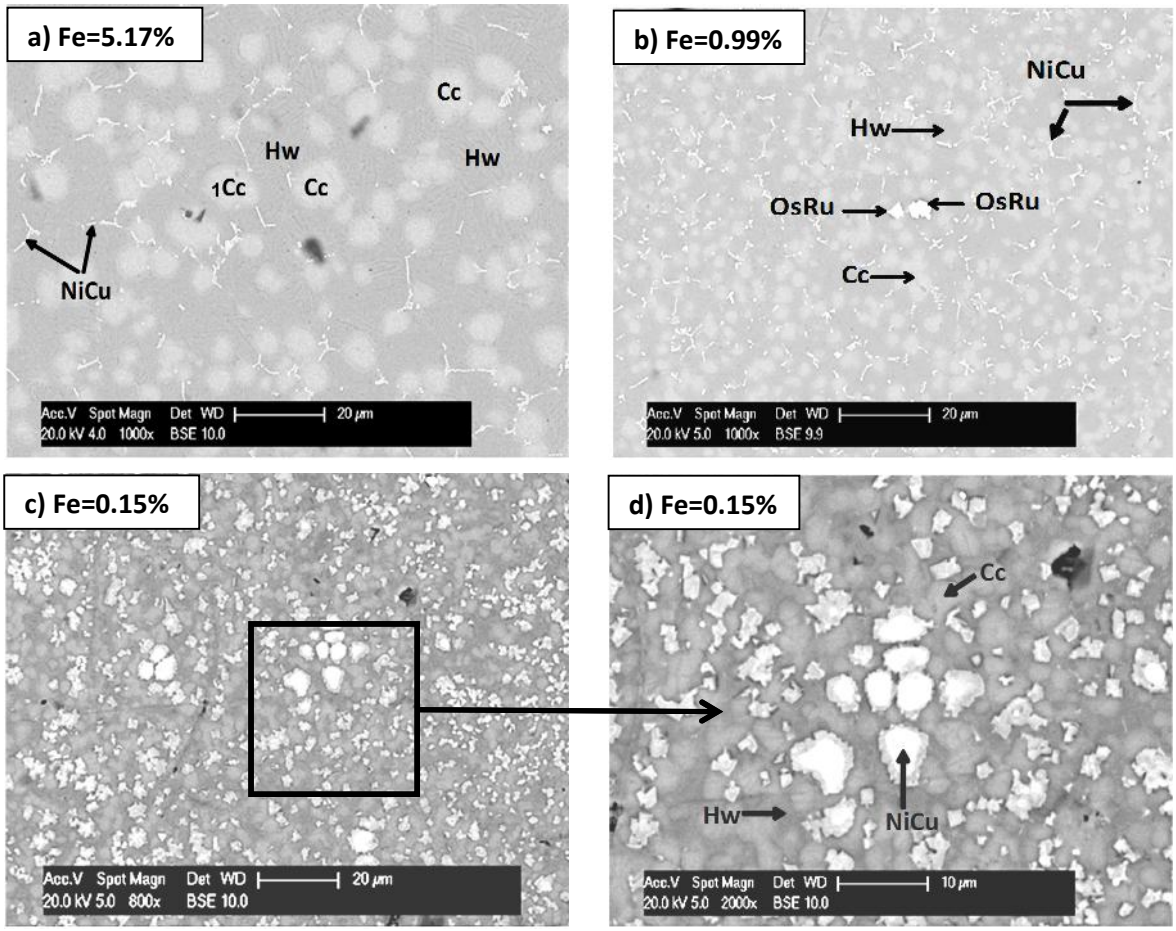

Figure 4.2: Comparative SEM BSE micrographs showing the presence of nickel sulfide (Hw), copper sulfide (Cc) and NiCu-alloy minerals with respect to (a) 5.17% Fe matte at 20µm size scale, (b) 0.99% Fe matte at 20µm size scale, (c) 0.15% Fe matte at 20µm size scale, and (d) 0.15% Fe matte at 10µm size scale.

The SEM BSE micrograph for iron endpoint 5.17% in Figure 4.2(a) confirms the dominant abundance of anhedral nickel sulfide or heazlewoodite (Hw) minerals, possibly forming a

cementing matrix, embedding euhedral grains of the major copper sulfide or chalcocite (Cc) minerals. The sizes of the euhedral chalcocite grains differ and 1Cc, for instance, is approximately 12µm and 8µm in the elongated x and y-directions. The cementing matrix of heazlewoodite can be as large as 15µm between Cc grains and also appears to be compositionally zoned. The Cc grains also exhibit compositional zonation with less well-defined grain boundaries.

In comparison, SEM BSE micrographs for iron endpoints 0.99% and 0.15%, in Figures 4.2(b), (c) and (d), exhibit notably smaller anhedral Hw and euhedral to subhedral Cc grains. Moreover, the Hw and Cc grain boundaries at the 10µm size scale for iron endpoint 0.15% in Figure 4.2(d) appear complexly intergrown.

The relevant microstructures were subsequently characterized intimately at higher magnification and resolution on specially prepared electron transparent samples for iron endpoints 5.17% and 0.99%. Transmission electron microscopic EDX analysis (described in Chapter 3, sub-section 3.5.3) at different points on a 5.17% Fe matte particle section confirms the presence of a nickel sulfide mineral containing 65.9% Ni, 25.7% S, 6.2% Cu, 1.3% Fe, 0.9% Co and a copper sulfide mineral containing 73.4% Cu, 19.8% S, 2.1% Ni and 3.9% Fe. Different points analyzed on a 0.99% Fe matte indicate a nickel sulfide mineral containing 74.5% Ni, 25.5% S and copper sulfide minerals containing 77.6–78.2% Cu, 18.5–19.8% S and 2.6–3.3% Ni. Figure 4.3 permits for the comparative examination of bright field TEM micrographs of the nickel sulfide and copper sulfide mineral structures for the iron endpoints 5.17% and 0.99%.

The bright field TEM micrograph in Figure 4.3(a), for iron endpoint 5.17%, confirms the euhedral form and compositional zonation of the Cc grains, as noted previously in Figure 4.2(a). The Cc grain shown in Figure 4.3(a) is approximately 2.3µm x 3.1µm and relatively smaller than the larger variant sizes in Figure 4.2(a). Bright field TEM micrographs of the Cc grain at a higher magnification are available for examination in the atlas of microstructures in Appendix B (Figures B.2 to B.4). Heazlewoodite is also present, as indicated, although it is dominated by irregular mass-thickness contrast. The Cc grain in Figure 4.3(b) for iron endpoint 0.99 % is considerably smaller (approximately 540nm x 760nm) than in Figure 4.3(a). The Hw grain (matrix) in Figure 4.3(b) can also be associated with the location of a

NiCu-alloy grain. Significant diffraction could also be obtained from the analyzed grains and the diffraction patterns, as indicated in Figure 4.3(a), could be matched with that of heazlewoodite (Ni_3S_2) and chalcocite (Cu_2S) natural minerals.

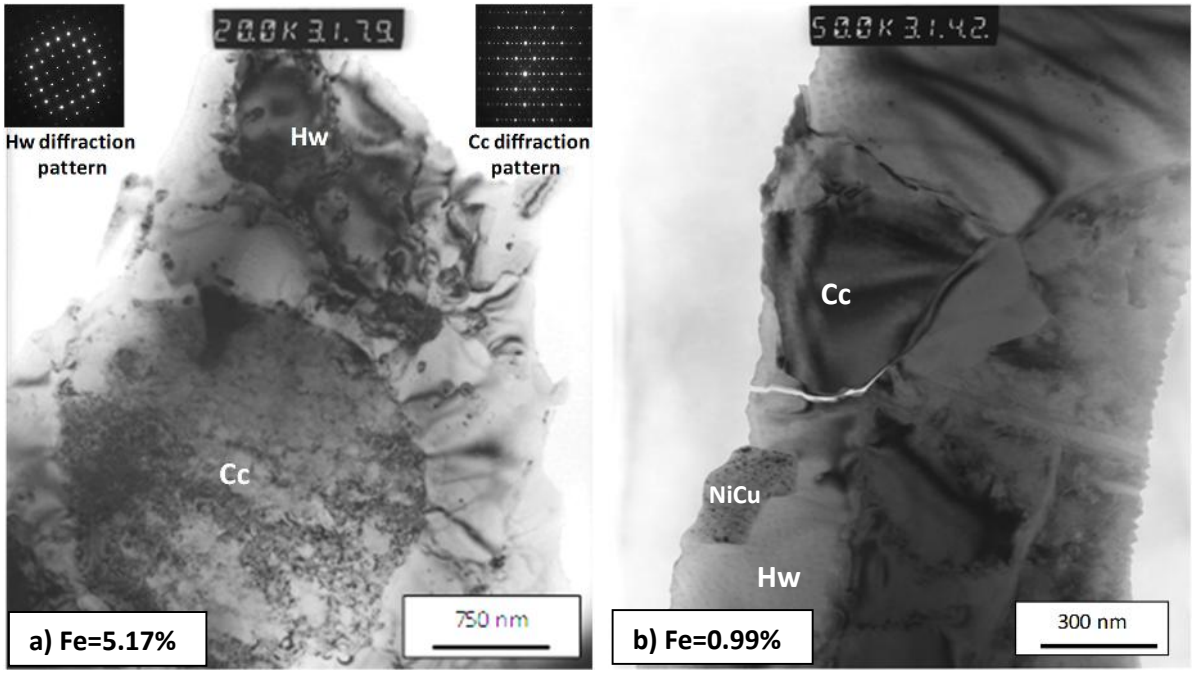

Figure 4.3: Comparative bright field TEM micrographs showing nickel sulfide (Hw), copper sulfide (Cc) and NiCu-alloy minerals for (a) 5.17% Fe matte at 750nm size scale, and (b) 0.99% Fe matte at 300nm size scale.

Discussion

The following discussion is specific to nickel sulfide or heazlewoodite mineral structures and is mostly based on the preceding results. Table 4.2, shown previously in sub-section 4.2.1, reveals a much lower bulk Ni:S ratio (1.85) for iron endpoint 5.17%, compared to 2.55 and 2.58 for iron endpoints 0.99% and 0.15%, respectively. Quantitative X-ray diffraction indicates that nickel sulfide or heazlewoodite structures constitute the dominant mineral for all three mattes investigated. Moreover, the 5.17% Fe matte is characterized by a significantly higher heazlewoodite relative abundance than the 0.99% Fe and 0.15% Fe matte. The bulk metal-to-sulfur ratio was previously found to influence the partitioning of base metals into monosulfide solid solution and sulfide melt in relation to the Ni-Cu-Fe-S-PGM system (Ballhaus et al., 2001). It is therefore possible to regard the bulk chemistry of Lonmin matte as highly relevant to its constituent mineral formation. In addition, the

chemistry of the bulk matte produced by the Kalgoorlie Nickel Smelter in Western Australia was found to be influential with respect to mineral formation for different cooling methods (Page, 1982). The crystal form of heazlewoodite was not reported by XRD analysis in sub-section 4.2.3, but is more likely to be a hexagonal structure (Kullerud and Yund, 1962).

Nickel sulfide specific composition distinctions, based exclusively on EDX analysis, are manifested by a shift in the average Ni:S ratios from 2.3 for 5.17% Fe matte to 2.8 and 2.7 for the 0.99% and 0.15% Fe mattes, respectively. Heazlewoodite structures for the lower iron mattes contain notably less dissolved iron and cobalt. The composition of nickel sulfide structures will be investigated in considerable detail in the following chapter. Anhedral forms like heazlewoodite minerals possibly crystallized in a restricted melt environment with limited space for the development of well rounded forms, as for chalcocite minerals. Heazlewoodite crystallization most likely occurs at low temperatures and is possible the last mineral to form, thus establishing a cementing matrix embedding euhedral Cc grains as observed by the SEM BSE micrographs. According to Kullerud and Yund (1962), the higher temperature tetragonal polymorph α-Ni_3S_2 inverts at 556 ^oC to hexagonal Ni_3S_2. Bright field TEM micrographs show that the boundary for Hw cannot be clearly distinguished as for Cc grains. Quantitative X-ray diffraction analysis indicates that 5.17% Fe matte also contains measurable pentlandite and, in contrast, could not be observed by SEM or TEM based mineralogical examination. The pentlandite minerals could be incorporated in the structure of the cementing matrix, possibly leading to larger grain sizes, as observed for 5.17% Fe matte.

The subsequent deliberation is relevant to copper sulfide or chalcocite structures with respect to different iron endpoints. Quantitative X-ray diffraction analysis suggests that tetragonal chalcocite constitutes a minor mineral in the 5.17% matte and, in contrast, is present at a higher abundance in the 0.99% and 0.15% Fe matte. The bulk chemical analysis reveals higher Cu:S ratios (1.57 and 1.54) for iron endpoints 0.99% and 0.15%, compared to a Cu:S ratio of 1.06 for iron endpoint 5.17%. Bulk matte chemistry appears also relevant to the formation of copper sulfide structures. Chalcocite minerals for the 5.17% Fe matte have a distinctive average ratio of 3.0 in comparison to 3.8 and 3.7 for 0.99% and 0.15% Fe matte, and also contain fewer impurities. The composition of copper sulfide minerals will be

elaborated upon in the following chapter. Bright field TEM micrographs indicate mineralogical zoning of the impurities in the high iron matte. The presence of euhedral forms like chalcocite may signify that these crystallize early from the molten matte, without hindrance from other minerals. Evans (1981) found chalcocite to be intergrown with djurleite ($Cu_{1.96}S$) at low temperatures, while Posfai and Buseck (1994) used HRTEM to investigate this feature on the nanoscale. The complexity of identifying djurleite by SEM or TEM is apparent and it may be difficult to distinguish from chalcocite as well.

4.2.4.2. Base Metal Alloy

Results

Scanning electron microscopy EDX analysis at different points on 5.17% Fe matte particle sections indicates the presence of nickel-dominant alloy mineral structures containing 48.1–54.5% Ni, 11.7–12.7% Pt, 5.2–6.4% Cu, 5.4–10.6% Fe, 1.4–1.6% Co and 20.7–21.9% S. The small grain sizes and form, as annotated in Figure 4.2(a), probably affected the quality of analysis and significant amounts of sulfur were detected. The low relative abundance of the base metal alloy structures for iron endpoint 5.17%, noted as accessory mineral in sub-section 4.2.3, can possibly be correlated with the subordinate presence of characteristically bright, delicate and vein-like nickel-dominant structures, as can be seen in Figure 4.2(a). Moreover, the microstructures can be as long as 7µm and characteristic of a complex intergrowth pattern with heazlewoodite. The alloy structures, although containing moderate concentrations of platinum and probably erroneous sulfur is characterised further by very high Ni:Cu ratios of between 7.5 and 10.5.

The SEM BSE micrograph for iron endpoint 0.99% in Figure 4.2(b), also exhibits alloy structures similar in external morphological characteristics to those for iron endpoint 5.17%, albeit at a higher relative abundance. In addition, SEM EDX analysis and imaging at additional points for iron endpoint 0.99% indicates the presence of NiCu-dominant alloy structures containing variable Ni:Cu ratios, platinum concentration and morphological characteristics. Figure 4.4 allows for a comparative mineralogical examination of the variable compositional and morphological characteristics of the NiCu-dominant alloy structures within and between iron endpoints 0.99% and 0.15%.

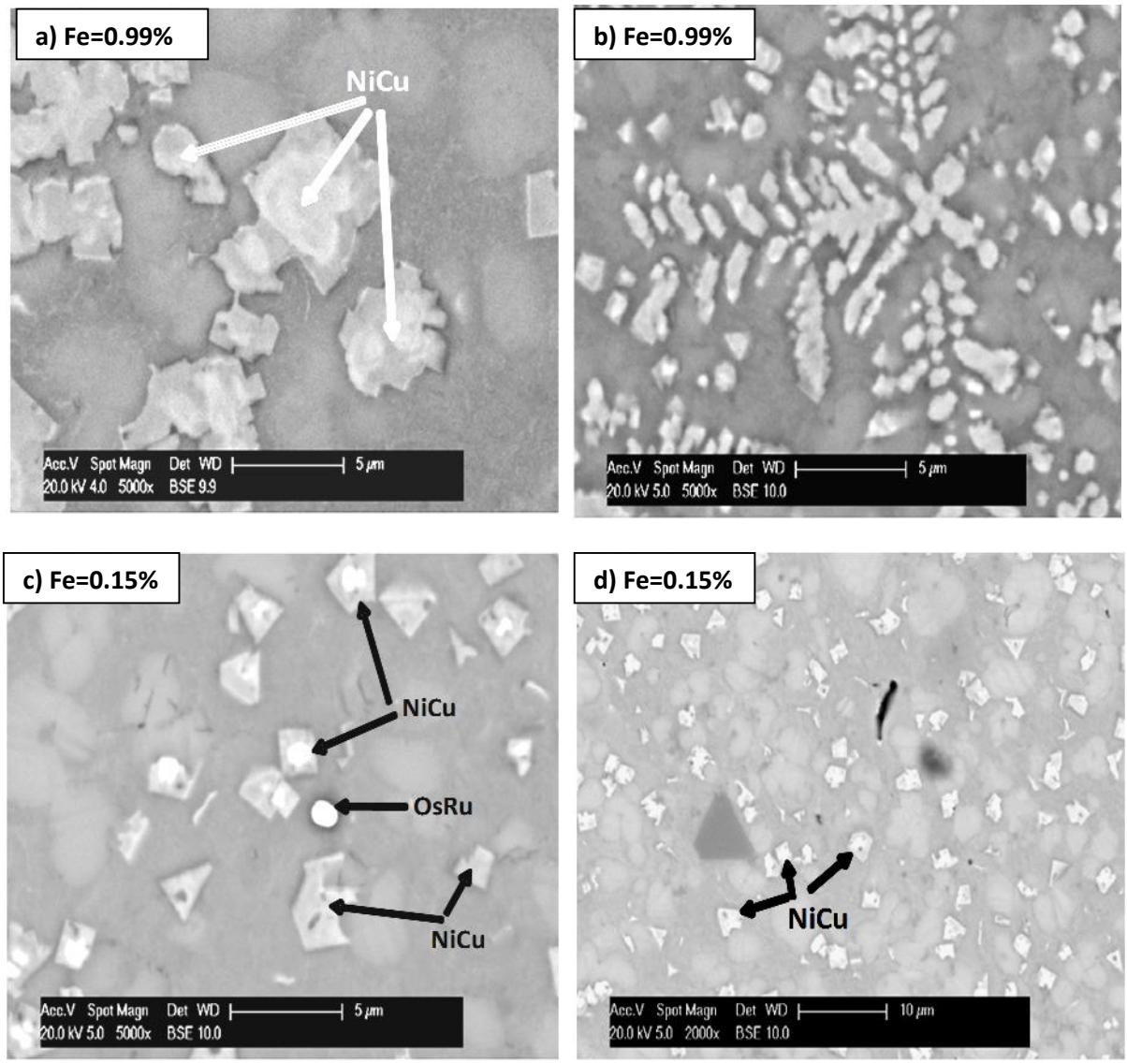

Figure 4.4: Comparative SEM BSE micrographs showing NiCu-alloy mineral structures with respect to (a) 0.99% Fe matte at 5µm size scale, (b) 0.99% Fe matte at 5µm size scale, (c) 0.15% Fe matte at 5µm size scale, and (d) 0.15% Fe matte at 10µm size scale.

The SEM BSE micrograph for iron endpoint 0.99% in Figures 4.4(a) and (b) exhibits the development of subhedral to cubic forms of NiCu-dominant alloy structures with the absence of a well-developed core. The alloy structures in Figure 4.4(b) appear to be arranged in a skeletal pattern. X-ray microanalysis of the annotated alloy form in Figure 4.4(a) reveals the structure to contain 51.4% Ni, 45.1% Cu, 3.0% Pt and 0.5% Pd. The grain size is approximately 5µm X 5µm, with a characteristic low Ni:Cu ratio of 1.1 and low platinum concentration. A further characteristic alloy form for iron endpoint 0.99% (not shown here, but it will be investigated in considerable detail in the next chapter on base

metal and PGM mineralization) is the development of a very bright core, enriched in platinum and surrounded by dendritic-like, predominantly nickel–copper containing subhedral to cubic forms. The most significant external morphological characteristics with respect to the NiCu-alloy structures for iron endpoint 0.15% include the variable forms, as noted in Figures 4.4(c) and (d). The compositional characteristics include grains with large Ni:Cu ratios (2.3–3.2), low platinum and sulfur concentration in contrast to grains with small Ni:Cu ratios (1.1–1.4) and moderate platinum.

Figures 4.5(a) and (b) permit a comparative mineralogical examination, at higher magnification and resolution, of bright field TEM micrographs with respect to the alloy forms for iron endpoints 5.17% and 0.99%, respectively. Figure 4.5(c) provides penetrative dark field HRSTEM elemental mapping of the composition of the alloy form for iron endpoint 5.17%.

Transmission electron microscopy imaging for iron endpoint 5.17% confirms the form (delicate, vein-like structure and notably discontinuous here) of the platinum containing nickel-dominant alloy structure noted in the bright field TEM micrograph in Figure 4.5(a). X-ray microanalysis indicates that the structure contains 53.3% Ni, 19.5% Pt, 5.5% Cu, 4.4% Fe, 0.9% Co, 0.4% Pd, 0.1% Rh and 15.9% S, and also manifests a high Ni:Cu ratio of 9.7. In contrast, HRSTEM elemental mapping of a similar alloy form for iron endpoint 5.17%, noted in Figure 4.5(c), reveals that the inner core of the structure can contain considerably more platinum and copper, as indicated by the concentration of purple and blue false colors, respectively. The elemental mapping also reveals that the concentration of nickel and sulfur can predominantly be associated with the rim of the structure as well as the adjacent sulfide matrix.

Figures 4.3(b), shown previously, and 4.5b exhibit subhedral NiCu-dominant alloy structures of relatively small grain sizes with a significant compositional zonation. The grain in Figure 4.3(b) is approximately 150nm x 250nm and contains 44.5% Ni, 25.2% Pt, 17.9% Cu, 3.4% Fe, 2.7% Rh, 1.3% Pd and 0.8% Co with a Ni:Cu ratio of 1.8. The approximate sizes of grains A and B in Figure 4.5(b), upon examination, can be indicated as 200nm x 560nm and 280nm x 190nm, respectively. Grain A is also illustrated at higher magnification in the atlas of microstructures in Appendix B (Figure B.5). Microanalysis furthermore reveals grains A and B

to contain 55.5% Ni, 21.0% Cu, 15.6% Pt, 3.5% Fe, 1.5% Pd, 1.3% Ru, 0.8% Rh, 0.7% Co and 54.3% Ni, 19.4% Cu, 11.5% Pt, 4.2% Fe, 3.1% Pd, 2.5% Ru, 2.1% Rh, 1.0% Co, 0.7% S, respectively. The Ni:Cu ratios of grains A and B can also be indicated as 2.6 and 2.8, respectively.

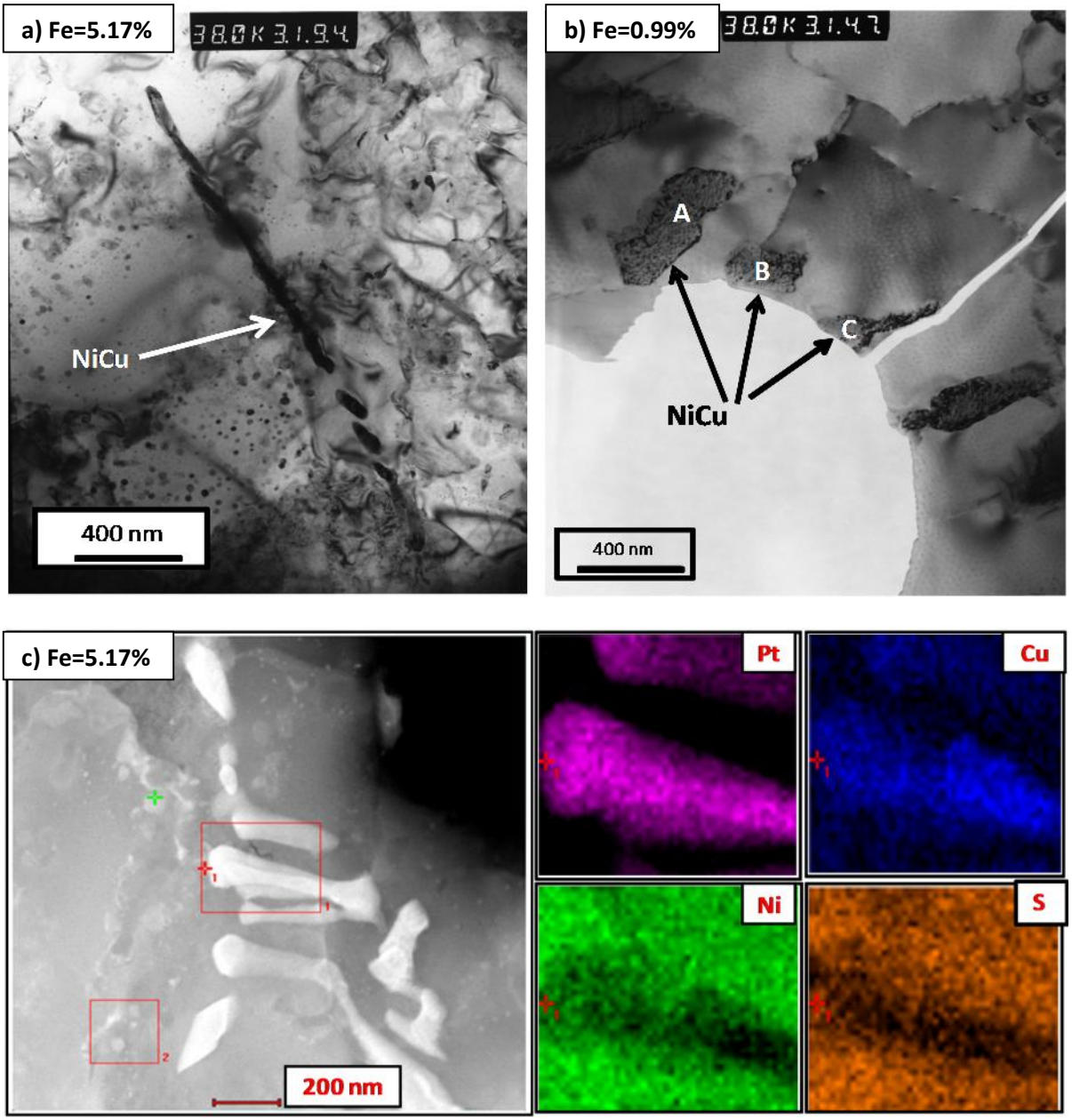

Figure 4.5: Comparative TEM micrographs showing NiCu-alloy mineral structures with respect to (a) 5.17% Fe matte, (b) 0.99% Fe matte at 400nm size scales, respectively, and (c) elemental mapping of vein-like alloy form for 5.17% Fe matte at 200nm size scale.

Discussion

Quantitative X-ray diffraction analysis for the 5.17% Fe matte indicates an awaruite structured base metal alloy mineral present in very low relative abundance. In comparison, volume% estimation diagrams (Lof, 1982) set the relative abundance at 3%, with respect to Figure 4.2(a). The crystal structure of awaruite was not reported by XRD analysis in section 4.2.3, but has been described previously by Rubin (1991) as face-centred cubic. In contrast, the mineralogical examination reveals the structures to be nickel-dominant and acting as collectors of PGMs, manifested by the platinum concentration present. Dark field HRSTEM elemental mapping was used successfully to show that the core is more likely to be associated with more platinum and copper, and less nickel and sulfur, as revealed by SEM and TEM EDX analysis. The structures investigated are extremely fine grained and possibly characteristic of an exsolution origin.

The NiCu-dominant, PGM-containing alloy structures investigated for 0.99% and 0.15% Fe mattes are characteristic of an exsolution origin followed by microtextural changes. These changes are likely the result of chemical exchange with other constituent elements, including PGMs. Subhedral forms exhibit limited crystal face formation (Hurlbut and Klein, 1985) and can be correlated with the observed NiCu-dominant alloy structures for the lower iron mattes. It is therefore of considerable economic value. The increase in bulk density for the lower iron mattes can possibly be related to the higher relative abundance of NiCu-alloy structures. According to Schouwstra (2008) and based on SEM EDX analysis, a 0.5% Fe matte from Lonmin revealed the highest alloy abundance amongst several PGM producers. Slow-cooled and quenched matte samples from the Kalgoorlie Nickel Smelter in Western Australia also displayed skeletally arranged awaruite mineral structures (Page, 1982) similar to observations in Figure 4.4(b), with respect to NiCu-alloy structures in 0.99% Fe matte.

4.2.4.3. Osmium Ruthenium Alloy

Results

The OsRu-alloy structures occur mainly as discrete, bright euhedral to subhedral grains of varying size and composition set in the heazlewoodite matrix. Figures 4.2(b), 4.4(c) and

Figure 4.6 provides for a comparative mineralogical examination of the observed OsRu-alloy structures for the different iron endpoints.

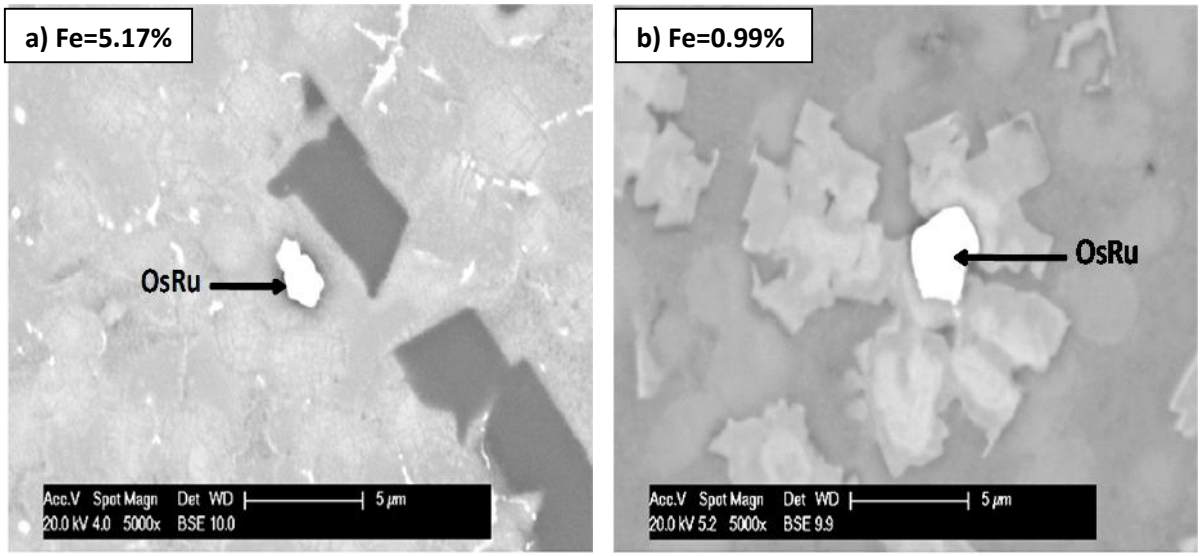

Figure 4.6: Comparative SEM BSE micrographs showing OsRu-alloy structures with respect to (a) 5.17% Fe matte and (b) 0.99% Fe matte at 5µm size scales, respectively.

The SEM BSE micrograph for iron endpoint 5.17% in Figure 4.6(a) exhibits the presence of a bright subhedral Os-dominant grain with a characteristic composition of 87.0% Os, 5.3% Ni, 2.9% Ru, 2.6% Cu, 1.6% Fe and 0.7% S. Further observations reveal that the characteristic composition can be associated with grains generally between 1–2µm with Os:Ru ratios between 30.0–49.1. Grains smaller than 1µm characteristically contain 29.0–36.3% Os, 24.5–32.9% Pt, 15.3–15.8% Ni, 7.2–7.8% Ir, 4.6–5.4% Cu, 4.7% Fe, 0.8 Co and 5.6% S. Iron endpoint 0.99% can predominantly be associated with larger Os-dominant grains between 2–7µm with characteristic compositions of 82.4–92.5% Os, 1.6–10.8% Ru, 3.3–6.7% Ni, 1.7–2.7% Cu and Os:Ru ratios between 7.4–59.5. The SEM BSE micrographs in Figures 4.2(b), shown previously, and 4.6(b) confirm the larger sizes and euhedral to subhedral form of the alloy structures. In comparison, iron endpoint 0.15% can be associated with smaller Os-dominant grains between 1–3µm with characteristic compositions of 72.4–84.0% Os, 6.7–7.3% Ru, 5.3–12.5% Ni, 3.1–3.4% Cu, 1.3–5.4% S and Os:Ru ratios between 10.6–11.5. The SEM BSE micrograph in Figure 4.4(c), shown previously, confirms the smaller and euhedral nature of the alloy structures.

Discussion

The OsRu-alloy structure was not identified by XRD analysis in section 4.2.3, but volume% estimation diagrams estimate the relative abundance to be below 1% (Lof, 1982). Lonmin currently does not report osmium production data across the process route. Osmium and ruthenium may initially combine with oxygen during converting and would be lost to the converter gas phase (Eksteen et al., 2011). Overall, the OsRu-alloy examined by SEM occurs as discrete structures, set in the nickel sulfide matrix and often in close proximity to NiCu-alloy structures, as shown in Figure 4.6b above. The OsRu-structures for 5.17% Fe matte appear smaller in size with larger Os:Ru ratios compared to the structures for 0.99% and 0.15% Fe matte.

4.2.4.4. Spinel

Results

Scanning electron microscopy EDX analysis for 5.17% Fe matte reveals the presence of iron-dominant spinel structures with characteristic compositions of 55.9–76.0% Fe, 19.3–20.7% O and 3.3–5.2% Ni. Figure 4.7 provides for a comparative mineralogical analysis of spinel structures for the different iron endpoints.

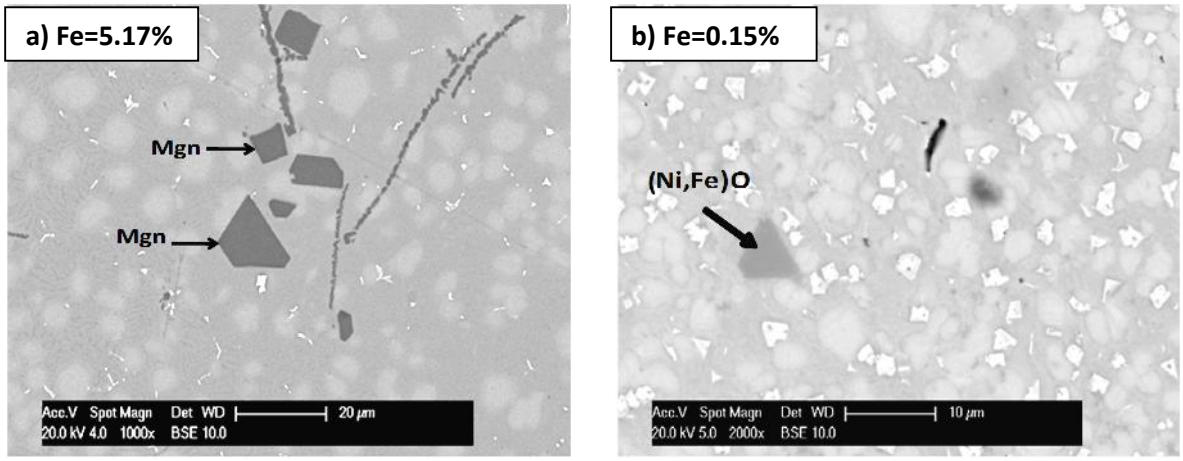

Figure 4.7: SEM BSE micrographs showing spinel structures with respect to (a) 5.17% Fe matte at 20µm size scale and (b) 0.15% Fe matte at 10µm size scale.

The SEM BSE micrograph in Figure 4.7(a) exhibits strikingly dark, well-formed euhedral forms with surprisingly similar composition and which vary in dimensions from approximately 12µm x 13µm to irregular vein-like forms with a dissimilar composition and also significantly lower in iron concentration. The structures interestingly, appear to be set

in the sulfide matrix. Moreover, X-ray microanalysis for the same iron endpoint reveals the presence of spinel structures with nickel-dominant cores containing 44.5–45.9% Ni, 33.5–33.8% Fe and 16.8–17.2% O, as well as iron-dominant rims containing 46.5–56.0% Fe, 18.6–19.1% Ni and 14.9– 16.8% O. The structures also appear to be set in the sulfide matrix and are approximately 9µm x 15µm. In comparison, X-ray microanalysis for iron endpoint 0.99% reveals the presence of iron-dominant and nickel-dominant spinel structures with the absence of characteristic core and rim features. The structures contain 59.6–68.6% Fe, 19.9–21.1% O, 8.3–12.4% Ni and 37.0–59.1% Ni, 21.9–31.8% Fe, 11.1–16.9% O, respectively. In contrast, X-ray microanalysis for iron endpoint 0.15% reveals the presence of nickel-dominant spinel structures containing 52.3–52.9% Ni, 18.7–25.9% Fe and 17.3% O as indicated in Figure 4.7(b).

Discussion

Quantitative X-ray diffraction indicates magnetite and trevorite present below 5% relative abundance, in the high and low iron mattes, respectively. Mineralogical examinations for the high iron matte confirm the presence of characteristic magnetite and, in contrast to XRD results, distinctively mantled iron-nickel oxide structures. The lower iron matte appears characteristic of increasing nickel-dominant spinel structures, which is in agreement with the QXRD result with respect to trevorite. The oxygen concentrations in the lower iron mattes are 1.49% and 1.24%, which are much in excess to be consumed by the lower residual iron alone. Nickel is thus oxidized, as copper may be too noble. Schouwstra (2008) reported that spinel structures in Lonmin matte indicated the highest nickel concentration amongst various PGM producers. Spinel structures would be insoluble during downstream matte leaching and thereby reduce the grade of the resultant PGM concentrate (Jones, 2005).

4.3. Key Findings

The investigation of 5.17%, 0.99% and 0.15% Fe mattes with respect to bulk chemistry, density, mineral identification, relative abundances, composition and morphology in this chapter suggest the following key findings:

i. The attained iron endpoints evidently influence the overall finished matte composition. An optimum base metal and PGM concentration was achieved with

an iron endpoint of 0.99%. The Co and Pb concentration, on the contrary, attained a maximum with an iron endpoint of 5.17%. The bulk chemistry of the specific mattes was found to be influential during the subsequent formation of minerals;

ii. The bulk density of the specific converter mattes was found to increase with the attainment of lower iron endpoints. It would be reasonable to relate the higher relative abundance, basic composition and crystal structure of NiCu-alloy and refractory spinel structures in the lower iron mattes to the corresponding increase in matte density;

iii. Sulfide minerals were identified as the dominant structures present for all three converter mattes investigated. Nickel sulfide matched to heazlewoodite structures constitute the dominant mineral and display a significantly higher relative abundance in the 5.17% Fe matte. The structures are the primary source of nickel. The nickel sulfide in the high iron matte can be considered as chemically and morphologically different to that in the lower iron mattes. Subtle chemical and mineralogical differences exist between the nickel sulfide in the lower iron mattes;

iv. Copper sulfide matched to chalcocite structures display a higher relative abundance in the lower iron mattes and can also be considered as chemically and mineralogically dissimilar to that in the high iron matte. Slight differences exist between the copper sulfide in the lower iron mattes. The structures are also the primary source of copper;

v. The PGM-containing NiCu-alloy structures exhibit a significantly higher relative abundance in the lower iron mattes. The structures are of considerable economic importance as the primary source of PGMs and additional nickel and copper. Although variable in composition and morphological forms, their exsolution origin can be related to fine-grained vein-like morphologies followed by exsolution modifications. The 5.17% Fe matte is particularly characteristic of the fine-grained vein-like morphologies which would require fine grinding of matte particles in order to be liberated from the nickel sulfide matrix;

vi. Osmium-dominant alloy structures are estimated to be below 1% for all three mattes investigated. The OsRu-alloy structures present in the high iron matte can

also be regarded as chemically and morphologically different to that in the lower iron mattes; and

vii. Spinel structures are present in both the high and low iron mattes between 2% and 5% relative abundance, and are characterized by an increase in nickel concentration for the lower iron mattes. These structures are regarded as deleterious and would reduce the concentration of the PGM concentrate produce during leaching.

This chapter has endeavoured to provide plant metallurgists with an improved understanding of the effect of variable iron endpoint on matte mineralogy. It has also provided the basis for the next chapter in which the mineralization of base metals and PGMs will be systematically investigated and presented in relation to the industrial converter iron endpoints attained.

4.4. Relevant Publication

Thyse, E.L., Akdogan, G., Eksteen, J.J., 2011. The effect of changes in iron endpoint during Peirce-Smith converting on PGE-containing nickel converter matte mineralization. ***Minerals Engineering,*** Special Issue: Processing of Nickel Ores & Concentrates, Volume 24, Issue 7, pp. 688 – 697.

Chapter 5
BASE METAL AND PGM MINERALIZATION

5.1. Introduction

The investigations conducted in Chapter 4 have revealed a basic dependence between the Peirce-Smith converter iron endpoint attained and the resultant mineralogy of the granulated matte. It would be important to provide further insight into the dependence between iron endpoint specific mineralogy, base metal and PGM mineral chemistry and the genesis of mineral structures. The aim of this chapter is to systematically investigate the mineral chemistry, specifically, the partitioning of base metals and PGMs into nickel sulfide, copper sulfide and base metal alloy as a function of the iron endpoint. This includes understanding the mineralization mechanism of the economically significant base metal alloy microstructure, 3D visualization and related analysis.

5.2. Results and Discussion

The results of the electron probe microanalysis indicative of the sulfide mineral chemistry are initially reported below in relation to the iron endpoint investigated. This is followed by the similar reporting of the electron probe microanalysis specific to the base metal alloy mineral chemistry, which is subsequently used to derive an understanding of the PGM mineralization mechanism. The illustration of fine microstructure detail is central to the development of such an understanding. Finally, the 3D visualization and analysis of matte microstructure with respect to the lowest iron endpoint is reported.

5.2.1. Sulfide Mineral Chemistry

The accurate electron probe microanalysis, performed using WDS to achieve low detection limits, was essential to a comprehensive investigation of the nickel and copper sulfide mineral chemistry as a function of iron endpoint. The analytical technique is described in Chapter 3 (sub-section 3.5.4).

5.2.1.1. Nickel Sulfide

Results

Electron probe microanalysis was conducted on 50 selected matte particle sections with respect to heazlewoodite-type structures and different iron endpoints. Figure 5.1 illustrates the principal mineral chemistry pertaining to the heazlewoodite-type structures analyzed for the 5.17%, 0.99% and 0.15% Fe mattes. The principal mineral chemistry is available for examination in Appendix C (Table C.1).

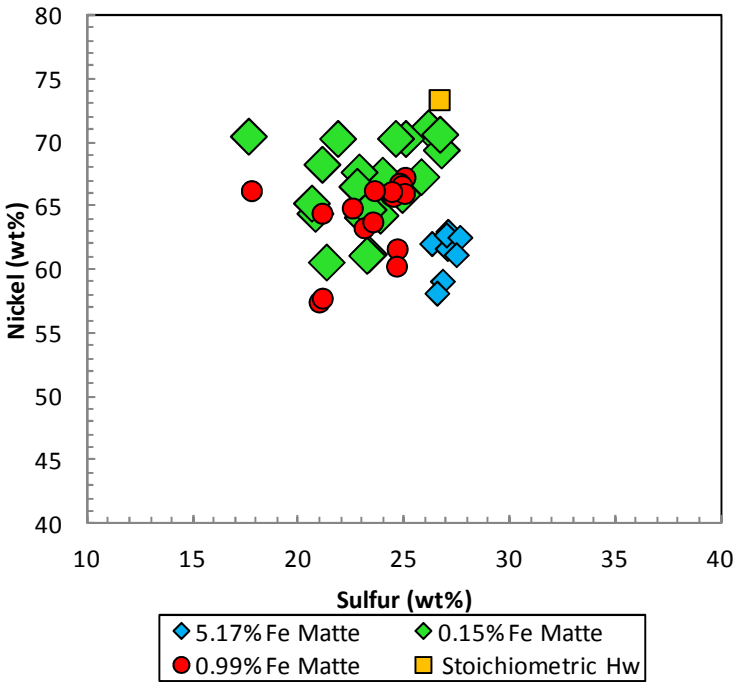

Figure 5.1: The principal mineral chemistry of the heazlewoodite-type structures with respect to the 5.17%, 0.99% and 0.15% Fe mattes obtained through electron probe microanalysis.

The electron probe microanalyses verify the presence of invariably Ni- and S-rich mineral structures for all three iron endpoints investigated. All concentrations are in weight% unless specifically reported otherwise. The principal Ni concentration range for mineral structures in the high iron matte averages 61.36%, but varies between 58.07% and 62.94%. The corresponding principal S concentration varies narrowly between 26.34% and 27.68%, with an average of 27.04%. The standard deviation from the average Ni and S concentrations are 1.59% and 0.39%, respectively. In contrast, the Ni and S concentrations for mineral structures in the lower iron endpoints vary noticeably more, as illustrated in Figure 5.1. In particular, the Ni concentration range for mineral structures in the lowest iron matte varies

between 60.52% and 71.08%, with an average of 66.56% and a standard deviation of 3.30%. The corresponding S concentration varies between 17.66% and 26.80%, including an average of 23.34% and a standard deviation of 2.22%. It is evident from the analyses and illustration in Figure 5.1 that the Ni concentration, albeit more variable, increases in heazlewoodite-type structures with the corresponding attainment of a lower iron endpoint. The S concentration, on the contrary (and evidently more variable), decreases in heazlewoodite-type structures with the lowering of iron endpoint. The results are in good agreement with the SEM EDX based findings in Chapter 4 (sub-section 4.2.4.1). The stoichiometric composition of heazlewoodite (Hw) is also illustrated in Figure 5.1.

Table 5.1 below reports the major to minor concentration of base metals present in the analyzed heazlewoodite-type structures or nickel sulfide minerals in relation to iron endpoint.

Table 5.1: The range and average concentration of base metals present in the nickel sulfide minerals acquired through electron probe microanalysis.

Element	5.17% Fe		0.99% Fe		0.15% Fe	
	Range (wt%)	Average (wt%)	Range (wt%)	Average (wt%)	Range (wt%)	Average (wt%)
Fe	4.77-6.76	5.52 *(0.69)	0.03-1.46	0.83 *(0.55)	0.03-0.26	0.09 *(0.05)
Cu	0.17-2.72	0.89 *(0.10)	0.33-13.95	5.75 *(4.65)	0.97-13.84	5.49 *(3.98)
Co	0.99-1.11	1.05 *(0.04)	0.09-0.80	0.48 *(0.31)	0.20-0.68	0.48 *(0.11)
Pb	0.12-0.20	0.15 *(0.02)	0.14-0.22	0.18 *(0.03)	0.13-0.30	0.21 *(0.05)

* Standard deviations in parenthesis.

The base metals (Fe, Cu, Co and Pb) are present in major and minor concentrations for most of the nickel sulfide mineral structures analyzed. According to Table 5.1, Cu and Fe display the highest concentration of the base metals present in the nickel sulfide minerals. Furthermore, the nickel sulfide minerals for the lower iron mattes contain a higher average Cu and Pb concentration compared to minerals for the high iron matte. Conversely, nickel sulfide minerals for the high iron matte contain a notably higher average Fe and minor Co concentration than minerals for the lower iron mattes.

Table 5.2 reports the minor to trace concentration of PGMs present in the analyzed nickel sulfide minerals in relation to iron endpoint.

Table 5.2: The range and average concentration of PGMs present in the nickel sulfide minerals obtained through electron probe microanalysis**.**

Element	5.17% Fe		0.99% Fe		0.15% Fe	
	Range (ppm)	Average (ppm)	Range (ppm)	Average (ppm)	Range (ppm)	Average (ppm)
Pd	1216-2665	1713 *(490)	620-3381	1196 *(737)	808-2280	1685 *(558)
Pt	923-2282	1358 *(428)	840-2949	1283 *(572)	801-6771	2037 *(1729)
Rh	817-939	873 *(60)	863	863	854-1339	1054 *(176)
Ir	829-1478	1071 *(212)	819-1459	989 *(215)	827-1405	1010 *(169)

* Standard deviations in parenthesis.

More than half of the nickel sulfide minerals analyzed contain detectable Pd, Pt and Ir in minor to trace concentrations, as evident in Table 5.2. Rhodium is present in less than half of the nickel sulfide minerals analyzed and in relatively lower concentrations. The sum of the PGMs present is the highest in the nickel sulfide minerals for the lowest iron matte. The nickel sulfide minerals also appear to be Ru and Os-poor as no detectable concentrations of both PGMs are present. This result supports the previous finding in Chapter 4 (sub-section 4.2.4.3), which demonstrates that Os and Ru would preferentially form discrete alloy structures.

Discussion

It is important to note that the concentrations acquired refer to the electron probe microanalyses at the core of the minerals. In general, the concentration of the principal constituents (Ni and S) of the nickel sulfide minerals for all three iron endpoints fluctuates measurably. These fluctuations reflect the variable presence of base metals and PGMs incorporated or partitioned into the nickel sulfide minerals, in particularly Cu and Fe. As a consequence, the nickel sulfide minerals exhibit considerable non-stoichiometry. It therefore seems apparent that Cu-enriched nickel sulfide minerals are a common

characteristic of particularly the lower iron matte systems and, therefore, also of the converter plant settings. Table 5.1 indicates the maximum solubility of Cu in nickel sulfide minerals for the 0.99% Fe matte as 13.95%. The high iron matte, though, is characterized by Fe- and Cu-enriched nickel sulfide minerals. According to Vaughan (2005) and Firdu and Taskinen (2010), sulfide minerals are known to exhibit compositional variations, non-stiochiometry and solid solution characteristics.

The corresponding variable concentrations of principal Ni and major Cu suggest that mutual solid solubility warrants consideration. In addition, complete solubility between Ni and Cu is obvious from Ni-Cu phase diagrams (Predel, 1994), as both have the same crystal structure (face-centred cubic) and nearly the same radii. It therefore seems reasonable to suggest that Cu partitioning represents the atomic substitution of principal Ni by Cu. The partitioning of the co-existing base metals and PGMs most likely occurred during the crystallization event of the nickel sulfide mineral structures. Schouwstra (2000) developed an empirical understanding of the crystallization processes for a slow-cooled ingot within the industrial context of the Anglo Platinum beneficiation route. The crystallization paths of the relevant fast-cooled mineral structures within the Lonmin industrial context will be investigated in considerable detail in the next chapter.

5.2.1.2. Copper Sulfide

Results

Forty three matte particle sections were selected for electron probe microanalysis with respect to chalcocite-type structures and different iron endpoints. Figure 5.2 demonstrates the principal mineral chemistry for the chalcocite-type structures analyzed for the 5.17%, 0.99% and 0.15% Fe mattes. The principal mineral chemistry is reported in Appendix C (Table C.2).

The electron probe microanalyses confirm the presence of Cu- and S-rich mineral structures for all three iron endpoints investigated. The principal Cu concentration range for the mineral structures in the high iron matte averages 60.02%, but varies between 53.24% and 66.06%. The standard deviation from the average Cu concentration is 4.29%. The related principal S concentration varies closely between 22.35% and 23.76%, with an average of

23.11%. The standard deviation from the average S concentration is 0.42%. The Cu concentration range for mineral structures in the lowest iron matte varies between 65.92% and 76.57%, with an average of 71.32% and a standard deviation of 3.05%. The related S concentration varies between 19.23% and 20.76%, with an average of 20.12% and a standard deviation of 0.46%.

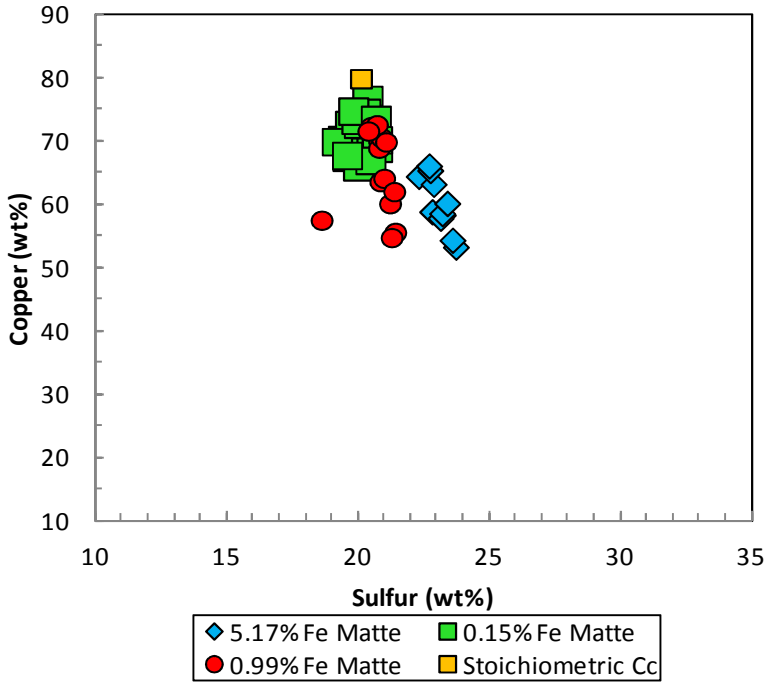

Figure 5.2: The principal mineral chemistry of the chalcocite-type structures acquired through electron probe microanalysis in relation to the 5.17%, 0.99% and 0.15% Fe mattes.

The analyses and demonstration in Figure 5.2 indicates that the Cu concentration increases in chalcocite-type structures with the lowering in iron endpoint. In contrast, the S concentration decreases in chalcocite-type structures with the lowering in iron endpoint. The results are also in broad agreement with the findings in Chapter 4 (sub-section 4.2.4.1). The standard deviation from the average S concentration for all three mattes is notably small, rendering S largely stable. Figure 5.2 also displays the stoichiometric composition of chalcocite (Cc).

Table 5.3 reports the major to minor concentration of base metals present in the analyzed chalcocite-type structures or copper sulfide minerals in relation to iron endpoint.

Table 5.3: The range and average concentration of base metals present in the copper sulfide minerals obtained through electron probe microanalysis.

Element	5.17% Fe		0.99% Fe		0.15% Fe	
	Range (wt%)	Average (wt%)	Range (wt%)	Average (wt%)	Range (wt%)	Average (wt%)
Fe	4.58-6.47	5.26 *(0.56)	0.61-1.40	1.01 *(0.19)	0.05-0.73	0.13 *(0.16)
Ni	4.63-16.23	9.47 *(3.89)	2.92-18.91	9.70 *(5.98)	3.92-15.23	8.42 *(2.84)
Co	0.22-0.36	0.28 *(0.05)	0.17-0.29	0.22 *(0.04)	0.11-0.28	0.16 *(0.04)
Pb	†N.D.	†N.D.	0.12-0.14	0.13 *(0.01)	†N.D.	†N.D.

* Standard deviations in parenthesis.

†N.D.: Not Detected.

All the copper sulfide minerals analyzed contain major Ni and major to minor Fe and Co concentrations. Only three of the copper sulfide minerals analyzed for the 0.99% Fe matte contain minor Pb concentrations. Table 5.3 indicates that Ni and Fe exhibit the highest concentration of the base metals present in the copper sulfide minerals. The copper sulfide minerals for the high iron matte contain a significantly higher average Fe and minor Co concentration than minerals for the lower iron mattes.

Table 5.4 reports the minor to trace concentration of PGMs present in the analyzed copper sulfide minerals in relation to iron endpoint.

Table 5.4: The range and average concentration of PGMs present in the copper sulfide minerals acquired through electron probe microanalysis.

Element	5.17% Fe		0.99% Fe		0.15% Fe	
	Range (ppm)	Average (ppm)	Range (ppm)	Average (ppm)	Range (ppm)	Average (ppm)
Pd	797	797	†N.D.	†N.D.	†N.D.	†N.D.
Pt	†N.D.	†N.D.	891-902	897 *(8)	7225	7225
Rh	861-883	872 *(16)	756-1085	921 *(233)	733-941	818 *(89)

* Standard deviations in parenthesis.

† N.D.: Not Detected.

Only nine out of forty three copper sulfide minerals analyzed exhibit trace concentrations of Rh, as evident in Table 5.4. The PGMs of Pt and Pd are present in fewer copper sulfide minerals and iron endpoints. The copper sulfide minerals also seem Ir-, Ru- and Os-poor as no detectable concentrations are present. This lends further support to the findings in Chapter 4 (sub-section 4.2.4.3) that suggest the preferential formation of OsRu-alloy structures.

Discussion

Overall, the concentration of the principal constituents (Cu and S) of the analyzed copper sulfide minerals varies considerably. These variations suggest the partitioning of Ni, Fe and Co into copper sulfide minerals, with resultant non-stoichiometry. This seems to imply that Ni-enriched copper sulfide minerals are a characteristic feature of all three matte systems and, therefore, also converter plant conditions. Page (1982) investigated the mineralogy of slow-cooled, water quenched and rapidly air-cooled flash smelting matte samples and suggested afterwards that the resultant mineral structures crystallized under non-equilibrium operating conditions. According to Tables 5.1 and 5.3, shown previously, there appears to be, on average, more Ni present in copper sulfides than Cu in nickel sulfides.

The corresponding variable concentration of principal Cu and major Ni suggests that mutual solid solubility is relevant. Major Ni partitioning would therefore represent the atomic substitution of principal Cu by Ni. The partitioning of the co-existing base metals and almost negligible Rh was most likely established during the crystallization event of the copper sulfides. It was suggested in Chapter 4 (sub-section 4.2.4.1) that copper sulfide minerals may crystallize early from the molten or parent matte. This would imply that Rh may be the early limited primary PGM to exsolve from the parent matte and to partition into a crystallizing mineral structure.

In addition, Table 5.5 reports the partition coefficient (based on the simple ratio of average concentration) of Fe, Co and Rh between nickel and copper sulfide minerals for the different iron-containing mattes. The average concentrations of Fe, Co and Rh for the different mineral structures were previously reported in Tables 5.1 to 5.4.

Table 5.5: The partition coefficients of Fe, Co and Rh between nickel and copper sulfide minerals for the 5.17%, 0.99% and 0.15% Fe mattes.

Element	5.17% Fe	0.99% Fe	0.15% Fe
	Partition Coefficient	Partition Coefficient	Partition Coefficient
Fe	1.05	0.82	0.69
Co	3.75	2.18	3.00
Rh	1.00	0.94	1.29

* Partition coefficient = average concentration of constituent element in nickel sulfide / average concentration of constituent element in copper sulfide.

Table 5.5 indicates that Fe is preferentially concentrated in copper sulfide minerals for the lower iron mattes and in the nickel sulfide minerals for the high iron matte. Morimoto and Koto (1970) found that Fe readily partitions into natural digenite (Cu_9S_5) structures. The partition coefficient of Co, shown in Table 5.5, suggests that the base metal is preferentially concentrated in the nickel sulfide minerals. No obvious partitioning trend can be concluded for Rh from Table 5.5. Ballhaus et al., (2001) found that the partition coefficient for nickel between monosulfide solid solution and sulfide melt were significantly influenced by the metal/sulfur atomic ratio and temperature. The same authors concluded that the metal/sulfur atomic ratio had little influence on the partition coefficient for PGMs. The influence of the metal/sulfur ratio on the partitioning of base metals and PGMs into nickel and copper sulfide minerals requires further investigation as it is beyond the scope of the current study.

5.2.2. Base Metal Alloy Chemistry

The morphology of the base metal alloy is provided as initial background to the subsequent reporting of the electron probe microanalysis. This is followed by the suggestion of a PGM mineralization mechanism for the base metal alloy.

5.2.2.1. Alloy Morphology

Figure 5.3 provides illustration of the characteristic intimate intergrowth relationship between the nickel sulfide, copper sulfide and base metal alloy, albeit for the 0.15% Fe

matte. The compositional micrograph (obtained using FEG SEM based mixed backscattered and secondary electron signals), shown in Figure 5.3(a), in association with the mineral-specific assemblage mapping, shown in Figure 5.3(b), demonstrates the dominant abundance of heazlewoodite (Hw) or anhedral nickel sulfide minerals, forming a cementing matrix, embedding chalcocite (Cc) or euhedral copper sulfide minerals. The location of the NiCu or base metal alloy can also be associated with the Hw matrix. Moreover, in false color contrast, the marked specificity of the principal constituents of Ni, Cu and S (as previously discussed in sub-sections 5.2.1.1 and 5.2.1.2) as well as Pt, concentrated in the relevant minerals, are shown in Figures 5.3(c) to (f), respectively. Note for example, in Figure 5.3(e), the higher concentration of S in the Hw matrix compared to the lower concentration of S in Cc. This illustration is in good agreement with the differences found in S concentration between the nickel and copper sulfide minerals in sub-sections 5.2.1.1 and 5.2.1.2.

Most intriguing in Figures 5.3(a) and (b) is the NiCu-alloy, enriched in Pt and characterized by cored dendritic-like, subhedral to cubic structures. There can be significant variation in the composition and morphology of the NiCu-alloy, as found in Chapter 4 (sub-section 4.2.4.2). Figure 5.4 provides a comparative examination with respect to various morphologies.

It was commonly observed for the lower iron mattes, as shown in Figure 5.4(a), that many NiCu-alloy morphologies are possible in close proximity upon crystallization. Grain shapes can be described as vein-like or net-like in appearance, as indicated in Figure 5.4(b). The normalized processing of EDX spectrum 1, in Figure 5.4(b), indicates the presence of a NiCu-alloy containing 67.81% Ni, 29.79% Cu, 2.00% S and 0.41% Co. Typical grain shapes with a closer mineralogical resemblance include the more common subhedral, euhedral and even larger cubic morphologies, as shown in Figures 5.4(c) and (d). The most noticeable occurrence of the NiCu-alloy is as large compositionally zoned or cored dendritic-like structures.

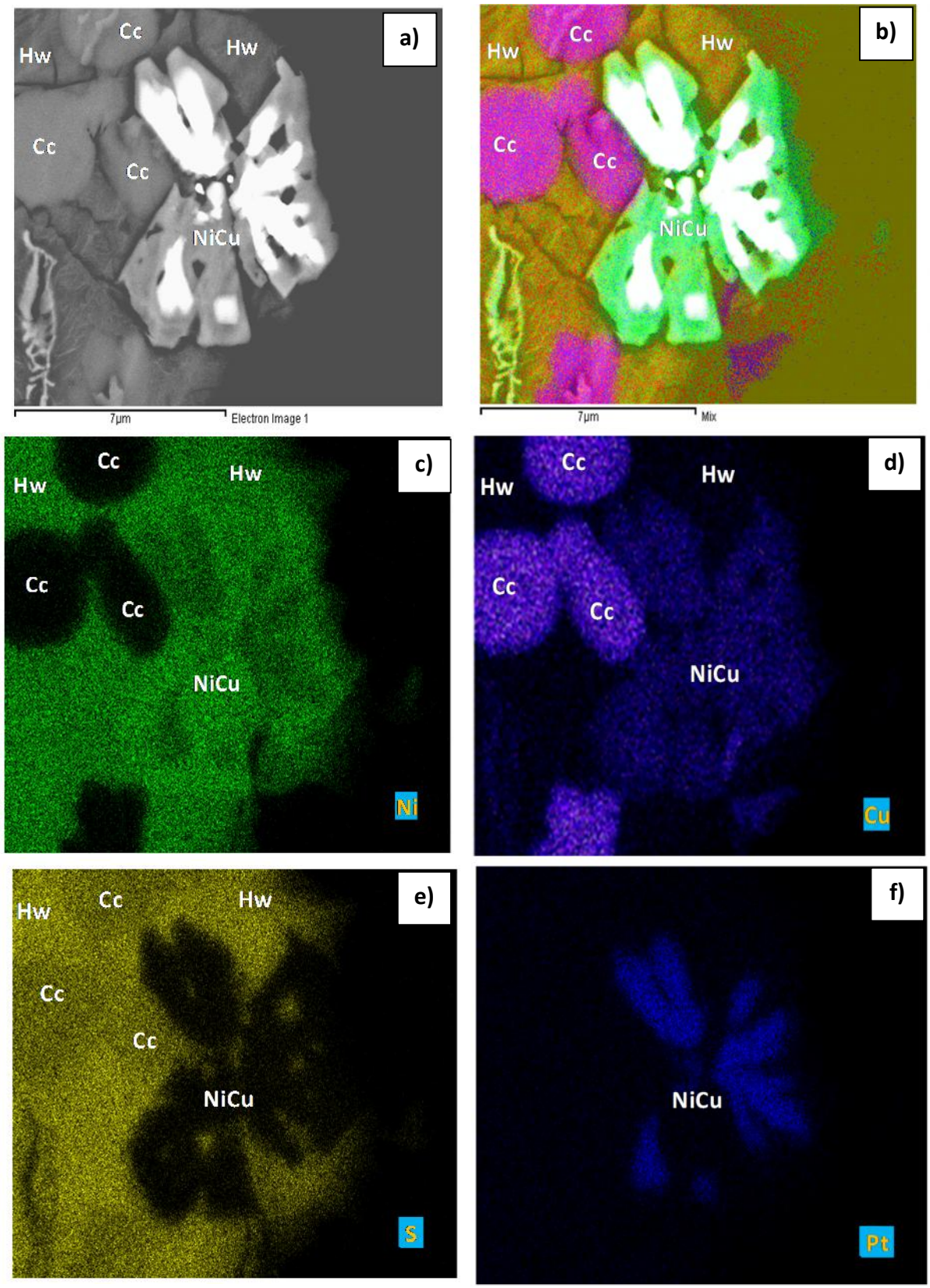

Figure 5.3: FEG SEM based (a) compositional micrograph at 7µm size scale, (b) mineral-specific assemblage mapping at 7µm size scale, and (c-f) mineral-related principal constituent mapping of Ni, Cu, S including Pt with respect to nickel sulfide (Hw), copper sulfide (Cc) and base metal alloy (NiCu).

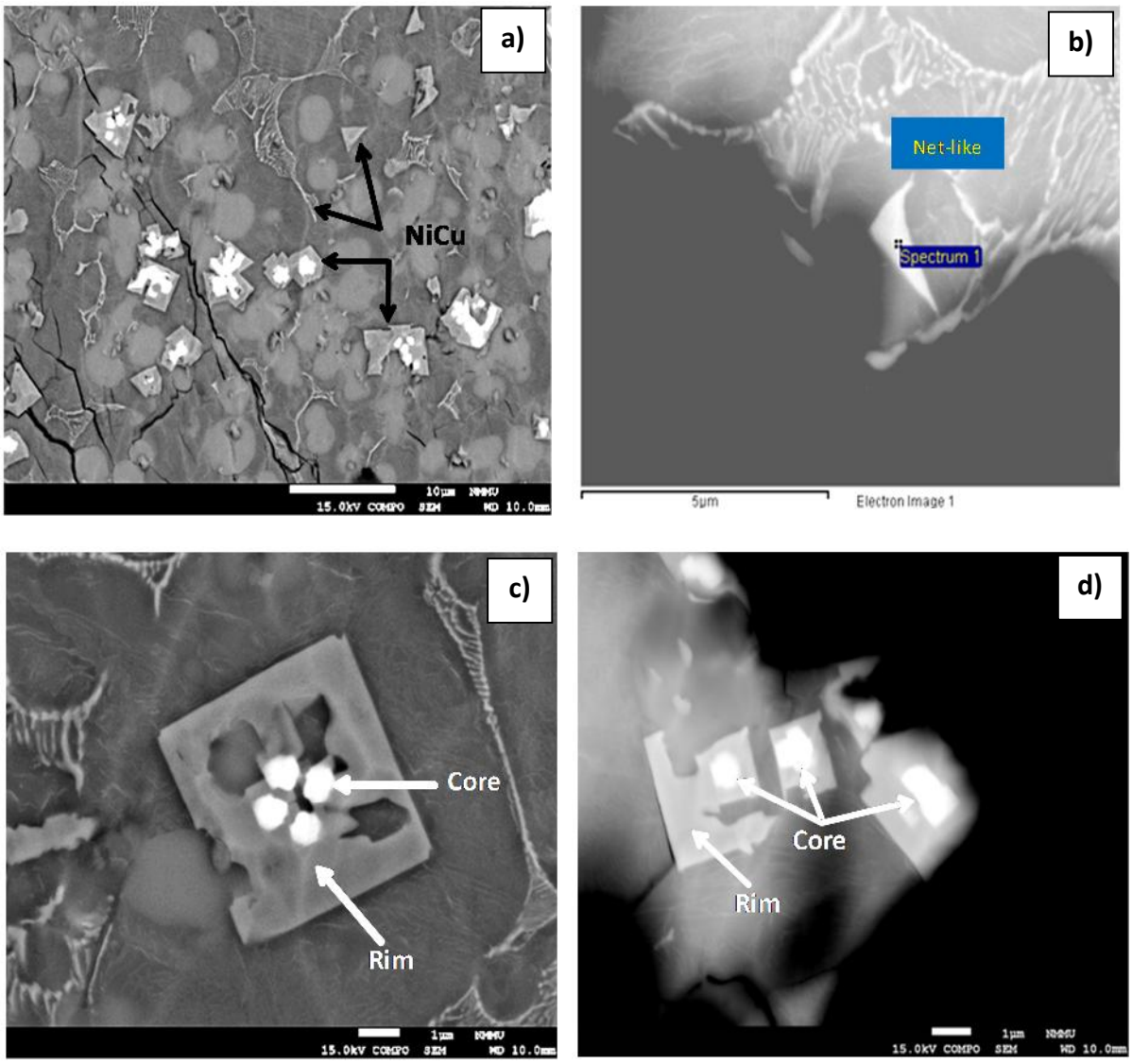

Figure 5.4: Comparative NiCu-alloy assemblages are shown relating to (a) various morphologies at 10µm size scale, (b) net-like morphology at 5µm size scale, (c) cored cubic morphology at 1µm size scale, and (d) cored euhedral to cubic morphologies at 1µm size scale.

5.2.2.2. Alloy Chemistry

Results

Electron probe microanalysis was also performed on 45 matte particle sections, selected with respect to NiCu-alloy and different iron endpoints. The principal mineral chemistry characteristic of the NiCu-alloy for the different iron endpoints is illustrated in Figure 5.5. The principal mineral chemistry is available for assessment in Appendix C (Table C.3).

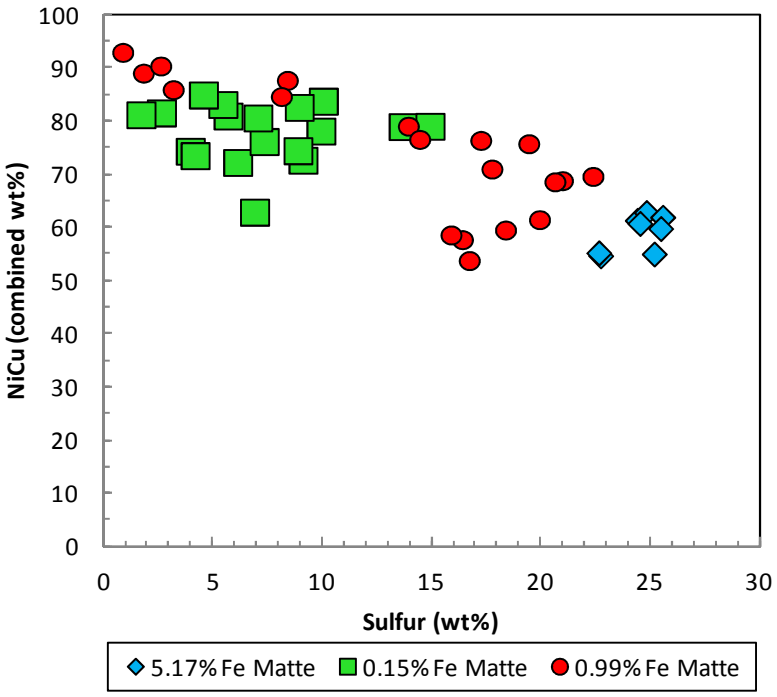

Figure 5.5: The principal mineral chemistry of the NiCu-alloy for the 5.17%, 0.99% and 0.15% Fe mattes acquired through electron probe microanalysis.

The electron probe microanalyses substantiate the presence of Ni-, Cu- and S-rich alloy for all three mattes investigated. The combined Ni and Cu (denoted as NiCu) as well as S concentration are reported in weight%. The principal NiCu concentration range for alloy in the high iron matte averages 58.95%, but varies between 54.68% and 62.82%. The related S concentration varies between 22.69% and 25.61%, with an average of 24.46%. The standard deviation from the average NiCu and S concentrations is 3.41% and 1.15%, respectively. Based on the electron probe microanalysis, the average Ni:Cu ratio for alloy in the high iron matte can be specified as 8.61.

Figure 5.5 illustrates distinct dissimilar NiCu and S concentrations for alloy between all three mattes. The average NiCu concentration for alloy in the 0.99% and 0.15% Fe mattes can be indicated as 74.08% and 77.85%, with standard deviations of 12.24% and 5.47%, respectively. The corresponding S concentrations for these lower iron mattes is, respectively, 13.69% and 7.34% with standard deviations of 7.15% and 3.52%. It is evident from the analyses and illustration in Figure 5.5 that alloy in the 0.99% Fe matte exhibit the highest variation with respect to principal mineral chemistry. This may be due to its bulk matte chemistry, which revealed the highest PGM, moderate Ni and lowest S concentration,

than the 5.17% and 0.15% Fe mattes. This most likely influenced the competition for these elements during crystallization processes which resulted in highly variable principal chemistry. The average Ni:Cu ratio for alloy in the 0.99% and 0.15% Fe mattes can be denoted as 3.49 and 2.26, respectively. It is also evident from the analyses and illustration in Figure 5.5 that the NiCu concentration increases, while the S concentration and Ni:Cu ratio decreases for alloy, in particular, the lower iron mattes. The results are in broad agreement with the SEM EDX based findings in Chapter 4 (sub-section 4.2.4.2).

The major to trace concentration of base metals present in the analyzed NiCu or base metal alloy is reported for the three mattes in Table 5.6.

Table 5.6: The range and average concentration of base metals present in the NiCu-alloy acquired through electron probe microanalysis.

Element	5.17% Fe		0.99% Fe		0.15% Fe	
	Range (wt%)	Average (wt%)	Range (wt%)	Average (wt%)	Range (wt%)	Average (wt%)
Fe	3.87-7.11	5.12 *(0.95)	0.08-2.67	1.09 *(1.03)	0.12-0.24	0.17 *(0.04)
Co	0.74-0.99	0.84 *(0.09)	0.08-0.70	0.36 *(0.25)	0.25-0.69	0.53 *(0.10)
Pb	0.18-1.71	0.47 *(0.56)	0.13-1.17	0.34 *(0.41)	0.16-0.95	0.24 *(0.18)

* Standard deviations in parenthesis.

The base metals (Fe and Co) are present in major, minor and trace concentrations for all the NiCu-alloy analyzed. The base metal of Pb is present in minor concentration in more than half of the NiCu-alloy analyzed. Table 5.6 reports the highest Fe concentration of the base metals present in the NiCu-alloy. Moreover, the NiCu-alloy for the high iron matte contains a notably higher average Fe and minor Pb concentration than the alloy for the lower iron mattes. No apparent concentration trend for Co can be concluded from Table 5.6.

Table 5.7 reports the major to trace concentration of PGMs present in the analyzed NiCu-alloy in relation to iron endpoint.

Table 5.7: The range and average concentration of PGMs present in the NiCu-alloy obtained through electron probe microanalysis.

Element	5.17% Fe		0.99% Fe		0.15% Fe	
	Range (wt%)	Average (wt%)	Range (wt%)	Average (wt%)	Range (wt%)	Average (wt%)
Pd	0.12-0.29	0.18 *(0.05)	0.07-0.67	0.32 *(0.18)	0.20-0.73	0.37 *(0.13)
Pt	3.21-10.80	6.84 *(2.83)	0.11-17.02	4.99 *(6.53)	1.16-18.24	8.85 *(5.74)
Rh	0.07-0.18	0.12 *(0.03)	0.08-0.31	0.19 *(0.06)	0.15-0.29	0.23 *(0.04)
Ru	†N.D.	†N.D.	0.16-0.34	0.25 *(0.13)	0.15-0.29	0.23 *(0.04)
Ir	0.14-1.54	0.55 *(0.45)	0.08-2.82	0.69 *(0.82)	0.09-2.84	0.75 *(0.66)
Os	0.54-11.62	5.68 *(5.59)	1.17-6.45	3.81 *(3.73)	0.08-5.79	1.51 *(2.14)

* Standard deviations in parenthesis.

† N.D.: Not Detected.

All the NiCu-alloy analyzed contains Pd and Pt in major to trace concentrations, as reported in Table 5.7. Platinum evidently displays the highest concentration of PGMs present in the NiCu-alloy. More than half of the NiCu-alloy analyzed contains Rh and Ir in major to trace concentrations. The PGMs of Os and Ru are present in less than half of the NiCu-alloy analyzed, but in relative high concentrations. It is interesting to find these PGMs sporadically present in the NiCu-alloy, despite the demonstrated tendency of Os and Ru to form discrete alloy. It is evident from Table 5.7 that the Pd, Rh and Ir concentration increases for NiCu-alloy as a function of lowering the iron endpoint. This is conversely true for the Os concentration trend. The concentration trend for Pt and Ru is not obvious from Table 5.7.

Figure 5.6 considers specifically the Pt concentration in relation to the NiCu concentration for base metal alloy in the different mattes. The Pt concentration is also included in the principal mineral chemistry for the NiCu-alloy in Appendix C (Table C.3).

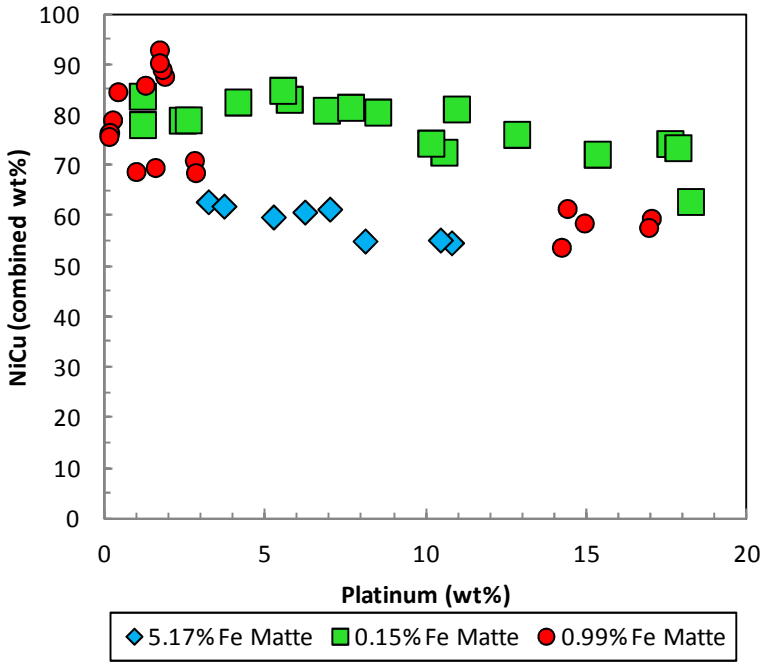

Figure 5.6: Platinum concentration in relation to the combined nickel and copper (NiCu) concentration for base metal alloy in the 5.17%, 0.99% and 0.15% Fe mattes.

Note that the standard deviation from the average NiCu and Pt concentration is reported on page 92 and in Table 5.7, respectively. The trend in Figure 5.6 notably suggests an increase in Pt concentration with a decrease in NiCu concentration. Mineralogical examinations in Chapter 4 (sub-section 4.2.4.2) and sub-section 5.2.2.1 in this chapter, in particular, reveal that the decrease in the NiCu concentration can be associated with the depletion of nickel (less Ni in alloy). In addition, the lower Ni:Cu ratios previously reported in this section for the 0.99% and 0.15% Fe mattes are characteristic of an increase in the Cu concentration.

Discussion

The S concentration for NiCu-alloy appears to be a strong function of the total base metals and PGMs incorporated in the microstructure. The variable concentration of principal Ni, Cu as well as Pt, suggest that mutual solid solubility may also be relevant. The solid-solubility of Ni, Cu and Pt therefore warrants consideration and will be examined in the following sub-section. There is hardly any data available in the open literature relating the partitioning of base metals and more specifically PGMs into NiCu-alloy to the iron endpoint attained. Table 5.8 reports the partition coefficient of the relevant base metals and PGMs between the NiCu-alloy and nickel sulfide minerals for the different iron containing mattes. The average

concentration of the base metals and PGMs for the different minerals was previously reported in Tables 5.1, 5.2, 5.6 and 5.7.

Table 5.8: The partition coefficients of base metals and PGMs between NiCu-alloy and nickel sulfide minerals for the 5.17%, 0.99% and 0.15% Fe mattes.

Element	5.17% Fe	0.99% Fe	0.15% Fe
	Partition Coefficient	Partition Coefficient	Partition Coefficient
Fe	0.93	1.31	1.89
Co	0.80	0.75	1.10
Pb	3.13	1.89	1.14
Pd	1.05	2.68	2.20
Pt	47.50	38.89	43.45
Rh	1.37	2.20	2.18
Ir	5.14	6.98	7.43

* Partition coefficient = average concentration of constituent element in NiCu-alloy / average concentration of constituent element in nickel sulfide.

The partition coefficients of Pd, Pt, Rh and Ir in Table 5.8 suggest that these PGMs would preferentially partition into NiCu-alloy. This confirms that NiCu-alloy is the prime collector of PGM during cooling and solidification of the parent matte. The marked specificity of Pt for NiCu-alloy is demonstrated by a maximum concentration of 18.24%, reported previously in Table 5.7, for the lowest iron matte. The partitioning of the concomitant base metals and PGMs (in particularly Pt) probably occurred during the crystallization event of the NiCu-alloy.

5.2.2.3. Platinum-Group Metal Mineralization

Results

A further relevant investigation includes the electron probe microanalysis of a specifically larger dendritic-like NiCu-alloy similar to that shown previously in Figure 5.3(a). Table 5.9

reports the concentration of the visible core and a number of dendritic lobe-like structures for the NiCu-alloy.

Table 5.9: The electron probe microanalyses with respect to the core and lobes of a dendritic-like NiCu-alloy.

Element	Core (wt%)	Lobe 1 (wt%)	Lobe 2 (wt%)	Lobe 3 (wt%)	Lobe 4 (wt%)
Ni	47.94	60.40	52.68	39.01	41.40
Cu	28.65	13.15	19.77	36.53	30.66
S	6.25	13.56	10.49	10.88	13.17
Pd	0.52	0.45	0.47	0.36	0.45
Pt	4.45	2.15	3.93	2.47	2.41
Rh	0.20	0.24	0.18	0.19	0.21
Ru	0.26	†N.D.	0.21	0.07	0.14
Ir	0.26	0.18	0.28	0.13	0.16
Os	†N.D.	†N.D.	†N.D.	†N.D.	†N.D.

† N.D.: Not Detected.

Table 5.9 indicates that the core and lobes contain detectable PGM concentrations. The core is relatively enriched in Pt and depleted in S compared to the lobes. The core can further be described as having a distinct Ni:Cu ratio of 1.6 while the lobes exhibit a variable Ni:Cu ratio between 1.1 and 4.6. The PGMs present in the NiCu-alloy can either possibly be dissolved or occur as discrete microscopically identifiable inclusions in the host alloy structure. The technique of electron probe microanalysis is not able to discriminate between PGMs in substitutional or interstitial solid-solution and as discrete micro-inclusions. It is important to acquire such knowledge as the resultant microstructure forms an integral part to the downstream processing characteristics of the host NiCu-alloy. The NiCu-alloy was therefore characterized at even higher magnification and resolution using TEM. The bright field TEM micrographs obtained are shown in Figure 5.7.

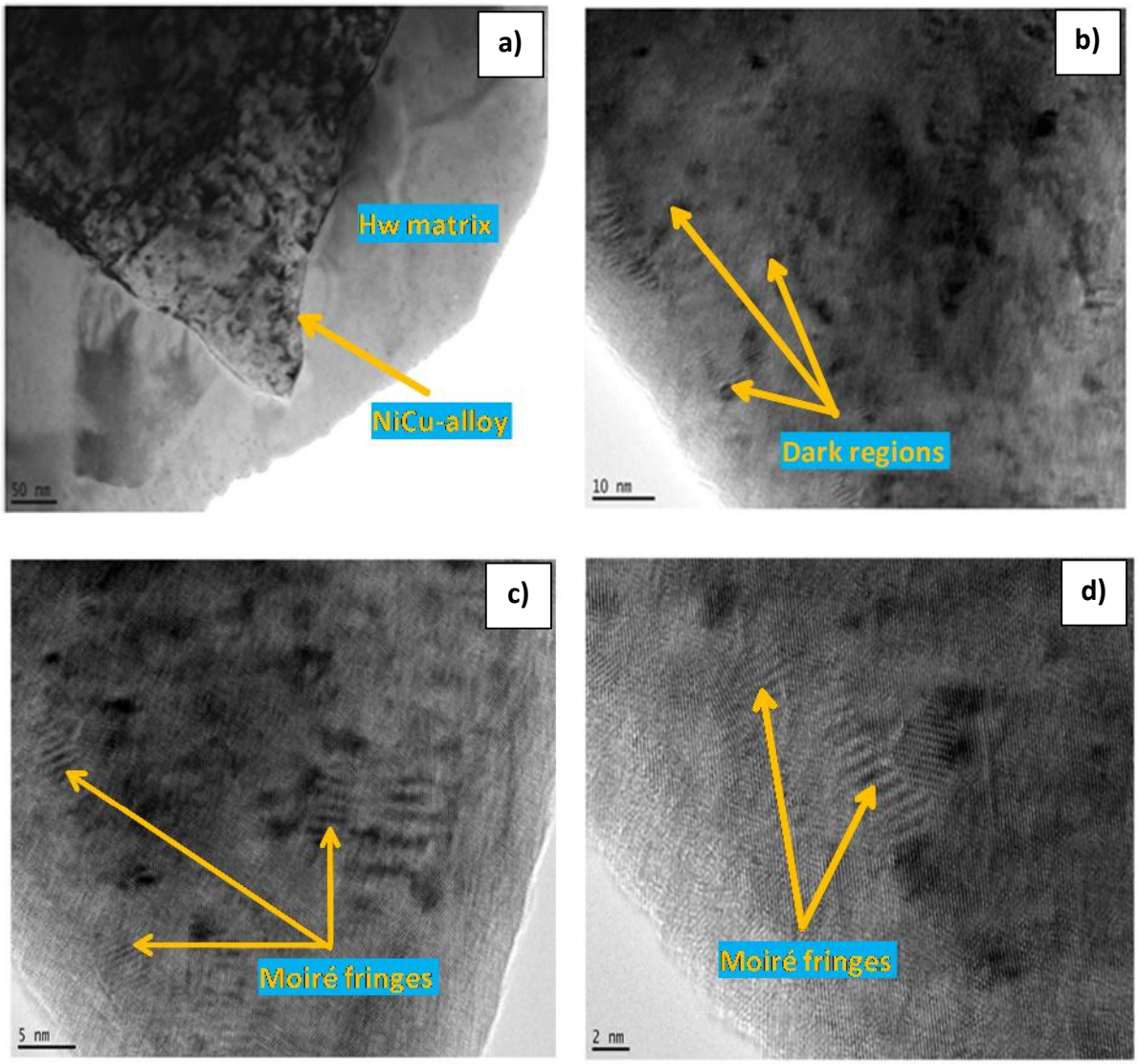

Figure 5.7: Bright field TEM micrographs of the same NiCu-alloy with respect to possible PGM characteristics for the (a) structure at 50nm size scale, (b) dark regions at 10nm size scale, (c) moiré fringes at 5nm size scale, and (d) moiré fringes at 2nm size scale.

Figure 5.7(a) shows a bright field TEM micrograph of the NiCu-alloy structure set in the Hw matrix. The dark regions present in the alloy structure, as illustrated in Figures 5.7(a) to (d), are probably due to lattice defects. An EDX point analysis of the dark regions did not reveal a higher concentration of PGMs present within these regions. Moreover, it proved difficult to obtain accurate compositional information from the dark regions due to probe diameter limitations. Moiré fringes are also present in the bright field micrographs and particularly visible at 5nm and 2nm size scales in Figures 5.7(c) and (d), respectively. This is possibly due to surface oxidation of the alloy structure. In general, no direct evidence for the presence of

distinct PGM-inclusions or precipitates within the NiCu-alloy was found. According to Hume-Rothery (1969), solid-solubility of a metal in another occurs if the atomic radii of the relevant metals are dissimilar by less than 15%. The atomic radii of Ni, Cu and Pt are well established at 1.24Å, 1.28Å and 1.38Å, respectively. The relative difference of the atomic radii is less than 15%. It is therefore not unreasonable to expect Pt to be completely miscible in the NiCu-alloy structure. The PGMs are therefore most likely incorporated within the NiCu-alloy in solid-solution.

Discussion

Schouwstra (2000) proposed a Pt and Pd mineralization mechanism for PGM-containing alloy within a slow-cooled ingot. The proposed mineralization mechanism is based on practical mineralogical observations and not entirely understood. In particular, there are conflicting views as to why and how Pt partitioning actually occurs from the parent sulfide matte into the crystallizing alloy. The most reasonable explanation for why Pt partitioning occurs is that the surface energy of its nuclei is lower when in contact with an alloy interface (Porter and Easterling, 1992). This would therefore create a driving force that allows for the movement of Pt atoms from the parent sulfide matte *via* an alloy/matte interface into the crystallizing alloy structure. This, however, requires further investigation.

The information, obtained mostly from this chapter, is used to derive an understanding of the PGM mineralization mechanism for NiCu-alloy with respect to fast-cooling. Despite variable alloy composition and morphology, the broad mineralogical equivalence suggests a similar mechanism is responsible for PGM mineralization (Rubin, 1991). The crystallization of primary alloy crystal is possibly dominated by the formation of minuscule NiCu nuclei, which act as a site for continuing chemical transformation and growth. The transfer of atoms may be enhanced by low energy interfaces and complete miscibility, specifically between Ni, Cu and Pt.

If an alloy crystal remains in interfacial contact with the parent sulfide matte, but relatively rapid crystallization (related to fast-cooling) does not allow complete exchange between the matte and crystallizing alloy, the effect will be the formation of delicate vein-like exsolution structures, as shown in Figure 5.8.

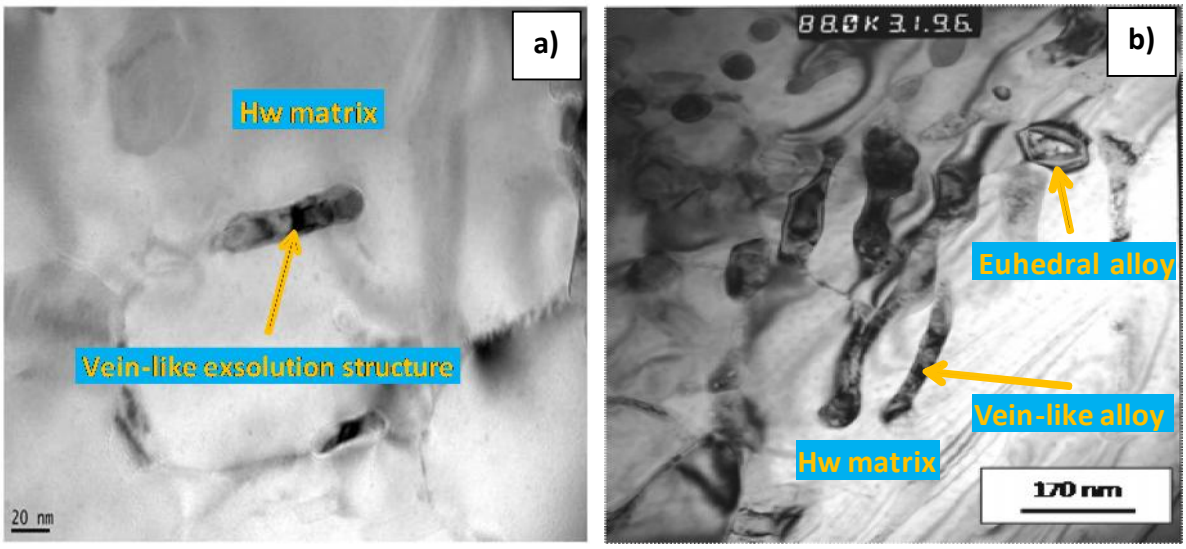

Figure 5.8: High resolution bright field TEM micrographs of (a) a vein-like exsolution structure at 20nm size scale and (b) primary crystallized alloy structures at 170nm size scale.

The vein-like exsolution structure in Figure 5.8(a) is approximately 80nm in length, 20nm wide, appears to be compositionally zoned and set in the Hw matrix. Vein-like microstructures are therefore evidence of fast-cooling, whereas other subsequent morphologies could have formed by a slower or uneven cooling rate. The normalized processing of EDX spectra for the primary crystallized vein and more euhedral-like alloy structures, as shown in Figure 5.8(b), confirms the presence of NiCu-alloy containing 69.3% Ni, 21.6% Cu, 6.4% S, 2.0% Pt and 66.3% Ni, 25.1% Cu, 4.4% S, respectively. Vein-like alloy structures will also react continuously with the parent sulfide matte to produce more subhedral to euhedral alloy crystals while collecting PGMs.

It is expected that faster cooling rates would permit kinetic factors to have a dominant influence in determining alloy microstructure (Porter and Easterling, 1992). A diffusion process most likely ensures the adjustment of elemental chemistry as a function of cooling temperature. It is further anticipated that an alloy crystal would grow in the direction of the heat dissipated. As the initial alloy assemblage progressively grows, the parent sulfide matte becomes increasingly Cu- and PGM-rich. This would allow for the gradual transfer of Cu and PGM atoms from the parent sulfide matte to the crystallizing alloy structure. Prior mineralogical observations suggest the simultaneous depletion of nickel in the alloy. Schouwstra (2000) also found that variable alloy composition is most likely a result of Pt substituting for Ni in the alloy structure. The resulting NiCu-alloy develops a Cu- and Pt-rich

core and an outer rim being more Ni- and S-rich. Following progressive Pt diffusion, if available, the core develops a dendritic-like structure with subsequent lower Cu and Pt concentrations.

5.2.3. 3D Matte Microstructure

The application of mineralogy to the analysis of Ni-PGM containing converter matte was thus far based on 2D in-plane projections of 3D mineral structures. The specialist, and complimentary, technique of TEM in arrangement with recent developments in FIB SEM tomography allowed for the innovative 3D visualization and analysis of solidified converter matte microstructure with respect to the lowest iron-containing matte. These specialist techniques are described in Chapter 3 (sub-sections 3.5.3 and 3.5.5).

5.2.3.1. TEM Analysis of Lamella

Results

The selected site of interest (SOI), central to this examination, was previously shown in Figure 3.4(a) of Chapter 3. The SOI is characterized by a bright PGM and dendritic-like structures. Figure 5.9 provides 2D in-plane imaging and analysis of the prepared lamella (section along the selected SOI) using both the STEM and EDX attachments.

Figure 5.9(a), in particular, provides illustration of the distribution and morphology of minerals present along the section to an approximate depth of 4µm. The section seems dominated by a morphologically indistinguishable and underlying nickel sulfide microstructure. The PGM structure, previously observed in Figure 3.4(a), extends within the nickel sulfide microstructure in Figure 5.9(a) and EDX analyses reveal the presence of an Os-dominant core along with a lower concentration transition-zone and rim. The size of the Os-dominant mineral structure in Figure 5.9(a) is estimated as just below 1µm in the elongated x- and y-directions. The EDX analyses indicate the presence of a smaller Pt-dominant core directly below the Os-dominant mineral structure in Figure 5.9(a). Noticeable dendritic-like structures appear to extend from the Pt-core and can be as wide as 2µm while located relatively deep within the nickel sulfide microstructure.

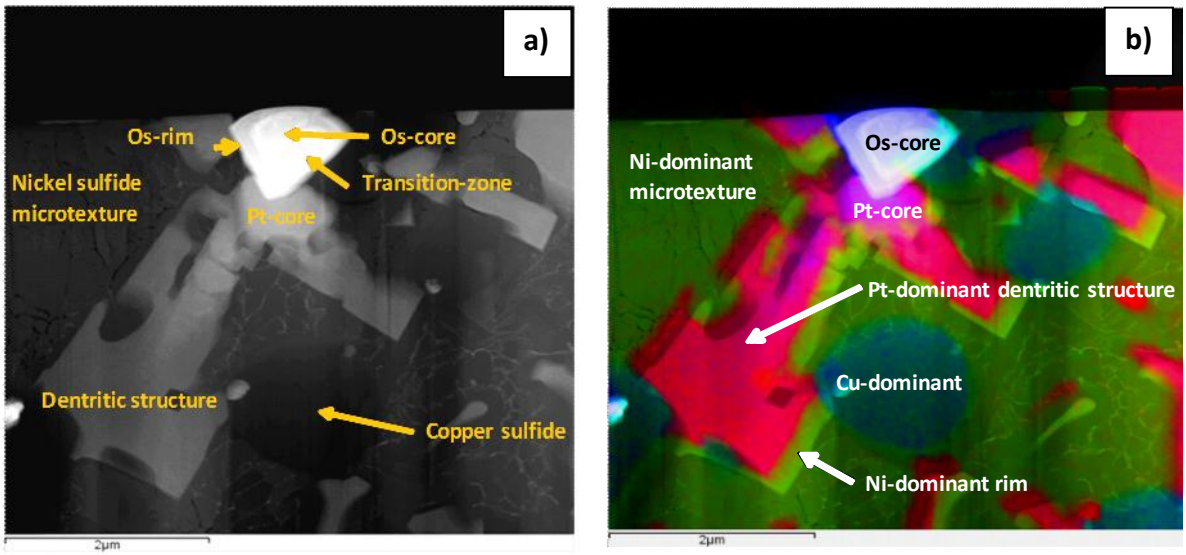

Figure 5.9: STEM and EDX based micrographs of the prepared lamella showing the (a) mineral distribution and morphology and (b) mineral element mapping at 2 µm size scales, respectively.

The EDX analyses further reveal the presence of well-rounded copper sulfide minerals in Figure 5.9(a). The most rounded copper sulfide mineral exhibits a diameter close to 1µm and is also located deeper within the nickel sulfide microstructure. The boundary of the copper sulfide mineral and the nickel sulfide microstructure appears reasonably well-defined and not complexly intergrown.

Figure 5.9(b) provides illustration of mineral element mapping to aid specifically with determination of predominant element distribution in dendritic-like structures. False red color mapping, in Figure 5.9(b), illustrates the distribution of predominantly Pt within the larger inner zones of dendritic-like structures. In contrast, the false lighter green color mapping in the same figure illustrates the distribution of predominantly Ni within outer rims of dendritic-like structures. In addition, false blue and darker green color mapping illustrates the distribution of predominantly Cu and Ni within copper sulfide minerals and the nickel sulfide microstructure, respectively.

Discussion

The prior 2D in-plane and current section analyses signify that mineral structures are geometrically arranged within the underlying nickel sulfide microstructure at mostly dissimilar sizes. The 2D to section associations for the Os-dominant structure, in the previous Figures 3.4(a) and 5.9(a), is estimated at 1 x 1.5µm to 1 x 1µm, respectively. The

copper sulfide mineral along the section, although not observable in prior 2D analysis, may have a true diameter close to 1µm. It is possible, therefore, to provide estimation of the size that matte particles must be ground in order to achieve liberation of the osmium and copper sulfide mineral structures. In addition, it would not seem practical to assign a single size to the nickel sulfide microstructure.

5.2.3.2. Tomography and Analysis

Tomography reconstruction and rendering of the rectangular volume, as shown in Figure 3.6(a) of Chapter 3, allows for color and grayscale based 3D visualization and analyses of the mineral structures, as illustrated in Figure 5.10.

Figure 5.10(a) illustrates that dissimilar mineral morphology in arrangement with mineral surface color coding permits the discrimination between 3D copper sulfide and NiCu-alloy. Copper sulfide within the rectangular volume is represented by regular sized, well-shaped and blue surface color coded structures. In contrast, the NiCu-alloy displays different color coding. The reconstructed nickel sulfide microstructure is projected throughout the rectangular volume and represented by excluding surface color coded information. Figure 5.10(b) illustrates a higher fidelity 3D reconstruction of a copper sulfide mineral present within the rectangular volume. The color based 3D visualization in Figure 5.10(b) confirms the euhedral morphology associated with copper sulfide minerals. The copper sulfide mineral also exhibits a diameter of approximately 3µm.

Figure 5.10(c) illustrates 3D NiCu-alloy extracted from the rectangular volume for improved visualization and analyses. The color based 3D visualization assists in distinguishing between morphological forms and additionally provides an indication of volume distribution within the rectangular volume. Moreover, gray levels are integrated into reconstruction and Figure 5.10(d) allows for grayscale based 3D visualization of identical alloy structures. The difference in gray level signifies compositional zones within alloy structures. It is difficult inspecting aspects of variable morphology and composition within 3D alloy structures at the mineralogical scale in Figures 5.10(c) and (d).

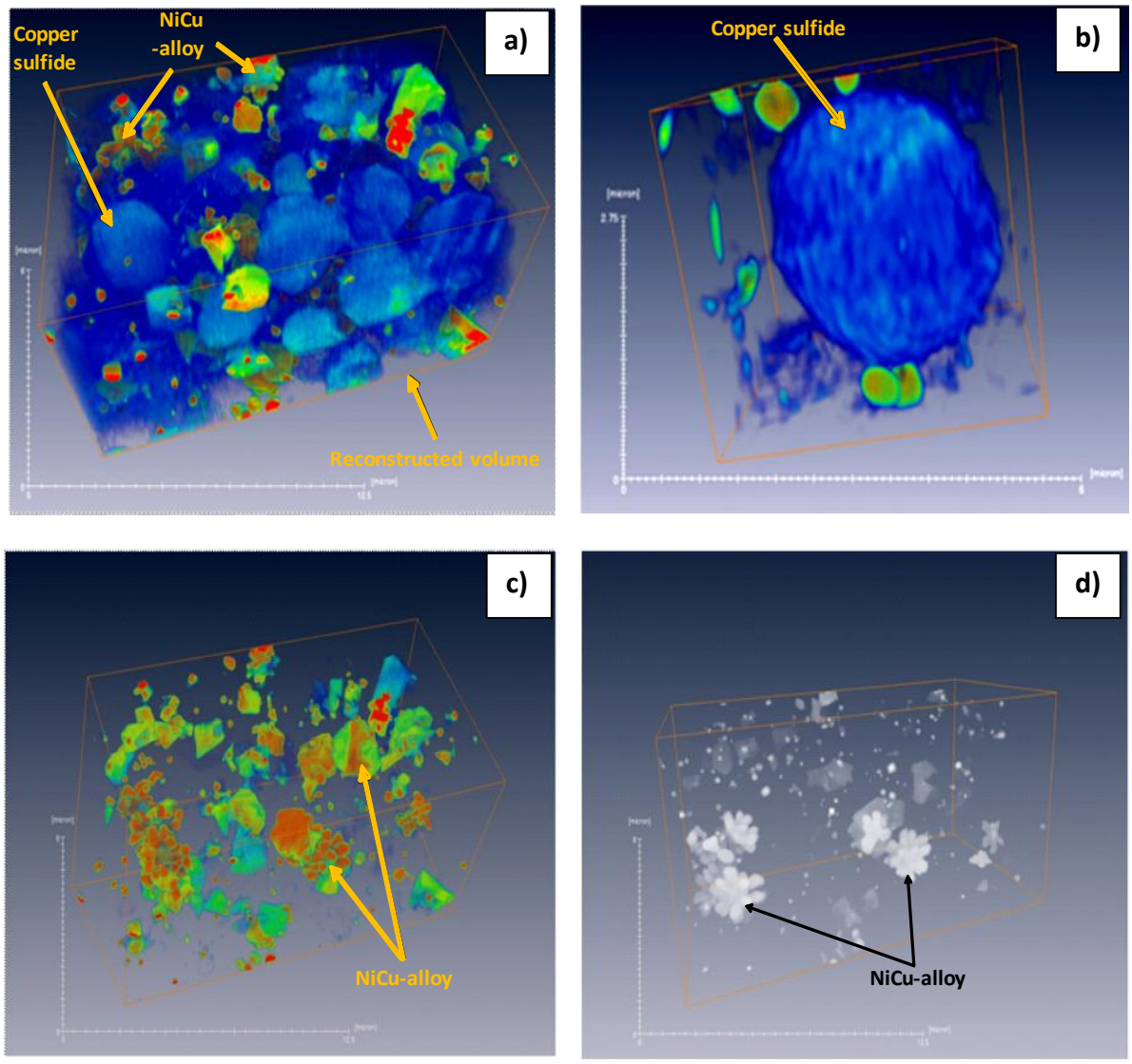

Figure 5.10: Tomograms showing the (a) 3D mineral structures present within the rectangular volume at 12.5 x 6µm size scales, (b) 3D copper sulfide mineral at 6 x 2.75µm size scales, (c) 3D NiCu-alloy at 12.5 x 6µm size scales, and (d) grayscale based 3D NiCu-alloy at 12.5 x 6µm size scales.

Figure 5.11 presents color and grayscale based 3D visualization of corresponding NiCu-alloy extracted from volume distributions in Figures 5.10(c) and (d). The 3D visualization in Figure 5.11(a) represents a notably small alloy structure with surface color coding providing illustration of cubic face formation. The size of the cubic faces is estimated at 1.5 x 1µm. The 3D visualization is therefore effective to assign a cubic morphology to such an alloy structure. The corresponding grayscale based 3D visualization in Figure 5.11(b) illustrates compositional zones correlating to the presence of a bright Pt-dominant core and a darker

Ni-dominant rim. The Pt-core appears small and exhibits a diameter of approximately 0.5µm.

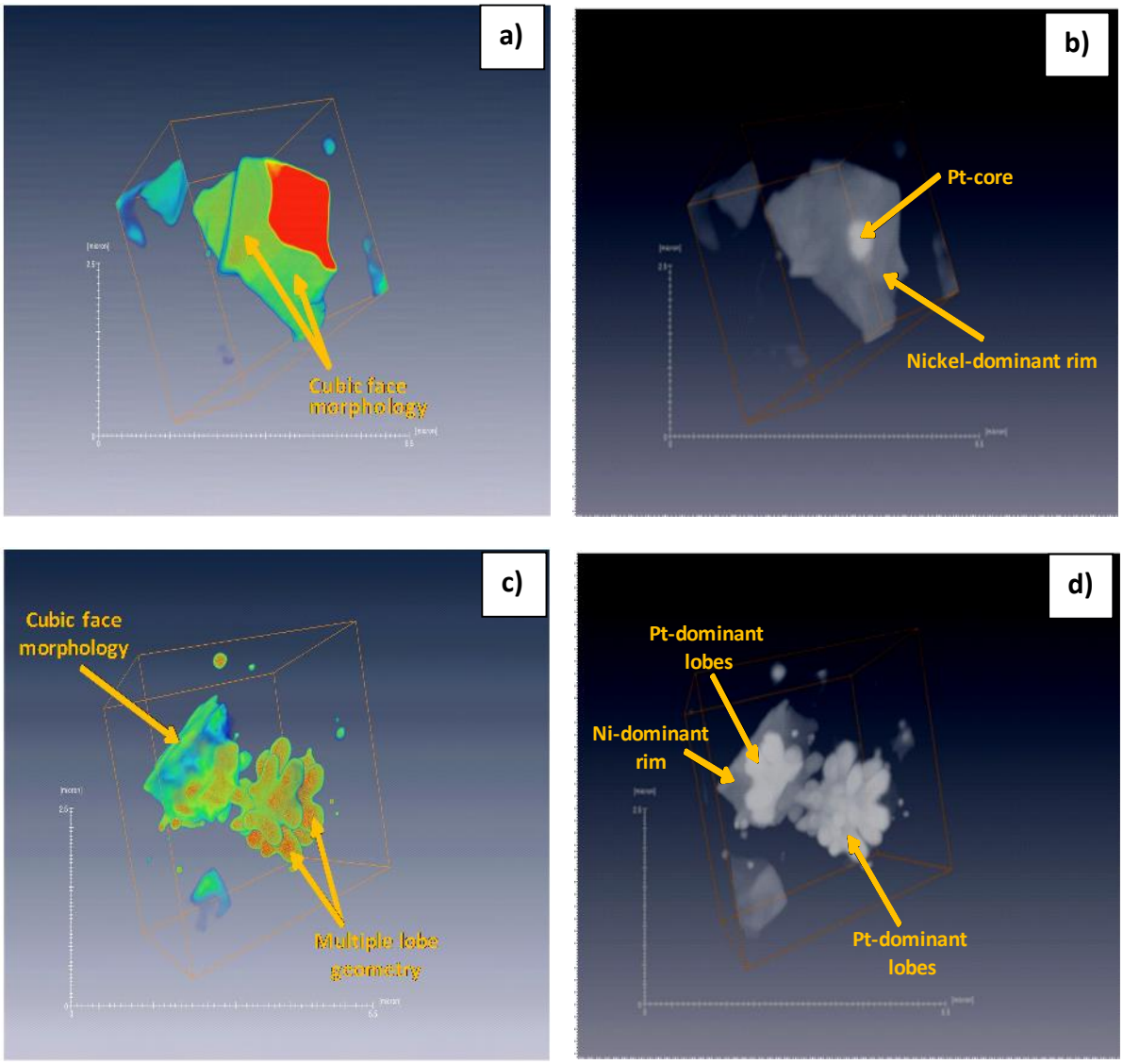

Figure 5.11: 3D visualization of selected NiCu-alloy structures with respect to (a) color based cubic morphology at 6.5 x 2.5µm size scales, (b) corresponding grayscale based compositional zones at 6.5 x 2.5µm size scale, (c) color based cubic morphology and multi-lobe geometry at 5.5 x 2.5µm size scale, and (d) corresponding grayscale based compositional zones at 5.5 x 2.5µm size scales.

Figure 5.11(c) represents a NiCu-alloy with some face formation and possibly of the cubic morphological variety. An alloy structure with a seemingly multi-lobe geometrical arrangement is also noted in Figure 5.11(c). It will be difficult to assign a single size to such an alloy structure. The grayscale based 3D visualization in Figure 5.11(d) illustrates the dominant presence of bright Pt-dominant lobes corresponding to the multi-lobe geometrical

arrangement and cubic morphology in Figure 5.11(c). Previous analyses suggest that these 3D Pt-dominant lobes correspond to the 2D Pt-dominant inner zones of the dendritic-like structures illustrated in Figure 5.9(b) previously. It is relatively difficult to examine aspects of morphology of Pt-dominant lobes at the mineralogical scales in Figure 5.11.

Figure 5.12 allows for color based 3D visualization and analysis of Pt-dominant lobes extracted from a single dendritic-like NiCu-alloy.

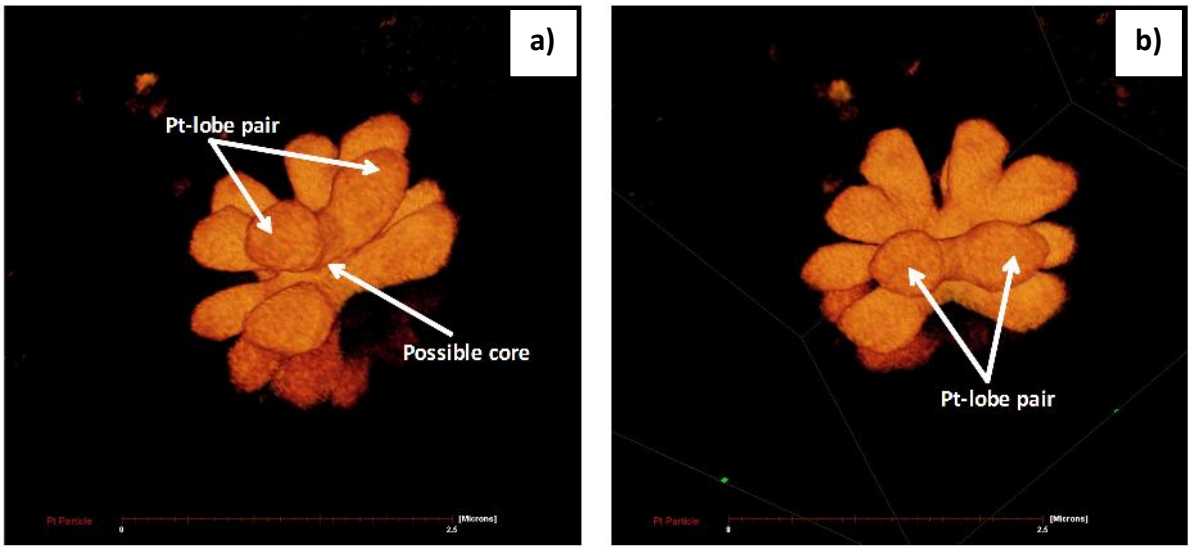

Figure 5.12: Color based 3D visualization of identical Pt-dominant lobes extracted from a single dendritic-like NiCu-alloy showing (a) spatial orientation 1 and (b) spatial orientation 2 at 2.5µm size scale.

Figures 5.12(a) and (b) illustrate high-fidelity reconstruction of identical Pt-dominant lobes extracted specifically from a Ni-dominant rim within a dendritic-like NiCu-alloy. The Pt-lobes appear developed and may be described as having a common core from which pairs of lobes extend towards a similar direction. The description is comparable to the 2D dendritic-like structure development shown previously in Figure 5.9. There are seemingly six pairs of lobes in Figure 5.12, with a single lobe exhibiting an estimated length and thickness of 2µm and 0.6µm. It is notable that the estimated thickness of developed lobes in Figure 5.12, appears in good agreement with the estimated diameter measurements of the less developed Pt-core, shown previously in Figure 5.11(b).

Measurements include the distribution of mineral structures within the reconstructed rectangular volume. The results are reported in Table 5.10 below.

Table 5.10: The volumetric distribution of mineral structures present within the 3D reconstructed rectangular volume.

Mineral Structure	**Volumetric Distribution (%)**
Nickel sulfide microstructure	77.7
Copper sulfide	12.1
NiCu-alloy (with Pt-core and lobes)	9.6
Pt-core and lobes	0.6

The results are reported in decreasing order in Table 5.10. It is evident from Table 5.10 that the reconstructed volume is dominated by the presence of the nickel sulfide microstructure. This is followed by the significantly lower volumetric distribution of copper sulfide and NiCu-alloy. These results are in broad agreement with those previously acquired using quantitative XRD reported in Table 4.4 (sub-section 4.2.3 of Chapter 4). Moreover, it was possible to measure the volumetric distribution of the combined Pt-dominant cores and lobes, which is reported as 0.6% in Table 5.10. The volumetric distribution of the Ni-dominant rims can be deduced and therefore contributes 9.0% of the reconstructed volume.

This measurement was not previously possible and further underscores how fine-scaled Pt-dominant features are located within Ni-dominant rims and therefore of substantial economic importance to downstream metallurgical processes. It is reasonable to suggest that the downstream metallurgical properties of such a rectangular volume are dependent on the volumetric distribution, morphology, composition and geometrical arrangement of the mineral structures present. It is therefore important to consider the widest possible application of both the 2D analyses and 3D insights gained to the integrated metallurgical processing of solidified nickel converter matte. Movies of 3D mineral structures are available for download (and therefore viewing) from a link in Appendix C.

5.3. Key Findings

Electron probe microanalysis, in conjunction with 2D and 3D mineralogical examinations relating to specific mineral chemistry, PGM mineralization and 3D visualization for the different iron-containing mattes in this chapter suggest the following key findings:

i. The constituent converter matte minerals of nickel sulfide, copper sulfide and base metal alloy for the different iron-containing mattes are not pure minerals, but include evidence of mineral and iron endpoint specific base metal and PGM heterogeneities, which may impact on its downstream processing;

ii. The mineral chemistry specific to nickel sulfide for the 5.17% Fe matte is characteristic of relatively low principal Ni and high S concentrations, while accommodating, in particular, high Fe and Co partitioning into the primary mineral structure. In contrast, the mineral chemistry of nickel sulfide for the 0.99% and 0.15% Fe mattes reveals higher principal Ni and lower S concentrations, while permitting higher Cu and Pb partitioning into the primary mineral structure. Moreover, the comparatively minor partitioning of PGMs into nickel sulfide minerals is characteristic of all three mattes although at a higher combined concentration for the 0.15% Fe matte;

iii. The mineral chemistry of copper sulfide minerals for the 5.17% Fe matte may be described as relatively low in principal Cu and high in S concentrations, while permitting high Fe and Co partitioning into the primary mineral structure. In comparison, the mineral chemistry of copper sulfide for the 0.99% and 0.15% mattes is characteristic of higher principal Cu and lower S concentrations. All three mattes are also distinctive of major Ni partitioning into the host mineral structure. In addition, the limited partitioning of Rh into copper sulfide minerals is common to all three mattes;

iv. The mineral chemistry of base metal alloy for the high iron-containing matte is characteristic of relatively low principal NiCu and high S concentration, while incorporating relatively high concentrations of Fe, Pb and Os in the host mineral structure. The lower iron-containing mattes, in contrast, display higher principal NiCu and lower S concentrations, while allowing the incorporation of higher concentrations of Pd, Rh and Ir into the mineral structure. The distinct partitioning of major Pt into the base metal alloy is common to all three mattes;

v. It is proposed that the combined effect of bulk chemistry, crystallization sequence, substitutional solid-solution chemical exchange, uneven cooling rates and

direction of heat dissipation may be responsible for the characteristic PGM mineralization of the base metal alloy and manifested by the variety in its composition and morphology; and

vi. Complimentary TEM analysis is specifically effective in providing prior mineral distribution and morphological detail along a 2D section. Innovative tomography reconstruction and rendering are used successfully to permit color and grayscale based 3D visualization of mineral structures within a rectangular volume. High-fidelity 3D reconstructions are produced for complex, fine-scaled dendritic-like Pt-bearing structures.

This chapter has aimed to provide an improved insight into base metal and PGM mineral chemistry as well as the mineralization mechanism of the NiCu-alloy and new developments in 3D converter matte mineral structures. The next chapter is concerned with developing a fundamental understanding of converter matte solidification during which the intricate processes responsible for the characteristic mineral chemistry and mineralogy are described as a function of iron endpoint specific starting composition.

5.4. Relevant Publications

Thyse, E.L., Akdogan, G., Taskinen, P., Eksteen, J.J., 2011. The distribution of metallic elements in granulated nickel converter matte phases. ***Proceedings, Southern African Pyrometallurgy 2011,*** Edited by R.T Jones and P. den Hoed, Southern African Institute of Mining and Metallurgy, Johannesburg, 6 – 9 March 2011, pp. 173 – 184.

Thyse, E.L., Akdogan, G., Olivier, E.J., Neethling, J.H., Taskinen, P., Eksteen, J.J., 2011. Partitioning of PGEs in nickel converter matte phases: Direct observations by electron microscopy and electron probe microanalysis. ***Minerals Engineering,*** Special Issue, Process Mineralogy, Volume 24, Issue 12, pp. 1288-1298.

Thyse, E.L., Akdogan, G., Olivier, E.J., O'Connell, J.H., Neethling, J.H., Taskinen, P., Eksteen J.J., 2013. 3D insights into nickel converter matte phases: Direct observations via TEM and FIB SEM tomography. ***Minerals Engineering,*** Special Issue, Process Mineralogy, Volume 52, pp. 2 - 7.

Chapter 6
UNDERSTANDING CONVERTER MATTE SOLIDIFICATION

6.1. Introduction

Chapters 4 and 5 assessed, in detail, the effect of variable iron endpoint on converter matte mineralogy, and base metal and PGM mineralization, upon fast-cooling of actual production samples. Consequently, several aspects related to converter matte mineralization can, at present, be explained for such Ni-PGM containing matte systems. To this effect some measure of understanding the solidification of liquid or molten converter matte has been achieved, but many details remain unknown. This chapter is therefore concerned with consolidating the prior understanding developed and examining, in detail, the fundamental intricacies of converter matte solidification and processes that occur by referring to equilibrium matte systems of analogous industrial endpoint composition and phase or mineral structures associated with actual fast-cooled mattes.

6.2. Results and Discussion

Molten converted mattes, in the Lonmin context, are complex metallurgical solutions of Ni, Cu, S, Fe, Co and O along with minor to trace concentrations of several other constituent elements, including Pb and PGMs. The following results, acquired through MTDATA based computational thermochemistry, as described in Chapter 3 (section 3.6), permit for the progressive build-up and discussion of relevant liquidus and ternary equilibria, as well as the complex multiphase cooling equilibria of iron endpoint specific industrial matte systems. This is followed by the comparison of calculated equilibria features with corresponding actual fast-cooled phase structures. It should be noted that the term phase is considered more suitable for usage in this chapter compared to the equivalent usage of mineral in the previous two chapters.

6.2.1. Liquidus Equilibria

Results

Figure 6.1 illustrates the calculated liquidus temperature range plotted as isothermal

contours for iron endpoint related Ni-Cu-S pseudo-ternary systems as an approximation of finalized converter matte composition. The Ni and Cu end member components, which assist in defining the system, are mixed with Fe to include the effect of iron endpoint on the calculations. Iron decreases to zero, in Figure 6.1, as the composition and sulfur shift to the pure S-apex.

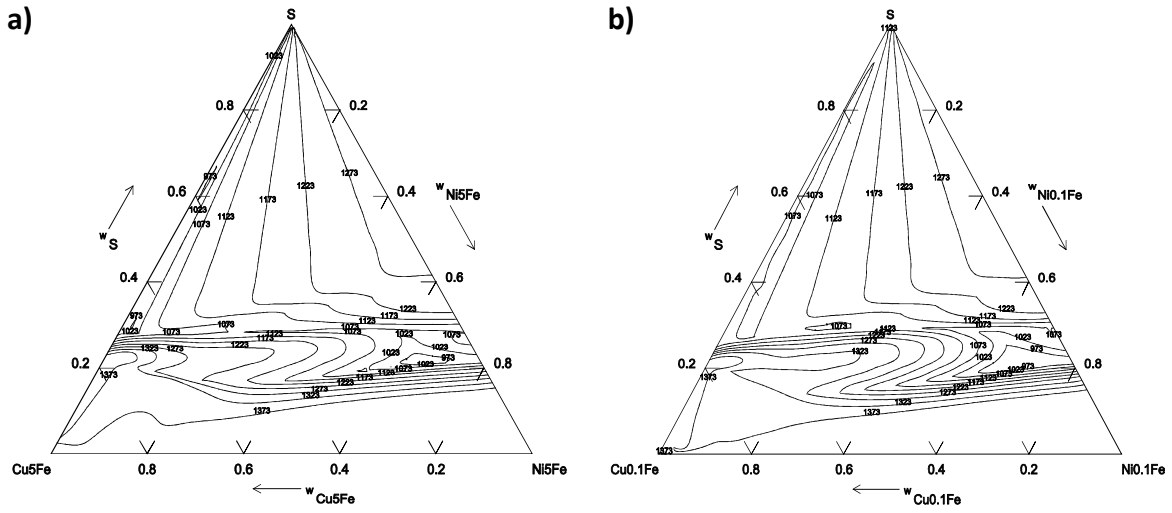

Figure 6.1: Calculated liquidus contour plots set from 1423 K (1150 ^{o}C) to 923 K (650 ^{o}C) with respect to (a) Ni5%Fe-Cu5%Fe-S and (b) Ni0.1%Fe-Cu0.1%Fe-S pseudo-ternary systems.

The liquidus contour plot in Figure 6.1(a) indicates that the liquid phase is stable from 1373 K (1100 ^{o}C) to 973 K (700 ^{o}C). Isothermal contours (annotated by numeric values) fall away from the Ni5Fe and Cu5Fe corners as well as along the upper Ni5Fe-S join. In particular, the direction of falling isothermal contours from the Cu5Fe corner towards a liquidus valley near the lower Ni5Fe-S join should be noted. Figure 6.1(a) also provides an impression of a liquidus valley near the lower Cu5Fe-S join.

Similarly, the examination of the liquidus contour plot in Figure 6.1(b) reveals the stabilization of liquid phase from 1373 K to 973 K and a liquidus valley facing the lower Ni0.1Fe-S join. Figure 6.1(b) also presents an impression of a flatter liquidus valley near the centre of this ternary system. Comparative liquidus equilibria results (although not included in this section) to that presented in Figure 6.1(b) were obtained for the Ni1%Fe-Cu1%Fe-S pseudo-ternary system.

Discussion

The results, in general, can be cautiously applied in showing the effect of pseudo-ternary constitution on the stable liquidus temperature range. The liquid phase has not been stable at the preset lower temperature of 923 K (650 ^{o}C), as considered in Chapter 3 (section 3.6). The liquidus temperature range of all three pseudo-ternary systems is therefore below 973 K but above 923 K. The value of preset temperature intervals may not be small enough to detect the lowest liquidus temperature range for the respective pseudo-ternary systems. The complexity of the pseudo-ternary system is increased and the results are presented and discussed in the following sub-section.

6.2.2. Ternary and Liquid Phase Equilibria

Results

Figure 6.2 illustrates the calculated liquidus temperature range plotted as isothermal contours for the Ni-Cu-S_5%Fe1%Co pseudo-ternary system with superimposed liquid phase starting and solidification circled points and primary phase fields. The Ni, Cu and S end member components are mixed with 5% Fe + 1% Co to include the effect on the calculation of the liquidus temperature range and primary phase fields. The composition of each point within the pseudo-ternary system contains set Fe and Co concentrations.

The liquidus contour plot in Figure 6.2 shows the liquid phase stable from 1648 K (1375 ^{o}C) to 948 K (675 ^{o}C). Note the lowering in the liquidus temperature range for this pseudo-ternary system compared to the results illustrated in Figure 6.1(a) previously. The difference can only be understood in the context of the pseudo-ternary constitution and smaller preset temperature interval, as specified in Chapter 3 (section 3.6). Figure 6.2 also shows the existence of a liquidus valley near the lower Ni-S-rich join, which represents the lowest temperature (948 K) at which the liquid phase can exist.

The starting (circled cross) and solidification (circled) points in Figure 6.2 are plotted based on a corresponding true liquid phase starting composition and calculated liquid phase assays in terms of the components which define the pseudo-ternary system. The liquid phase described within the pseudo-ternary system in Figure 6.2 is oxygen-free and thus the starting composition and calculated assays are re-normalized to 100% without oxygen. The

numerical compositions of the liquid phase at the respective circled points trace out the path the liquid follows as a function of changing Ni, Cu, S, Fe and Co concentrations.

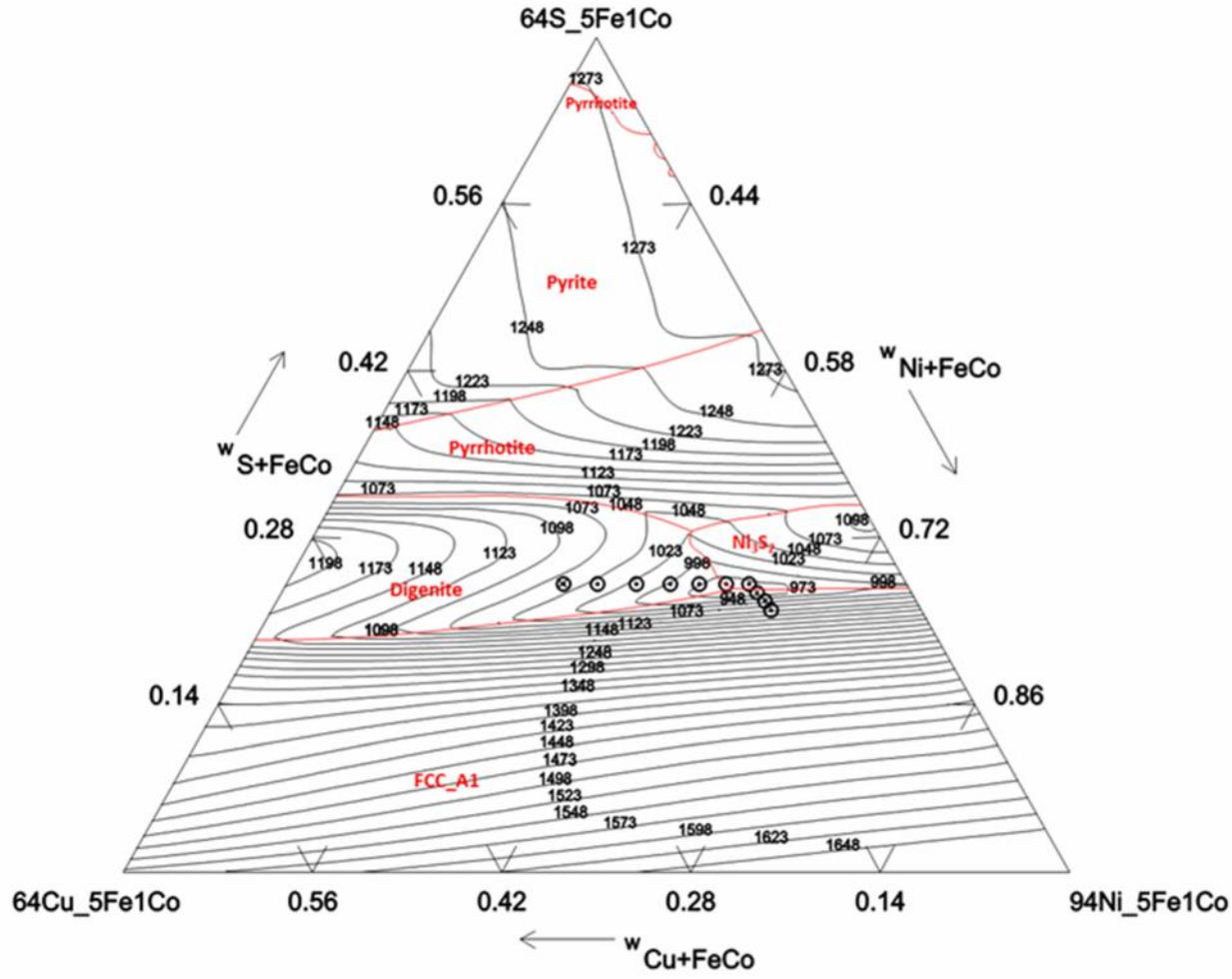

Figure 6.2: Calculated liquidus contour plot set from 1673 K (1400 ^{o}C) to 773 K (500 ^{o}C) with superimposed liquid phase starting and solidification circled points and primary phase fields for the Ni-Cu-S_5%Fe1%Co pseudo-ternary system.

More specifically, the starting composition, as indicated by the circled (cross) point in Figure 6.2 has 5.26% Fe in the liquid phase above liquidus temperature. The exact liquidus temperature is not known, but the calculated assays suggest that it is between 1123 K (850 ^{o}C) and 1098 K (825 ^{o}C). As the liquid phase moves below the liquidus temperature to 973 K (and directly away from the Cu-S-rich join in Figure 6.2), it becomes deficient in Cu and Fe, while being enriched in Ni and Co. No variation in sulfur concentration is calculated between 1123 K and 973 K. The residual liquid phase composition at 948 K (also the lowest liquidus contour within the pseudo-ternary system in Figure 6.2) is as follows: 62.60% Ni, 11.40% Cu,

1.79% Fe, 23.40% S and 0.79% Co. The liquid phase composition subsequently moves away from the liquidus valley. Table 6.1 reports the re-normalized starting compositions and calculated final assays (last liquids) with respect to the relevant pseudo-ternary system and liquidus temperature range.

Table 6.1: Re-normalized true starting compositions and final assays with respect to the relevant pseudo-ternary system and liquidus temperature range.

Liquid Constituent (%)	Ni-Cu-S_5%Fe1%Co		Ni-Cu-S_1%Fe0.5%Co		Ni-Cu-S_0.2%Fe0.3%Co	
	Start (1123K)	Final (898K)	Start (1123K)	Final (873K)	Start (1123K)	Final (873K)
Ni	44.50	64.80	49.10	66.18	50.17	66.22
Cu	25.40	11.10	30.25	12.06	29.90	12.72
S	24.10	21.90	19.25	20.91	19.41	20.63
Fe	5.26	1.45	1.02	0.46	0.15	0.06
Co	0.73	0.78	0.39	0.37	0.36	0.36

The last liquid phase composition with respect to the Ni-Cu-S_5%Fe1%Co pseudo-ternary system, as reported in Table 6.1, and plotted within the pseudo-ternary system in Figure 6.2, trace relatively afar from the liquidus valley. Figure 6.2 also provides the identity of the primary phases. The names are self-explanatory in most cases, except for FCC_A1, which refers to the metalized or alloy phase.

Figure 6.3 illustrates the calculated liquidus temperature range plotted as isothermal contours for the Ni-Cu-S_1%Fe0.5%Co pseudo-ternary system with superimposed liquid phase starting and solidification marked points and primary phase fields. Examination of the liquidus contour plot in Figure 6.3 shows that the liquid phase is stable from 1648 K (1375 ^{o}C) to 898 K (625 ^{o}C). Note the substantial lowering in the liquidus temperature range from 973 K (based on results from a comparable pseudo-ternary system in sub-section 6.2.1 previously) to 898 K. A liquidus valley representing the lowest temperature (898 K) at which the liquid phase can exist for this system is present near the lower Ni-S-rich join.

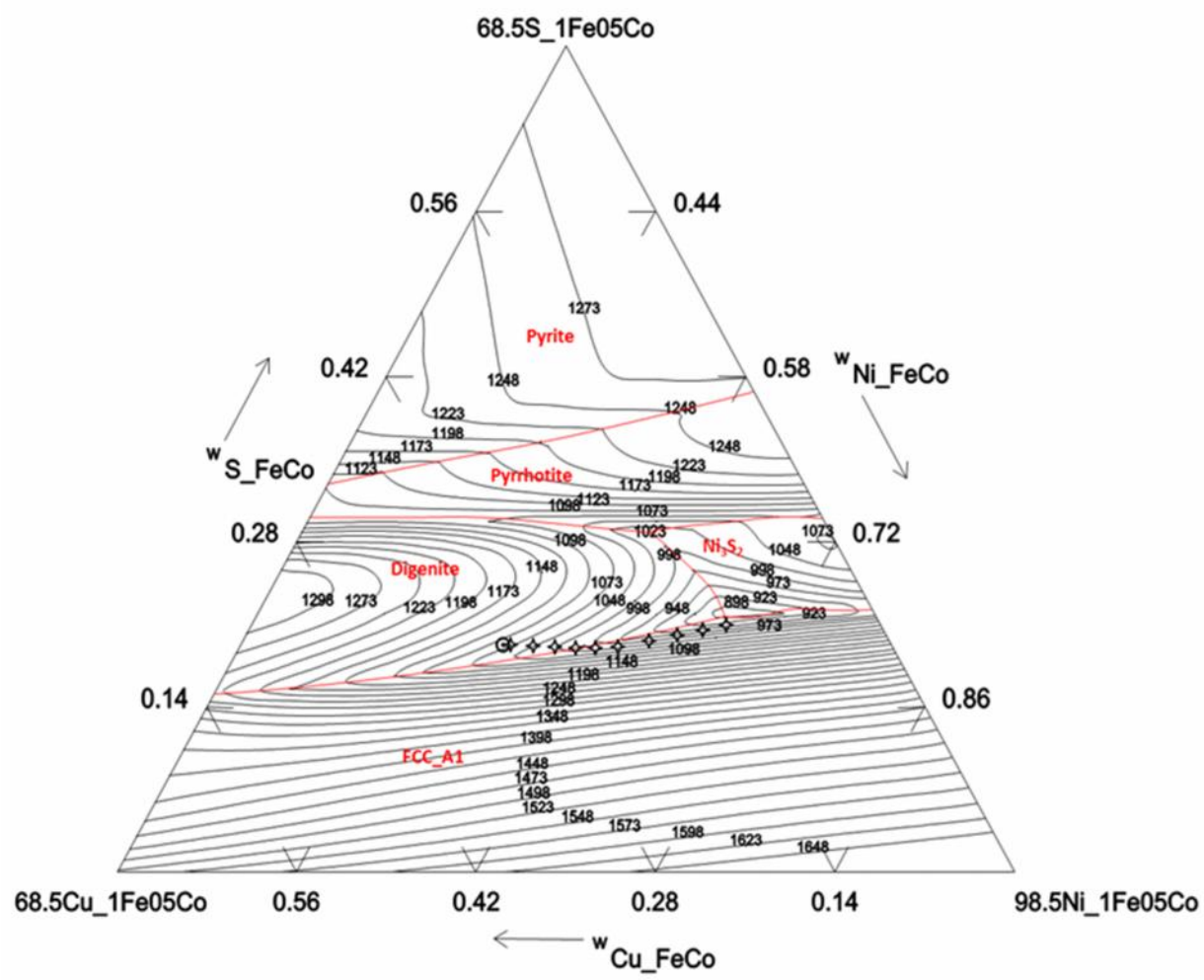

Figure 6.3: Calculated liquidus contour plot set from 1673 K (1400 °C) to 773 K (500 °C) with superimposed liquid phase starting and solidification marked points and primary phase fields for the Ni-Cu-S_1%Fe0.5%Co pseudo-ternary system.

The starting and solidification marked points in Figure 6.3 are similarly plotted based on a true liquid phase starting composition and calculated liquid phase assays with respect to the components which define the pseudo-ternary system. The starting composition, as reported in Table 6.1, and plotted within the pseudo-ternary system in Figure 6.3, has 1.02% Fe in the liquid phase above the liquidus temperature. When the liquid phase moves below the liquidus temperature to 998 K (and directly away from the Cu-S-rich join in Figure 6.3), it becomes deficient in Cu and S while being enriched in Ni with little variation in Fe. As the liquid phase moves from 998 K to 873 K (and upwards towards the liquidus valley within the ternary system in Figure 6.3), it becomes more deficient in Cu and now in Fe, while being further enriched in Ni and now in S. Little variation is calculated in Co concentration over the

complete liquidus temperature range. The residual liquid phase composition at 898 K (also the lowest liquidus contour within the pseudo-ternary system in Figure 6.3) is as follows: 64.49% Ni, 14.05% Cu, 20.51% S, 0.58% Fe and 0.37% Co. Notably, the last liquid phase composition, as plotted within the pseudo-ternary system in Figure 6.3, traces closer to the liquidus valley. Figure 6.3 also provides the identity of the primary phases.

Figure 6.4 demonstrates the calculated liquidus temperature range plotted as isothermal contours for the Ni-Cu-S_0.2%Fe0.3%Co pseudo-ternary system, with superimposed liquid phase starting and solidification marked points and primary phase fields. The liquidus contour plot in Figure 6.4 indicates that the liquid phase is stable from 1648 K (1375 ^{o}C) to 873 K (600 ^{o}C). A significant lowering in the liquidus temperature range is observed from 973 K (as demonstrated for a comparable pseudo-ternary system in sub-section 6.2.1 previously) to 873 K. Similarly, a liquidus valley is present near the lower Ni-S-rich join.

The starting composition, as reported previously in Table 6.1, and plotted within the pseudo-ternary system in Figure 6.4, has 0.15% Fe above liquidus temperature. The liquidus temperature has been established to occur between 1123 K (850 ^{o}C) and 1098 K (825 ^{o}C). The liquid phase, when moving below liquidus temperature to 973 K (and away from the Cu-S-rich join in Figure 6.4), becomes deficient in Cu and S while being enriched in Ni. There is no variation in Fe concentration between 1123 K and 1073 K. When the liquid phase moves upwards (within the pseudo-ternary system in Figure 6.4) towards the liquidus valley, it becomes more enriched in Cu and Fe while being further enriched in Ni and now in S. Little variation is also calculated in Co concentration over the complete liquidus temperature range. The last liquid Fe concentration at 873 K (also the lowest temperature within the pseudo-ternary system in Figure 6.4) is 0.06%. The last liquid phase composition (as plotted within Figure 6.4) also appears unable to trace the liquidus valley. The identity of the primary phases is also indicated in Figure 6.4.

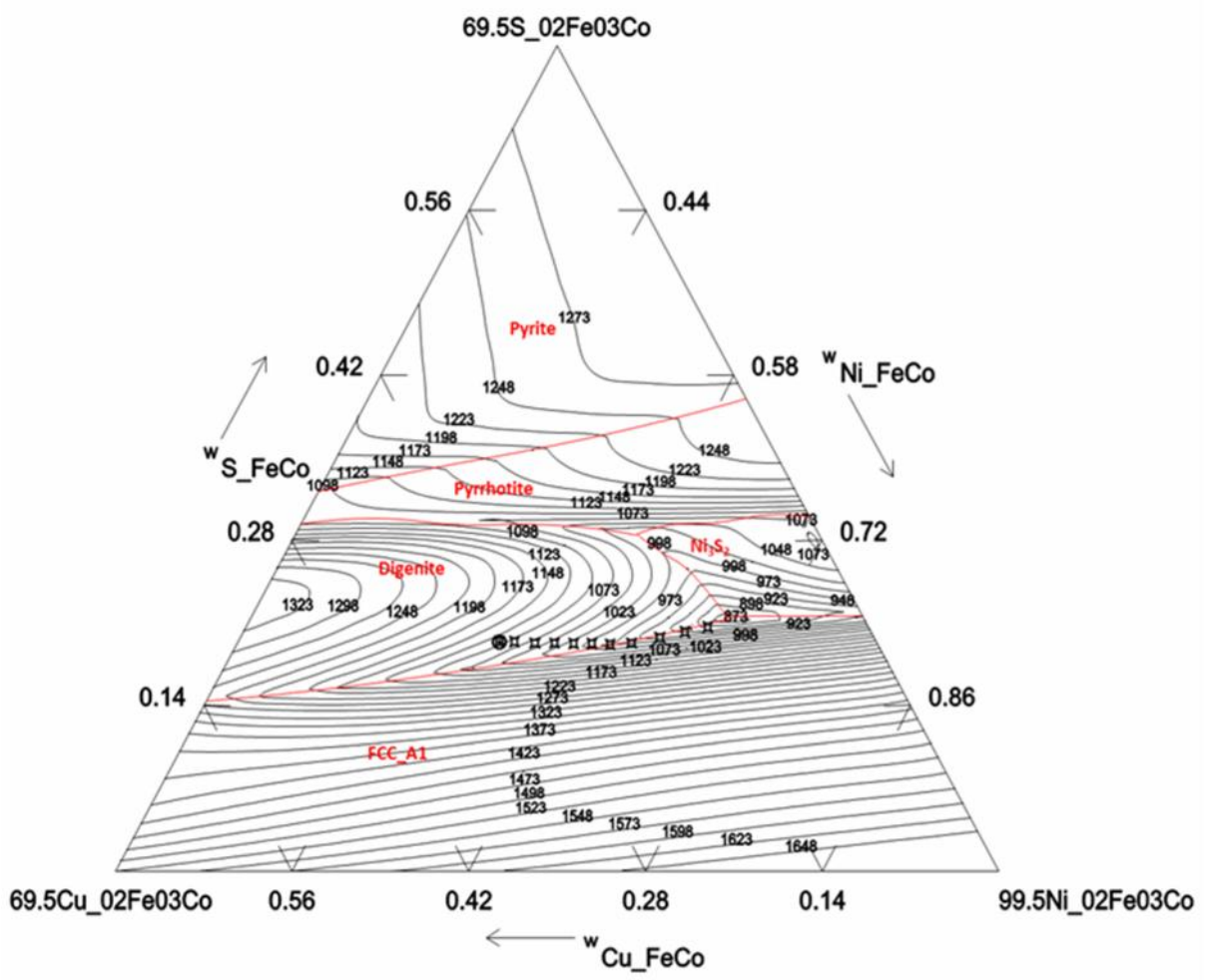

Figure 6.4: Calculated liquidus contour plot set from 1673 K (1400 °C) to 773 K (500 °C) with superimposed liquid phase starting and solidification marked points and primary phase fields for the Ni-Cu-S_0.2%Fe0.3%Co pseudo-ternary system.

Discussion

The effect of the end composition of different pseudo-ternary systems at fixed Fe and Co concentrations on the liquidus temperature range is noticeable. The liquidus temperature range is lowered when the fixed Fe and Co concentration decreases. Additionally, the comparable Co concentrations for the lower fixed (Fe and Co) systems appear not to have an effect in lowering the liquidus range to 873 K. Moreover, the value of the preset temperature interval may not have been small enough to detect the lowest temperature at which liquid can exist within the respective pseudo-ternary systems. It is therefore possible that these are simple pseudo-ternary systems exhibiting single ternary eutectic points.

The effect of the true starting composition on the liquidus temperature is not evident. A shorter preset temperature interval may provide the exact value. The compositional changes of the liquid phase are of particular interest as it serves to describe evolutionary aspects of the matte systems upon cooling. When the starting Fe concentration is lowered for a true composition, the temperature at which it starts to influence the compositional changes of the residual liquid phase is decreased. The more S present in the starting composition, the lower the temperature at which it influences the compositional changes of the residual liquid phase. Moreover, the effect of lowering the starting Co concentration on the residual liquid phase compositional changes is minimal. The exact eutectic point for the respective true liquid matte systems is not known. Co-existing liquid and crystallizing solid phase interaction will be considered in the next sub-section.

Figure 6.5 provides a comparative exhibition of the true liquid phase solidification path and primary phases with respect to the Ni-Cu-S_5%Fe1%Co and Ni-Cu-S_0.2%Fe0.3%Co ternary systems.

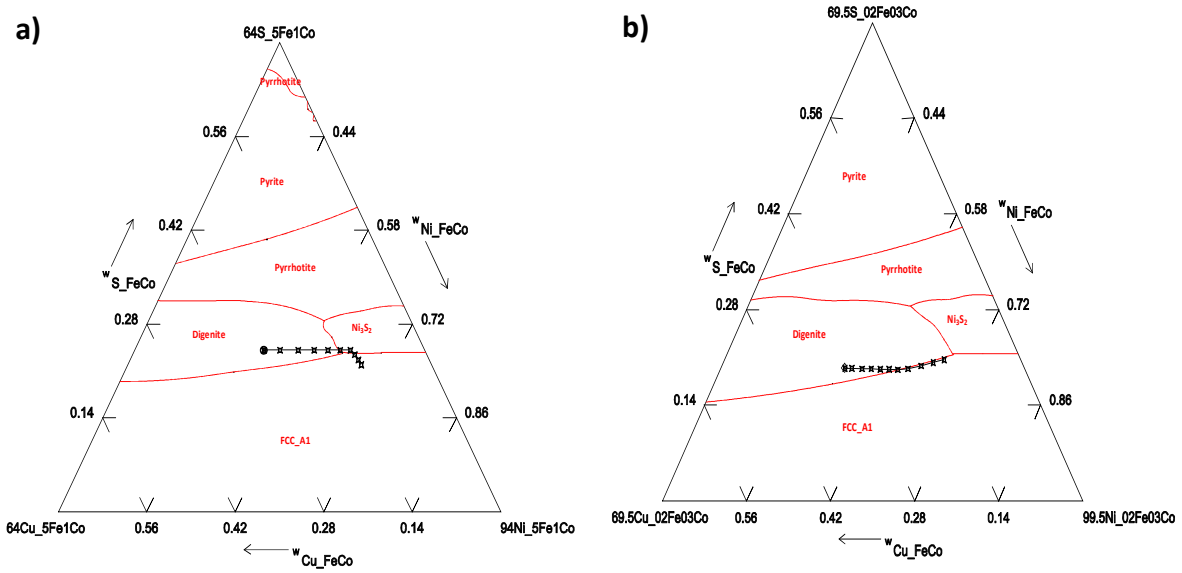

Figure 6.5: A comparative display of the true liquid phase solidification path and primary phase fields for (a) Ni-Cu-S_5%Fe1%Co and (b) Ni-Cu-S_0.2%Fe0.3%Co pseudo-ternary systems.

Note that the true liquid phase solidification points are not strictly located at the correct composition within the pseudo-ternary system due to its fixed Fe and Co concentration. Nonetheless, the combination provides a reasonable graphic display of the different solidification paths for the true liquid matte systems, as shown in Figure 6.5. Viljoen (2001)

also found different solidification paths as a function of variable iron concentration and temperature for the slow-cooled Ni-Cu-S matte system within the Anglo Platinum beneficiation context. The end composition of the pseudo-ternary system at fixed 5% Fe + 1% Co concentration is relatively far-off (particularly with respect to % Fe) from that for the true last liquid phase containing 1.45% Fe and 0.78% Co (also shown previously in Figure 6.2 and reported in Table 6.1). In comparison, the end composition of the pseudo-ternary system at fixed 0.2% Fe + 0.3% Co is relatively closer to the true last liquid phase containing 0.06% Fe and 0.36% Co (also shown previously in Figure 6.4 and reported in Table 6.1).

For this reason, the lower iron-containing true liquid matte systems appear to trace the possible eutectic point (within the pseudo-ternary systems) better than the high iron-containing true liquid matte systems. Moreover, the ternary eutectic point within the lowest iron-containing true liquid matte system may be at such a temperature that the solidification path calculation using steps of 25 K is unable to compute the exact value. Consequently, the last point of the solidification path seems additionally unable to trace the possible ternary eutectic point within Figure 6.4. A shorter temperature step may bring the last solidification point closer.

6.2.3. Multiphase Cooling Equilibria

Figure 6.6 displays calculated multiphase and phase-specific equilibria features for a true liquid phase starting composition as a function of specified cooling temperature range. The starting composition comprises 43.80% Ni, 25.00% Cu, 23.69% S, 5.17% Fe, 1.62% O and 0.72% Co and is analogous to the high iron-containing matte system. Figure 6.6(a), in particular, demonstrates the path that the liquid phase follows in relation to crystallizing primary and lower temperature phase mass sequences. Elemental compositions were calculated for the respective phase mass plots allowing assessment of co-existing liquid and crystallizing primary solid phase constituent interactions. The MTDATA phase mass and compositional analyses are available for inspection in Appendix D (Tables D.1 to D.6). Figure 6.6(b) specifically examines the path followed by components of the liquid phase in relation to correlating primary solid phase formations as a function of varying constituent mass fractions.

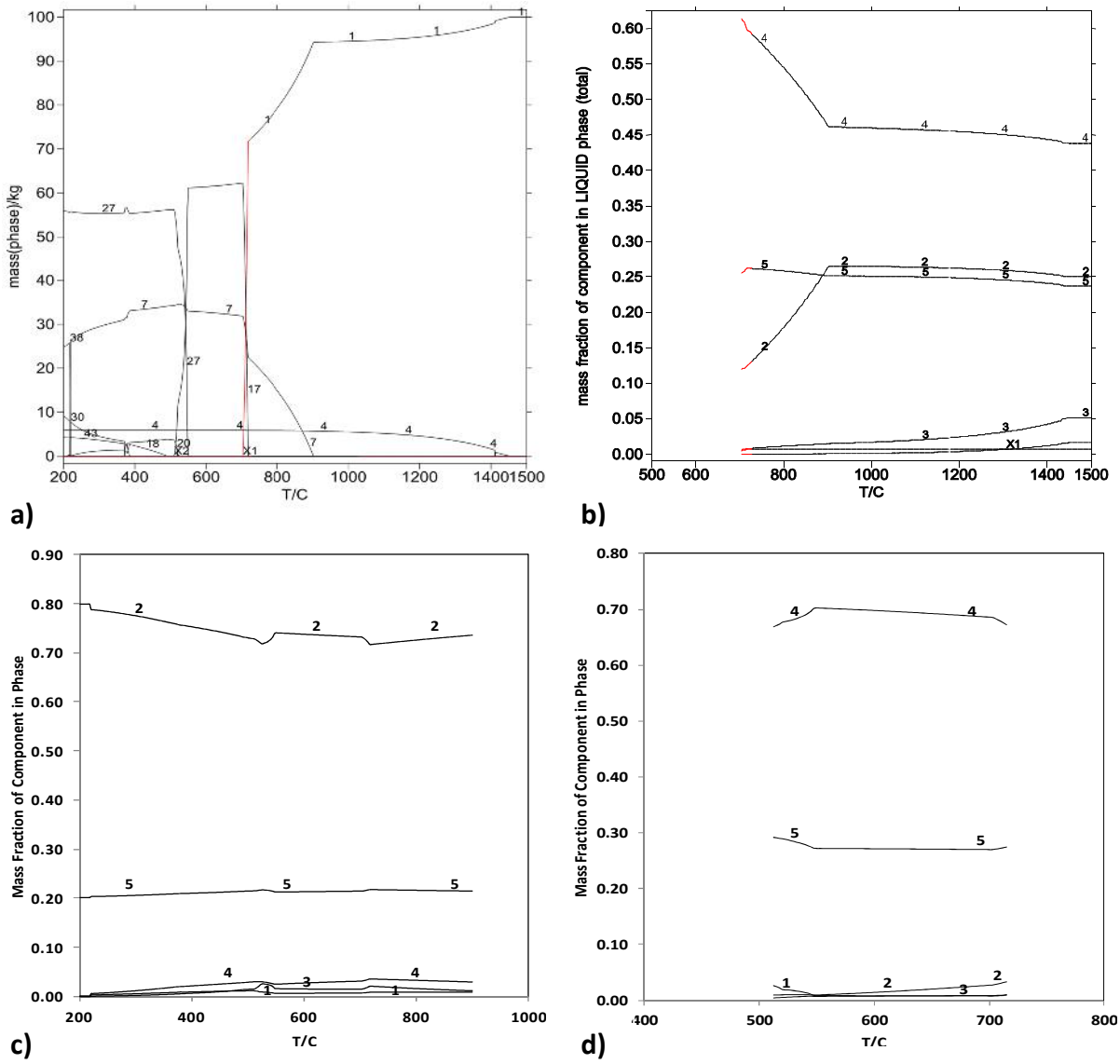

Phase 1-liquid matte : Phase 4-spinel : Phase 7-digenite : Phase 17-Ni_3S_2 : Phase 18-pentlandite : Phase 20-pyrrhotite : Phase 27-heazlewoodite : Phase 30-chalcopyrite : Phase 38-beta-chalcocite : Phase 43-Ni_7S_6 : Component 1-Co : Component 2-Cu : Component 3-Fe : Component 4-Ni : Component 5-S : Component 6-O : X1=component 1,6

Figure 6.6: Calculated multiphase cooling equilibria features for the high iron-containing matte system showing the (a) liquid phase mass path in relation to crystallizing primary and lower temperature phase mass sequences, (b) components of the liquid phase, (c) components of digenite and equivalent beta-chalcocite, and (d) components of Ni_3S_2 with respect to varying mass fractions.

A single liquid phase exists, annotated as phase 1 in Figure 6.6(a), at the highest temperature (1500 ^oC) and phase mass amount (100%). The liquid phase may be considered as being homogeneous with respect to the specified and subsequently fast diffusing reacting

compositions. It is well established that high temperatures permit instant constituent transport equilibrium.

The readily formation of seemingly molten oxide and spinel, annotated as phase 4 in Figure 6.6(a), occurs at high temperatures, namely 1452.5 ^{o}C and 1410 ^{o}C, respectively. The primary spinel comprises 61.54% Fe, 27.48% O, 10.09% Ni and 0.86% Co and its nucleation is most likely coupled to dissolve oxygen in liquid phase, high temperatures and therefore favourable transport equilibrium. Sulfide melts were reported by Ballhaus et al., (2001) as particularly responsive to oxidation and magnetite may appear as an early phase if dissolved oxygen is present. Moreover, such a combined formation of molten oxide and spinel crystallize therefore during the actual converting process and is included within the equilibrium cooled solid matte. Kyllo et al., (1992) confirmed that during the first converter blow period, nearly 84% of blown oxygen combines with the bath constituents, resulting in a high level of magnetite present. Such a formation can possibly be investigated further in the Fe-Ni-O ternary sub-system, including the lowest melting point. The single liquid phase amount is consumed to 99% by the crystallization of molten oxide and spinel with respect to Fe, O, Ni and Co exsolution. The liquid phase requires shifting composition and temperature to maintain the liquid and solid phase as stable and therefore in equilibrium. The composition of the residual liquid phase at 1410 ^{o}C, as illustrated in Figure 6.6(b), has become deficient in Fe and O, while being enriched in Ni, Cu and S. A minuscule variation in Co concentration was observed.

The crystallization of digenite, phase 7 in Figure 6.6(a), occurs at 900 ^{o}C and is therefore the first solid phase to crystallize during equilibrium cooling. The exact liquidus point within this multiphase cooling system is therefore known, in contrast to the suggested temperature range (850 ^{o}C to 825 ^{o}C) within the comparable (oxygen-free) true liquid matte system in sub-section 6.2.2. Primary digenite comprises 73.57% Cu, 21.50% S, 2.90% Ni, 1.19% Fe and 0.84% Co. The residual liquid phase amount is consumed to 94% by the crystallization of solid digenite with respect to Cu, S, Ni, Fe and Co exsolution along co-existing spinel crystallization. At a temperature step directly below 900 ^{0}C, the liquid phase becomes more deficient in Fe, O, Co and now gradually Cu, while being increasingly enriched in Ni and S.

Subsequent notable liquid phase compositional changes include an increase in Cu deficiency and related Ni enrichment, as evident by the distinct path behavior in Figure 6.6(b).

The crystallization of Ni_3S_2, phase 17 in Figure 6.6(a), occurs at 715 ^oC and is the second solid phase to crystallize during equilibrium cooling. Primary Ni_3S_2 comprises 67.29% Ni, 27.47% S, 3.25% Cu, 1.01% Fe and 0.98% Co. The residual liquid phase amount is consumed to 55% by the crystallization of solid Ni_3S_2 with respect to Ni, S, Cu, Fe and Co exsolution along co-existing spinel and digenite crystallization. The composition of the residual liquid phase at 715 ^oC has become significantly deficient in Cu and enriched in Ni. Further liquid phase compositional changes include the near depletion of O, continuous deficiency in Fe and Co and gradual S enrichment. The liquid phase amount is consumed to a minimum of 6% at 705 ^oC. The temperature of the eutectic is probably directly below 705 ^oC, but above 702.5 ^oC, as the value of the preset temperature interval (2.5 ^oC) may not be small enough to detect the lowest temperature at which the liquid phase can exist.

In comparison, the lowest temperature at which the liquid phase can exist within the associated oxygen-free Ni-Cu-S_5%Fe1%Co ternary and true liquid matte systems were computed as 675 ^oC and 625 ^oC, respectively. These values suggest that the predicted last liquid phase, particularly between the multiphase and oxygen-free true liquid matte systems occurs in a wide temperature band. The composition of the last residual liquid phase at 705 ^oC prior to the liquid reaching the eutectic comprises 61.41% Ni, 25.52% S, 11.96% Cu, 0.60% Fe and 0.51% Co and signified by the end of the plots of the constituent mass fractions paths in Figure 6.6(b). The liquid phase, amid compositional changes, moves towards and remains at the temperature of the eutectic until the last residual liquid phase crystallizes into the last solid phases of spinel, digenite and Ni_3S_2. The spinel, digenite and Ni_3S_2 solid phase amounts at 702.5 ^oC after the last liquid has crystallized are computed as 6%, 32% and 62%, respectively.

Figure 6.6(a) also demonstrates the path spinel phase (4) follows during sub-solidus equilibrium cooling to 200 ^oC. The spinel phase amount remains near 6% and the end member comprises 62.03% Fe, 27.49% O, 10.12% Co and 0.37% Ni. The spinel composition after the eutectic event is more enriched in Fe (70.22% at 702.5 ^oC) than the primary and end member phases. Digenite sub-solidus equilibrium cooling to 220 ^oC is examined in detail

below. The digenite phase amount at 220 °C is computed as 26% and comprises 78.78% Cu, 20.35% S, 0.52% Ni, 0.06% Fe and 0.28% Co. The digenite composition at 220 °C is more enriched in Cu than the primary phase. The inversion of digenite to a structural form equivalent to beta-chalcocite, phase 38 in Figure 6.6(a), occurs between transition cooling temperatures 220 °C and 217 °C. The polymorph composition at 217 °C consists of 79.85% Cu and 20.15% S. The end member phase amount at 200 °C is computed as 25% with a comparable composition. It is thus notable that the composition of digenite (and spinel) continues to vary during sub-solidus equilibrium cooling.

Figure 6.6(c) examines the path followed by components of digenite and beta-chalcocite over the crystallization temperature range. Early sub-solidus enrichment in Cu correlates well with deficiencies in Ni, Fe and Co and *vice versa* during a subsequent shorter temperature range. A slight variation in S constituent mass fraction is also evident over the crystallization temperature range in Figure 6.6(c). The sub-solidus element enrichment or deficiency processes may also be dependent on the concurrent movement of Cu atoms, but in opposite directions to Ni, Fe and Co atoms through the near stable S atomic arrangement and developing digenite and equivalent beta-chalcocite phase structures. Copper demonstrates the largest mobility, making such a diffusion process probably further dependent on the existing interstitial disorder of the Cu atoms of the developing phase structures. It is well established that the order of phase structures increases in accordance with decreasing temperatures as the atoms that do not match the internal structure are forced to leave (Porter and Easterling, 1992). In this regard, it is notable that the beta-chalcocite end member composition consists only of Cu and S. A more inclusive description of such a process would have to consider element diffusion coefficients and the interconnected cooling rate. These require further investigation as it is beyond the scope of this study.

The sub-solidus equilibrium cooling of Ni_3S_2 to 512 °C was also examined in detail. The Ni_3S_2 composition at 702.5 °C consists of 68.60% Ni, 27.04% S, 2.69% Cu, 0.90% Fe and 0.76% Co while the end member composition comprises 66.92% Ni, 29.12% S, 9.29% Cu, 3.61% Fe and 2.67% Co. Figure 6.6(d) examines the path followed by the components of Ni_3S_2 with respect to changing constituent mass fractions. Examination of Figure 6.6(d) reveals that

enrichment in Ni correlates with deficiencies in S, Cu, Fe and Co over the cooling temperature range 715 ^{o}C to 702.5 ^{o}C, providing indication of substitutional element mobilities, including S. Variation in S constituent mass fraction is more evident (compared to behavior within digenite) over the crystallization temperature range, as shown in Figure 6.6(d). The crystallization of heazlewoodite, phase 27 in Figure 6.6(a), occurs between the cooling temperature range 547.5 ^{o}C to 200 ^{o}C. Primary heazlewoodite contains 73.15% Ni, 26.70% S, 0.16% Co and seemingly co-exists as a low temperature polymorph alongside Ni_3S_2 crystallization to 512.5 ^{o}C. The heazlewoodite phase amount at 200 ^{o}C is 56% with a comparable composition. Remaining low temperature stable phase formations include the crystallization of pyrrhotite (phase 20), pentlandite (phase 18), chalcopyrite (phase 30) and Ni_7S_6 (phase 43), as shown in Figure 6.6(a). These low temperature phase structuring processes could be reliant on the earlier forced out, but available, constituents of ordered phases. The chalcopyrite phase mass at 200 ^{o}C is 9% and consists of 57.03% Cu, 26.33% S and 16.64% Fe. The Ni_7S_6 phase mass at 200 ^{o}C is 4% and contains 68.11% Ni and 31.89% S.

In contrast, Figure 6.7 displays calculated multiphase and phase-specific equilibria features for a dissimilar liquid phase starting composition consisting of 49.50% Ni, 29.50% Cu, 19.15% S, 1.24% O, 0.36% Co and 0.15% Fe and is analogous to the low iron-containing matte system. Notable dissimilarities with the previous liquid phase starting composition are the higher Ni and Cu and the lower S, O, Co and Fe concentrations.

Figure 6.7(a) demonstrates that the crystallization of halite (phase 14) occurs relatively early at a temperature of 1365 ^{o}C, although at a lower value compared to the molten oxide and spinel formations within the preceding multiphase cooling system. Primary halite comprises 68.54% Ni, 21.79% O, 6.45% Fe, 3.20% Co and 0.03% Cu and its nucleation also appears coupled to dissolved oxygen, favorable high temperature transport equilibrium and, moreover, high Ni and low Fe concentrations in the starting liquid phase. Halite crystallizes during the converting process and will report to the equilibrium cooled solid matte. The liquid phase (1) amount is minutely consumed by the crystallization of halite in relation to Ni, O, Fe, Co and Cu exsolution. The residual liquid phase at a temperature interval directly below 1365 ^{o}C has become deficient in Ni, O, Fe and Co, while enrichment occurs in Cu and S, as can be seen from Figure 6.7(b).

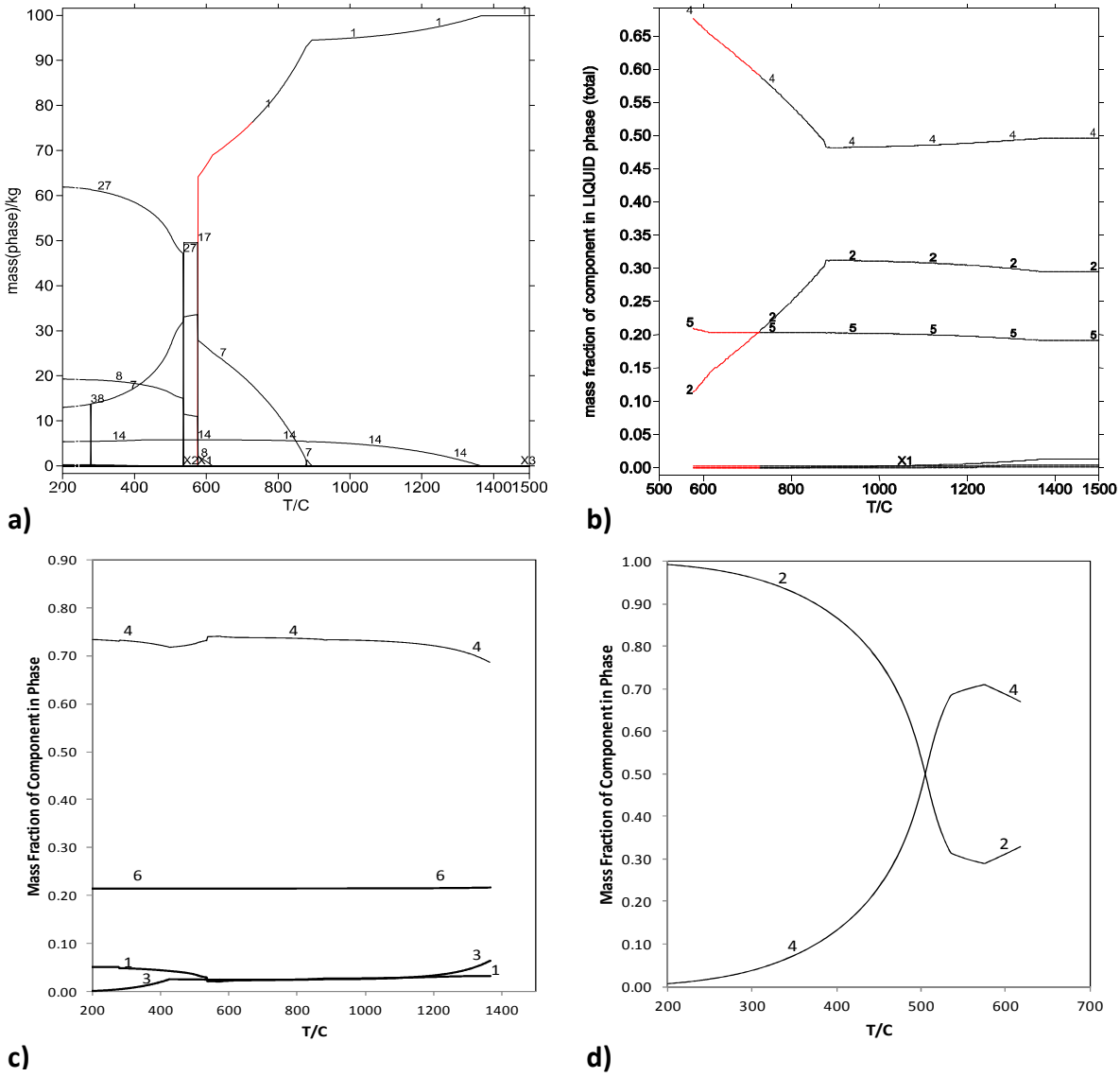

Phase 1-liquid matte : Phase 7-digenite : Phase 8-FCC_A1 : Phase 14-halite : Phase 17-Ni_3S_2 : Phase 27-heazlewoodite : Phase 38-beta-chalcocite : Component 1-Co : Component 2-Cu : Component 3-Fe : Component 4-Ni : Component 5-S : Component 6-O : X1=component 1,3,6

Figure 6.7: Calculated multiphase cooling equilibria features for the low iron-containing matte system showing the (a) liquid phase mass path in relation to crystallizing primary and lower temperature phase mass sequences, (b) components of the liquid phase, (c) components of halite phase, and (d) components of FCC_A1 phase with respect to changing constituent mass fractions.

The crystallization of digenite, phase 7 in Figure 6.7(a), occurs at 877.5 ^{o}C and is the first solid phase to crystallize during equilibrium cooling. The liquidus point within this system is therefore known and occurs at a relative lower value than within the preceding system. Primary digenite comprises 77.14% Cu, 20.68% S, 1.72% Ni, 0.40% Co and 0.06% Fe, which is

more enriched in Cu and poorer in S, Ni, Co and Fe than the associated primary composition within the preceding system. The residual liquid phase amount is consumed to 93% by the crystallization of solid digenite in relation to Cu, S, Ni, Co and Fe exsolution along co-existing halite crystallization. The residual liquid phase compositional changes at 850 ^{o}C consist of increasing deficiencies in O, Fe, Co and now noticeably Cu with continuous enrichment in S and Ni, as illustrated in Figure 6.7(b).

The crystallization of FCC_A1, phase 8 in Figure 6.7(a), occurs at 617.5 ^{o}C and hence the second solid phase to crystallize during equilibrium cooling. Primary FCC_A1 comprises 66.95% Ni, 32.79% Cu, 0.25% Co and trace amounts of Fe and S. The residual liquid phase amount is consumed to 69% by the crystallization of solid FCC_A1 with respect to mostly Ni, Cu and Co exsolution along co-existing halite and digenite crystallization. The residual liquid phase compositional changes at a temperature interval directly below 617.5 ^{o}C consist of further deficiencies in O, Fe and Cu and enrichment in Ni, S and now Co. The liquid phase amount is consumed to a minimum of 64% at 577.5 ^{o}C. The temperature of the eutectic would probably be between 577.5 ^{o}C and 575 ^{o}C, which is significantly lower than within the preceding system. The lowest temperature at which the liquid phase can exist within both the related oxygen-free Ni-Cu-S_0.2%Fe0.3%Co ternary and true liquid matte systems was calculated as 600 ^{o}C.

These values suggest that the predicted last liquid phase within the respective systems occurs in a narrower temperature band. The last residual liquid phase composition at 577.5 ^{o}C, before the liquid reaches the eutectic comprises 67.52% Ni, 20.92% S, 11.32% Cu and 0.24% Co and is illustrated by the end of the plots of the constituent mass fraction paths in Figure 6.7(b). The last liquid composition is more enriched in Ni and poorer in S than within the preceding multiphase system. The liquid phase remains at the eutectic until the last residual liquid phase isothermally solidifies into halite, digenite, FCC_A1 and Ni_3S_2. The halite, digenite, FCC_A1 and Ni_3S_2 phase amounts in the solid phase at 575 ^{o}C (after the crystallization of last liquid) are calculated as 6%, 33%, 11% and 50%, respectively.

Halite sub-solidus equilibrium cooling to 200 ^{o}C was examined in detail. The end member phase amount is 5% and comprises 73.35% Ni, 21.42% O, 5.10% Co and 0.13% Fe. End member phases are more enriched in Ni and Co and poorer in Fe than the primary

formations. Figure 6.7(c) specifically examines the path followed by the components of halite over the crystallization temperature range. Early sub-solidus element mobilities suggest diffusion based upon the migration of Ni atoms through the stable O atomic arrangement, substituting Fe and Co atoms in developing phase structures. At subsequent lower temperatures, Ni atoms migrate in the opposite direction, being substituted by Co atoms. During end member compositional adjustments, Ni and Co atoms substitute Fe atoms and are thereby required to leave the developed phase structures.

Digenite sub-solidus equilibrium cooling occurs to 280 ^{o}C. The end member phase amount is 14% and comprises 79.19% Cu, 20.27% S, 0.42% Ni and 0.11% Co. The inversion of digenite to beta-chalcocite, phase 38 in Figure 6.7(a), occurs between the transition cooling temperatures 280 ^{o}C and 277.5 ^{o}C and thereafter the concentration consists of 79.85% Cu and 20.15% S. The polymorph phase amount at 200 ^{o}C is 13% with a similar composition. The polymorph phase amount is significantly lower than the associated phase amount within the preceding system. It is further notable that the respective inversion point occurs at a 60 ^{o}C higher value than within the preceding high iron-containing system. This is probably dependent on the earlier attainment of the required crystal structure and composition.

Sub-solidus equilibrium cooling of FCC_A1 to 200 ^{o}C was also examined in detail. The FCC_A1 composition at 575 ^{o}C comprises 70.92% Ni, 28.83% Cu and 0.24% Co and reflects the highest Ni content of developing FCC_A1 phase structures. The end member phase amount is 19 % and consists of an alloy of mainly 99.23% Cu and 0.77% Ni. Figure 6.7(d) examines the path that the components of FCC_A1 inversely follow over the crystallization temperature range. The initial enrichment in Ni, as evident in Figure 6.7(d), occurs during liquid-solid chemical exchange and, as a result, reaches a maximum after the eutectic event at 575 ^{o}C. This is based upon the migration in opposite directions of Ni atoms substituting mainly Cu and Co atoms in developing phase structures. During sub-solidus equilibrium cooling, the Ni atoms would migrate in the opposite direction, being substituted by Cu atoms towards attainment of the end member composition. These observations support the previous finding in Chapter 5 (sub-section 5.2.2.3), which suggests that Ni and Cu may be completely soluble in one another.

The crystallization of Ni_3S_2, phase 17 in Figure 6.7(a), occurs isothermally during the eutectic event and the primary composition at 575 ^oC comprises 74.51% Ni, 24.70% S, 0.55% Cu, 0.24% Co and trace amounts of Fe. The temperature at formation is notably lower compared to within the preceding system, whereas the composition is higher in Ni, and lower in S and Cu concentrations. The inversion of Ni_3S_2 to heazlewoodite, phase 27 in Figure 6.7(a), occurs between cooling temperatures 537.5 ^oC and 535 ^oC and thereafter comprises 73.20% Ni, 26.70% S and 0.10% Co. The polymorph phase amount at 200 ^oC is 62%, with a similar composition. The polymorph phase amount is higher than the associated phase amount within the preceding system. Low temperature stable phase formation includes the sub-solidus crystallization of spinel between 422.5 ^oC and 200 ^oC with a minuscule phase mass. The spinel phase structuring process is probably dependent on the forced out Fe atoms during earlier phase ordering.

In general, the examination of calculated multiphase cooling equilibria for variable Ni-Cu-S-Fe-Co-O liquid phase systems provides a quantitative understanding of converter matte solidification processes to within ±2.5 ^oC. Currently available knowledge in literature on the solidification of industrial converter matte systems has been expanded. The starting compositions, including oxygen, are seen to exert a measurably different chemical effect on the compositional path followed by the relevant liquid phase. The liquidus-solidus gap of 197.5 ^oC within the high iron-containing multiphase systems is narrower than the comparative gap of 302.5 ^oC within the low iron-containing system. In contrast, sub-solidus equilibrium cooling to 200 ^oC within the high iron-containing system occurs over a wider temperature band of 302.5 ^oC than the comparative band of 175 ^oC within the low iron-containing system.

The internal liquid phase constituent interactions are not included in this study and would be complex to describe during which the concentration of each constituent within the instant residual liquid would influence the behaviour of others. According to Ballhaus et al., (2001), sulfur and oxygen fugacities of sulfide melts are related and will most likely control the metal/sulfur and metal/oxygen ratios. It would be rational to suggest that such ratios within instant residual liquid matte would influence the interstitial disorder of co-existing solids and therefore affect substitutional element mobilities. The effect of S and O

concentrations upon the residual liquid phase element ratios and co-existing liquid-solid elemental exchange requires consideration in future studies. Moreover, thermodynamic descriptions for Pb and PGMs are not supported by the base matte database used and therefore not included in the multiphase cooling equilibria calculations. The potential addition of these would increase the complexity within such equilibrium systems and warrants consideration.

6.2.4. Industrial Matte Systems

Equilibria relations provide an indication of achievable theoretical limits, while reaction kinetics and process dynamics influence practical pyrometallurgy (Rosenqvist, 1978). It is therefore of practical value to compare calculated equilibria features with related fast-cooled industrial matte observations such as automated mineralogy and the previously determined relative mineral abundance, composition and microstructure.

6.2.4.1. Automated Mineralogy

Automated analysis, as described in Chapter 3 (sub-section 3.5.6), allowed for the acquisition of grain X-ray maps and phase modal abundance. Figure 6.8 is illustrative of the complementary, but technically challenging, X-ray mapping attainment of fine-scale and pixel based grain areas within a matte particle for the 0.99% Fe matte.

The results of the grain X-ray mapping, illustrated in Figure 6.8, are in broad agreement with previous mineralogical observations, as found in Chapters 4 (sub-section 4.2.4) and 5 (sub-sections 5.2.1, 5.2.2 and 5.2.3). Figure 6.8 also provides the identity of the pixel based grain areas present. The names are self-explanatory, except for alloy_2, alloy_1, FeNiO and SiO, which refer to NiCu-alloy, OsRu-alloy, spinel and slag-associated silica, respectively.

The results of the phase modal abundance, acquired through the MLA based XMOD analytical routine, are reported in Table 6.2, allowing comparison within and between correlated fast-cooled matte systems, which is denoted by iron concentration or endpoint.

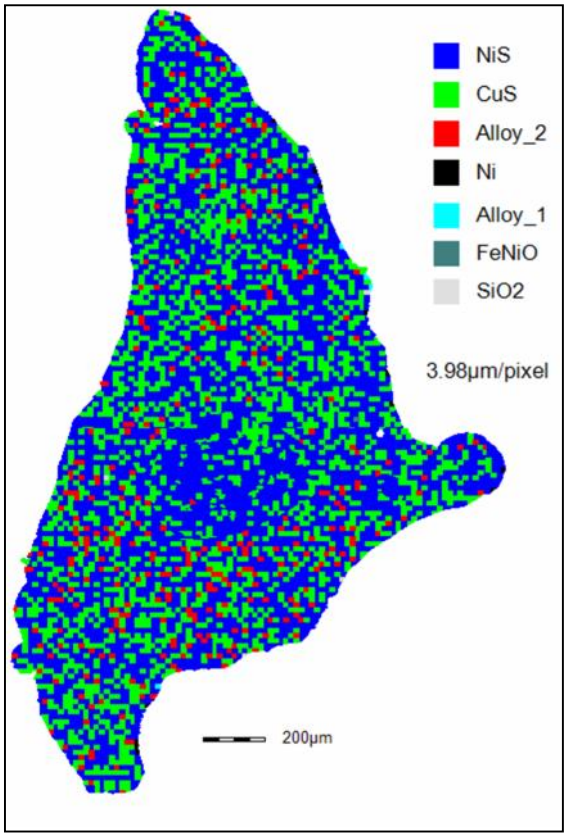

Figure 6.8: Mapping of an industrial solidified matte particle for the 0.99% Fe matte acquired through the MLA based GXMAP analytical routine showing the relative morphology and abundance of the various fine-scale and pixel based grain areas present at 200µm size scale.

Table 6.2: Phase modal abundance acquired through the MLA based XMOD analytical routine with respect to X-ray point count area% of fast-cooled matte systems denoted by iron endpoints 5.17%, 0.99% and 0.15%.

Phase Constituent	**5.17% Fe Matte**	**0.99% Fe Matte**	**0.15% Fe Matte**
	Point Count (Area%)	**Point Count (Area%)**	**Point Count (Area%)**
Nickel sulfide	73.18	59.70	62.64
Copper sulfide	23.29	35.32	32.35
Metallic	0.55	0.41	0.61
Nickel oxide	0.51	0.69	0.78
Iron oxide	0.17	0.05	0.01
Alloy	0.14	1.25	1.27
Fayalite	0.09	0.03	[†]N.I.

[†]N.I.: Not Identified.

Table 6.2 reports the results in decreasing order, in which nickel sulfide constitutes the prevalent point count areas, with 73.18% of total particle areas. This is followed by copper sulfide, and the combination with nickel sulfide constitutes over 96% of particle areas. An unexpected and mostly unexplained result to date is the finding of native Ni and Cu point count areas of 0.55% reported as metallic. This requires investigation through further work. Additional results include point count areas for nickel oxide (0.51%), iron oxide (0.17%), alloy (0.14%) and entrained fayalitic slag (0.09%). Notable differences in results between the matte systems include that the point count area% for nickel sulfide, iron oxide and fayalite decreases for lower iron endpoints. In contrast, the point count area% for copper sulfide, nickel oxide and alloy increases for lower iron endpoints. It should be noted that alloy refers to the combined point count area% for alloy_1 and alloy_2.

Although these are fundamentally different techniques, the results obtained by the MLA based XMOD analytical routine, quantitative XRD (as reported in Chapter 3, Table 4.4) and the equilibrium phase amounts to 200 ^{o}C for nickel sulfide and copper sulfide (as reported in sub-section 6.2.3 of this chapter), within each matte system generally concur with respect to the abundance of phases. The trends in results obtained *via* MLA based XMOD and quantitative XRD for nickel sulfide and copper sulfide between matte systems also concur. Comparative trends obtained for equilibrium phase amounts to 200 ^{o}C demonstrate a contrary increase in nickel sulfide and contrary decrease in copper sulfide between matte systems, and are thus not in good agreement with results obtained from the other techniques. Notably, the trend in results obtained for equilibrium phase amounts to 500 ^{o}C for nickel sulfide between matte systems is in agreement with trends for the other techniques. This may be an indication that the prediction of low temperature phase amounts of nickel and copper sulfide is less accurate than prediction for high temperature phase amounts. This aspect requires further consideration. Nickel oxide results obtained *via* MLA based XMOD within the high iron matte system constitutes a higher point count area% than for iron oxide in contrast to results for the other techniques. Trends in results for both nickel oxide and iron oxide between matte systems are in good agreement for all techniques and provide an indication of the extent of matte blowing. Alloy results obtained *via* MLA based XMOD and quantitative XRD appear low within the high iron matte system and, in

comparison, fail to crystallize in a similar equilibrium system. The trends in alloy between matte systems are nevertheless in good agreement.

Based on the relative phase amounts of different techniques, it cannot be asserted that equilibrium conditions were achieved during industrial converter matte cooling. There are reasonable levels of agreement and also less commonplace inconsistencies that can serve as a manifestation regarding the processes of solidification. The true state of the matte systems may be recognized by comparing the previously determined electron probe microanalyses of the preserved microstructure to the current calculated equilibria compositions.

6.2.4.2. Composition

The electron probe microanalyses of 10 nickel sulfide phase structures within the high iron matte system reveals that these structures, on average, comprise 61.36% Ni, 27.04% S, 5.52% Fe, 0.89% Cu, 1.05% Co and 0.15% Pb. The electron probe microanalysis of nickel sulfide was previously covered in Chapter 5 (sub-section 5.2.1.1). The constituent elements exhibited variation and were seemingly not mixed in stoichiometric proportions within the nickel sulfide phase structures. Electron probe microanalysis further reveals the presence of a nickel sulfide phase structure within the high iron matte system comprising 42.43% Ni, 25.62% S, 21.86% Cu, 5.39% Fe, 0.74% Co and 0.16% Pb. There is a large departure from the average Ni and Cu concentrations for this particular phase structure. The Ni concentration of the equilibrium end member at 200 ^{o}C is 11.72% higher than the average determined by electron probe microanalysis. The equilibrium S and Co concentrations are 0.34% and 0.83% lower than the determined averages. The nickel sulfide phase structures therefore exhibit chemical non-equilibrium within the high iron industrial matte system.

The electron probe microanalyses of 22 nickel sulfide phase structures within the low iron matte system indicates that these structures, on average, comprise 66.56% Ni, 23.34% S, 5.49% Cu, 0.48% Co, 0.21% Pb and 0.09% Fe. In particular the average concentration is more enriched in Ni, Cu and Pb, and poorer in S, Co and Fe than related structures within the high iron matte system. Moreover, the equilibrium Ni and S concentration of nickel sulfide is 6.69% and 3.36% higher than the determined averages. The equilibrium Co concentration is 0.42% lower than the determined average. It can similarly be concluded that nickel sulfide

phase structures within the low iron matte system exhibit chemical non-equilibrium, with a lower Ni and higher S discrepancy than for the high iron matte system.

The electron probe microanalysis of copper sulfide was also covered in Chapter 5 (sub-section 5.2.1.2). The electron probe microanalyses of 11 copper sulfide phase structures within the high iron matte system shows that these structures, on average, comprise 60.02% Cu, 23.11% S, 5.26% Fe, 9.47% Ni and 0.28% Co. The elements of Cu and Ni varied considerably and along with other constituents were not mixed in stoichiometric proportions within the copper sulfide phase structures. Electron probe microanalysis also reveals the existence of two less commonplace copper sulfide phase structures comprising, on average, 39.40% Cu, 27.82% Ni, 24.00% S, 5.01% Fe and 0.52% Co. The Cu concentration of the equilibrium end member at 200 ^{o}C is 19.83% higher than the determined average. The equilibrium S concentration is 2.96% lower than the determined average. The copper sulfide phase structures therefore exhibit chemical non-equilibrium within the high iron industrial matte system.

The microanalyses of 18 copper sulfide phase structures within the low iron matte system reveals that these structures, on average, comprise 71.32% Cu, 20.12% S, 8.42% Ni, 0.16% Co and 0.13% Fe. The average concentration is more enriched in Cu and poorer in the rest of the constituent elements than the related structures within the high iron matte system. The equilibrium Cu and S concentrations within the low iron matte system is 8.53% and 0.03% higher than the determined averages. It can be concluded that the copper sulfide phase structures within the low iron matte system exhibit chemical non-equilibrium, with a lower Cu and S difference than within the high iron matte system.

It is notable that the nickel sulfide and copper sulfide phase structures within the low iron matte system attained lower Ni and Cu chemical equilibrium discrepancies. It is also noteworthy to consider that the wider liquidus-solidus gap may occur within the low iron matte system, allowing relatively more time for liquid-solid element exchange. Moreover, a few determined nickel sulfide and copper sulfide phase structures display considerable non-stoichiometry with respect to Ni and Cu concentrations. This was observed regularly during MLA based XMOD analysis and incorporated among the results for nickel sulfide and copper

sulfide phase structures. The transformational chemical order may be related to the competition for phase crystallization and growth during the last stages of the eutectic event.

6.2.4.3. Microtexture

The texture of the microstructure is also an important feature to consider and Figure 6.9 provides illustration of the characteristic fast-cooled microtexture for a low iron matte system.

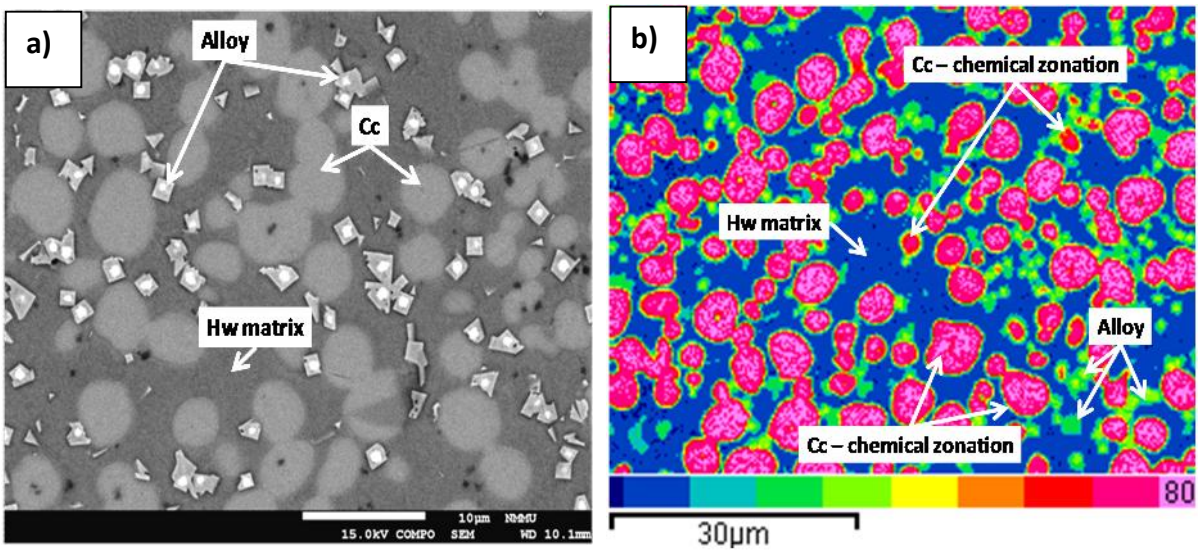

Figure 6.9: FEG SEM based micrographs of the (a) overall microtexture at 10µm size scale and (b) microtexture related Cu distribution at 30µm size scale for the low iron matte system.

Nickel sulfide represents the continuous solid phase embedding well-formed copper sulfide and alloy phase structures, as shown in Figure 6.9(a). The microtexture in Figure 6.9(a) appears in good agreement with calculated equilibrium crystallization sequences for the low iron matte system. The microtexture for the high iron matte system was found, in Chapter 4 (sub-section 4.2.4.1), to be more coarse and distinct with less diffused grain boundaries between nickel sulfide and copper sulfide phase structures. It is worth considering that sub-solidus equilibrium cooling within the high iron matte system may possibly occur over a wider temperature range. A previous study by Schouwstra (2003) suggested that the effect of a faster cooling rate for the same starting composition will result in similar phase formations but that the end members will have an overall finer texture. It is now evident that the effect of a faster cooling rate on the attainment of early chemical order and end member composition should also be considered.

The microtexture of phase structures with respect to the preserved chemical element distributions should thus be examined as an aid in understanding some of the physical processes which may occur during fast-cooling. Figure 6.9(b) maps in false colour contrast (see the relative colour scale at the bottom of the micrograph) the Cu distribution within and between nickel sulfide (Hw), copper sulfide (Cc) and alloy phase structures. It can be seen from Figure 6.9(b) that copper sulfide phase structures preserved three concentric-like chemical or reaction zones as the Cu moved inwards along horizontal and vertical pathways substituting for Ni, Co and Fe. The copper sulfide microtextural development was therefore most likely governed by these non-equilibrium element exchanges. Moreover, the mapping also indicates that alloy phase structures preserved two reaction zones as Cu moved inwards substituting for Ni. This was found, in sub-section 6.2.3 of this chapter, to occur during sub-solidus cooling. It has also been shown, in Chapter 5 (sub-section 5.2.2.3), that the inwards movement of Cu facilitates the partitioning of platinum, if available, to these phase structures which would allow for the development of alloy phase structures with characteristic Pt-dominant cores.

6.3. Key Findings

The examination of iron endpoint specific converter matte systems with respect to calculated liquidus, ternary and multiphase cooling equilibria as well as subsequent comparison with actual fast-cooled phase structures in order to enhance understanding of converter matte solidification, suggests the following key findings:

i. The effect of the end composition of the NiFe-CuFe-S ternary matte systems at 5%, 1% and 0.1% Fe concentration, as relatively simple approximations of final converter matte composition, found that ternary constitution and, therefore iron endpoint, had little effect on the stable liquidus temperature range;

ii. The effect of the end composition of the Ni-Cu-S_FeCo ternary matte systems at 5%Fe1%Co, 1%Fe0.5%Co and 0.2%Fe0.3%Co concentration, as increasingly complex approximations of final converter matte composition, has been quantified. The liquidus temperature range for the respective matte systems is lowered when the fixed Fe and Co concentrations decrease;

iii. The solidification pathway of iron endpoint specific oxygen-free liquid matte systems within corresponding Ni-Cu-S_FeCo ternaries has been estimated. It has been shown that variations in the iron endpoint specific starting composition of the oxygen-free liquid matte alter the pathway of solidification towards the eutectic;

iv. The examination of multiphase cooling equilibria for true liquid phase starting compositions analogous to the high and low iron-containing industrial matte systems provided a coherent and quantitative understanding of both liquid and solid phase solidification to within ±2.5 ^{o}C; and

v. The actual nickel sulfide and copper sulfide phase structures have shown to exhibit chemical non-equilibrium within the high and low-iron-containing matte systems when compared to calculated equilibrium phase compositions. This is indicative of non-equilibrium converter plant solidification conditions.

This chapter has developed a fundamental and coherent understanding of the critical converter matte solidification processes. The ultimate or next investigative study chapter is concerned with understanding the effect of the iron endpoint specific resultant mineralogy on the downstream processing characteristics of solidified converter matte within the Lonmin beneficiation context.

6.4. Relevant Publication

Thyse, E.L., Akdogan, G., Taskinen, P., Viljoen, K.S., Eksteen, J.J., 2013. Towards understanding nickel converter matte solidification. ***Minerals Engineering,*** Special Issue, Processing of Nickel Ores and Concentrates, Volume 54, pp. 39-51.

Chapter 7
INTEGRATED DOWNSTREAM PROCESSING CHARACTERISTICS

7.1. Introduction

As described in Chapter 2, there is little in-depth study on the downstream processing characteristics of solidified Ni-PGM converter matte as an intermediate product, particularly related to grinding and liberation behavior closely associated with leaching, and also as a function of iron endpoint. Moreover, there is limited physical property data available, such as hardness and breakage of converter matte mineral structures that allows for considering a possible dependence between iron endpoint related mineralogy and the downstream processing characteristics of converter matte. The initial aim of this chapter is to investigate a relationship between indentation hardness, breakage and iron endpoint specific mineralogy of solidified converter matte mineral structures. This, in turn, allows for a subsequent investigation that aims to relate the systematic effect of iron endpoint to the integrated downstream processing characteristics of solidified converter matte.

7.2. Results and Discussion

Of immediate importance is the nano-indentation testing results as empirical physical measurements indicative of the relative hardness of nickel sulfide, copper sulfide and the NiCu-alloy. The indentation-induced breakage of the respective mineral structures are subsequently illustrated and discussed. This is followed by the underlying challenge to associate the mineral indentation hardness and breakage with actual grinding and liberation results, as well as previously published leaching data, within the Lonmin beneficiation framework.

7.2.1. Physical Property

The testing of specific mineral physical properties such as indentation hardness and breakage may be of primary significance in relating the grinding and liberation characteristics of converter matte.

7.2.1.1. Indentation Hardness

Figure 7.1 illustrates the residual hardness impressions for the nano-indentations made on a prepared particle section of the 0.15% Fe matte. The nano-indentation technique is described in Chapter 3 (sub-section 3.5.7).

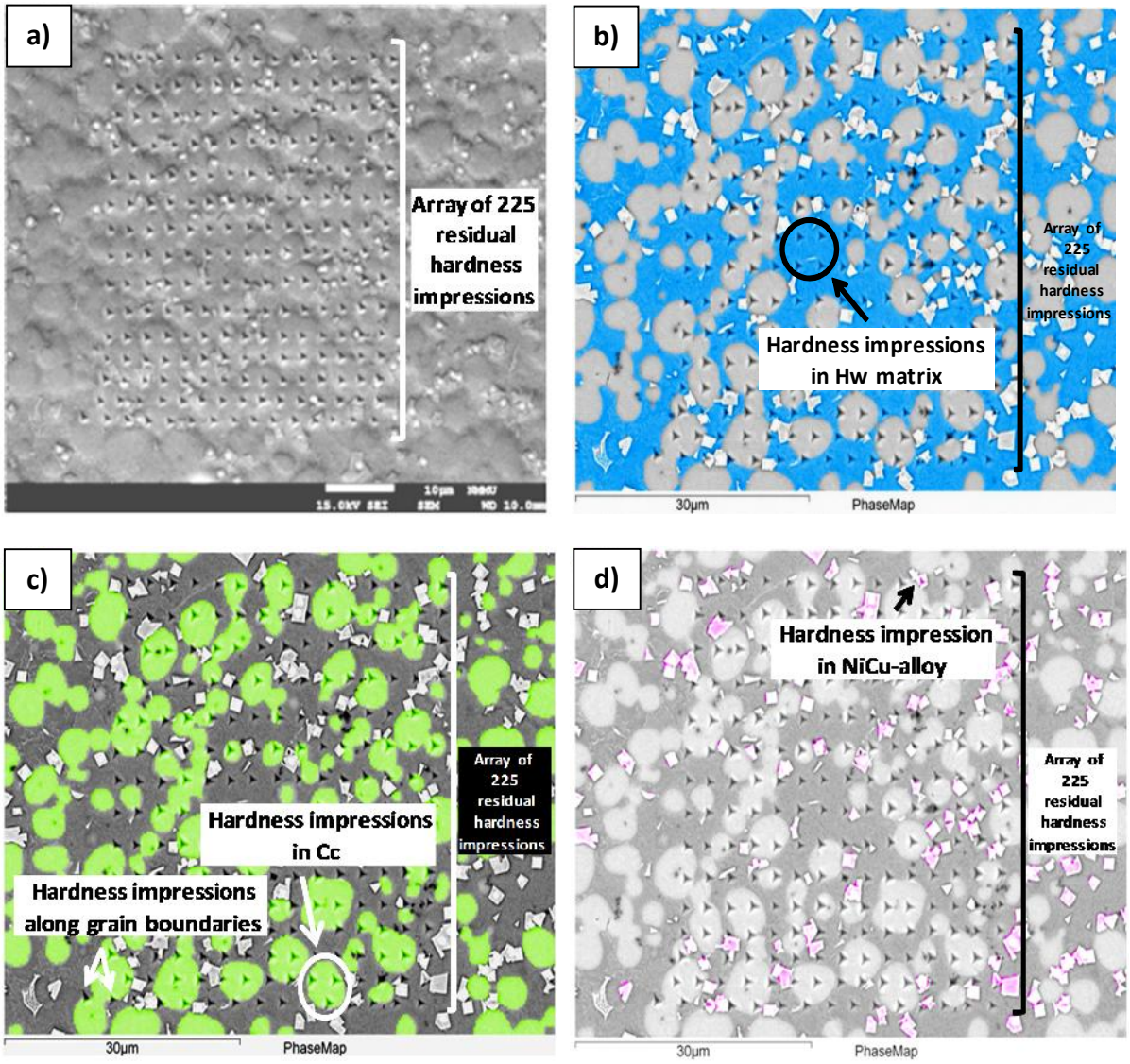

Figure 7.1: Residual hardness impressions on a 0.15% Fe matte particle section are shown with respect to (a) spacing and array arrangement at 10µm size scale, (b) false blue color nickel sulfide (Hw) map, (c) false green color copper sulfide (Cc) map, and (d) false pink color NiCu-alloy map at 30µm size scales, respectively.

The secondary electron micrograph in Figure 7.1(a) indicates a sequential residual hardness impression spacing of approximately 3.5µm. To illustrate the site of specific mineral residual hardness impressions, the compositional micrographs in Figures 7.1(b), (c) and (d) map the

nickel sulfide (Hw) matrix, copper sulfide (Cc) and NiCu-alloy present. Examination of Figure 7.1(b) reveals 66 residual hardness impressions with respect to the Hw matrix. The experimental data obtained during the dynamic loading and unloading of the Hw matrix surfaces indicates an average indentation load and penetration-depth measurement of 4.7mN and 209nm, respectively. Figure 7.1(c) exhibits 61 residual hardness impressions in Cc, with an average indentation load and penetration-depth measurement of 2.3mN and 209nm, respectively. Inspection of Figure 7.1(d) indicates seven residual hardness impressions in the NiCu-alloy, with an average indentation load and penetration-depth value of 5.3mN and 207nm.

Particularly noteworthy in Figures 7.1(b), (c) and (d) are the residual hardness impressions related to mineral boundary surfaces. Close examination of Figures 7.1(b), (c) and (d) reveals 22 residual hardness impressions in Cc/Hw matrix boundaries, with an average indentation load and penetration-depth measurement of 3.7mN and 207nm, respectively. Fifteen residual hardness impressions are associated with NiCu-alloy/Hw matrix boundaries, with an average indentation load and penetration-depth value of 4.4mN and 208nm. Only two residual hardness impressions are related to Cc/NiCu-alloy boundaries, with an average indentation load and penetration-depth measurement of 2.8mN and 208nm.

Similarly to Figure 7.1, the site of residual hardness impressions for nano-indentations made on a prepared particle section of the 5.17% Fe matte with respect to Hw, Cc, NiCu-alloy, magnetite and mineral boundaries is illustrated in Appendix E (Figures E.1 to E.3). It follows from the illustrations in Appendix E that the Hw matrix and Cc surfaces are associated with 96 and 45 residual hardness impressions, respectively. Only three and two residual hardness impressions are related to NiCu-alloy and magnetite, respectively. Moreover, Cc/Hw and NiCu-alloy/Hw matrix boundary surfaces include 49 and nine residual hardness impressions. Two residual hardness impressions are located in Cc/NiCu-alloy boundaries, while a single impression is associated with a vein-like magnetite/Hw matrix boundary.

The principal results of the mineral indentation hardness testing of both the highest and lowest iron-containing mattes are reported in Table 7.1.

Table 7.1: The average and standard deviation of the indentation hardness of solidified converter matte minerals in relation to iron endpoint and in contrast to the relevant mohs-scale.

Mineral	5.17% Fe Matte		0.15% Fe Matte		Mohs-scale
	Average Indentation Hardness (MPa)	Standard Deviation (MPa)	Average Indentation Hardness (MPa)	Standard Deviation (MPa)	
Copper sulfide	2978	407	1975	442	2.5-3.0
Nickel sulfide	5587	483	4456	653	4.0
NiCu-alloy	5670	694	4981	1021	5.0
Magnetite	7786	1066	*N.I	*N.I.	5.5-6.5

* N.I.: Not Indented.

Table 7.1 reports the average indentation hardness of minerals for both iron endpoints in order of increasing value. The softest mineral is copper sulfide, which exhibits the highest average indentation hardness of 2978MPa within the 5.17% Fe matte. The standard deviation reports the extent of dispersion from the average indentation hardness. The increasingly harder minerals are nickel sulfide and NiCu-alloy, which also demonstrates the highest average indentation hardness within the 5.17% Fe matte. Magnetite is found to be the hardest mineral within the 5.17% Fe matte, with an average hardness of 7786MPa.

In the literature, there is sparse micro-hardness data available pertaining to converter matte mineral structures with which to compare the results in Table 7.1. For this reason the results are compared to mohs-scale hardness. Chalcocite (Cu_2S) and healewoodite (Ni_3S_2) natural minerals score a conventional mohs-scale hardness of 2.5-3 and 4, respectively, in Table 7.1. Awaruite (Ni_3Fe), the natural alloy of nickel and iron, and magnetite (Fe_3O_4), meanwhile, score a mohs-scale hardness of 5 and 5.5-6.5, respectively, in Table 7.1. The average indentation hardness of mineral structures in Table 7.1 is thus in good agreement with the corresponding order of the conventional mohs-scale hardness. This is almost certainly a first comparison and plausible agreement. In addition, Figure 7.2 illustrates the indentation hardness of particular minerals within the 0.15% Fe matte as a function of the measured penetration-depth.

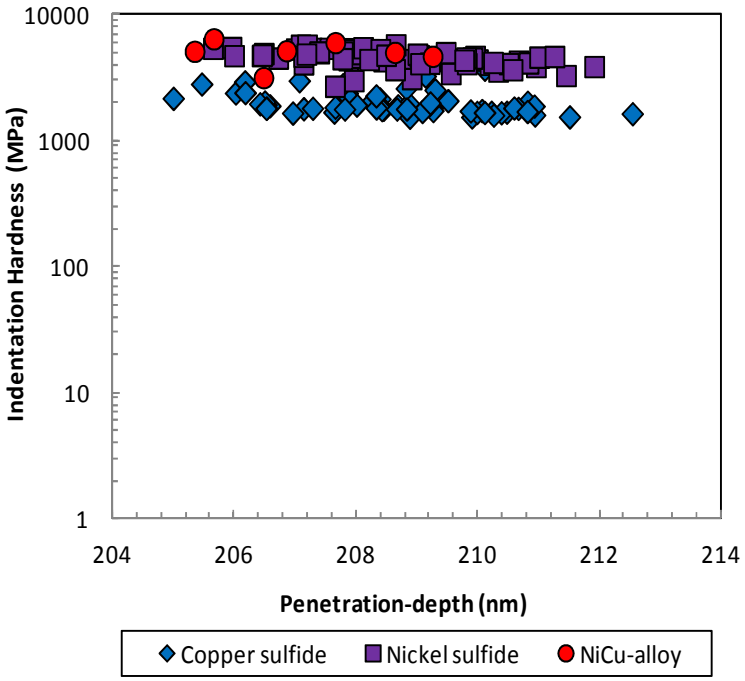

Figure 7.2: The indentation hardness of copper sulfide, nickel sulfide and NiCu-alloy within the 0.15% Fe matte as a function of penetration-depth.

The differences in indentation hardness within and between copper sulfide, nickel sulfide and NiCu-alloy are apparent from the respective plots in Figure 7.2. It is notable from the experimental data obtained that the softer the mineral, the lower the applied load required to attain a similar penetration-depth. Figure 7.2 also displays a modest decrease in the specific mineral hardness with increasing penetration-depth.

The principal results of the mineral boundary indentation testing of both the 5.17% and 0.15% Fe mattes are reported in Table 7.2. The average indentation hardness of the relevant mineral boundaries within the 5.17% and 0.15% Fe mattes is reported in order of increasing values in Table 7.2. The copper sulfide/NiCu-alloy boundary is the softest, and displays the highest average indentation hardness of 3124MPa within the 5.17% Fe matte. According to this table, the copper sulfide/nickel sulfide and NiCu-alloy/nickel sulfide boundaries are harder, particularly, within the 5.17% Fe matte. A single vein-like magnetite/nickel sulfide boundary exhibits the highest average indentation hardness of 5225MPa, also within the 5.17% Fe matte.

Table 7.2: The average and standard deviation of the boundary indentation hardness of solidified converter matte minerals with respect to iron endpoint.

Mineral Boundary	5.17% Fe Matte		0.15% Fe Matte	
	Average Indentation Hardness (MPa)	Standard Deviation (MPa)	Average Indentation Hardness (MPa)	Standard Deviation (MPa)
Copper sulfide/ NiCu-alloy	3124	59	2396	674
Copper sulfide/ Nickel sulfide	4490	586	3410	548
NiCu-alloy/ Nickel sulfide	4769	831	4032	562
Vein-like magnetite/ Nickel sulfide	5225	—	*N.I.	*N.I.

* N.I.: Not Indented.

Figure 7.3 illustrates the boundary indentation hardness within the 0.15% Fe matte in relation to the penetration-depth achieved.

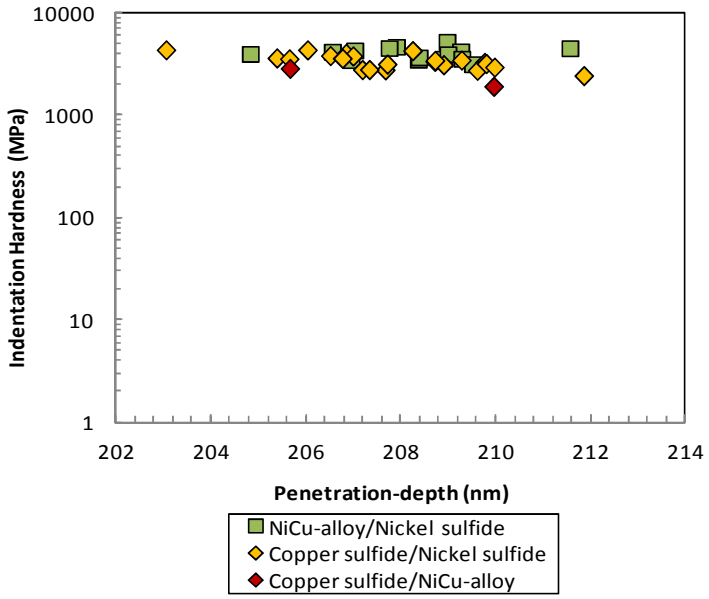

Figure 7.3: The indentation hardness of the copper sulfide/NiCu-alloy, copper sulfide/nickel sulfide and NiCu-alloy/nickel sulfide mineral boundaries within the 0.15% Fe matte as a function of penetration-depth.

The distinction between the specific boundary indentation hardness in Figure 7.3 is not as apparent as the differences in specific mineral indentation hardness, shown previously in Figure 7.2. Mineral boundaries are regarded as discontinuities of the crystal structure and as a weakness in the mechanical strength of minerals. The effect on the plots in Figure 7.3 is manifested by overlapping values in boundary indentation hardness. The presence of pre-existing fractures and pores, which develop during the solidification process, can possibly contribute to some uncertainty in the boundary indentation hardness obtained. This requires further investigation. Figure 7.3 also demonstrates a small decrease in the indentation hardness for the copper sulfide/nickel sulfide boundaries as a function of increasing penetration-depth.

An understanding based on elasto-plastic deformation as an indicator of the mineral and boundary indentation hardness would have to consider relations between physical properties, mineralogy and mineral chemistry. Vaughan and Craig (1978) found that the physical properties of natural sulfide minerals are closely linked to the composition achieved and, hence, mineralogy. The non-stoichiometry of the converter matte mineral structures, as found in Chapter 5 (sub-sections 5.2.1.1 and 5.2.1.2), is expected to influence indentation hardness. This is possibly manifested in the variability of the specific mineral and boundary indentation hardness observed in Figures 7.2 and 7.3.

Figure 7.4 provides useful representations of the indentation hardness for the minerals tested within the grid of the 0.15% Fe matte.

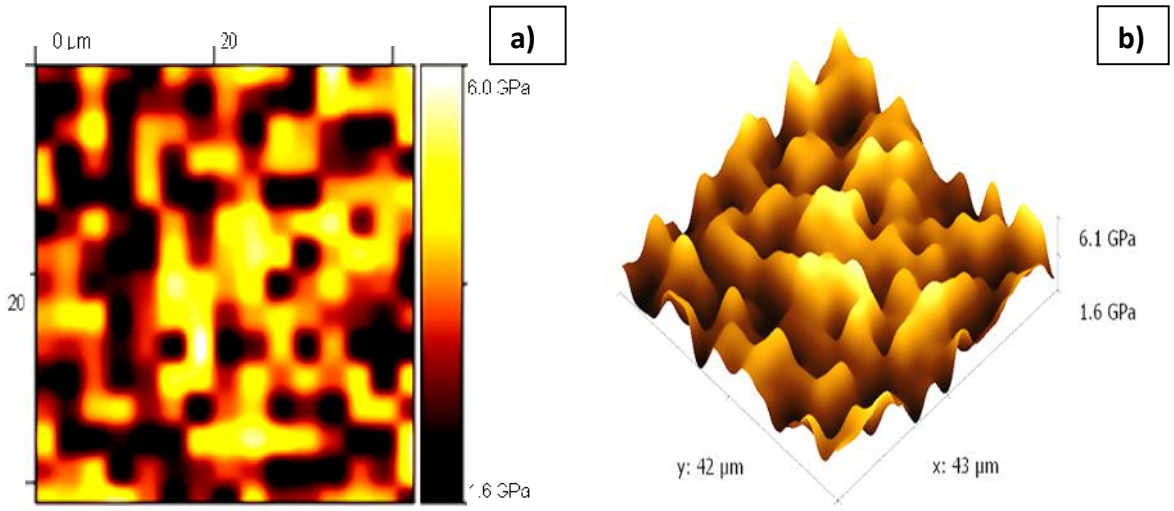

Figure 7.4: The representation of collected indentation test data within the grid of the 0.15% Fe matte through the use of (a) 2D hardness mapping and (b) 3D surface response.

Figure 7.4(a) presents a 2D hardness map that is correlated to the indentation test data collected within the particular grid. The 3D surface response, shown in Figure 7.4(b), demonstrates that the combined indentation hardness for the grid is probably controlled by the harder nickel sulfide and NiCu-alloy, as indicated by the respective peak areas. The average indentation hardness for the grid is calculated to be 3392MPa. Considering mineral abundance, this finding suggests that particle and hence composite bulk indentation hardness is likely controlled by the nickel sulfide and NiCu-alloy present. The average indentation hardness for the grid on the 5.17% Fe matte particle section is calculated to be 4669MPa, which is evidently higher than for the 0.15% Fe matte.

7.2.1.2. Breakage

The breakage that occurs as a result of the application of a single indentation-induced force to mineral surfaces within the 0.15% Fe matte is illustrated in Figure 7.5. The indentation-induced breakage technique is described in Chapter 3 (sub-section 3.5.7).

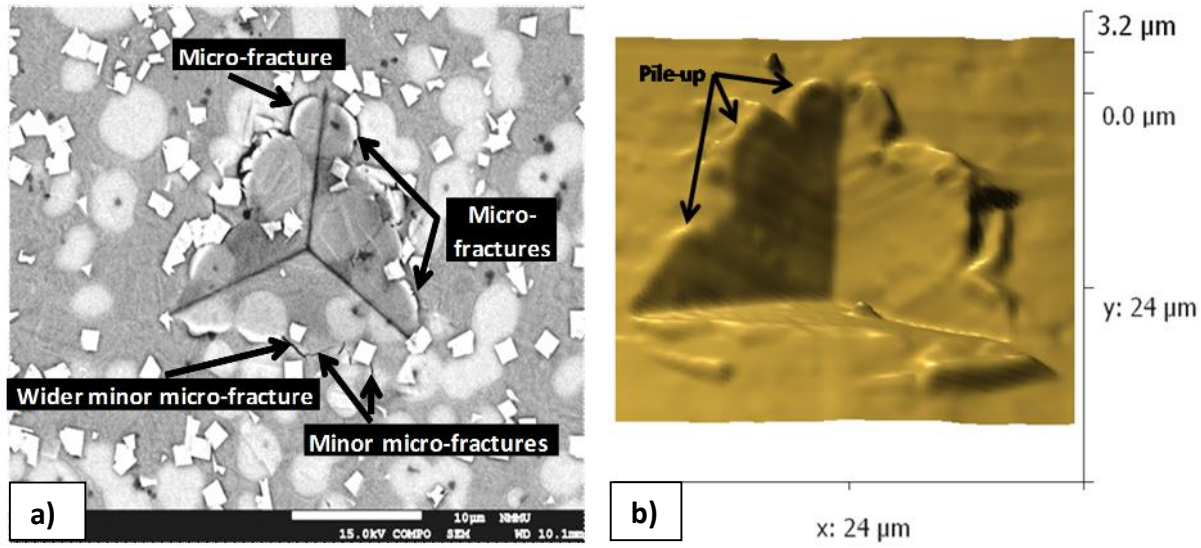

Figure 7.5: Single indentation-induce breakage of mineral surfaces within the 0.15% Fe matte showing (a) a residual impression at 10µm size scale and (b) a 3D topographical micrograph of the corresponding residual impression, including pile-up.

Figure 7.5(a) indicates fracture patterns essentially aligned with the corners of the residual impression. Micro-fractures are evident along curving copper sulfide boundaries in Figure 7.5(a). Minor micro-fractures occur on the surface of the nickel sulfide matrix in Figure 7.5(a), with a few appearing wider, and seem to extend deeper into the surface. Several of

the micro-fractures can be associated with mineral boundary damage. A 3D topographical micrograph, shown in Figure 7.5(b), suggests considerable pile-up around the damaged curved copper sulfide boundaries. The residual depth of the impression in Figure 7.5(b) is indicated as 3.2µm.

Figure 7.6 allows for an assessment of indentation-induced breakage across a larger surface area within the 0.15% Fe matte by using an array of nine overlapping residual impressions.

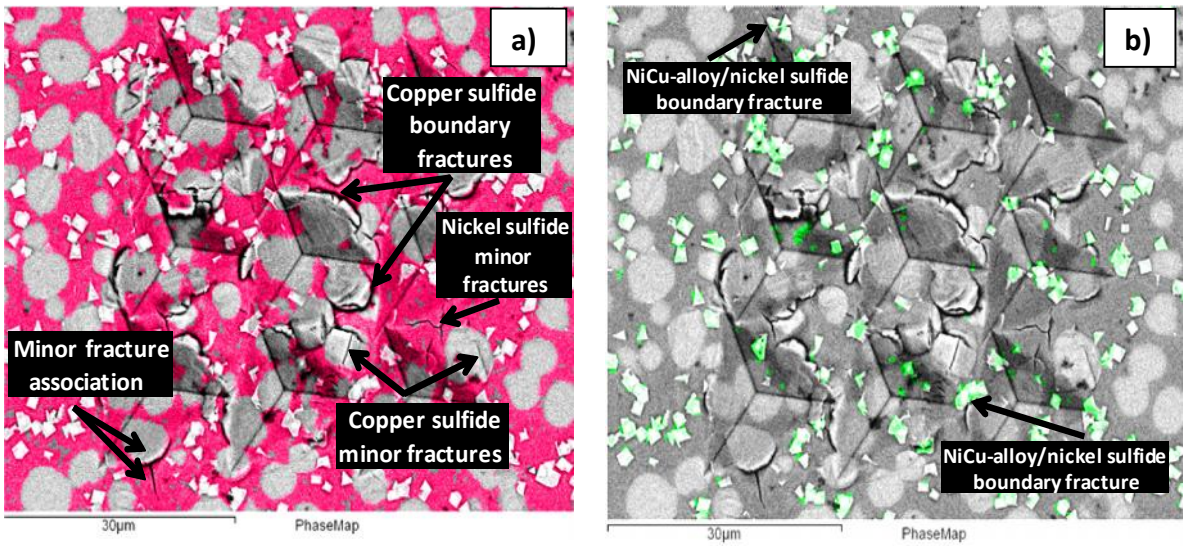

Figure 7.6: Multiple indentation-induced breakage with respect to (a) a false red color nickel sulfide map and (b) a false green color NiCu-alloy map at 30µm size scales, respectively.

Examination of Figures 7.6(a) and (b), using false color mapping, indicates that the minerals exhibit comparable damage and fracture patterns to that resulting from the single indentation-induced breakage, shown previously in Figure 7.5(a). A noticeable difference is the presence of minor fractures within the copper sulfide minerals, which is annotated in Figure 7.6(a). These minor fractures can also be associated with copper sulfide boundary and nickel sulfide fractures. This is shown in Figure 7.6(a). Examination of Figure 7.6(b) reveals that only boundary damage and fracture patterns can be associated with the NiCu-alloy.

The breakage of copper sulfide, nickel sulfide and NiCu-alloy under indentation loading, within the 0.15% Fe matte, appears to be related to the indentation hardness achieved. The softest mineral, which is copper sulfide, provides evidence that boundaries act as sites for stress concentration. It follows that when the local boundary elasto-plastic limit of copper

sulfide is exceeded, minute fractures may initiate, with incremental propagation to minor- and micro-fractures. The elasto-plastic limit of many natural sulfide minerals, including copper sulfide, is not known. The boundary fractures of copper sulfide minerals are also irregularly associated with minor fractures within the minerals. Copper sulfide minerals therefore seem to display brittle behavior under indentation loading and, as a consequence, may be easy to grind.

There is a smaller degree of breakage attainable for the harder nickel sulfide matrix. In comparison, a notable lack of breakage is attained for the NiCu-alloy, which suggests ductile behavior under indentation loading. This may render the NiCu-alloy more resistant to grinding. Although the indentation-induced breakage of minerals within the 5.17% Fe matte was not tested, a similar order of mineral breakage is expected as to that described above, with probably less damage and less developed fractures. This expectation is based on the higher average indentation hardness achieved for minerals tested within the 5.17% Fe matte.

It is, furthermore, reasonable to expect that different mineral breakage characteristics, would during grinding of converter matte, result in correspondingly different mineral breakage rates, liberation and breakage energy requirements. Knowledge of the mineral breakage rates in relation to indentation hardness and breakage mechanisms can be used to understand why and how swiftly matte particles are reduced to sizes within the mineral grain scale and removed accordingly from the actual grinding process, and also as a function of iron endpoint.

7.2.2. Batch Grinding Characteristics

The laboratory batch grinding testwork conducted with respect to the solidified 5.17% and 0.15% Fe mattes is described in Chapter 3 (section 3.7). The following sub-sections include the results and discussion of the specific energy-particle size reduction relationship, in addition to the particle and mineral breakage rates.

7.2.2.1. Specific Energy-Particle Size Relationship

Figure 7.7 shows the matte feed size distributions on a linear ordinate and logarithmic abscissa resulting from using a √2-series of sieves from 6.70mm to 53µm.

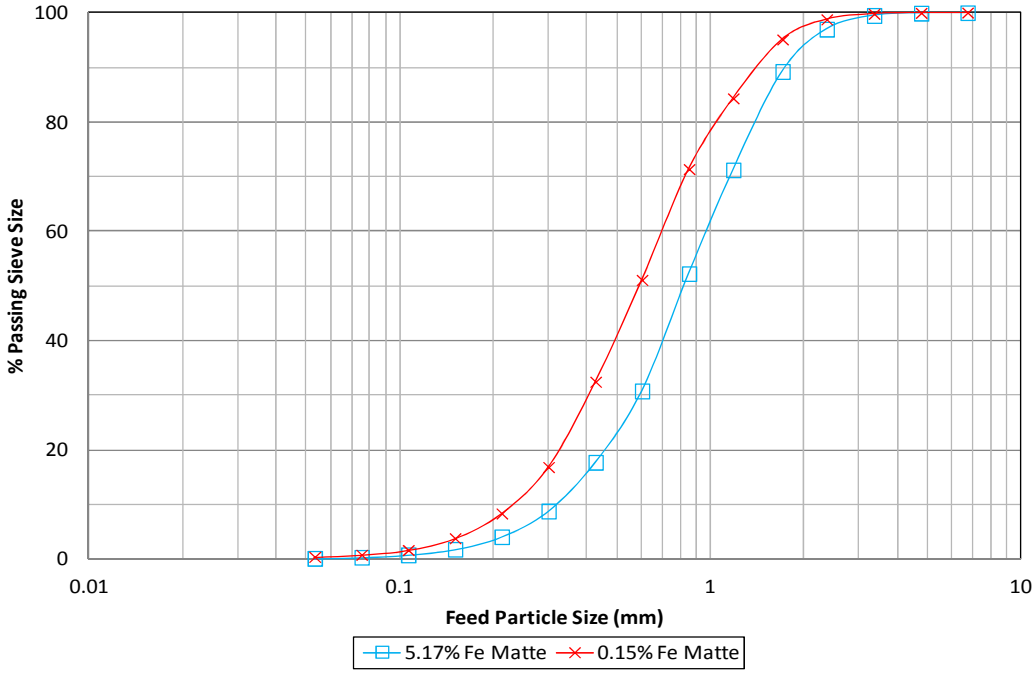

Figure 7.7: Feed particle size distributions of the solidified 5.17% and 0.15% Fe mattes obtained through √2-series sieve analysis.

The cumulative mass percentage passing sieve size is plotted against the feed particle size in Figure 7.7. The feed particle size data is available for assessment in Appendix F (Tables F.1 and F.2). The particle size distribution for both mattes in Figure 7.7 exhibits similarly shaped plots, which can be regarded as characteristic of a Gaudin-Schuhmann size distribution, as described by Crabtree et al., (1964). The particle size distribution plot for the 5.17% Fe matte in Figure 7.7 appears distinctly coarser compared to that of the 0.15% Fe matte. This is particularly evident in the -2.36mm to +150µm size range and is pronounced for the cumulative mass percentage passing the 600µm sieve size. The latter passing the 600µm sieve size is 30.77% for the 5.17% Fe matte, in contrast to 51.07% for the 0.15% Fe matte. This demonstrates that more particles present within the 0.15% Fe matte feed are smaller than 600µm compared to particles within the 5.17% Fe matte.

It was previously found in Chapter 4 (sub-section 4.2.4.1) that the dominant nickel sulfide and copper sulfide grains within particles of the 0.15% Fe matte also appear smaller than the corresponding grains within particles of the 5.17% Fe matte. This seems to suggest that particle sizes can implicitly be linked to grain sizes and may, therefore be regarded as an effect of the iron endpoint. This would imply that the difference in particle size distributions

observed in Figure 7.7 is a systematic consequence of the effect of the converter iron endpoint achieved. It is assumed that practical operational conditions did not contribute to the observed differences in grain and particle sizes. Figure 7.8 shows the product size distribution and breakage resulting from grinding the respective matte feed at 5kWh/t specific energy input in a laboratory ball mill.

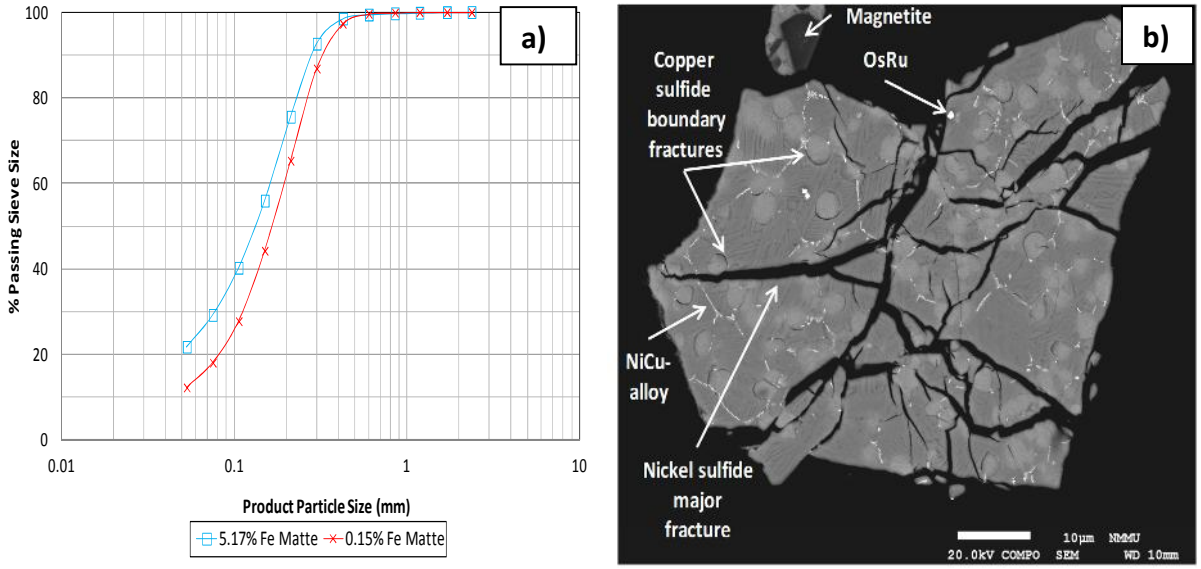

Figure 7.8: Laboratory ball mill grinding of the 5.17% and 0.15% Fe matte feed at 5kWh/t specific energy with respect to (a) product size distribution and (b) breakage of a particle fragment of the 5.17% Fe matte at 10µm size scale.

Most interesting in Figure 7.8(a) is the comparative coarser product size distribution plot below the 600µm size ranges for the 0.15% Fe matte. This is contrary to the initial feed particle size distributions shown in Figure 7.7. However, the product size distribution plot for the 5.17% Fe matte in Figure 7.8(a) remains fractionally coarser in the -2.36mm to +600µm size range. This is not apparent from the product size distribution plots in Figure 7.8(a) due to the congestion of data points in the coarse end. The product size data resulting from grinding at 5kWh/t is reported in Appendix F (Tables F.1 and F.2) for examination. Ninety percent of the product from the industrial batch grinding unit within the Lonmin BMR is required to be less than 100µm (Bircumshaw, 2008). Figure 7.8(a) demonstrates that grinding at 5kWh/t specific energy results in 40.17% of the product mass passing the 106µm sieve size for the 5.17% Fe matte compared to 27.64% for the 0.15% Fe matte.

Figure 7.8(b) illustrates ball mill-induced breakage of what seems to be a particle fragment of the 5.17% Fe matte. The coarser particle fragment as a result appears interlocked in smaller fragments. Crabtree et al., (1964) found that impact, abrasion and chipping interactions are responsible for particle size reduction due to grinding. Examination of the ball mill-induced breakage in Figure 7.8(b) mostly suggests a comparable mineral response to that found previously under indentation loading, albeit for the 0.15% Fe matte. A particular difference though, which is evident in Figure 7.8(b), is the noticeably larger or major fractures associated with the nickel sulfide matrix. These fractures are excessively larger than the copper sulfide boundary fractures, both in Figure 7.8(b) and induced under indentation loading.

Figure 7.8(b) also illustrates a lack of breakage attained for the vein-like NiCu-alloy, OsRu-alloy and magnetite present. This is in agreement with the response of NiCu-alloy under indentation loading. It is reasonable to suggest that further grinding at a higher specific energy input may be required to liberate the vein-like NiCu-alloy and OsRu-alloy in Figure 7.8(b) from the nickel sulfide matrix. The product size distribution and breakage resulting from further grinding the matte feed at 15kWh/t specific energy input is illustrated in Figure 7.9.

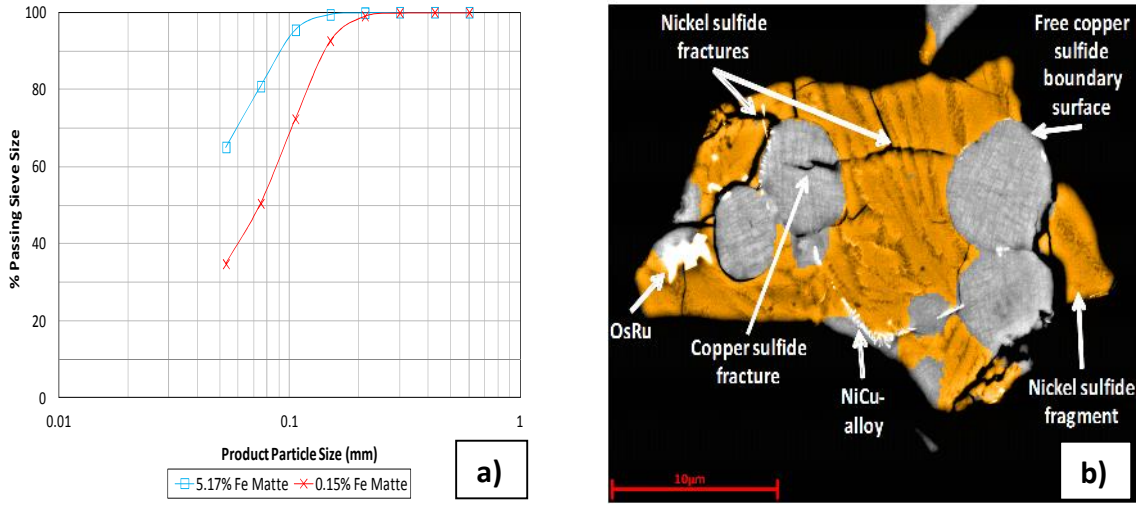

Figure 7.9: Laboratory ball mill grinding at 15kWh/t specific energy of the 5.17% and 0.15% Fe matte feed with respect to (a) product size distribution and (b) particle fragmentation of the 5.17% Fe matte at 10µm size scale.

The product size distribution plot for the 0.15% Fe matte in Figure 7.9(a) appears decreasingly coarser in the size ranges below 600µm compared to that of the 5.17% Fe

matte. The product size data is available for examination in Appendix F (Tables F.1 and F.2). Figure 7.9(a) shows that grinding at 15kWh/t specific energy yields 95.45% of the product mass being less than 106µm for the 5.17% Fe matte in contrast to 72.32% for the 0.15% Fe matte.

Figure 7.9(b), aided by false color mapping of the nickel sulfide matrix, displays ball mill-induced breakage of a resultant smaller particle fragment of the 5.17% Fe matte. The decreasing particle fragment in Figure 7.9(b) exhibits a similar mineral breakage mechanism for the copper sulfide and nickel sulfide matrix to that found previously for grinding at 5kWh/t specific energy. It is interesting to note the available free copper sulfide boundary surface and nickel sulfide fragment in Figure 7.9(b). The NiCu-alloy and OsRu-alloy, in Figure 7.9(b), remains locked within the nickel sulfide matrix and is mostly unaffected by the increase in specific grinding energy. However, the OsRu-alloy in Figure 7.9(b) appears to have been deformed by the grinding interactions. Figure 7.10 shows the final product size distribution and breakage resulting from grinding the matte feed at 25kWh/t specific energy input.

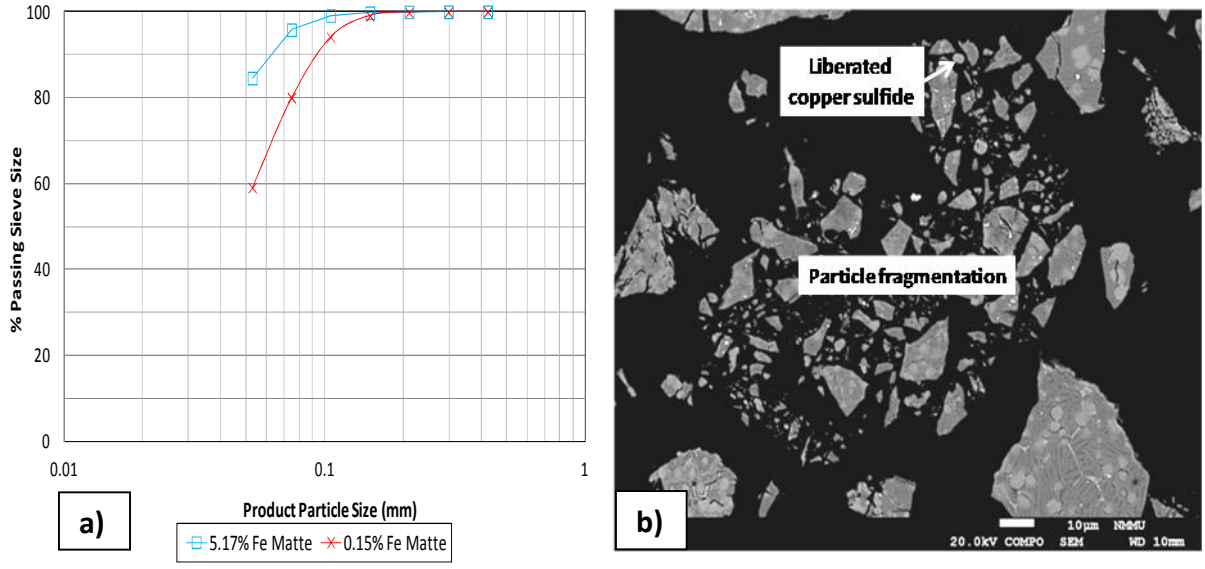

Figure 7.10: Laboratory ball mill grinding at 25kWh/t specific energy of the 5.17% and 0.15% Fe matte feed with respect to (a) final product size distribution and (b) particle fragmentation of the 5.17% Fe matte at 10µm size scale.

The product size distribution plot for the 0.15% Fe matte in Figure 7.10(a) appears coarser in the size ranges below 425µm compared to that of the 5.17% Fe matte. The final product size

data is also available for assessment in Appendix F (Tables F.1 and F.2). Grinding at 25kWh/t specific energy results in 99.17% of the product mass passing the 106µm sieve size for the high iron-containing matte in contrast to 94.09% for the low iron-containing matte. This is displayed in Figure 7.10(a). Figure 7.10(b) shows particle fragments of the 5.17% Fe matte characteristic of the corresponding size distribution plot in Figure 7.10(a). A liberated copper sulfide mineral is also annotated in Figure 7.10(b). In order to acquire a measurable understanding of fragmentation, the breakage rates of particles are considered in the following sub-section.

7.2.2.2. Particle Breakage Rates

It is difficult in most cases to separate the breakage rate from the discharge rate expressed in equation 3.3 within Chapter 3 (section 3.7). For simplicity, the two are combined and plotted as the logarithmic r/d versus product particle size. The breakage and discharge rates are represented by r and d, respectively. For batch grinding systems, this would provide the breakage rate directly since there is no discharge. Figure 7.11 shows the effect of specific energy on the logarithmic r/d versus product particle size relationship for the 5.17% and 0.15% Fe mattes.

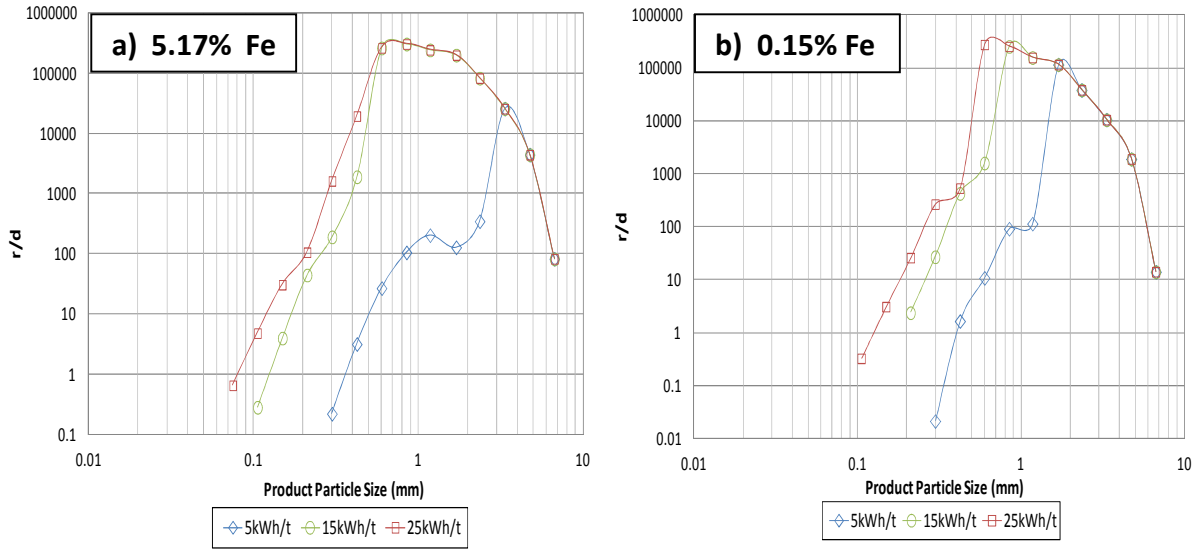

Figure 7.11: Effect of specific energy on the logarithmic r/d versus product particle size relationship for the (a) 5.17% and (b) 0.15% Fe mattes.

Figure 7.11(a) shows that the r/d ratio increases with an increase in specific energy for product particles of the 5.17% Fe matte in the +75µm to -3.35µm size range. It follows that

the breakage rates are the lowest when the specific energy is 5kWh/t, whereas the breakage rates are the highest when the specific energy is 25kWh/t. The increase in breakage rates with an increase in specific energy can be attributed to the higher amount of energy available for breakage. It is noteworthy that for product particle sizes above 3.35mm, the breakage rates at 5, 15 and 25kWh/t specific energy are largely similar and decrease with an increase in the product particle size. More than 95% of particle feed material for all tests are below 3.35mm in size. This means that there are considerably fewer matte particles present in the size fraction greater than 3.35mm to cause significant differences in the breakage rates at the various specific energies.

The decrease in breakage rates for product particles above 3.35mm may have been as a result of a cushioning effect of fine particles on potentially breakable coarse particles, resulting in poor fragmentation. Another reason for the decrease in breakage rates for particles above 3.35mm may be that the particles are too large relative to the media size, resulting in poor media-particle contact. Figure 7.11(b) shows that the r/d ratio increases with an increase in specific energy for product particles of the 0.15% Fe matte in the +106µm to -1.7mm size range. The reasons for the decrease in breakage rates at the coarse end in Figure 7.11(b) are similar to those proposed for Figure 7.11(a).

The breakage rates are subsequently compared with respect to iron endpoint at constant specific energy. Figure 7.12 shows the effect of the iron endpoint on the logarithmic r/d versus product particle size relationship at 5kWh/t specific energy. Figure 7.12 demonstrates that the breakage rates for the 5.17% Fe matte are higher at the coarse (+3.35mm to -6.7mm) and fine (+300µm to -1.7mm) ends compared to that for the 0.15% Fe matte. However, the breakage rates for the 0.15% Fe matte are higher in the intermediate (+1.7mm to -3.35mm) size range, in contrast to that for the 5.17% Fe matte. It is reasonable to expect particle breakage rates to be influenced by the grinding response of the variable constituent minerals. This may have resulted in the differences in breakage rates observed between the 5.17% and 0.15% Fe mattes.

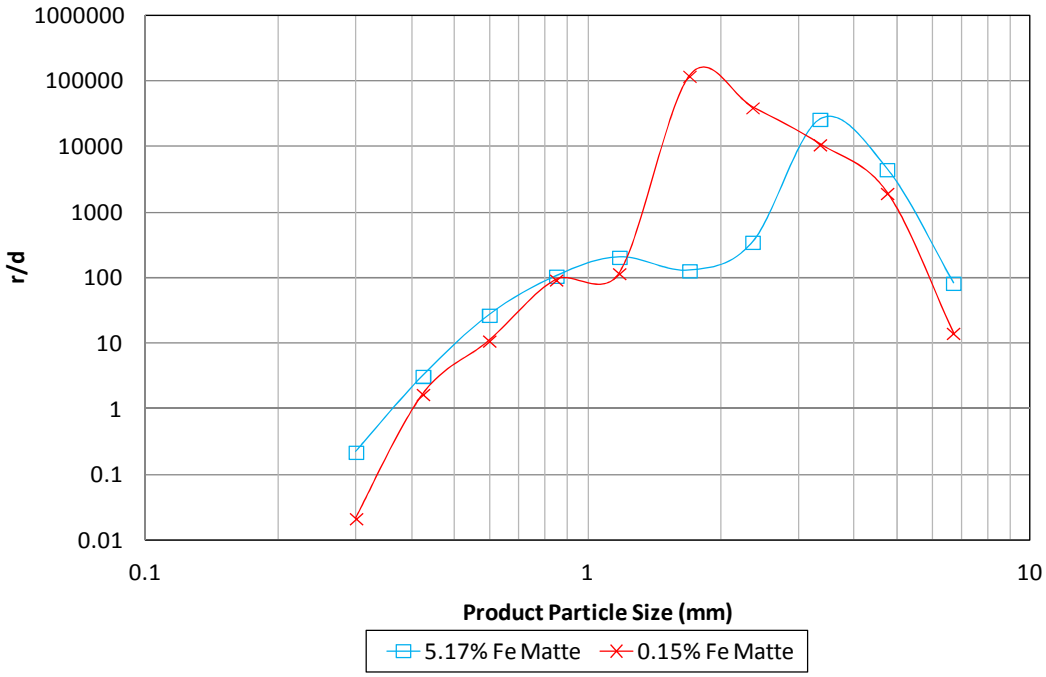

Figure 7.12: Effect of the iron endpoint on the breakage rates of the 5.17% and 0.15% Fe mattes at 5kWh/t specific energy.

Figure 7.13 shows the effect of the iron endpoint on the logarithmic r/d versus product particle size relationship for the 5.17% and 0.15% Fe mattes at 15kWh/t and 25kWh/t specific energy.

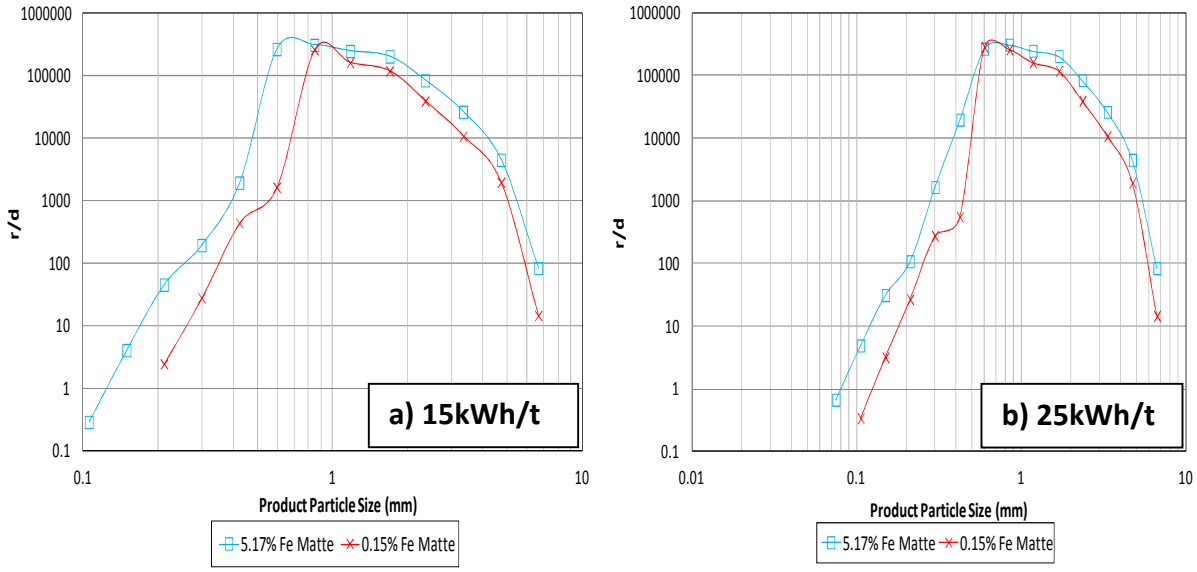

Figure 7.13: Effect of the iron endpoint on the breakage rates of the 5.17% and 0.15% Fe mattes at (a) 15kWh/t and (b) 25kWh/t specific energy.

Figure 7.13(a) shows that at 15kWh/t specific energy, the breakage rates are higher for the 5.17% Fe matte in contrast to that for the 0.15% Fe matte. Similarly, at 25kWh/t specific energy, as demonstrated in Figure 7.13(b), the breakage rates are higher for the 5.17% Fe matte compared to that for the 0.15% Fe matte. These findings indicate that it is eventually easier to grind particles of the 5.17% Fe matte than particles of the 0.15% Fe matte. This is in agreement with the grinding response of the nickel sulfide matrix of the 5.17% Fe matte observed in Figures 7.8(b), 7.9(b) and 7.10(b) in sub-section 7.2.2.1 of this chapter. It was previously found in Chapter 4 (sub-section 4.2.3) that nickel sulfide constitutes 77.89% and 63.67% of the minerals present within the 5.17% and 0.15% Fe mattes, respectively. The dominant abundance of this mineral within the 5.17% Fe matte would have increased the media-nickel sulfide contact and may have contributed to the higher breakage rates observed.

During particle grinding of both mattes at 15kWh/t and 25kWh/t specific energy, the breakage rates increase with an increase in particle size to a peak, and thereafter decrease with a further increase in particle size. The peaks seen in Figures 7.13(a) and (b) are a manifestation of the decrease in breakage rates in the fine end due to an increase in particle strength and a decrease in the breakage rates in the coarse end. The latter could be due to either a cushioning effect of breakable coarse particles by fines or coarse particles being too large relative to the media.

7.2.2.3. Mineral Breakage Rates

The breakage rates of minerals seemingly influence that of the host particles and are therefore considered below. The effect of specific energy on the logarithmic r/d versus grain size relationship of copper sulfide present within the 5.17% and 0.15% Fe mattes is illustrated in Figure 7.14.

Figures 7.14(a) and (b) indicate that the r/d ratio of copper sulfide of the 5.17% Fe and 0.15% Fe mattes mainly increases in accordance with an increase in specific energy. The breakage rates of copper sulfide minerals are the highest at 25kWh/t specific energy for both mattes. Comparable trends in breakage rates for the respective host particles of this mineral were previously displayed in Figures 7.11(a) and (b). More than 80% of the mineral feed material for the different investigations is less than 32µm. There are consequently

fewer copper sulfide grains present in the +32µm size fraction that can be considered significant. Nonetheless, the breakage rates observed in Figures 7.14(a) and (b) appear unaffected in the coarse end by possible cushioning of breakable copper sulfide grains by fines and also poor media-grain contact.

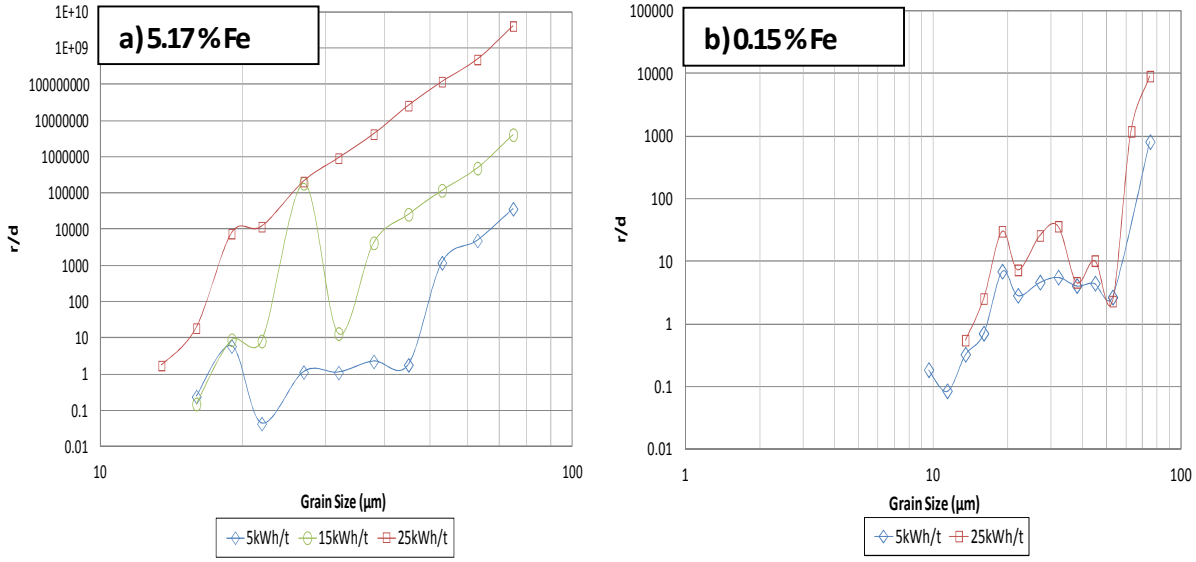

Figure 7.14: Effect of specific energy on the logarithmic r/d versus grain size relationship of copper sulfide present within the (a) 5.17% and (b) 0.15% Fe mattes.

The effect of the iron endpoint on the logarithmic r/d versus grain size relationship of copper sulfide found within both mattes at 5kWh/t and 25kWh/t specific energy is demonstrated in Figure 7.15.

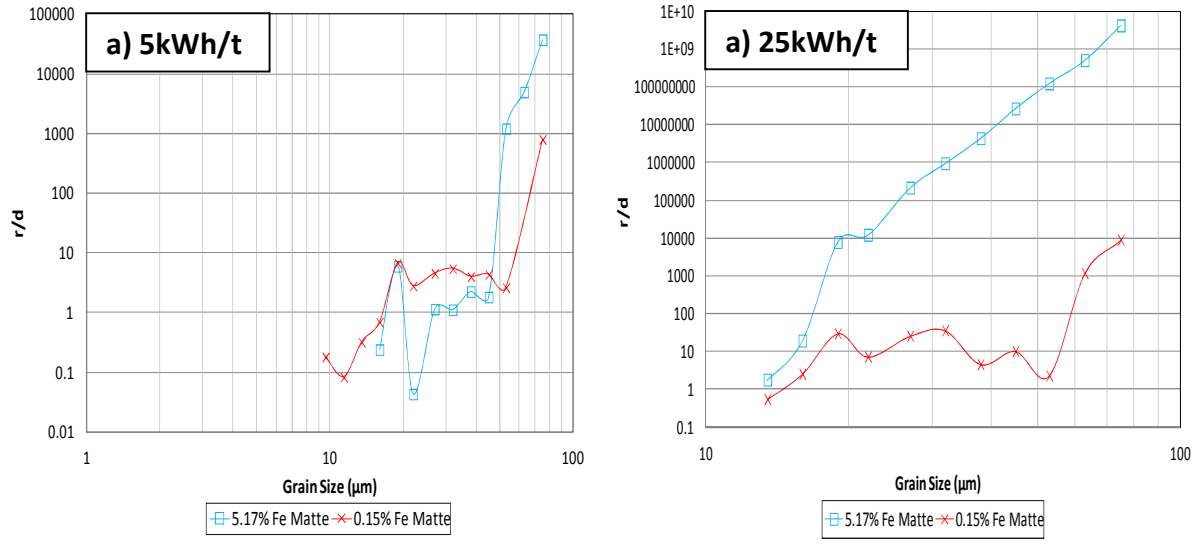

Figure 7.15: Effect of the iron endpoint on the breakage rates of copper sulfide found within the 5.17% Fe and 0.15% Fe mattes at (a) 5kWh/t and (b) 25kWh/t specific energy.

The breakage rates of copper sulfide in the 5.17% Fe matte, observed in Figure 7.15(a), are higher in the +53µm to -75µm size range, in contrast to that for the 0.15% Fe matte. The breakage rates of copper sulfide for the 0.15% Fe matte are higher, though, in the +8.1µm to -53µm size range. The comparatively higher breakage rates of this mineral in the 0.15% Fe matte at 5kWh/t may be interrelated with the higher breakage rates previously observed in Figure 7.12 for the host particles in an intermediate size range. Moreover, the breakage rates of copper sulfide at 5kWh/t for both mattes appear lower overall than the breakage rates of the host particles at the same specific energy.

Figure 7.15(b) shows that the breakage rates at 25kWh/t are ultimately higher for copper sulfide in the 5.17% Fe matte compared to that of the mineral in the 0.15% Fe matte. This finding is thus in agreement with that observed for the respective host particles at 25kWh/t specific energy. Figure 7.15(b) further demonstrates a decrease in breakage rates with a decrease in grain size. The decrease in breakage rates is considered a consequence of the increasing grain strength with decreasing grain size.

The influence of specific energy on the logarithmic r/d versus grain size relationship of the NiCu-alloy found within the 0.15% Fe matte is shown in Figure 7.16.

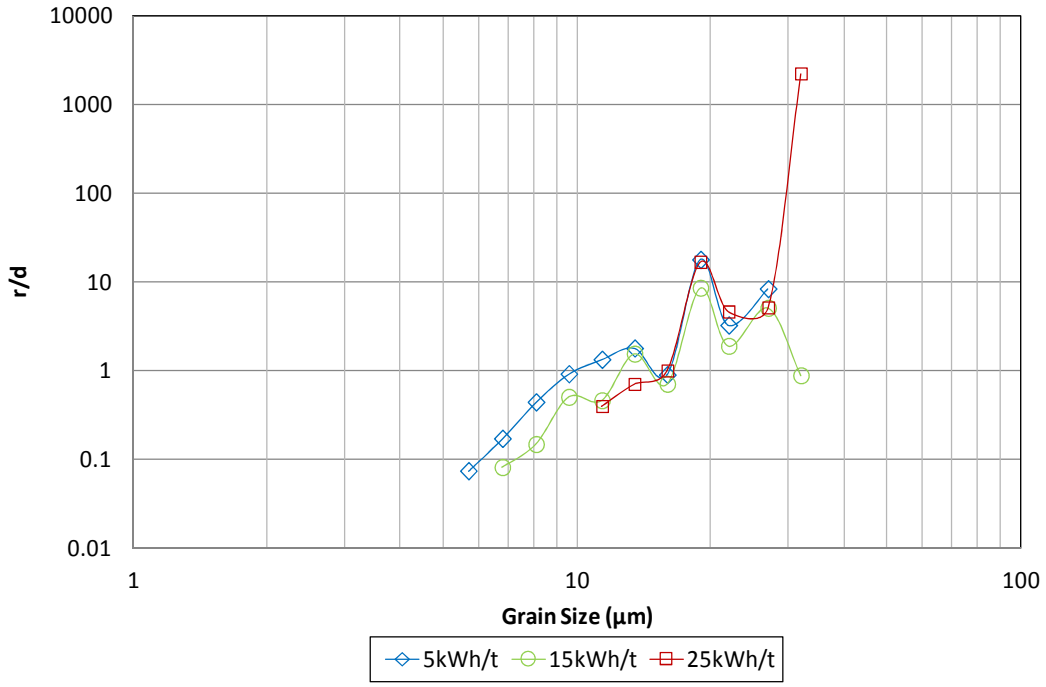

Figure 7.16: Effect of specific energy on the logarithmic r/d versus grain size relationship of the NiCu-alloy present within the 0.15% Fe matte.

The r/d ratio of the NiCu-alloy for the 0.15% Fe matte, displayed in Figure 7.16, fluctuates with an increase in specific energy. This is in contrast to the apparent trends in breakage rates observed previously for copper sulfide and particles of both mattes. However, Figure 7.16 shows that the breakage rates also decrease, overall, in relation to decreasing grain size for a specific energy. In excess of 70% of the NiCu-alloy feed material for all investigations is below 13.5µm in size. The breakage rates of the NiCu-alloy at 5, 15 and 25kWh/t for the 0.15% Fe matte seem lower than that of the associated copper sulfide and host particles. These lower breakage rates support a previous suggestion in sub-section 7.2.1.2 of this chapter that the NiCu-alloy is probably more challenging to grind than nickel sulfide and copper sulfide. The results displayed in Figure 7.16 may also reflect elasto-plastic deformation of the NiCu-alloy with limited attainment of actual breakage. In Chapter 4 (sub-section 4.2.3), it was shown that the 0.15% Fe matte contains 14.23% of the NiCu-alloy compared to 0.80% for the 5.17% Fe matte. The higher abundance of this alloy in the 0.15% Fe matte could have contributed to the comparatively lower particle breakage rates observed for this particular matte.

In summation, the initial matte feed of the 5.17% Fe matte is characterized by a coarser particle size distribution than that of the 0.15% Fe matte. The laboratory batch grinding of the converter mattes at specific energy inputs resulted in iron endpoint related product size distributions. A significant finding, which is contrary to the researcher's expectation, is that a smaller measure of specific energy would be necessary to produce the required product size for the Lonmin BMR using the 5.17% Fe matte. The comparative trends observed in breakage rates for particles and minerals are largely supportive of this finding.

It would appear that most of the specific energy available for grinding is expended breaking the nickel sulfide matrix. A higher degree of breakage is achieved for the nickel sulfide matrix of the 5.17% Fe matte. Considering a 3D rectangular volume, as shown in Chapter 5 (Figure 5.10(a), sub-section 5.2.3.2), it is conceivable that a large network of fractures, coupled to increase media-matrix contact, can result in the rapid size reduction of the initial particles and sulfide minerals within the 5.17% Fe matte. In addition, Vaughan and Craig (1978) reported that a constituent iron concentration of more than two percent can render sulfide minerals increasingly brittle. This requires further investigation with respect to

sulfide minerals present within the high iron-containing matte. Nevertheless, this sub-section has developed a unique understanding of the matte grinding process based mostly on physical property and mineralogy. The effect of such features on grinding is rarely covered in comminution literature. It is important to incorporate the knowledge gained thus far into the subsequent analysis of the mineral liberation characteristics of converter matte.

7.2.3. Mineral Liberation Characteristics

The analytical technique, described in Chapter 3 (section 3.8), reports liberation data based on particle composition as well as free surface area. Figure 7.17, shows for instance, the effect of specific energy on the liberation distributions of copper sulfide and NiCu-alloy present within the 0.15% Fe matte. These liberation distributions are based on particle composition across complete size ranges.

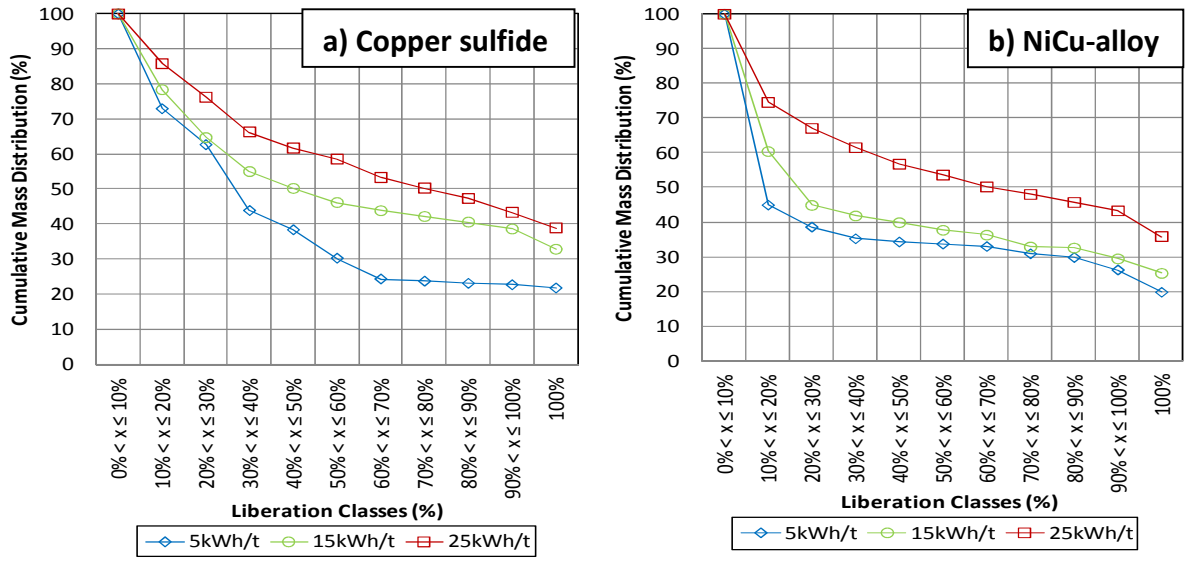

Figure 7.17: Effect of specific energy on the liberation distributions of (a) copper sulfide and (b) NiCu-alloy present within the 0.15% Fe matte.

The cumulative mass distribution is plotted against the liberation classes in Figure 7.17. Note that a cumulative display is commonly used to represent the contribution of particles within each liberation class with respect to the overall quantity. The liberation classes, displayed in 10% intervals in Figure 7.17, are a measure of the constituent wt% of the mineral (of interest) with respect to particle composition. Liberation class intervals can be grouped to provide an indication of complete liberation (x = 100%), reasonable liberation

(60% < x ≤ 100%), intermediate (30% < x ≤ 60%) and poor liberation (0% < x ≤ 30%). It is apparent from Figures 7.17(a) and (b) that an overall higher degree of copper sulfide and NiCu-alloy liberation is achieved with an increase in specific energy. The complete liberation (x = 100%) of copper sulfide and NiCu-alloy is the highest at 25kWh/t specific energy. This mainly follows expectation, as an increase in grinding energy was found to result in higher breakage rates of particles, to sizes within grain scale, and therefore liberation of the constituent minerals.

The mineral liberation distributions are consequently compared with regard to both mattes at constant specific energy. Figure 7.18 illustrates the effect of the iron endpoint on the liberation distributions of copper sulfide at 5kWh/t and 25kWh/t specific energy.

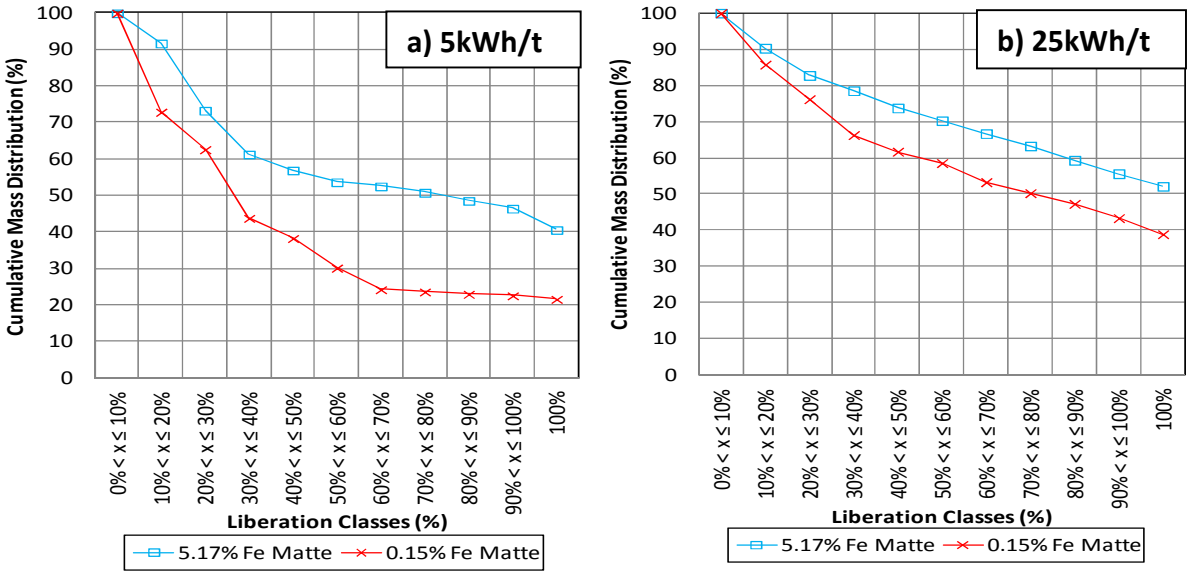

Figure 7.18: Effect of the iron endpoint on the liberation distributions of copper sulfide present within the 5.17% Fe and 0.15% Fe mattes at (a) 5kWh/t and (b) 25kWh/t specific energy.

Figure 7.18(a) demonstrates that at 5kWh/t specific energy, the degree of copper sulfide liberation is higher for the 5.17% Fe matte compared to the 0.15% Fe matte. In particular, 38.66% of particles within the 5.17% Fe matte can be considered as poorly liberated, compared to 56.17% within the 0.15% Fe matte. Furthermore, 40.67% of particles within the 5.17% Fe matte are completely liberated at 5kWh/t specific energy, in contrast to 21.69% within the 0.15% Fe matte. This can be observed clearly for the complete liberation class (x = 100%) in Figure 7.18(a). The comparative breakage rates of particles within the

5.17% Fe matte are found to be higher in the coarse and fine ends at 5kWh/t specific energy, which explains the liberation behavior.

At 25kWh/t specific energy, as displayed in Figure 7.18(b), the degree of copper sulfide liberation is higher for the 5.17% Fe matte than for the 0.15% Fe matte. Predictably fewer particles are poorly liberated for both mattes at 25kWh/t specific energy. In conjunction, 52.13% of particles within the 5.17% Fe matte are completely liberated, compared to 38.89% within the 0.15% Fe matte. This is displayed in Figure 7.18(b). The increased production of completely liberated copper sulfide at 25kWh/t specific energy is in agreement with the corresponding higher particle breakage rates achieved and, therefore, liberation behavior.

Figure 7.19 shows the effect of iron endpoint on the liberation distributions of the NiCu-alloy at 25kWh/t specific energy. Pixel based mapping of particle fragments of the 0.15% Fe matte for the same energy is also illustrated.

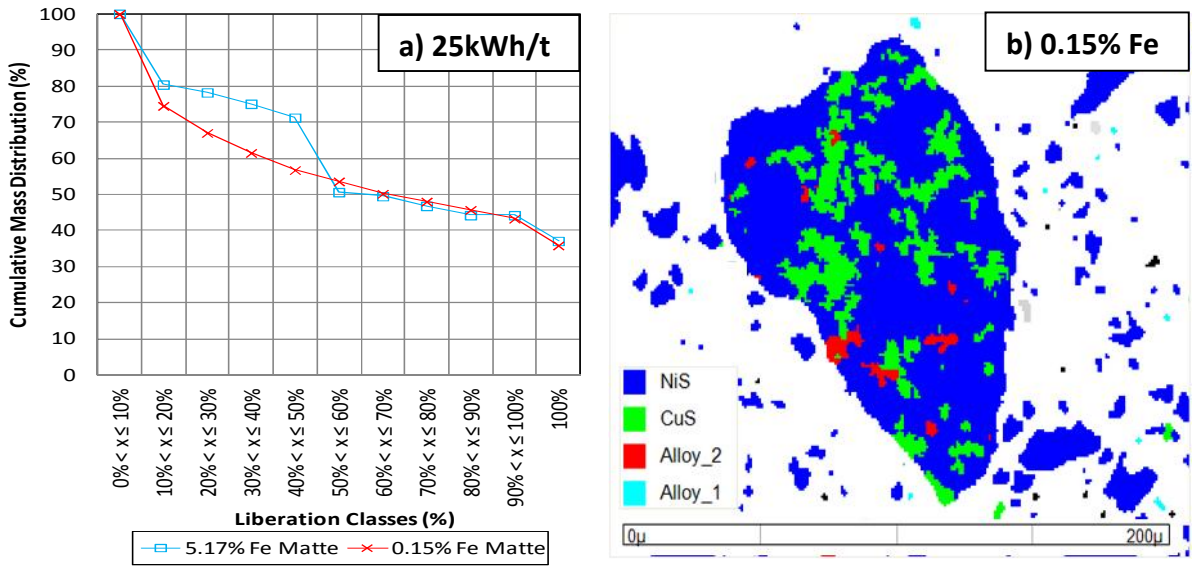

Figure 7.19: Effect of the iron endpoint on the liberation distributions of (a) NiCu-alloy present within the 5.17% Fe and 0.15% Fe mattes and (b) pixel based mapping of particle fragments of the 0.15% Fe matte at 200µm size scale for 25kWh/t specific energy, respectively.

The degree of NiCu-alloy liberation at 25kWh/t specific energy, as shown in Figure 7.19(a), is higher for the 5.17% Fe matte in the poor- to intermediate-liberation class intervals. The complete liberation of particles within the 5.17% Fe matte can also be seen in Figure 7.19(a) as marginally higher than within the 0.15% Fe matte. It is noticeable that a relatively low

measure of complete liberation is achieved for both the NiCu-alloy and copper sulfide within the different mattes at the ultimate specific grinding energy. This is supportive of a previous suggestion in sub-section 7.2.2.3 of this chapter that most of the available energy for grinding is actually used in breaking the nickel sulfide matrix. Figure 7.19(b), for example, is illustrative of nickel sulfide-dominant particle fragmentation at 25kWh/t specific energy for the 0.15% Fe matte. The large particle fragment is indicative of poorly liberated copper sulfide and NiCu-alloy (alloy_2), which mainly appears locked within the nickel sulfide matrix. Liberated OsRu-alloy (alloy_1), although not annotated, can also be observed in Figure 7.19(b), upon close inspection.

Considering the particle size distributions already obtained at 25kWh/t specific energy for both mattes, and that the current Lonmin BMR target size has already been achieved, fine grinding would be required to completely liberate the remainder of the copper sulfide and NiCu-alloy within both mattes. In addition, ultrafine grinding may even be necessary to completely liberate the characteristically vein-like NiCu-alloy and intergrown copper sulfide from the nickel sulfide matrix of the 5.17% Fe and 0.15% Fe mattes, respectively. It is important to recognize that complete liberation of copper sulfide and NiCu-alloy by particle composition would also ensure complete availability of the respective mineral surface area, which is an important enabling requirement for the subsequent leaching step.

7.2.4. Matte Leaching

Ultimately, the sequential effect of iron endpoint, including the effect on grinding and liberation characteristics of converter matte particles, can be conceptually related to the first stage atmospheric leach. The results of the closely associated study by van Schalkwyk et al., (2011; 2013) are used as the basis for this conceptual connection. Chapter 2 (sub-section 2.6.2) defined the purpose of the first stage atmospheric leach within the BMR as optimizing Ni extraction, while at the same time precipitating all Cu in the spent electrolyte circulated from the electrolytic tank house. According to van Schalkwyk et al., (2011), the extraction of Ni from converter matte particles occurs by way of direct sulfuric acid and oxygen leaching and by the replacement of leachable Ni with Cu from the spent electrolyte. The latter mechanism is reportedly governed by metathesis and cementation reactions (van Schalkwyk et al., 2011). It is further expected that Cu cementation will also permit for the removal of

Rh, Ru and Ir from spent electrolyte. These PGMs are required as part of the solid residue resulting from the first stage atmospheric leach. When remaining in solution, the PGMs are crystallized as part of the nickel sulfate crystals and become a loss.

It was proposed that converter matte particles, characteristic of variable iron endpoints, will affect the selective leach chemistry of Ni dissolution and Cu cementation with measurable variations in metal extraction. The aim of the related study was therefore to quantify and characterize the dissolution kinetics of Ni into solution and the cementation kinetics of Cu onto converter matte as a function of iron endpoint as well as spent electrolyte composition. The conditions in the first stage atmospheric leach within the BMR were experimentally simulated as closely as possible (van Schalkwyk et al., 2011; 2013). Converter mattes with different iron endpoints were investigated subsequent to the completion of grinding tests to the required product size of the BMR. The iron endpoints investigated were characteristic of 5.72%, 0.83% and 0.53% Fe.

Van Schalkwyk et al., (2013) reported 40% Ni extraction from high iron matte particles, in contrast to 67% Ni extraction from low iron matte particles. The differences between the mineralogy and mineral chemistry of the various mattes, as discussed in Chapters 4 (sub-section 4.2.4) and 5 (section 5.2), appear to have a dominant influence on the degree of Ni extraction achieved. The primary source of leachable Ni in high iron matte particles is located within the higher abundant nickel sulfide matrix, but at a lower elemental concentration compared to that for low iron matte particles. Additional sources of Ni within high iron matte particles include the significantly lower abundant, but highly reactive NiCu-alloy (albeit with high Ni:Cu ratios), and the less leachable pentlandite $(Fe,Ni)_9S_8$ and Ni partitioned into host copper sulfide minerals. These differences are thus supportive of the lower degree of Ni extraction obtained from high iron matte particles.

On the contrary, high iron matte particles are expected to attain a higher degree of particle fragmentation due to grinding than particles of the low iron matte. This means that more surface area of the nickel sulfide matrix of the high iron matte would be available for the enhancement of Ni dissolution kinetics. The complete liberation of NiCu-alloy within high iron matte particles would most likely be low, but marginally higher than from those within the low iron matte. This will therefore also expose completely free NiCu-alloy surface area

for the promotion of Ni dissolution kinetics. Interestingly, van Schalkwyk et al., (2013) illustrated the existence of intact Pt-dominant cores subsequent to the leaching of the associated Ni-dominant rims. It can thus be suggested that the 3D measurement pertaining to Pt-core and lobes, which is reported in Table 5.10 (Chapter 5, sub-section 5.2.3.2), is indicative of the volumetric distribution of PGMs after the dissolution of Ni from alloy.

Copper in solution was found to precipitate initially at a faster rate during the investigation of high iron matte than for low iron matte particles (van Schalkwyk et al., 2013). The extent of precipitation was limited, however, and the dissolution of Cu from high iron matte particles followed soon thereafter. The reason for the faster rate of Cu precipitation initially during the leaching of high iron matte particles is not clear. The dissolution of Cu from high iron matte particles is considered related to the availability of excess acid due to the simultaneous, but low extent of Ni dissolution. In addition, an overall higher degree of liberation was most likely obtained for copper sulfide minerals of high iron matte particles, resulting in readily available mineral surface area for direct reaction with acid and oxygen and, hence, Cu dissolution. Even so, the extent of Cu cementation and, more importantly, that of Rh, Ru and Ir, proved more significant with low iron matte particles. It is further thought that the elevated concentration of Fe in high iron matte permits for the reaction with Cu in solution, which may result in undesirable iron compounds. Van Schalkwyk et al., (2013) also indicated that based on operator experience alone, an iron endpoint range of 1.6% to 0.6% Fe is preferred for the treatment of converter matte at the first stage atmospheric leach section within the Lonmin BMR.

7.3. Key Findings

The investigation of the physical property, batch grinding and mineral liberation characteristics of the 5.17% and 0.15% Fe mattes with connection to leaching in this chapter suggest the following key findings:

i. The relevant minerals and associated boundaries did not demonstrate the same indentation hardness. The minerals and boundaries within the high iron matte were found to be harder than within the low iron matte. The indentation-induced

breakage of nickel sulfide, copper sulfide and NiCu-alloy appeared preferential and related to the indentation hardness.

ii. The resultant particle size distribution of solidified matte could be associated with the specific iron endpoint achieved. The high iron matte obtained a coarser particle size distribution than the low iron matte. However, the application of various specific energies to solidified matte grinding resulted in the high iron matte obtaining a finer product size distribution than the low iron matte. The grinding-induced breakage of matte particles seems more complex than under indentation loading and is dominated by the fragmentation of the nickel sulfide matrix.

iii. Particles of the high and low iron matte were found to break at a faster rate with an increase in the application of specific energy to grinding. Moreover, particles of the high iron matte were observed to break at a faster rate with an increase in specific energy than particles of the low iron matte.

iv. Copper sulfide minerals present within the high and low iron matte particles were found to break at an overall faster rate with an increase in the application of specific energy to grinding. It was also observed that copper sulfide minerals present within the high iron matte particles broke at a faster rate than within the low iron matte particles. The trend in the breakage rate as a function of grinding energy of the NiCu-alloy present within the low iron matte particles was not obvious.

v. The overall liberation of copper sulfide and NiCu-alloy within particles of the low iron matte was found to increase with the application of more specific energy to grinding. It was also observed that a higher degree of overall liberation was achieved for copper sulfide and NiCu-alloy present within the high iron matte particles compared to particles within the low iron matte.

vi. A lower degree of Ni extraction was achieved from minerals within the high iron matte as opposed to minerals from the low iron matte. The extent of Cu cementation and that of Rh, Ru and Ir were found to be more favorable onto particles of the low iron matte than onto high iron matte particles.

This chapter has methodically investigated the downstream processing characteristics of iron endpoint specific solidified converter matte within the beneficiation framework of the Lonmin BMR. The final chapter follows and provides conclusions and recommendations based on understanding the extensive effect of iron endpoint on the production of base metals and PGMs from Peirce-Smith converter matte with relevance to the selection of a desired iron endpoint.

7.4. Relevant Publications

Thyse, E.L., Akdogan, G., Olivier, E.J., Neethling, J.H., Goosen. W.E., Eksteen, J.J., 2011. The effect of granulated nickel converter matte mineralogy on phase-specific hardness and associated breakage characteristics. **Proceedings, 10th International Congress for Applied Mineralogy,** 1 – 5 August 2011, Trondheim, Norway, pp.673 – 681.

van Schalkwyk, R.F., Eksteen, J.J., Petersen, J., Thyse, E.L., Akdogan, G., 2011. An experimental evaluation of the leaching kinetics of PGM-containing Ni-Cu-Fe-S Peirce-Smith converter matte, under atmospheric leach conditions. **Minerals Engineering,** Special Issue: Processing of Nickel Ores & Concentrates, Volume 24, Issue 7, pp. 524 – 534.

Chapter 8
CONCLUSIONS AND RECOMMENDATIONS

8.1. Conclusions

The primary aim of this study was to systematically investigate and develop a quantitative basis for understanding the effect of converter iron endpoint on matte mineralogy, base metal and PGM mineralization and solidification. The secondary aim was to relate the iron endpoint specific mineralogy to the processing characteristics of the different mattes, with the intended purpose of identifying a desired endpoint in step with downstream unit process requirements and technology. Based on the relevant publications and associated industrial and scholarly contributions, these aims can be considered as being mostly accomplished. The selection of a desired iron endpoint will add finality to the aims. The conclusions that follow are based on the sequential effect of the respective high and low iron endpoints on the production of base metals and PGMs from Peirce-Smith converter matte at Lonmin with relevance to endpoint selection.

8.1.1. Effect of High Iron Endpoint

Three industrial Peirce-Smith converter mattes attained iron endpoints of 5.17%, 0.99% and 0.15% and were simultaneously investigated. Within the Lonmin operational framework, an iron endpoint of 5.17% would be indicative of high iron-containing matte, while iron endpoints 0.99% and 0.15% would be indicative of low iron-containing mattes.

The base metals of Co and Pb (although not important to Lonmin), as well as S, achieved a maximum bulk concentration in converter matte with an iron endpoint of 5.17%. This high iron matte also reported the lowest bulk density of 5.64 g/cc. The base metal of Ni, which is important to Lonmin, was found to be concentrated primarily in dominant nickel sulfide mineral structures, which revealed diffraction patterns similar to that of the natural mineral of heazlewoodite. The attainment of an iron endpoint of 5.17% resulted in a higher relative abundance of nickel sulfide mineral structures present in the converter matte. However, the mineral chemistry was distinctive of lower principal Ni and higher S concentrations, while

accommodating, in particular, Fe, Co and minor PGMs into the mineral structures. The morphology of the nickel sulfide mineral structures for the high iron matte was characteristic of a cementing matrix with relatively larger and well-defined grain areas.

Theoretical solidification pathways provided a fundamental understanding of the evolution of molten matte systems in relation to crystallizing solid phases and composition. The solidification pathway for the high iron matte system has shown heazlewoodite crystallizing at relatively low temperatures with near stoichiometric compositions. The average concentration of Ni in the actual nickel sulfide matrix of the high iron matte has revealed a large departure from the concentration of Ni in the equilibrium end member phase. The nickel sulfide matrix of the 5.17% Fe matte also demonstrated higher indentation hardness than within the low iron matte. In contrast, during laboratory grinding, the nickel sulfide matrix of the high iron matte seemed to have the least resistance to grinding. The atmospheric leaching of high iron matte particles resulted in a significantly lower degree of Ni extraction than was the case for low iron matte particles.

Copper sulfide mineral structures matched to chalcocite natural mineral were found to be the primary source of Cu, which is also an important base metal to Lonmin. A further effect of the high iron endpoint on the mineralogy of converter matte included a lower relative abundance of copper sulfide mineral structures, with characteristically lower principal Cu and higher S concentrations. The effect on mineral chemistry resulted in the partitioning of especially Ni, Fe, Co and limited Rh into the mineral structures. The morphology of the copper sulfide structures for the high iron matte was characteristic of relatively larger euhedral forms embedded in the nickel sulfide matrix.

The copper sulfide mineral of digenite was the first solid phase to crystallize during equilibrium cooling of the high iron matte system. The inversion of digenite to beta-chalcocite was found to occur at a relatively low temperature. The final concentration of Cu in beta-chalcocite is significantly higher than the concentration of Cu in actual copper sulfide mineral structures of the high iron matte. Copper sulfide mineral structures of the high iron matte obtained higher indentation hardness than within the low iron matte. The breakage rates and associated liberation of copper sulfide mineral structures proved to be higher for the 5.17% Fe matte than for the low iron matte. When leaching high iron matte, the

cementation of Cu and that of Rh, Ru and Ir, however, was found to be less favorable. Undesirable iron compounds could also form when leaching high iron matte.

Mineral structures of NiCu-alloy were identified as an additional source of Ni and Cu. More importantly, the NiCu-alloy structures were found to be the primary collector and source of PGMs. The five PGMs of Pt, Pd, Rh, Ru and Ir are of considerable economic importance to Lonmin. However, the NiCu-alloy structures demonstrated a significantly lower relative abundance in the high iron matte. The mineral chemistry was also characteristic of a lower combined NiCu (including high Ni:Cu ratios), higher S concentration and readily partitioned Pt. The morphology of the NiCu-alloy structures in the high iron matte could mostly be described as fine and vein-like and appeared set in the nickel sulfide matrix. The NiCu-alloy was found not to crystallize during equilibrium cooling simulations of the high iron matte system. NiCu-alloy structures in the 5.17% Fe matte displayed higher indentation hardness than within the low iron matte, which also seemed to result in a lack of breakage under indentation loading and during laboratory grinding. A higher degree of liberation was achieved in the poor- to intermediate-liberation class intervals for NiCu-alloy structures in the 5.17% Fe matte than was the case for structures in the low iron matte.

Osmium ruthenium alloy structures were found to be the primary source of the sixth PGM of Os. Although the production of Os is not important to Lonmin, mineralogical observations suggested that the relative abundance of discrete OsRu-alloy structures is below 1 volume%. The mineral chemistry of OsRu-alloy structures within the high iron matte exhibited higher Os:Ru ratios. Smaller euhedral to subhedral forms were characteristic of the morphology of discrete OsRu-alloy structures present in the high iron matte. In addition, Os was sporadically present at relatively high concentrations in solid-solution within NiCu-alloy structures of the high iron matte. A lack of breakage was observed for the discrete OsRu-alloy structures during laboratory grinding of the high iron matte.

Iron-dominant and distinctively mantled iron-nickel oxide spinel structures were present within the high iron matte in low relative abundance. Diffraction patterns of the iron-dominant spinel structures could be matched to that of the natural mineral of magnetite. The mineral chemistry of iron-dominant spinel structures appeared to vary with morphological forms and the well-formed euhedral forms were particularly characteristic of

a higher Fe concentration. These spinel structures also appeared embedded in the nickel sulfide matrix. Theoretically, the crystallization of spinel occurred at high temperatures and during the converting of high iron matte. The iron-dominant spinel was also found to be the hardest mineral within the high iron matte. A lack of breakage was observed for this mineral during laboratory grinding. Moreover, spinel structures like these would be difficult to dissolve under atmospheric leach conditions and as a result contaminate the PGM concentrate.

8.1.2. Effect of Low Iron Endpoints

The five most important PGMs achieved the highest combined bulk concentration in converter matte with an iron endpoint of 0.99%. The highest combined bulk concentration of the base metals of Ni, Cu and Co was achieved for the 0.15% Fe matte. However, the combined bulk concentration of base metals and PGMs proved to be the most valuable for the 0.99% Fe matte. The 0.99% and 0.15% Fe mattes also reported increasing bulk densities of 5.93 and 6.07 g/cc, respectively.

The attainment of the lower iron endpoints resulted in a notable lower relative abundance of nickel sulfide mineral structures present in the converter mattes. The mineral chemistry, however, revealed higher principal Ni and lower S concentrations, while accommodating, more specifically, Cu, Pb and also minor PGMs into the mineral structures. The morphology of the nickel sulfide matrix of the lower iron mattes was characteristic of relatively smaller grain areas with intergrown boundaries. Morphological detail of the nickel sulfide matrix of the 0.15% Fe matte was also illustrated along a 2D section to an approximate depth of 4µm.

The solidification pathway for the low iron matte system indicated that heazlewoodite crystallization occurred at a lower temperature than within the high iron matte system and also with a composition close to stoichiometry. The average Ni concentration of the nickel sulfide matrix of the 0.15% Fe matte has revealed a smaller departure from the Ni concentration in the equilibrium end member phase. The nickel sulfide matrix of the 0.15% Fe matte showed lower indentation hardness than within the high iron matte. On the contrary, the nickel sulfide matrix of the 0.15% Fe matte proved to be more challenging to grind. A notably higher degree of Ni extraction was achieved as a result of atmospheric leaching of low iron matte particles.

A higher relative abundance of copper sulfide mineral structures in converter matte was considered an effect of low iron endpoints on matte mineralogy. These copper sulfide mineral structures exhibited higher principal Cu and lower S concentrations. The effect on mineral chemistry was further manifested by the partitioning of Ni and limited Rh into the mineral structures. The morphology of the copper sulfide mineral structures present in the low iron mattes could be described as being reflective of smaller euhedral to subhedral forms embedded in the nickel sulfide matrix. Moreover, this morphological form was confirmed by the production of a high fidelity 3D reconstruction of a copper sulfide mineral structure of the 0.15% Fe matte.

During equilibrium cooling of the low iron matte system, the copper sulfide mineral of digenite was also the first solid phase to crystallize, but at a lower temperature than within the high iron matte system. However, the inversion of digenite to beta-chalcocite occurred at a higher temperature. Furthermore, the average concentration of Cu in copper sulfide minerals of the low iron matte displayed a smaller departure from the Cu concentration in the equilibrium end member phase. Lower indentation hardness was demonstrated by copper sulfide mineral structures of the 0.15% Fe matte. Contrary to expectation, these mineral structures exhibited lower breakage rates and liberation. The cementation of Cu and that of the associated PGMs was more favorable onto particles of the low iron matte.

The NiCu-alloy structures were present at a significantly higher relative abundance in the low iron mattes, with notably higher principal NiCu and lower S concentrations. Higher concentrations of Pd, Rh and Ir were characteristic of the mineral chemistry of the NiCu-alloy structures in the low iron mattes. The distinct partitioning of Pt into NiCu-alloy structures was also common to the low iron mattes. The morphology of these NiCu-alloy structures was characteristic of variable forms, including fine-grained vein-like structures, which appeared related to the exsolution origin. However, the most developed form of the NiCu-alloy was observed to be relatively large, cored, dentritic-like structures. Tomography reconstructions allowed for color and grayscale based 3D visualization of the various morphological forms of the NiCu-alloy structure. High-fidelity tomography reconstructions could also be produced for the 3D visualization of cored, dentritic-like, Pt-bearing structures.

Moreover, the volumetric distribution of combined Pt-dominant cores and lobes within Ni-dominant rims in a rectangular volume of the 0.15% Fe matte could be measured. An understanding of the complex PGM collection process for the fast-cooled NiCu-alloy structures was developed based on the observed mineralogy and mineral chemistry. The theoretical solidification pathway of the low iron matte system indicated the crystallization of FCC_A1, a base metal alloy, corresponding to the actual NiCu-alloy structure. This solid phase was the second to crystallize during equilibrium cooling and at a moderate temperature. The highest Ni concentration of the FCC_A1 phase occurred at 575 oC. The NiCu-alloy structures of the 0.15% Fe matte displayed lower indentation hardness than within the high iron matte. The breakage rates of NiCu-alloy structures of the low iron matte were found to decrease according to decreasing grain size for a specific energy. The complete liberation of NiCu-alloy structures of the 0.15% Fe matte was also found to be marginally lower.

The relative abundance of OsRu-alloy structures for the low iron mattes was estimated to be below 1%. The mineral chemistry of OsRu-alloy structures within the low iron mattes was distinctive of smaller Os:Ru ratios. Relatively lower Os concentrations were sporadically present in solid-solution within NiCu-alloy structures of the low iron mattes. The morphology of these alloy structures was characteristic of larger euhedral to subhedral forms. Morphological detail along a 2D section showed such a discrete Os-dominant structure extending into the nickel sulfide matrix of the 0.15% Fe matte. Completely liberated OsRu-alloy structures could also be observed for the low iron matte.

Nickel-dominant spinel structures were present in increased relative abundance in the low iron mattes. These nickel-dominant spinel structures could be associated with the natural mineral of trevorite. The lowest relative abundance of the nickel-dominant spinel structure occurred in the 0.99% Fe matte. These spinel structures obtained the highest Ni concentration in the 0.15% Fe matte. The theoretical crystallization of Ni-dominant spinel occurred during conversion of the 0.15% Fe matte and at a relatively lower temperature than the early crystallization of iron-dominant spinel in the 5.17% Fe matte system. It would also be difficult to leach these Ni-dominant spinel structures under atmospheric conditions.

8.1.3. Selection of a Desired Iron Endpoint

The selection of a desired iron endpoint requires consideration of which iron level to terminate the converting reactions. An initial requirement would be for maximum enrichment of the important base metals and PGMs within the bulk molten matte during the finishing blow. However, the most important requirement would be for the optimal processing of the resultant converter matte within the constraints of the BMR. The capacity and unit process technology of the BMR were developed within a small iron setpoint range.

The high iron or 5.17% Fe matte can be considered as an example of underblown converter matte. Such a matte is particularly characteristic of elevated Fe, S and O bulk concentrations. The effect of attaining a high iron endpoint with respect to the initial and downstream requirements has been concluded in sub-section 8.1.1. To attain such high iron-containing matte requires less blowing volume which can be regarded as an operational cost saving opportunity. In addition, less sulfur dioxide would be produced which will reduce the gas treatment cost.

Conversely, the lowest iron or 0.15% Fe matte is characteristic of an overblown matte. This matte was susceptible to excessive blowing, resulting in, for example, the formation of abundant deleterious Ni-dominant spinel structures. The financial implications for attaining such a matte would be largely negative and affected by Ni losses, poorer refractory life of converters, lower quality BMR product and additional production time.

Instead, the 0.99% Fe matte achieved the highest combined bulk concentration of the valuable metals important to Lonmin, as well as the lowest abundance of deleterious Ni-dominant spinel. The financial benefit of attaining an iron endpoint around 1% has previously been quantified by Lonmin and estimated at R15.1 million per annum (Bezuidenhout, 2008). The effect of the low iron mattes is concluded in sub-section 8.1.2. In addition, practical experience based on operation of the Lonmin BMR suggested an endpoint range of 1.6% to 0.6% Fe (van Schalkwyk et al., 2013). It is therefore recommended that an endpoint range of 1.6% to 0.99% Fe is used for producing converter matte with a metallurgical quality within the setpoints of the Lonmin BMR. The envisaged automated monitoring and control can be based on a practical endpoint range of 1.6% to 1.0% Fe.

8.2. Future Research

Recommendations for future research include the following:

i. A study of the mineralogy and mineral chemistry of the associated slag phase as a function of blowing converter matte to 1.6% to 1.0% Fe, through the application of high resolution electron microscopy, could be undertaken. The purpose of such an investigation would be to quantify the potential losses of valuable base metals and PGMs to the slag phase. Such information can be used to account for losses between the smelter complex and the BMR.

ii. The partitioning trends of impurities such as selenium, tellurium, arsenic and antimony into mineral structures as a function of the desired endpoint range of 1.6% to 1.0% Fe could be investigated. The use of electron probe microanalysis would be a prerequisite for such an investigation. This information may be useful to the downstream removal of selenium, tellurium and arsenic from PGM residue through alkaline pressure leaching. The concentration of these impurities is tabled in Appendix G with respect to the iron endpoints investigated.

iii. A detailed analysis of the solid-solution characteristics of the NiCu-alloy mineral structure using aberration corrected high resolution transmission electron microscopy with electron energy loss spectroscopy (EELS) attachments could be conducted.

iv. An experimental investigation or simulation of the differences in interfacial energy levels between the parent matte and crystallizing NiCu-alloy during matte cooling could be performed. Such approaches would provide an improved understanding of the PGM collection mechanism of the NiCu-alloy structure. In addition, the influence of the S concentration on the parent matte element ratios and co-existing matte-alloy element exchange requires consideration. The diffusion process and cooling rate also warrant an inclusive description.

v. The presence of native Ni and Cu or metallics in converter matte could be investigated.

vi. The distribution of Pb and PGMs during matte cooling can be determined experimentally, as these were not supported by the Mtox matte database. The assessment of the data and literature review of earlier observations can be included in such a study.

vii. The influence of mineral chemistry on the indentation hardness of individual nickel sulfide, copper sulfide and NiCu-alloy structures can be determined.

viii. The simulation of a continuous ball mill circuit (possibly closed and open circuits for matte within the desirable iron endpoint range) with post-classification based on the mineralogical data could be considered. The question as to whether it is possible to design such a circuit based predominantly on the mineralogical information obtained requires understanding. It would also be important to establish the net power required for such a grinding model.

ix. The possibility of separating the base metal sulfides from the PGM-containing alloy structures post-grinding could be investigated. The respective fractions can then be leached separately with the purpose of ultimately reducing the processing pipeline, particularly of the PGMs.

x. Three dimensional liberation data using tomography with respect to the first stage atmospheric leach circuit could be generated. This data can potentially be incorporated into a grinding model for converter matte in the iron endpoint range.

xi. An additional prospect would be to determine the influence of 3D mineral specific breakage morphology on the downstream leaching systems.

GLOSSARY

Please find below some definitions relevant to this study in addition to those included within the dissertation:

Accessory Mineral	Mineral with a relative abundance less than 5wt%
Anhedral	Description specific to minerals or phases with no identifiable morphological form
Bessemerizing	A term originating from the steelmaking industry describing the blowing of hot metal with air
Dominant mineral	Mineral with a relative abundance greater than 50wt%
Euhedral	Morphological description of well-developed mineral or phase forms
Eutectic	Lowest specific temperature or composition at which exsolution can occur
Exsolution	Separation of minerals or phases from the parent liquid upon cooling
Fidelity	The extent of equality with the original source
Lamella	Morphological description characteristic of a delicate, membrane-like structure
Ligand	A chemical constituent that usually bonds with available metals
Liquidus	Refers to the specific temperature at which solid crystals can exist with the melt
Mass pull	Express the concentrate to feed ore ratio
Matte fall	Indicative of matte production relative to a hundred tons of concentrate
Microstructure	Refers to the external appearance of minerals or phases on the meso-scale

Microtexture	Refers to a broader description including microstructure morphology, chemistry and crystal structure
Minor Mineral	Mineral with a relative abundance between 5 and 15wt%
Non-ferrous processes	Processes that does not involve the treatment of significant iron-containing material
Polymorph	A mineral or phase with the ability to attain various crystal forms
Solid-solution	A homogeneous mixture of solutes in solvent in the solid state
Subhedral	Morphological forms of limited development
Tomography	Technique of acquiring 3D images from 2D in-plane projections
Tuyeres	Piping that includes nozzles used for the injection of air during matte blowing

REFERENCES

Andrews, D.R.A., Brenan, J.M., 2002. The solubility of ruthenium in sulfide liquid: implications for platinum group mineral stability and sulfide melt-silicate melt partitioning. ***Chemical Geology,*** Volume 192, pp. 163 – 181.

Andrews, L., 2007. The use of electron microbeam techniques in metallurgical analysis. ***The Journal of The Southern African Institute of Mining and Metallurgy,*** Volume 107, Number 2, pp. 79 – 82.

Andrews, L., 2008. Base metal losses to furnace slag during processing of platinum-bearing concentrates. ***Master's Thesis,*** Faculty of Engineering, Built Environment and Information Technology, University of Pretoria, South Africa, 145 pages.

Andrews, L., den Hoed, P., 2011. Mineralogical solutions for pyrometallurgical problems. ***The Journal of The Southern African Institute of Mining and Metallurgy,*** Volume 111, pp. 675 – 680.

Arnold, R.G., Malik, O.P., 1975. The NiS-S system above 980 degrees C; a revision. ***Economic Geology,*** Volume 70, Number 1, pp. 176 – 182.

Aspola, L., Matusewicz, R., Haavanlammi, K., Hughes, S., 2012. Outotec smelting solutions for the PGM industry. ***Platinum 2012 The Southern African Institute of Mining and Metallurgy,*** pp. 235 – 250.

Austin, L.G., 1971. A review: introduction to the mathematical description of grinding as a rate process. ***Powder Technology,*** Volume 5, pp. 1 – 17.

Austin, L.G., Julianelli, K., Sampaio de Souza, A., Schneider, C.L., 2007. Simulation of wet ball milling of iron ore at Carajas, Brazil. ***International Journal of Mineral Processing,*** Volume 84, pp. 157 – 171.

Austin, L.G., Klimpel, R.R., Luckie, P.T., 1984. Process engineering of size reduction: ball milling. ***Published: Society of Mining Engineers, American Institute of Mining, Metallurgical, and Petroleum Engineers, Inc.,*** New York, ISBN 0 – 89520 – 421 – 5, 561 pages.

Ballhaus, C., Tredoux, M., Späth, A., 2001. Phase relations in the Fe-Ni-Cu-PGE-S system at magmatic temperature and application to massive sulfide ores of the Sudbury Igneous Complex. ***Journal of Petrology,*** Volume 42, Number 10, pp. 1911 – 1926.

Barry, T.I., Dinsdale, A.T., Gisby, J.A., 1993. Predictive thermochemistry and phase equilibria of slags. ***JOM The Member Journal of the Minerals Metals and Materials Society,*** Volume 45, Number 4, pp. 32 – 38.

Barry, T.I., Dinsdale, A.T., Gisby, J.A., Hallstedt, B., Hillert, M., Jansson, B., Jonsson, S., Sundman, B., Taylor, J.R., 1992. The compound energy model for ionic solutions with applications to solid oxides. ***Journal of Phase Equilibria,*** Volume 13, Number 5, pp. 459 – 475.

Barton, P.B., 1973. Solid-solutions in the system Cu-Fe-S, part I; The Cu-S and CuFe-S joins. ***Economic Geology,*** Volume 68, Number 4, pp. 455 – 465.

Bateman, 2013. Matte granulation systems, ***http://www.labrisltd.com.tr,*** Accessed: 25 October 2013.

Bezuidenhout, G.A., 2008. Technical and commercial evaluation of impact of iron endpoint control in converter (Semtech trial). ***Lonmin Group Internal Communication,*** 16 pages.

Bezuidenhout, G.A., Eksteen, J.J., Wendt, W., 2010. Endpoint control in PGM-containing nickel matte converting using flame emission spectroscopy. ***Processing of Nickel Ores and Concentrates '10,*** Minerals Engineering International, Falmouth, United Kingdom.

Bircumshaw, L., 2008. Base metal refinery process overview. ***Lonmin Group Internal Communication,*** 10 pages.

Bond, F.C., 1952. The third theory of comminution. ***American Institute of Mining Engineers Transactions,*** Volume 193, pp. 484 – 494.

Bond, F.C., 1960. Confirmation of the third theory. ***American Institute of Mining Engineers Transactions,*** Volume 217, pp. 139 – 153.

British Geological Survey, 2009. Platinum, ***http:/www.MineralsUK.com,*** Accessed: 26 June 2013.

Byerley, J.J., Takebe, N., 1972. Thermodynamics of the Fe-Ni-S system at 1250 ^{o}C. ***Metallurgical Transactions,*** Volume 3, pp. 559 – 564.

Cabri, L.J., 1973. New data on phase relations in the Cu-Fe-S system. ***Economic Geology,*** Volume 68, pp. 443 – 454.

Castaing, R., 1960. Electron Probe Microanalysis. ***Advances in Electronics and Electron Physics,*** Volume 13, pp. 317 – 386.

Chakrabarti, D.J., Laughlin, D.E., 1983. The Cu-S (copper-sulfur) system. ***Bulletin of Alloy Phase Diagrams,*** Volume 4, Number 3, pp. 254 – 271.

Clark, L.A., Kullerud, G., 1963. The sulfur-rich portion of the Fe-Ni-S system. ***Economic Geology,*** Volume 58, Number 6, pp. 853 – 885.

Crabtree, D.D., Kinasevich, R.S., Mular, A.L., Meloy, T.P., Fuerstenau, D.W., 1964. Mechanisms of size reduction in comminution systems part I. Impact, abrasion, and chipping grinding. ***AIME Transactions,*** pp. 201 – 206.

Craig, J.R., 1973. Pyrite-pentlandite assemblages and other low temperature relations in the Fe-Ni-S system. ***American Journal of Science,*** Cooper Volume 273 – A, pp. 496 – 510.

Cramb, A.W., 2012. A short history of metals. Carnegie Mellon University, ***http/:/neon.nems.cmu/cramb/Processing/history.html,*** Accessed: 01 January 2013.

Crundwell, F., Moats, M., Ramachandran, V., Robinson, T., Davenport, W.G., 2011. Extractive metallurgy of nickel, cobalt and platinum-group metals. ***Published: Elsevier Ltd,*** ISBN 9780080968094, 622 pages.

Davies, R.H., Dinsdale, A.T., Gisby, J.A., Robinson, J.A.J., Martin, S.M., 2002. MTDATA – thermodynamic and phase equilibrium software from the National Physical Laboratory. ***Calphad,*** Volume 26, Number 2, pp. 229–271.

de Villiers, J., Verryn, S., 2007. Modern techniques in X-ray diffraction applied to metallurgy. ***The Journal of The Southern African Institute of Mining and Metallurgy,*** Volume 107, pp. 83 – 86.

Dinsdale, A.T., 1984. The generation and application of metallurgical thermodynamic data. ***PhD Dissertation,*** Materials Engineering Department, Brunel University, UK.

Djurle, S., 1958. An X-ray study on the system Cu-S. ***Acta Chemica Scandinavica,*** Volume 12, pp. 1415 – 1426.

Eksi, D., Hakan Benzer, A., Sargin, A., Genc, O., 2011. A new method for determination of fine particle breakage. ***Minerals Engineering,*** Special Issue, Volume 24, Issues 3 – 4, pp. 216 – 220.

Eksteen, J.J., Van Beek, B., Bezuidenhout, G.A., 2011. Cracking a hard nut: An overview of Lonmin's operations directed at smelting of UG2-rich concentrate blends. ***Southern African Pyrometallurgy 2011,*** Edited by R.T. Jones and P. Den Hoed, Southern African Institute of Mining and Metallurgy, pp. 231 – 251.

Evans, Jr., T., 1981. Copper coordination in low chalcocite and djurleite and other copper-rich sulfides. ***American Mineralogist,*** Volume 66, pp. 807 – 818.

Ferrow, E.A., 1994. Mössbauer effect and TEM in mineralogy. ***Hyperfine Interactions,*** Volume 90, pp. 121 – 134.

Firdu, F.T., Taskinen, P., 2010. Sulfide mineralogy – Literature review. ***Published: Aalto University School of Science and Technology,*** Department of Materials Science and Engineering, Thermodynamics and Modeling of Metallurgical Processes, 53 pages.

Fleet, M.E., 1972. The crystal structure of α-Ni_7S_6. ***Acta Crystallographica,*** Volume B28, part 4, pp. 1237 – 1241.

Fleet, M.E., 1977. The crystal structure of heazlewoodite, and metallic bonds in sulfide minerals. ***American Mineralogist,*** Volume 62, pp. 341 – 345.

Fleet, M.E., Pan, Y., 1994. Fractional crystallization of anhydrous sulfide liquid in the system Fe-Ni-Cu-S, with application to magmatic sulfide deposits. ***Geochimica et Cosmochimica Acta,*** Volume 58, Number 16, pp. 3369 – 3377.

Fleet, M.E., Stone, W.E., 1990. Partitioning of platinum-group elements in the Fe-Ni-S system and their fractionation in nature. ***Geochimica et Cosmochimica Acta,*** Volume 55, pp. 245 – 253.

Fraser, O.B.J., 1952. Developments in nickel. ***Industrial and Engineering Chemistry,*** Volume 44, Number 5, pp. 950 – 954.

Gay, S.L., 1999. Numerical verification of a non-preferential-breakage liberation model. ***International Journal of Mineral Processing,*** Volume 57, pp. 125 – 134.

Gay, S.L., 2004a. A liberation model for comminution based on probability theory. ***Minerals Engineering,*** Volume 17, pp. 525 – 534.

Gay, S.L., 2004b. Simple texture-based liberation modelling of ores. ***Minerals Engineering,*** Volume 17, pp. 1209 – 1216.

George, D.B., Chen, W.J., Mackey, P.J., Weddick, A.J., 1999. Copper 99: Smelting operations and advances. ***Published: The Minerals, Metals and Materials Society,*** Volume 5, 727 pages.

Gisby, J.A, Dinsdale, A.T., Taskinen, P., 2007. Predictive thermochemistry of oxide and sulfide systems. ***Proceedings of EMC 2007,*** Volume 4, Düsseldorf, DGBM, Clausthal-Zellerfeld, pp. 1721 - 1736.

Gisby, J.A., Dinsdale, A.T., Barton-Jones, I., Gibbon, A., Taskinen, P., 2002. Predicting phase equilibria in oxide and sulphide systems. ***Sulfide Smelting 2002,*** Edited by R.L., Stephens, H.Y., Sohn, TMS, Warrendale (PA), pp. 533 - 545.

Gottlieb, P., Wilkie, D., Sutherland, D., Ho-Tun, E., Suthers, S., Perera, K., Jenkins, B., Spencer, S., Butcher, A., Rayner, J., 2000. Using quantitative electron microscopy for process mineralogy applications. ***JOM The Member Journal of The Minerals, Metals and Materials Society,*** pp. 24 – 25.

Govender, S., 2006. Micro PIXE analyses of furnace and converter mattes for the determination of trace element distribution and concentrations. ***Master's Thesis,*** Department of Physics, University of Zululand, South Africa, 109 pages.

Grobéty, B., 2005. Minerals at the atomic scale. ***3rd Swiss Geosciences Meeting,*** Zürich, pp. 59 – 60.

Gu, Y., 2003. Automated SEM based mineral liberation analysis: An introduction to JKMRC / FEI Mineral Liberation Analyzer. ***Journal of Minerals and Materials and Engineering,*** Volume 2, Number 1, pp. 33 – 41.

Habashi, F., 1999. Textbook of hydrometallurgy. ***Published: Métallurgie Extractive Québec,*** ISBN 2 – 980 – 3247 – 7 – 9 (second edition), 739 pages.

Habashi, F., 2005. A short history of hydrometallurgy. ***Hydrometallurgy,*** Volume 79, pp. 15 – 22.

Hagni, R.D., Vierrether, C.B., Pignolet-Brandom, S., 1987. Applied mineralogy of pyrometallurgical products. ***Journal of Metals,*** Volume 39, Number 1, pp. 8 – 10.

Hawley, J.E., Colgrove, G.L., Zurbrigg, H.F., 1943. The Fe-Ni-S system, and introduction with new data on the crystallization of pyrhotite and pentlandite. ***Economic Geology,*** Volume 38, Number 5, pp. 335 – 388.

Hayes, P., 2003. Process principles in minerals and materials production, third edition. ***Published: Hayes Publishing Co,*** ISBN 0 – 9589197 – 3 – 9 (student edition), 734 pages.

Herrera-Urbina, R., Hanson, J.S., Harris, G.H., Furstenau, D.W., 1990. Principles and practice of sulphide mineral flotation. Sulphide deposits – their origin and processing. ***The Institution of Mining and Metallurgy,*** Elsevier Science Publishers Ltd., pp. 87 – 101.

Hofirek, Z., Kerfoot, D.G.E., 1992. The chemistry of the nickel-copper matte leach and its applications to process control and optimisation. ***Hydrometallurgy,*** Volume 29, Number 1-3, pp. 357 – 381.

Hofirek, Z., Nofal, P.J., 1995. Pressure leach capacity expansion using oxygen-enriched air at RBMR (Pty) Ltd. ***Hydrometallurgy,*** Volume 39, pp. 91 – 116.

Holwell, D.A., McDonald, I., 2010. A review of the behaviour of platinum group elements within natural magmatic sulfide ore systems. ***Johnson Matthey Platinum Metals Review,*** Volume 54, Number 1, pp. 26 – 36.

Hume-Rothery, W., 1969. Atomic theory for students of metallurgy. ***Published: The Institute of Metals,*** London, 5th reprint, 342 pages.

Hurlbut, C.S., Klein, C., 1985. Manual of Mineralogy. ***Published: Wiley,*** ISBN 0- 471-80580-7, 20th edition, 596 pages.

Jacobs, M., 2006. Process description and abbreviated history of Anglo Platinum's Waterval Smelter. ***Southern African Pyrometallurgy 2006,*** Edited by R.T. Jones, South African Institute of Mining and Metallurgy, pp. 17 – 28.

Jones, R.T., 2004. JOM world nonferrous smelter survey, Part II: Platinum group metals. ***JOM The Member Journal of The Minerals, Metals and Materials Society,*** Volume 56, Issue 12, pp. 59 – 63.

Jones, R.T., 2005. An overview of Southern African PGM smelting. ***Nickel and Cobalt 2005, Challenges in Extraction and Production,*** Edited by J. Donald and R. Schonewille, CIM, pp. 147 – 178.

King, R.P., 1994a. Comminution and liberation of minerals. ***Minerals Engineering,*** Volume 7, Numbers 2/3, pp. 129 – 140.

King, R.P., 1994b. Linear stochastic models for mineral liberation. ***Powder Technology,*** Volume 81, pp. 217 – 234.

Kullerud, G., 1963. Thermal stability of pentlandite. ***The Canadian Mineralogist,*** Volume 7, Number 3, pp. 353 – 366.

Kullerud, G., Yoder, H.S., 1959. Pyrite stability relations in the Fe-S system. ***Economic Geology,*** Volume 54, Number 4, pp. 533 – 572.

Kullerud, G., Yund, R.A., 1962. The Ni-S system and related minerals. ***Journal of Petrology,*** Volume 3, Number 1, pp. 126 – 175.

Kyllo, A.K., Richards, G.G., 1991. A mathematical model of the nickel converter: Part I. Model development and verification. ***Metallurgical Transactions B,*** Volume 22B, pp. 153 – 161.

Kyllo, A.K., Richards, G.G., Marcuson, S.W., 1992. A mathematical model of the nickel converter: Part II. Application and analysis of converter operation. ***Metallurgical Transactions B,*** Volume 23B, pp. 573 – 582.

Leigh, G.M., Lyman, G.J., Gottlieb, P., 1996. Stereological estimates of liberation from mineral section measurements: a rederivation of Barbery's formulae with extensions. ***Powder Technology,*** Volume 87, pp. 141 – 152.

Liddell, K.S., McRae, L.B., Dunne, R.C., 1986. Process route for beneficiation of noble metals from Merensky and UG-2 ores. ***Mintek Review,*** Number 4, pp. 33 – 44.

Lloyd, G.E., 1987. Atomic number and crystallographic contrast images with the SEM: a review of backscattered electron techniques. ***Mineralogical Magazine,*** Volume 51, pp. 3 – 19.

Lof, P., 1982. Elsevier's Mineral and Rock Table. ***Published: Elsevier Scientific Publishing Company,*** New York.

Lorimer, G.W., 1987. Quantitative X-ray microanalysis of thin specimens in the transmission electron microscope; a review. ***Mineralogical Magazine,*** Volume 51, pp. 49 – 60.

Lynch, A.J., Rowland, C.A., 2005. The history of grinding. ***Published: Society of Mining, Metallurgical, and Exploration,*** Colorado, ISBN 0 – 87335 – 238 – 6, 207 pages.

Mäkinen, T., Taskinen, P., 2006. The state of the art in nickel smelting: Direct Outokumpu nickel technology. ***Sohn International Symposium Advanced Processing of Metals and Materials,*** Volume 8, pp. 313 – 325.

Merwin, H.E., Lombard, R.H., 1937. The system, Cu-Fe-S. ***Economic Geology,*** Volume 32, pp. 203 – 284.

Moh, G.H., Kullerud, G., 1963. The Cu-Ni-S system and low temperature mineral assemblages. ***Carnegie Inst. Washington,*** Year book 61, pp. 189 – 192.

Morimoto, N., Koto, K., 1970. Phase relations of the Cu-S system at low temperatures: stability of anilite. ***The American Mineralogist,*** Volume 55, pp. 106 – 117.

Mungall, J.E., 2007. Crystallization of magmatic sulphides: An empirical model and application to Sudbury ores. ***Geochimica et Cosmochimica Acta,*** Volume 71, pp. 2809 – 2819.

Nagamori, M., Ingraham, T.R., 1970. Thermodynamic properties of Ni-S melts between 700^{o} and 1100^{o} C. ***Metallurgical Transactions,*** Volume 1, pp. 1821 – 1825.

Napier-Munn, T.J., Morell, S., Morrison, R.D., Kojovic, T., 2005. Mineral comminution circuits their operation and optimisation. ***Published: Julius Kruttschnitt Mineral Research Centre,*** University of Queensland, ISBN 0 – 646 – 28861 – X, 413 pages.

Nell, J., 2004. Melting of platinum group metal concentrates in South Africa. ***The Journal of The South African Institute of Mining and Metallurgy,*** Volume 104, Number 9, pp. 423 – 428.

Norval, D., 2005. Metals and alloys water solidification a bridge from pyro- to hydrometallurgy. The Southern African Institute of Mining and Metallurgy, ***The Third Southern African Conference on Base Metals,*** pp. 97 – 106.

Norval, D., Oberholster, R.E., 2011. Further processing and granulation of slags with entrained metal and high metal compound content, with specific reference to present manganese slag dumps as well as additions due to daily production. ***Southern African Pyrometallurgy 2011,*** Edited by R.T. Jones and P. Den Hoed, Southern African Institute of Mining and Metallurgy, pp. 129 – 143.

Oliver, W.C., Pharr, G.M., 1992. An improved technique for determining hardness and elastic modulus using load and displacement sensing indentation experiments. ***Journal of Material Research,*** Volume 7, Number 6, pp. 1564 – 1583.

Page, M.L., 1982. A mineralogical study of nickel mattes from the Kalgoorlie nickel smelter, Kalgoorlie, Western Australia. ***Metallurgical and Materials Transactions B,*** Volume 13, Issue 2, pp. 141 – 152.

Peters, E., 1976. Direct leaching of sulfides: chemistry and applications. ***Metallurgical Transactions B,*** Volume 7B, pp. 505 – 517.

Petersen, L., Dahl, C.K., Esbensen, K.H., 2004. Representative mass reduction in sampling – a critical survey of techniques and hardware. ***Chemometrics and Intelligent Laboratory Systems,*** Volume 74, pp. 95 – 114.

Philibert, J., Tixier, R., 1968. Electron penetration and the atomic number correction in electron probe microanalysis. ***British Journal of Applied Physics,*** Series 2, Volume 1, pp. 685 – 694.

Pitard, F.F., 2005. Sampling correctness – a comprehensive guideline. ***Second World Conference on Sampling and Blending,*** Sunshine Coast, Queensland, Australia, pp. 55 – 66.

Porter, D.A., Easterling, K.E., 1992. Phase transformations in metals and alloys, second edition. ***Published: Chapman and Hall,*** London, 514 pages.

Posfai, M., Buseck, P.R., 1994. Djurleite, digenite, and chalcocite: Intergrowths and transformations. ***American Mineralogist,*** Volume 79, pp. 308 – 315.

Potter, R.W., 1977. An electrochemical investigation of the system copper-sulfur. ***Economic Geology,*** Volume 72, Number 8, pp. 1524 – 1542.

Predel, B., 1994. Phase equilibria, crystallographic and thermodynamic data of binary alloys. ***Published: New Series, Springer,*** Germany, Volume 5, Sub-volume a – g.

Raghavan, V., 2004. Fe-Ni-S (Iron-Nickel-Sulfur). ***Journal of Phase Equilibria and Diffusion,*** Volume 25, Number 4, pp. 373 – 381.

Reid, K.J., 1965. A solution to the batch grinding equation. ***Chemical Engineering Science,*** Volume 20, pp. 953 – 963.

Riekkola-Vanhanen, M., 1999. Finnish expert report on best available techniques in nickel production. ***Finnish Environment Institute,*** Helsinki, ISBN 952 – 11 – 0507 – 0, 63 pages.

Rietveld, H.M., 1969. A profile refinement method for nuclear and magnetic structures. ***Journal of Applied Crystallography,*** 2, pp. 65 – 71.

Ritter, M., Midgley, P.A., 2010. A practical approach to test the scope of FIB-SEM 3D reconstruction. ***Journal of Physics:*** Conference Series, Volume 241, Number 1.

Rogers, J., 1962. Principles of sulfide mineral flotation. Froth Flotation, 50th Anniversary Volume, Edited by D.W. Fuerstenau, ***The American Institute of Mining, Metallurgical, and Petroleum Engineers Inc.,*** New York, pp. 139 – 169.

Roseboom, E.H., 1966. An investigation of the system Cu-S and some natural copper sulfides between 25 degrees and 700 degrees C. ***Economic Geology,*** Volume 61, Number 4, pp. 641 – 672.

Rosenqvist, T., 1978. Phase equilibria in the pyrometallurgy of sulfide ores. ***Metallurgical Transactions B,*** Volume 9B, pp. 337 – 351.

Rubin, A.E., 1991. Euhedral awaruite in the Allende meteorite: Implications for the origin of awaruite- and magnetite-bearing nodules in CV3 chondrites. ***American Minerologist,*** Volume 76, pp. 1356 – 1362.

Schouwstra, R.P., 2000. The slow-cooling process: A mineralogical perspective. ***CIM Bulletin,*** Volume 93, Number 1036, pp. 168 – 171.

Schouwstra, R.P., 2003. The slow-cooling process: the impact of composition on the quality and subsequent processing of converter matte – a mineral resource management perspective. ***Master's Thesis,*** Faculty of Science, University of the Free State, South Africa, 78 pages.

Schouwstra, R.P., 2008. Converter matte characterisation. ***Anglo Research Mineralogical Department,*** Report No: M/07/238, 13 pages.

Selivanov, E.N., Gulyaeva, R.I., Nechvoglod, O.V., Avdeev, A.S., Kniss, S.V., 2009. Phase composition and the chemistry of oxidation of nickel converter matte. ***Russian Metallurgy (Metally),*** Volume 2, pp. 100 - 106.

Sharma, R.C., Chang, Y.A., 1980a. A thermodynamic analysis of the copper-sulfur system. ***Metallurgical Transactions B,*** Volume 11B, pp. 575 – 583.

Sharma, R.C., Chang, Y.A., 1980b. Thermodynamics and phase relationships of transition metal-sulfur systems: IV. Thermodynamic properties of the Ni-S liquid phase and the calculation of the Ni-S phase diagram. ***Metallurgical Transactions B,*** Volume 11B, pp. 139 – 146.

Shewman, R.W., 1966. Pentlandite phase relations in the Fe-Ni-S system and the stability of the pyrite-pentlandite assemblage. ***Master's Thesis,*** Department of Geological Sciences, McGill University, Canada.

Sineva, S.I., Starykh, R.V., Frolenkova, M.V., Zakhryapin, S.B., 2009. The study of liquidus and solidus surfaces of the four-component system Fe-Ni-Cu-S. Part I. Graphing of meltability in the three-component system Fe-Ni-Cu. ***Russian Metallurgy (Metally),*** Volume 2009, Number 3, pp. 263 – 270.

Southwick, L.M., 2008. William Peirce and E.A. Cappelen Smith and their amazing copper converting machine. ***JOM The Member Journal of The Minerals, Metals and Materials Society,*** Volume 60, Number 10, pp. 24 – 34.

Spencer, S., Sutherland, D., 2000. Stereological correction of mineral liberation grade distributions estimated by single sectioning of particles. ***Image Analysis and Stereology,*** Volume 19, pp. 175 – 182.

Sridhar, R., Toguri, J.M., Simeonov, S., 1997. Copper losses and thermodynamic considerations in copper smelting. ***Metallurgical and Materials Transactions B,*** Volume 28B, pp. 191 – 200.

Sridhara Rao, D.V., Muraleedharan, K., Humphreys, C.J., 2010. TEM specimen preparation techniques. ***Microscopy: Science, Technology, Applications and Education,*** FORMATEX Microscopy Series Number 4, Volume 2, pp. 1232 – 1244.

Starykh, R.V., Sineva, S.I., Frolenkova, M.V., Zakhrypin, S.B., 2009. Study of the liquidus and solidus surfaces in the quarternary Fe-Ni-Cu-S system: II. Constructing a meltability diagram for the ternary Fe-Ni-S sulfide system. ***Russian Metallurgy (Metally),*** Volume 2009, Number 5, pp. 447 – 453.

Steenekamp, N., Dunn, M.G., 1999. Operations of and improvements to the Lonrho platinum base metal refinery. ***Proceedings of the EPD Congress,*** Edited by B. Mishra, pp. 365 – 378.

Sugaki, A., Shima, H., Kitakaze, A., Harada, H., 1975. Isothermal phase relations in the system Cu-Fe-S under hydrothermal conditions at 350 ^{o}C and 300 ^{o}C. ***Economic Geology,*** Volume 70, pp. 806 – 823.

Sutherland, D.N., Gottlieb, P., 1991. Application of automated quantitative mineralogy in mineral processing. ***Minerals Engineering,*** Volume 4, Numbers 7 – 11, pp. 753 – 762.

Taskinen, P., Dinsdale, A.T., Gisby, J.A., 2005. Industrial slag chemistry: a case study of computational thermodynamics. ***Scandinavian Journal of Metallurgy,*** Volume 34, pp. 100 – 107.

Toulmin, III, P., Barton, Jr., P.B., 1964. A thermodynamic study of pyrite and pyrrhotite. ***Geochimica et Cosmochimica Acta,*** Volume 28, pp. 641 – 671.

Tshilombo, K.G., Pistorius, P.C., 2006. Oxygen activity measurements in simulated converter matte. ***Internation Platinum Conference 'Platinum Surges Ahead',*** The Southern African Institute of Mining and Metallurgy, pp. 247 – 251.

Uchic, M.D., Groeber, M.A., Dimiduk, D.M., Simmons, J.P., 2006. 3D microstructural characterization of nickel superalloys via serial-sectioning using a dual beam FIB-SEM. ***Scripta Materialia,*** Volume 55, pp. 23 – 28.

van Schalkwyk, R.F., Eksteen, J.J., Akdogan, G., 2013. Leaching of Ni-Cu-Fe-S converter matte at varying iron endpoints; mineralogical changes and behaviour of Ir, Rh and Ru. ***Hydrometallurgy,*** Volume 136, pp. 36 – 45.

van Schalkwyk, R.F., Eksteen, J.J., Petersen, J., Thyse, E.L., Akdogan, G., 2011. An experimental evaluation of the leaching kinetics of PGM-containing Ni-Cu-Fe-S Peirce-Smith converter matte, under atmospheric leach conditions. ***Minerals Engineering,*** Volume 24, Issue 6, pp. 524 – 534.

Vaughan, D.J., 2005. Sulphides: Minerals / Sulphides. ***Published: Elsevier Ltd,*** London, pp. 574 – 586.

Vaughan, D.J., Craig, J.R., 1978. Mineral chemistry of metal sulfides. ***Published: Cambridge University Press,*** Cambridge, 476 pages.

Viljoen, W., 2001. Phase relations in the system Cu-Fe-Ni-S and their application to the slow cooling of PGE matte. ***PhD Dissertation,*** Faculty of Natural and Agricultural Science, University of Pretoria, South Africa, 120 pages.

Waldner, P., Pelton, A.D., 2005. Thermodynamic modeling of the Fe-S system. ***Journal of Phase Equilibria and Diffusion,*** Volume 26, Number 1, pp. 23 – 38.

Warner, A.E.M., Diaz, C.M., Dalvi, A.D., Mackey, P.J., Tarasov, A.V., Jones, R.T., 2007. JOM world nonferrous smelter survey, Part IV: Nickel: Sulfide. ***JOM The Member Journal of The Minerals, Metals and Materials Society,*** Volume 59, Number 4, pp. 58 – 71.

Wiegel, R.L., 2010. Comparison of volumetric and section area particle compositions using the Gaudin random mineral liberation model. ***Minerals and Metallurgical Processing,*** Volume 27, Number 1, pp. 24 – 33.

Williams, K.L., 1960. An associate of awaruite with heazlewoodite. ***The American Mineralogist,*** Volume 45, pp. 450 – 453.

Wills B.A., Napier-Munn, T.J. 2006. Will's Mineral Processing Technology: An introduction to the practical aspects of ore treatment and mineral recovery. ***Published: Elsevier Science and Technology,*** Amsterdam, ISBN 0750644508, 444 pages.

Yan, D., Eaton, R., 1994. Breakage properties of ore blends. ***Minerals Engineering,*** Volume 7, Numbers 2/3, pp. 185 – 199.

Yund, R.A., Kullerud, G., 1966. Thermal stability of assemblages in the Cu-Fe-S system. ***Journal of Petrology,*** Volume 7, Number 3, pp. 454 – 488.

Zussman, J., 1987. Minerals and the electron microscope. ***Mineralogical Magazine,*** Volume 51, pp. 129 – 138.

APPENDIX A
SEM SAMPLE PREPARATION METHOD AND EQUIPMENT

Table A.1: Summary of the sample preparation method applied and the equipment used.

Samples:	Granulated converter matte						
Description:	Particles embedded in resin blocks						
Equipment:	Polishing pads, lubricants, diamond suspensions, grit paper, optical microscope and ultrasonic bath						
Grinding:	Machine:	 Polisher Saphir 520					
	N.B.	Between each polishing step, clean the sample in the ultrasonic bath (removes dirt and prevents cross-contamination)					
	Step 1	**Step 2**	**Step 3**	**Step 4**	**Step 5**	**Step 6**	**Step 7**
Media:	grit paper	Si carbide pad	Si carbide pad	aka-plaran (white woven)	verdutex (green)	chemomet (black furry)	chemomet (black furry)
Grain Size:	P150	30µm	9µm	6µm	3µm	1µm	0.25µm
Suspension:	none	none	none	6µm diamond suspension	3µm diamond suspension	1µm diamond suspension	0.25µm diamond suspension
Lubricant:	water	water	water	blue lube	blue lube	blue lube	colloidal silica
Direction:	→ →	→ →	→ →	→ →	→ →	→ →	→ ←
Pressure (N):	hand	50	50	50	50	20	20
Speed (rpm):	hand	150	150	150	150	150	150
Time:	own judgement	own judgment	> 10 min	>15 min	>30	>35	>40
Dose Rate:	regular	constant flow	constant	5 min	5 min	5 min	5 min
Lubricant Rate:	regular	constant	constant	30 sec	30 sec	30 sec	30 sec

APPENDIX B
ATLAS OF MICROSTRUCTURES

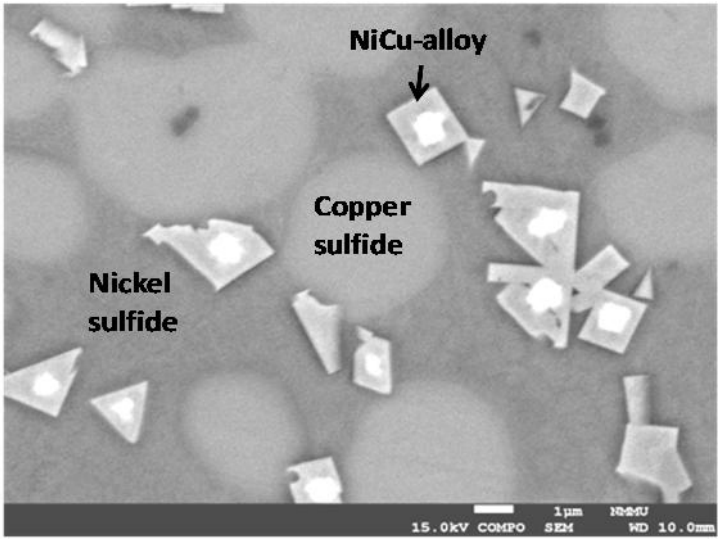

Figure B.1: SEM micrograph showing the presence of nickel sulfide, copper sulfide and NiCu-alloy minerals for the 0.15% Fe matte at 1µm size scale.

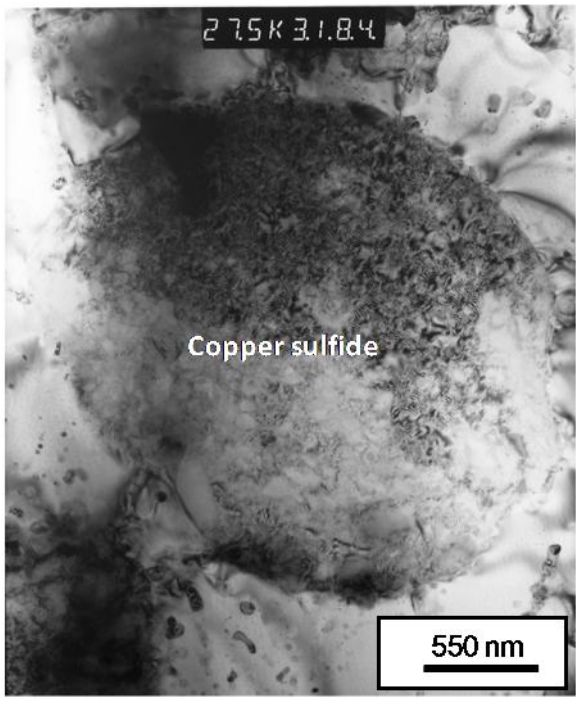

Figure B.2: Bright field TEM micrograph of a copper sulfide (Cc) mineral grain for the 5.17% Fe matte at 550nm size scale.

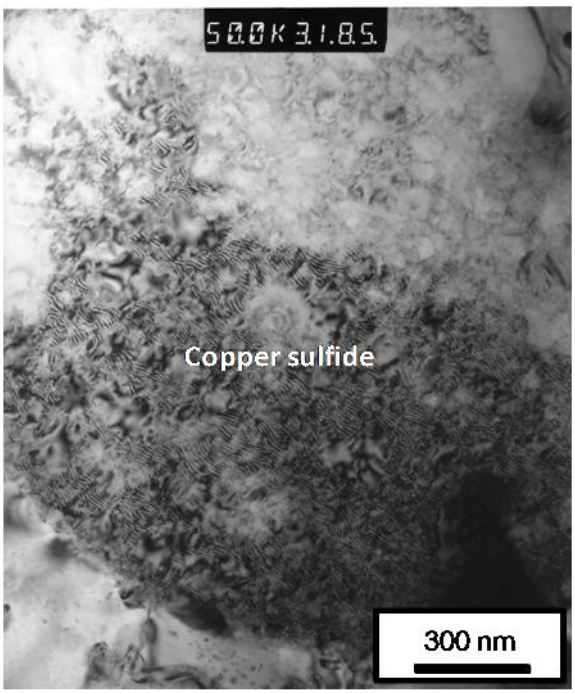

Figure B.3: Bright field TEM micrograph of the copper sulfide mineral grain for the 5.17% Fe matte at 300nm size scale.

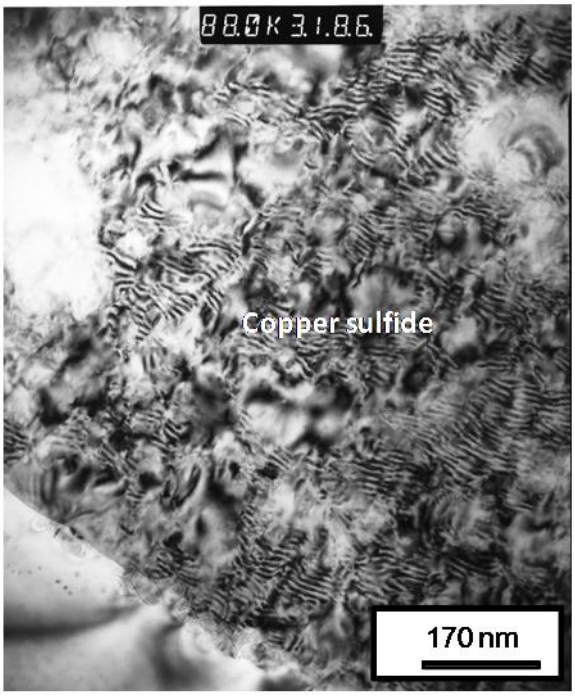

Figure B.4: Bright field TEM micrograph of the copper sulfide mineral grain for the 5.17% Fe matte at 170nm size scale.

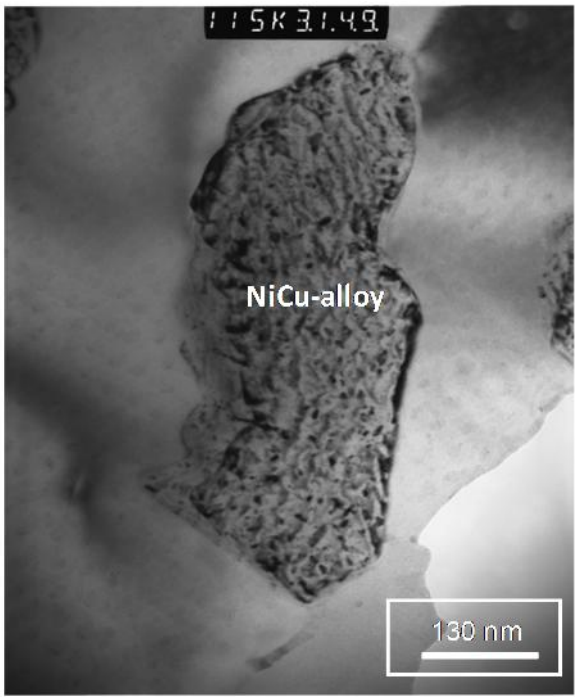

Figure B.5: Bright field TEM micrograph of a NiCu-alloy grain (A) with respect to the 0.99% Fe matte at 130nm size scale.

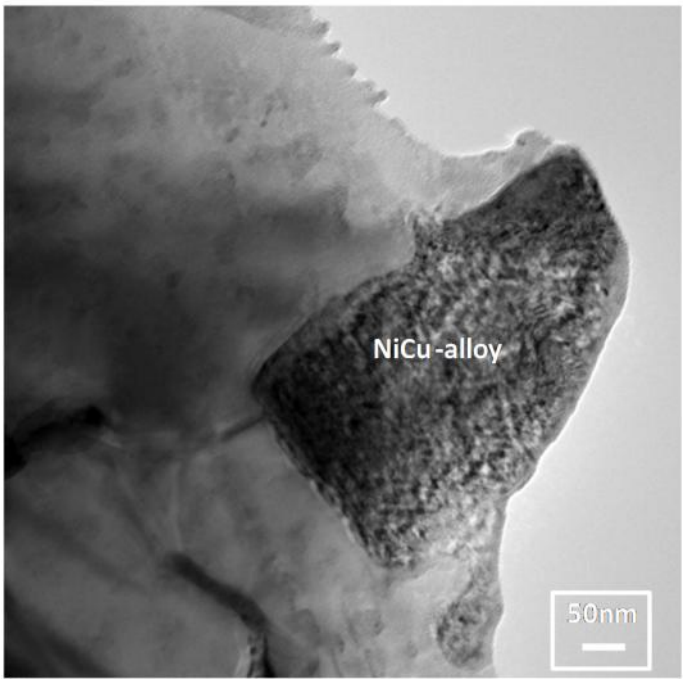

Figure B.6: Bright field TEM micrograph of a NiCu-alloy for the 0.99% Fe matte at 50nm size scale.

APPENDIX C
PRINCIPAL MINERAL CHEMISTRY AND 3D MOVIES

C.1. Principal Mineral Chemistry

Table C.1: Principal mineral chemistry of nickel sulfide minerals with respect to all three iron endpoints.

Matte	5.17% Fe		0.99% Fe		0.15% Fe	
Element	Ni (wt%)	S (wt%)	Ni (wt%)	S (wt%)	Ni (wt%)	S (wt%)
Analysis 1	62.11	27.10	65.76	24.41	71.08	26.18
Analysis 2	59.02	26.85	66.14	17.80	70.24	25.11
Analysis 3	61.63	27.08	63.22	23.14	69.34	26.80
Analysis 4	58.07	26.59	63.68	23.55	64.21	23.90
Analysis 5	61.98	26.34	57.38	21.01	67.35	24.01
Analysis 6	61.59	27.09	57.68	21.16	70.25	24.63
Analysis 7	62.94	27.10	64.78	22.58	67.24	25.84
Analysis 8	62.65	27.04	64.37	21.15	70.24	21.89
Analysis 9	62.47	27.68	65.70	24.51	61.16	23.34
Analysis 10	61.10	27.50	67.19	25.08	67.61	22.90
Analysis 11	†N.A.	†N.A.	66.72	24.82	64.35	20.82
Analysis 12	†N.A.	†N.A.	66.01	24.99	68.22	21.15
Analysis 13	†N.A.	†N.A.	66.54	24.92	70.42	17.66
Analysis 14	†N.A.	†N.A.	65.92	25.05	65.16	20.65
Analysis 15	†N.A.	†N.A.	61.56	24.71	60.52	21.35
Analysis 16	†N.A.	†N.A.	60.20	24.68	61.05	23.26

Element	Ni (wt%)	S (wt%)	Ni (wt%)	S (wt%)	Ni (wt%)	S (wt%)
Analysis 17	†N.A.	†N.A.	66.07	24.44	70.58	26.73
Analysis 18	†N.A.	†N.A.	66.15	23.63	65.84	24.94
Analysis 19	†N.A.	†N.A.	†N.A.	†N.A.	66.48	22.80
Analysis 20	†N.A.	†N.A.	†N.A.	†N.A.	64.34	23.09
Analysis 21	†N.A.	†N.A.	†N.A.	†N.A.	64.05	23.06
Analysis 22	†N.A.	†N.A.	†N.A.	†N.A.	64.66	23.33
Total Analyses	10	10	18	18	22	22
Minimum	58.07	26.34	57.38	17.80	60.52	17.66
Maximum	62.94	27.68	67.19	25.08	71.08	26.80
Average	61.36	27.04	64.17	23.42	66.56	23.34
Standard Deviation	1.59	0.39	3.03	1.99	3.30	2.22

†N.A.: - Not Analyzed.

Table C.2: Principal mineral chemistry of copper sulfide minerals for all three iron endpoints.

Matte	5.17% Fe		0.99% Fe		0.15% Fe	
Element	**Cu (wt%)**	**S (wt%)**	**Cu (wt%)**	**S (wt%)**	**Cu (wt%)**	**S (wt%)**
Analysis 1	58.30	23.26	57.49	18.65	73.43	20.29
Analysis 2	53.24	23.76	70.09	20.83	76.57	20.40
Analysis 3	54.33	23.64	68.87	20.84	70.22	19.46
Analysis 4	64.42	22.35	72.28	20.53	67.45	19.64
Analysis 5	63.17	22.92	70.48	20.94	71.72	20.55
Analysis 6	58.82	22.86	63.58	20.88	72.61	19.74
Analysis 7	65.34	22.79	55.57	21.46	68.86	20.76

Element	Cu (wt%)	S (wt%)	Cu (wt%)	S (wt%)	Cu (wt%)	S (wt%)
Analysis 8	57.80	23.18	60.10	21.25	65.92	20.04
Analysis 9	66.06	22.74	54.75	21.32	73.67	20.32
Analysis 10	58.54	23.24	72.57	20.76	74.51	20.31
Analysis 11	60.15	23.44	69.85	21.10	69.91	19.23
Analysis 12	†N.A.	†N.A.	64.10	21.03	72.66	20.07
Analysis 13	†N.A.	†N.A.	71.57	20.43	73.29	19.98
Analysis 14	†N.A.	†N.A.	62.01	21.41	74.72	19.86
Analysis 15	†N.A.	†N.A.	†N.A.	†N.A.	73.41	20.71
Analysis 16	†N.A.	†N.A.	†N.A.	†N.A.	70.19	20.76
Analysis 17	†N.A.	†N.A.	†N.A.	†N.A.	66.93	20.51
Analysis 18	†N.A.	†N.A.	†N.A.	†N.A.	67.73	19.62
Total Analyses	11	11	14	14	18	18
Minimum	53.24	22.35	54.75	18.65	65.92	19.23
Maximum	66.06	23.76	72.57	21.46	76.57	20.76
Average	60.02	23.11	65.24	20.82	71.32	20.12
Standard Deviation	4.29	0.42	6.41	0.70	3.05	0.46

Table C.3: Principal mineral chemistry of NiCu-alloy with respect to all three iron endpoints.

Matte	**5.17% Fe**			**0.99% Fe**			**0.15% Fe**		
Element	**NiCu (wt%)**	**S (wt%)**	**Pt (wt%)**	**NiCu (wt%)**	**S (wt%)**	**Pt (wt%)**	**NiCu (wt%)**	**S (wt%)**	**Pt (wt%)**
Analysis 1	54.68	22.78	10.80	87.68	8.45	1.85	72.24	6.18	15.33
Analysis 2	61.36	24.45	7.00	89.04	1.87	1.78	74.36	4.01	17.60
Analysis 3	62.82	24.87	3.21	84.63	8.18	0.39	73.52	4.23	17.85
Analysis 4	60.77	24.57	6.22	85.93	3.23	1.25	80.97	5.74	6.89
Analysis 5	55.03	25.23	8.10	92.94	0.92	1.69	76.18	7.39	12.83
Analysis 6	61.94	25.61	3.70	76.39	17.29	0.11	78.13	9.98	1.16
Analysis 7	55.23	22.69	10.45	90.38	2.66	1.69	81.55	2.69	7.65
Analysis 8	59.80	25.52	5.24	79.06	13.98	0.23	62.89	6.95	18.24
Analysis 9	†N.A.	†N.A.	†N.A.	76.57	14.50	0.14	72.66	9.17	10.56
Analysis 10	†N.A.	†N.A.	†N.A.	75.76	19.49	0.12	74.45	8.93	10.15
Analysis 11	†N.A.	†N.A.	†N.A.	59.54	18.43	17.02	83.77	10.09	1.16
Analysis 12	†N.A.	†N.A.	†N.A.	57.73	16.45	16.93	83.14	5.50	5.74
Analysis 13	†N.A.	†N.A.	†N.A.	58.61	15.93	14.93	80.61	7.10	8.49
Analysis 14	†N.A.	†N.A.	†N.A.	71.00	17.80	2.78	82.59	8.99	4.14
Analysis 15	†N.A.	†N.A.	†N.A.	68.82	21.03	0.96	78.98	13.74	2.41
Analysis 16	†N.A.	†N.A.	†N.A.	69.62	22.42	1.56	79.05	14.97	2.59
Analysis 17	†N.A.	†N.A.	†N.A.	53.80	16.77	14.22	81.21	1.76	10.95
Analysis 18	†N.A.	†N.A.	†N.A.	68.60	20.68	2.82	84.92	4.61	5.53
Analysis 19	†N.A.	†N.A.	†N.A.	61.48	19.98	14.40	†N.A.	†N.A.	†N.A.
Total Analyses	8	8	8	19	19	19	18	18	18
Minimum	54.68	22.69	3.21	53.80	0.92	0.11	62.89	1.76	1.16
Maximum	62.82	25.61	10.80	92.94	22.42	17.02	84.92	14.97	18.24
Average	58.95	24.46	6.84	74.08	13.69	4.99	77.85	7.34	8.85
Standard Deviation	3.41	1.15	2.83	12.24	7.15	6.53	5.47	3.52	5.74

C.2. 3D Movies

Movies of 3D mineral structures can be viewed and downloaded at http:/chrtem.nmmu.ac.za.

APPENDIX D
MTDATA PHASE MASS AND COMPOSITIONAL ANALYSIS

D.1. Phase Mass Analysis

Table D.1: Phase mass analyses at 100 °C intervals for phases within the high-iron containing matte system.

Temperature (°C)	Liquid (%)	Spinel (%)	Digenite (%)	Ni_3S_2 (%)	Heazlewoodite (%)	Beta-chalcocite (%)
1500	1.00E+02	0.00E+00	0.00E+00	0.00E+00	0.00E+00	0.00E+00
1400	9.83E+01	1.66E+00	0.00E+00	0.00E+00	0.00E+00	0.00E+00
1300	9.65E+01	3.52E+00	0.00E+00	0.00E+00	0.00E+00	0.00E+00
1200	9.54E+01	4.57E+00	0.00E+00	0.00E+00	0.00E+00	0.00E+00
1100	9.48E+01	5.18E+00	0.00E+00	0.00E+00	0.00E+00	0.00E+00
1000	9.45E+01	5.53E+00	0.00E+00	0.00E+00	0.00E+00	0.00E+00
900	9.38E+01	5.71E+00	4.77E-01	0.00E+00	0.00E+00	0.00E+00
800	7.92E+01	5.84E+00	1.50E+01	0.00E+00	0.00E+00	0.00E+00
700	0.00E+00	5.87E+00	3.19E+01	6.22E+01	0.00E+00	0.00E+00
600	0.00E+00	5.86E+00	3.27E+01	6.14E+01	0.00E+00	0.00E+00
500	0.00E+00	5.87E+00	3.42E+01	0.00E+00	5.62E+01	0.00E+00
400	0.00E+00	5.87E+00	3.32E+01	0.00E+00	5.54E+01	0.00E+00
300	0.00E+00	5.87E+00	2.95E+01	0.00E+00	5.53E+01	0.00E+00
200	0.00E+00	5.89E+00	0.00E+00	0.00E+00	5.59E+01	2.48E+01

* Note: Phase mass analysis within 2.5 °C is available upon request.

D.2. Phase Compositional Analysis

Table D.2: Components of the spinel phase within the high-iron containing matte system with respect to varying mass fractions.

Temperature (°C)	Co	Cu	Fe	Ni	S	O
1410	8.56E-03	3.53E-04	6.15E-01	1.01E-01	0.00E+00	2.75E-01
1300	1.00E-02	2.16E-04	6.18E-01	9.72E-02	0.00E+00	2.75E-01
1200	1.08E-02	1.28E-04	6.23E-01	9.06E-02	0.00E+00	2.75E-01
1100	1.12E-02	6.96E-05	6.33E-01	8.04E-02	0.00E+00	2.75E-01
1000	1.11E-02	3.66E-05	6.47E-01	6.69E-02	0.00E+00	2.75E-01
900	1.04E-02	1.67E-05	6.63E-01	5.08E-02	0.00E+00	2.76E-01
800	7.11E-03	3.66E-06	6.89E-01	2.75E-02	0.00E+00	2.76E-01
700	4.40E-03	6.92E-07	7.03E-01	1.70E-02	0.00E+00	2.76E-01
600	3.53E-03	9.02E-08	7.12E-01	8.00E-03	0.00E+00	2.76E-01
500	1.16E-02	1.17E-08	7.07E-01	5.27E-03	0.00E+00	2.76E-01
400	1.65E-02	0.00E+00	7.04E-01	3.83E-03	0.00E+00	2.76E-01
300	3.10E-02	0.00E+00	6.90E-01	2.66E-03	0.00E+00	2.76E-01
200	1.01E-01	0.00E+00	6.20E-01	3.66E-03	0.00E+00	2.75E-01

* Note: Mass fractions within 2.5 °C are available upon request.

Table D.3: Components of digenite within the high-iron containing matte system with respect to varying mass fractions.

Temperature (°C)	Co	Cu	Fe	Ni	S
900	8.37E-03	7.36E-01	1.19E-02	2.90E-02	2.15E-01
850	8.58E-03	7.31E-01	1.40E-02	3.08E-02	2.16E-01
800	8.69E-03	7.26E-01	1.65E-02	3.25E-02	2.17E-01
750	8.67E-03	7.20E-01	1.94E-02	3.42E-02	2.18E-01
700	6.87E-03	7.32E-01	1.54E-02	3.08E-02	2.15E-01
650	6.60E-03	7.35E-01	1.53E-02	2.91E-02	2.14E-01
600	6.29E-03	7.38E-01	1.56E-02	2.70E-02	2.14E-01
550	5.94E-03	7.40E-01	1.62E-02	2.45E-02	2.13E-01
500	1.13E-02	7.30E-01	1.48E-02	2.86E-02	2.15E-01
450	1.03E-02	7.42E-01	9.97E-03	2.47E-02	2.13E-01
400	9.01E-03	7.53E-01	6.77E-03	2.11E-02	2.11E-01
350	7.27E-03	7.64E-01	4.14E-03	1.64E-02	2.08E-01
300	5.44E-03	7.75E-01	2.35E-03	1.12E-02	2.06E-01
250	3.74E-03	7.84E-01	1.12E-03	7.11E-03	2.04E-01
220	2.84E-03	7.88E-01	6.20E-04	5.22E-03	2.04E-01

Table D.4: Components of Ni_3S_2 within the high-iron containing matte system with respect to varying mass fractions.

Temperature (°C)	Co	Cu	Fe	Ni	S
715	9.81E-03	3.25E-02	1.01E-02	6.73E-01	2.75E-01
700	7.63E-03	2.66E-02	8.97E-03	6.86E-01	2.70E-01
650	7.82E-03	1.98E-02	8.47E-03	6.93E-01	2.71E-01
600	8.04E-03	1.40E-02	7.88E-03	6.98E-01	2.72E-01
550	8.28E-03	9.42E-03	7.18E-03	7.03E-01	2.72E-01
512.5	2.67E-02	9.29E-03	3.61E-03	6.69E-01	2.91E-01

Table D.5: Components of heazlewoodite within the high-iron containing matte system with respect to varying mass fractions.

Temperature (°C)	Co	Cu	Fe	Ni	S
547.5	1.56E-03	0.00E+00	0.00E+00	7.31E-01	2.67E-01
500	3.91E-03	0.00E+00	0.00E+00	7.29E-01	2.67E-01
450	3.71E-03	0.00E+00	0.00E+00	7.29E-01	2.67E-01
400	3.33E-03	0.00E+00	0.00E+00	7.30E-01	2.67E-01
350	3.01E-03	0.00E+00	0.00E+00	7.30E-01	2.67E-01
300	3.03E-03	0.00E+00	0.00E+00	7.30E-01	2.67E-01
250	2.86E-03	0.00E+00	0.00E+00	7.30E-01	2.67E-01
200	2.22E-03	0.00E+00	0.00E+00	7.31E-01	2.67E-01

Table D.6: Components of beta-chalcocite within the high iron-containing matte system with respect to varying mass fractions.

Temperature (°C)	Co	Cu	Fe	Ni	S
217.5	0.00E+00	7.99E-01	0.00E+00	0.00E+00	2.01E-01
215	0.00E+00	7.99E-01	0.00E+00	0.00E+00	2.01E-01
212.5	0.00E+00	7.99E-01	0.00E+00	0.00E+00	2.01E-01
210	0.00E+00	7.99E-01	0.00E+00	0.00E+00	2.01E-01
207.5	0.00E+00	7.99E-01	0.00E+00	0.00E+00	2.01E-01
205	0.00E+00	7.99E-01	0.00E+00	0.00E+00	2.01E-01
202.5	0.00E+00	7.99E-01	0.00E+00	0.00E+00	2.01E-01
200	0.00E+00	7.99E-01	0.00E+00	0.00E+00	2.01E-01

APPENDIX E
RESIDUAL HARDNESS IMPRESSIONS

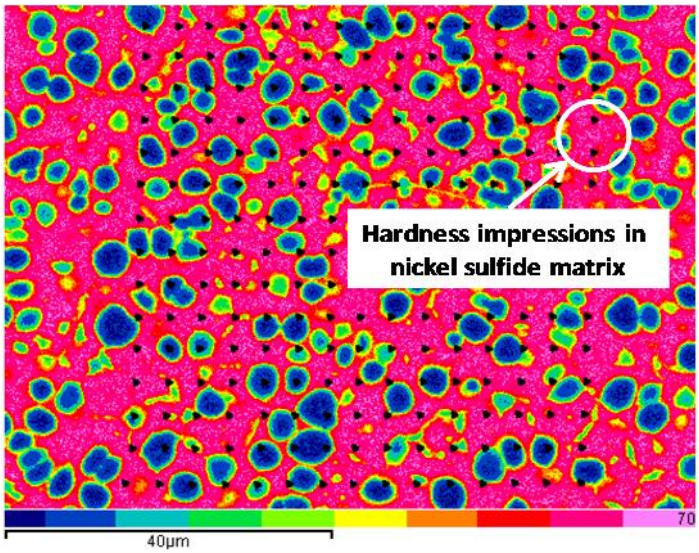

Figure E.1: Residual hardness impressions on a 5.17% Fe matte particle section with respect to a false pink color nickel sulfide map at 40µm size scale.

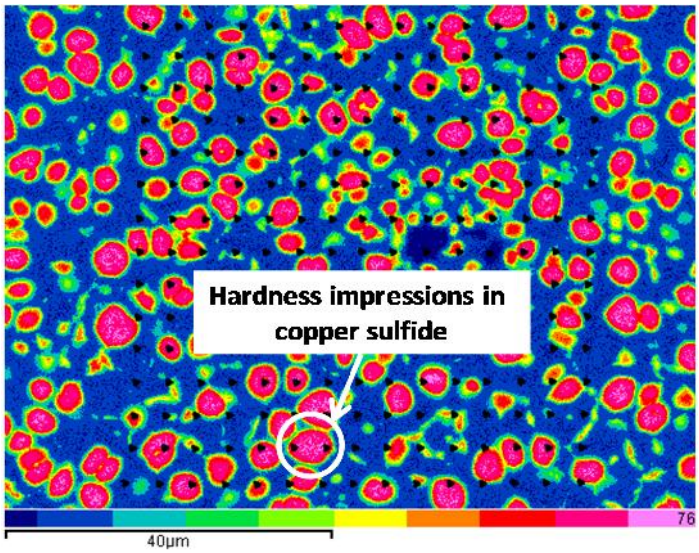

Figure E.2: Residual hardness impressions on a 5.17% Fe matte particle section with respect to a predominantly false pink color copper sulfide map at 40µm size scale.

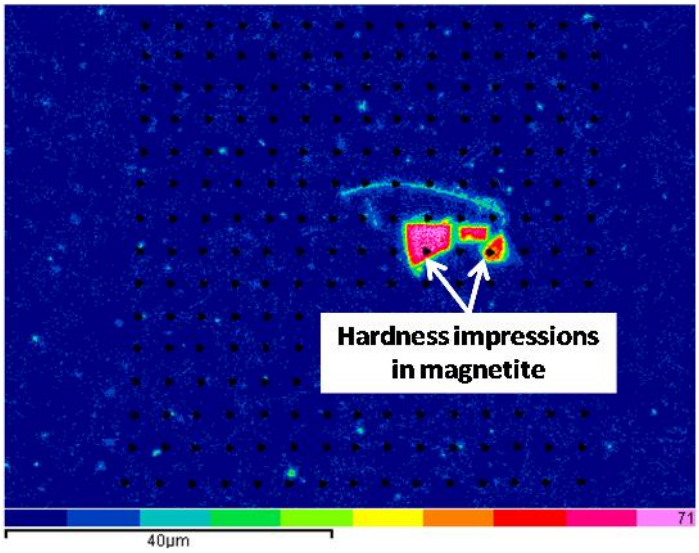

Figure E.3: Residual hardness impressions in magnetite at 40µm size scale on a particle section of the 5.17% Fe matte.

APPENDIX F
BATCH GRINDING SIZE DATA

Table F.1: Measured particle size distributions of the 5.17% Fe matte in terms of cumulative percentage passing sieve size.

Sieve Size (mm)	Feed (%)	5 kWh/t (%)	15 kWh/t (%)	25 kWh/t (%)
6.700	100.00	100.00	100.00	100.00
4.750	99.92	100.00	100.00	100.00
3.350	99.49	100.00	100.00	100.00
2.360	96.99	100.00	100.00	100.00
1.700	89.24	99.98	100.00	100.00
1.180	71.22	99.82	100.00	100.00
0.850	52.24	99.70	100.00	100.00
0.600	30.77	99.42	100.00	100.00
0.425	17.72	98.48	100.00	100.00
0.300	8.78	92.62	99.99	100.00
0.212	4.08	75.50	99.87	99.98
0.150	1.78	55.87	99.41	99.79
0.106	0.77	40.17	95.45	99.17
0.075	0.32	29.14	80.83	95.83
0.053	0.14	21.67	65.02	84.59

Table F.2: Measured particle size distributions of the 0.15% Fe matte in terms of cumulative percentage passing sieve size.

Sieve Size (mm)	Feed (%)	5 kWh/t (%)	15 kWh/t (%)	25 kWh/t (%)
6.700	100.00	100.00	100.00	100.00
4.750	99.98	100.00	100.00	100.00
3.350	99.79	100.00	100.00	100.00
2.360	98.76	100.00	100.00	100.00
1.700	95.11	100.00	100.00	100.00
1.180	84.31	100.00	100.00	100.00
0.850	71.37	99.86	100.00	100.00
0.600	51.07	99.59	100.00	100.00
0.425	32.44	97.26	99.98	100.00
0.300	16.85	86.77	99.91	99.95
0.212	8.35	65.20	99.06	99.86
0.150	3.79	44.12	92.58	99.04
0.106	1.65	27.64	72.32	94.09
0.075	0.80	17.94	50.40	80.03
0.053	0.39	12.14	34.69	59.12